THE UNIVERSITY OF
SYDNEY

COPYRIGHT AND USE OF THIS THESIS

This thesis must be used in accordance with the provisions of the Copyright Act 1968.

Reproduction of material protected by copyright may be an infringement of copyright and copyright owners may be entitled to take legal action against persons who infringe their copyright.

Section 51 (2) of the Copyright Act permits an authorized officer of a university library or archives to provide a copy (by communication or otherwise) of an unpublished thesis kept in the library or archives, to a person who satisfies the authorized officer that he or she requires the reproduction for the purposes of research or study.

The Copyright Act grants the creator of a work a number of moral rights, specifically the right of attribution, the right against false attribution and the right of integrity.

You may infringe the author's moral rights if you:

- fail to acknowledge the author of this thesis if you quote sections from the work
- attribute this thesis to another author
- subject this thesis to derogatory treatment which may prejudice the author's reputation

For further information contact the University's Director of Copyright Services

sydney.edu.au/copyright

Kinetics of Magnesium Extraction from Activated Serpentine by Carbonic Acid

A thesis submitted in fulfilment of the requirements for
the degree of
DOCTOR OF PHILOSOPHY

by

Ali Zafaranloo

School of Chemical and Biomolecular Engineering
The University of Sydney

September 2015

Declaration

I hereby declare that the work presented in this thesis is solely my own work and that, to the best of my knowledge, the work is original except where otherwise indicated by reference to other authors. No part of this work has been submitted for any other degree or diploma.

Ali Zafaranloo
September 2015

Abstract

The dissolution characteristic of thermally activated serpentine under the additive-free carbonic acid system plays a significant role in the success of the serpentine-based mineral carbonation process. It is believed that magnesium (as MgO in activated rock) is liberated by the protons associated with the MgO-CO_2-H_2O equilibria. The availability of protons is inhibited by the accumulation of magnesium in the aqueous phase as the extraction proceeds. Parallel with leaching, the precipitation of $MgCO_3$ under hydrothermal conditions further contributes to the complexity of this system. The OLI-MSE thermodynamic simulations provided predictions for the reaction pathways in the MgO-CO_2-H_2O system. Under the reaction conditions applicable for the *ex situ* mineral carbonation process, e.g., T = 423 K and P_{CO2} = 100 bar, the equilibrium solubility of magnesite is predicted as C_{Mg} ~0.0197 mol kg^{-1} at the corresponding pH of 5.3.

Experiments were carried out over a wide range of conditions, covering different reaction temperatures (from 303 to 473 K), pressures (from 10 to 160 bar), mass loading factors (from 0.03 to 1 min), and particle sizes (20 to 180 μm) by using a continuous fluidised bed reactor under the saturated CO_2-H_2O system.

The increase in concentrations of magnesium in the effluent corresponds to higher rates of extraction in the reactor; however, at sufficiently high rates, concentrations were found to be limited by the equilibrium solubility of $MgCO_3$. No evidence for $MgCO_3$ particles in the effluent or/in the reactor was found. It was concluded that the corresponding formation of solid magnesium carbonate species must be associated with the porous substrate. The experimental data for which magnesium concentrations were below the saturation value were correlated as,

$$\frac{dX_{Mg}}{dt} = k_{H^+} [H^+]^n e^{-E_a/RT} f(X)$$

The form of the rate function $f(X)$ at X_{Mg} ~0.25 showed a minimum standard deviation with $n \cong 1$ and also implied that $E_a \approx 0$, suggesting that

the rates at undersaturated conditions are directly proportional to the bulk aqueous activity of protons and that activation energy becomes negligible. It was further concluded that the difference between these results and those reported for the dissolution of crystalline serpentinite (e.g., $n \cong 0.53$ and $E_a \approx 10$ kcal mol^{-1} (Daval et al., 2013a)) may reflect the fact that the employed activated material is amorphous rather than crystalline.

The consensus of the mean form of rate functions $f(X)$ for the undersaturated data with the shrinking core models suggests that the product layer diffusion control shrinking core model more-or-less reproduces the trend in the data. However, due to the lack of sensitivity to particle size, it was concluded that this model cannot be correct, since the results for the variation in particle size (within a factor of nine) suggest that the reaction rates should be independent of the external surface area of the particles. This behaviour, however, was not matched within the product layer diffusion control model. It was therefore concluded that an alternative model similar to the grain models, in which the dependence of the rate on particle size is a balance between intergranular diffusion and reaction of the grains, may provide a better overall description of the reaction process.

It was also found that the relatively high extent of material removal during the dissolution process did not correspond to the significant development of internal voidage and porosity, suggesting that a major restructuring process is involved as particles react. Observations of the post-leached particles through SEM further indicated this surface restructuring phenomenon. Dissolution and reprecipitation of silica inside the internal reaction interfaces and/or on the outer surface of the particles are thought to be responsible for this surface restructuring process. The relatively high measured concentrations of silica in the aqueous leachate for almost all experimental cases indicate the reprecipitation of amorphous silica on the reacting surfaces, similar to the dissolution-reprecipitation mechanism observed in the literature.

Additionally, under saturated conditions, it was found that a very different rate-limiting mechanism governs the system – most likely as a result of the impulse of the state of equilibria in the carbonic acid system. The

dissolution and reprecipitation of the leached magnesium further inhibit the extraction of magnesium. The SEM-EDS analyses verified the formation of magnesite species through the reaction layers of the particles. Under such conditions, the extraction of magnesium was inhibited by the equilibrium.

In summary, this thesis contributes to the understanding of the kinetics of magnesium extraction at conditions corresponding to far-from-equilibrium and close to equilibrium. Under supersaturated conditions, parallel precipitation and deposition of carbonate species through the reaction interfaces of the solid/fluid inhibit magnesium extraction by limiting the diffusive transport of protons and leached aqueous magnesium species. In addition, the reactions associated with the dissolution and reprecipitation of silica species further influence the extraction of magnesium under undersaturated conditions, likely via a decrease in the interdiffusion of active aqueous species between the reaction layers.

Acknowledgements

First and foremost, I would like to express my sincere appreciation to my supervisor Professor Brian S. Haynes for his continuous support, guidance and patient during my Ph.D. project. This thesis would not have been possible without his valuable academic insight, and I am very thankful for his precise and thoughtful feedback on my thesis. I am grateful to have had Brain as my supervisor.

I would like to thank Dr. Jason Mann for his help and guidance at initial stages of my project, and I acknowledge him for our collaboration opportunities. Also, I would like to thank my co-supervisor Dr. Alejandro Montoya.

My thanks go to all members of the combustion group, past and present, specifically Ms. Marta Kremky, Mr. Sergio Londono, Dr. Kambiz Shojaee, Dr. Mohammad Zangouei, Dr. Zhenyi Guo, Dr. Zhanying Zheng, Dr. Asanka Rahubadda, Mr. Juan David Gonzalez Calderon, Ms. Radhika Moore, and Mr. James Lang for their help and friendship throughout my PhD. At the School of Chemical and Biomolecular Engineering, I would like to thank Dr. Jeffrey Shi, and Mr. Bogumil Eichstaedt, as well as all the administrative staff for their support and assistance.

My appreciation is extended to the Australian Centre for Microscopy & Microanalysis, specifically Dr. Patrick Trimby and Mr. Adam Sikorski, for all of their help and support. I would also like to acknowledge the financial support from Henry Bertie and Florence Mabel research scholarship of the University of Sydney and Orica Mining Services & MCi for incident funding towards my project.

Thanks to T.L. Procyshyn for her helps in editing some parts of this work. Thanks to all my good friends, Dr. Ali Fathi, Dr. Ali Negahi, and Mr. Mehdi Eizadjou for their friendship and assistance.

Finally, and above all, I would like to express my deepest appreciation to my parents, Surur and Amir, and my sister and brother-in-law, Nazanin and Arshia, for their unconditional love, constant encouragement and support throughout my life. I dedicate this thesis to my parents.

Contents

List of Figures

List of Tables

Nomenclature

A_s	reactive surface area of particles	(m^2 g^{-1})
A_r	reactor cross-section area	(cm^2)
a_i	activity of species i	(-)
C_i	molality of the aqueous elements i	(mol kg^{-1})
$C_{equilibrium}$	equilibrium concentration	(mol kg^{-1})
$C_A\vert_0$	molar concentration of solid	(mol cm^{-3})
d_p	intermediate particle size	(µm)
$d_{4,3}$	volume moment mean	(µm)
$d_{3,2}$	Sauter mean diameter	(µm)
d^*	dimensionless particle size parameter	(-)
$\mathcal{D}_{eA}$	diffusivity coefficient	(m^2 s^{-1})
E_α	the apparent activation energy	(kcal mol^{-1})
f_{CO_2}	carbon dioxide fugacity	(atm)
f^o	fugacity standard state	(1 atm)
$f(x)$	kinetic function form	(-)
K_{eq}	equilibrium constant	(-)
$k_{reactant}$	the intrinsic rate constant	(kg (s mol)$^{-1}$)
K_{sp}	solubility product	(-)
k_v	volumetric reaction rate constant	(mol s^{-1} cm^{-3})
J_{Ar}	mass flux of A in the radial direction	(kg m^{-2} s^{-1})
M_0	feed mass	(kg)
MW_i	the atomic weight of element i	(kg mol^{-1})
$\dot{m}_{water}$, $\dot{m}_{H2O}$	water mass flow rate	(g min^{-1})
$\dot{m}_m$	total mass flow rate	(g min^{-1})
$\dot{m}_{CO2}$	carbon dioxide mass flow rate	(g min^{-1})
m_{CO2}	carbon dioxide molality	(mol kg^{-1})
m^o	molality standard state	1(mol kg^{-1})
$N_i\vert_0$	initial number of moles of element i	(mol)
dN_i/dt	molar dissolution rate	(mol s^{-1})
n	apparent overall reaction order	(-)
P_{CO2}	carbon dioxide partial pressure	(bar)

$\frac{P}{P_0}$	relative pressure	(-)
R	gas constant	(kcal $K^{-1}mol^{-1}$)
R_0	initial particle radius	(m)
r_c	the radius of retreating interface	(m)
r_i	dissolution rate	(mol s^{-1})
T	temperature	(K)
t	time	(s)
u^*	dimensionless fluid superficial velocity	(-)
u	fluid superficial velocity through the reactor	(cm s^{-1})
u_{mf}	minimum fluidisation velocity	(cm s^{-1})
$\dot{V}_{mixtur\,flow}$	volumetric flow rate of mixture flow	(cm^3 min^{-1})
$V_{Reactor}$	the volume of the reactor	(cm^3)
X_i	the fractional extent of conversion	(-)
dX_i/dt	dissolution rate	(s^{-1})
$Y_i\|_0$	mass fraction of an element i	(-)
Greek		
ρ_f	density of the reactive fluid	(g cm^{-3})
ρ_m	density of the mixture fluid	(g cm^{-3})
ρ_s	density of solid particles	(g cm^{-3})
μ_f	viscosity of the reactive fluid	(g (cm s)$^{-1}$)
τ_m	mass loading factor	(min)
τ	the residence time of the reactor	(s)
γ_i	activity coefficient of species a_i	(-)

Chapter 1. Introduction

1 Introduction

Climate change is perhaps one of the most challenging issues humanity faces in the current century. The adverse effects of climate change have intensified over the past decades due to increasing demand and consumption of energy derived from the combustion of fossil fuels (i.e., coal, oil, and natural gas). The abundant use of fossil fuels has resulted in an increase in anthropogenic greenhouse gas (GHG) emissions. Carbon dioxide is the largest contributor of GHG, representing ~60% of total GHG emissions (InternationalEnergyAgency, 2014). Global CO_2 emissions reached 35.3 billion tonnes in 2013, which is approximately 56% higher than two decades ago (Jos G.J. Olivier et al., 2014). Atmospheric CO_2 levels have increased from 280 ppm during pre-industrial times to a record high of 400 ppm in June 2015 (Ed Dlugokencky and Pieter Tans), with a corresponding increase in global surface temperature of about 0.8 K. The period from 1983 to2012 – was the warmest 30 year period of the last 1400 years in the Northern Hemisphere. The uncontrolled release of GHG has resulted in an increase of the natural greenhouse effect; however, the impacts of this increase may not be immediately apparent since stability is an intrinsic characteristic of the interacting climate. Nevertheless, if the current trend in GHG emissions continues, more intense anthropogenic warming and rise in sea level are anticipated. Without climate change mitigation policies, it is projected that global GHG emissions in 2030 will increase by 25% to 90% relative to the year 2000 level (Pachauri et al., 2014).

The fifth assessment report from the Intergovernmental Panel on Climate Change (IPCC) confirms that, among all factors, human activities influence the climate system most profoundly (Pachauri et al., 2014). The International Energy Agency (IEA) reported that, of all human activities that produce GHG, the use of energy represents by far the largest source of CO_2 emissions, accounting for ~90% (InternationalEnergyAgency, 2014). These

CO_2 emissions result directly from oxidation of fossil fuels. According to IEA (2014), in 2012 fossil fuel sources accounted for 82% of the global primary energy supply. The growing worldwide demand for fossil fuels has played a significant role in the upward trend of CO_2 emissions. The IPCC proposed an upper limit on atmospheric CO_2 levels of 450 ppm to prevent irreversible climate change. The fifth IPCC assessment report indicates that, to avoid the worst effects of climate change, it is essential to reduce global CO_2 emissions by 40-70% by 2050 with respect to 2010 levels and to reduce emission levels to near zero or below by 2100. Considering the long life of CO_2 in the atmosphere, stabilising CO_2 concentrations at any level, requires a large reduction of CO_2 emissions from current levels. In 2005, the IPCC provided guidelines reviewing the various pathways to reduce GHG emissions (Metz et al., 2005). Among all, Carbon Capture and Storage, or Sequestration, (CCS) is the most suitable starting point for large-scale point-source CO_2 mitigation. According to predictions provided by the IPCC, the use of CCS coupled with additional mitigation policies, such as utilisation of less carbon-intensive fossil fuels along with an increase in the use of renewable energies, can potentially reduce CO_2 emissions by up to 18.5 Gt per annum by 2020. The current approaches to CCS within the industry are mainly reliant on geological sequestration. However, uncertainties regarding the potential capacity of global geological sequestration for large-scale CCS and the need for additional storage monitoring techniques have resulted in a significant drawback in process feasibility compared with that initially perceived by the IPCC in 2005 (Bachu et al., 2007, Eccles et al., 2009, Little and Jackson, 2010). An alternative for CCS is the injection of CO_2 into oceans, which is an immature technology that will alter the local chemical environment and likely has consequences on the ecosystem. Mineral carbonation offers a potentially more feasible option for CO_2 sequestration – as the products of mineral carbonation are stable and would provide storage capacity on a geological time scale (Lackner et al., 1995). In this process, CO_2 is reacted with metal oxide bearing minerals, and forms the corresponding carbonates (Mazzotti et al., 2005, O’Connor et al., 2005). Mineral carbonation mimics natural weathering phenomenon, but on an industrial scale. From a thermodynamics point of view, carbonates represent a lower energy state than CO_2 (Goff and Lackner, 1998b). The carbonation reaction is exothermic and can theoretically yield energy; thus, taking advantage of the natural chemistry of this process offers an excellent opportunity for reduction in CO_2 emissions.

1.1 Background for Carbon Mineralisation as a Path for Reduction in CO_2 Emission

The weathering of silicate minerals is important as approximately 92 wt.% of the earth's crust is composed of silicate minerals. In this regard, the concentration of carbon dioxide in the atmosphere over the last 100 million years has been influenced (if not controlled) by the transformation of calcium and magnesium containing silicate rocks into carbonate through the weathering and sedimentation processes (Berner et al., 1983). Approximately 10% of all atmospheric carbon dioxide is estimated to be exported to carbonates by the weathering of silicate worldwide per annum (Schopka et al., 2011, Gaillardet et al., 1999). Wilson et al. (2006) showed that abandoned serpentine-rich mine tailing at Clinton Creek, Canada, may contain carbonate levels up to 60 wt.%. This observation underlines that the carbon isotopic composition of such carbonates confirms their atmospheric origin (Wilson et al., 2006). Weathering of serpentinite has been regarded as a primary source of natural present day magnesium carbonates and is responsible for the majority of all large-scale sedimentary magnesite ($MgCO_3$) deposits (Möller, 1989). It is, however, worth noting that the kinetics of chemical weathering reactions under natural conditions are not sufficient to meet current anthropogenic CO_2 emissions (Seifritz, 1990). Lackner and co-workers proposed that employment of ultramafic rocks for industrial-scale mineral carbonation processes could be viewed as an alternative to reducing CO_2 emissions.

For the industrial approach, depending on the magnesium content of the ore, ~1.6 to 3.7 tonnes of ore are typically required to fix a tonne of CO_2 (O'Connor et al., 2005). Among the available mafic minerals, the serpentine mineral group is an attractive feedstock for the CCS process due to its great abundance and its relatively high MgO content. Serpentinised peridotite reserves are estimated to be in the hundreds of thousands of gigatonnes. Carbonation of this source could potentially mineralise the CO_2 produced from the combustion of all known coal reserves (10,00 Gt C) (Lackner, 2002, Lackner et al., 1995, Goff and Lackner, 1998b). Furthermore, Brent and Petrite (2008) showed that the scale of mining practice of serpentinite required for mineral carbonation is in common practice with rock and coal based mining operations.

1.1.1 Review of Research Development for Mineral Carbonation

Ex situ aqueous mineral carbonation is an accelerated form of natural weathering of silicate rocks through above-ground processes. The best-studied case is the aqueous mineral carbonation process was initially proposed by Albany NETL (O'Connor et al., 2005). This process occurs in two main steps. The first step is the detachment of magnesium from the mineral structure while leaving a SiO_2 rich layer. The second step is the precipitation of stable magnesium carbonate. The hypothesised sequence of the reactions is illustrated through (R 1.1 to R 1.3),

$$CO_2\,(aq) + H_2O\,(l) \rightleftharpoons H_2CO_3\,(aq) \rightleftharpoons H^+\,(aq) + HCO_3^-\,(aq) \qquad \text{(R 1.1)}$$

serpentine dissolution,

$$Mg_3Si_2O_5(OH)_4\,(s) + 6\,H^+(aq) \rightleftharpoons 3Mg^{2+}(aq) + 2SiO_2(s) + 5H_2O \qquad \text{(R 1.2)}$$

carbonation formation,

$$Mg^{2+}\,(aq) + HCO_3^-\,(aq) \rightleftharpoons MgCO_3\,(s) + H^+ \qquad \text{(R 1.3)}$$

where CO_2 is first dissolved in water to form carbonic acid (H_2CO_3), which is then dissociated to protons (H^+ or H_3O^+) and bicarbonate ions (HCO_3^-). The protons hydrolyse the mineral, resulting in the liberation of magnesium cations and the formation of free silica and water. The magnesium cations in the solution react with the bicarbonate ions to form solid magnesium carbonate ($MgCO_3$). Many research groups, such as Los Alamos National Laboratory (LANL), Åbo Akademi University, and National Energy Technology Laboratory (NETL), have observed that various strategies, such as using thermally activated serpentine, increasing the activity of carbon dioxide in the solution, and increasing the overall surface area of the feedstock through high-energy grinding, result in improvement of the overall yields of the carbonation process. However, the energy cost associated with very fine grinding of the feedstock directly contributes to decreasing the process viability (Huijgen and Comans, 2005, Huijgen et al., 2007, Gerdemann et al., 2007, Haug et al., 2010). On the other hand, thermal activation of feedstock was estimated to require up to ~250 kWh of electricity per tonne of serpentine (O'Connor et al., 2005). As a result, in 2005 the IPCC concluded that the carbonation of serpentine is not economically feasible. Since then, many studies have re-evaluated the different steps involved in the Albany NETL process. The method of thermal activation was reconsidered by Geerlings and Wesker (2007), who showed that thermal activation of serpentine is achievable using waste heat released from power generation processes. Another area of interest is the dissolution step, which is probably the rate-limiting step for serpentine carbonation. Many previous investigations have reported the potential passivating quality of silica layers during the dissolution of serpentinite minerals (Daval et al., 2011, Daval et al., 2013a). Almost all of the literature is in agreement that the rate of dissolution of silicate minerals declines as the silica layer on the mineral surface becomes thicker. Hence, some researchers, such as Béarat et al. (2006) and Julcour et al. (2015), have suggested that the removal of silica layers is possible through an *in situ* mechanical exfoliation process – but there is no information specified for the dissolution characteristics of the feedstock, rather than enhanced carbonation yields. While, other studies have examined the role of mineral acids in the extraction of magnesium from serpentinite minerals under low temperature and pressure conditions (Park et al., 2003, Park and Fan, 2004, Teir et al., 2007, Van Essendelft and Schobert, 2009a, Van Essendelft and Schobert, 2009b, Van Essendelft and Schobert, 2010). However, under such conditions, carbonate precipitation is observed to be thermodynamically unfavourable, and subsequent alkalisation is required. This alkalisation step requires a large amount of non-regenerable reagents, which makes these processes economically unfeasible. Attempts were also made by Park and co-workers to develop a low temperature and pressure carbonation process by using chelating agents and weak acids. In these works a range of leaching agents, such as dilute mixtures of oxalic acid and ethylenediaminetetraacetic acid (EDTA), were used as a replacement for strong mineral acids. Furthermore, Park and co-workers introduced a two-stages process (pH swing), where magnesium is first extracted from serpentine at a low pH, and then, through a second step, the extracted magnesium is converted to carbonates. However, the expenses associated with the use of acids (i.e., the recovery and regeneration process) and the requirements for alkaline agents to raise the pH for the precipitation of carbonates are regarded as drawbacks of this process. More recently, Steel et al. (2013) proposed a new pH swing process that uses tertiary amine to bind with protons at low temperatures and increase the pH to ~8, which is suitable for carbonate formation, and the amine then regenerates through the high-temperature process to produce the low pH favourable for magnesium extraction. They reported optimum dissolution conditions of serpentine achieved at relatively high-temperature conditions from 373 to 423 K by using a mixture of amine and organic acid. Nevertheless, difficulties in controlling the lower pH values (required for the dissolution reaction), including acid consumption and associated amine regeneration, remain important constraints for the practicality of this method at the industrial scale. Likewise, the application of strong alkaline solutions (e.g., NaOH that can dissolve silica) suggested by Blencoe et al. (2012), is deemed to be not practical due to difficulties related to the recovery of the NaOH catalyst. Wang and Maroto-Valer (2011) used ammonium salt NH_4HSO_4 to extract magnesium cations from serpentine in cooperation with NH_4HCO_3 to promote the precipitation stage. Conceptually, this route offers complete integration for the CCS process and allows operation at the relatively low pressure. However, the price of the additive and associated complex regeneration process is the main disadvantage of this process. In the Albany NETL process, it is believed that the presence of salts and bicarbonate in the optimum solution chemistry may facilitate the dissolution/precipitation processes. This belief was, however, challenged in other studies showing that salinity does not improve the dissolution kinetics of serpentine minerals (olivine) (Olsen, 2007, Prigiobbe et al., 2009).

Accordingly, additive free approaches under the high pressure-temperature carbonic acid system have the greatest potential for future development of mineral carbonation processes. A successful mineral carbonation process requires detailed knowledge of the dissolution and precipitation kinetics of the involved reactions. In the Albany NETL process, mineral dissolution and subsequent carbonation occur in a single unit of operation (batch reactor). If equilibrium is maintained at a solid-fluid interface among the reaction products and aqueous phases – the rate of the dissolution reaction will be proportional to the rates of forward and reverse of the equilibrated species. It is thus apparent that the success of the Albany NETL process relies heavily on the dissolution characteristics of thermally activated serpentine.

1.2 Research Objectives

The extraction of magnesium from thermally activated serpentine constitutes a great importance in the mineral carbonation process, due to its contribution in a final conversion step. Despite the preliminary work presented by O'Connor and co-workers the dissolution behaviour of activated serpentine at temperatures and pressures (up to 473 K and 150 bar, respectively) relevant to the *ex situ* mineral carbonation process remain poorly understood. Most of the relevant research focusing on the dissolution of activated serpentine under the carbonic acid system are limited to low-pressure conditions (Werner et al., 2014a, Werner et al., 2014b, Werner et al., 2013). The optimisation of magnesium extraction under the carbonic acid system requires an understanding of the interactions between the dominant phase equilibria, since a potential interference between the dissolution and carbonate precipitation reactions could represent an important constraint on the progress of the dissolution reaction. Furthermore, knowledge of silica structure, composition, and the dissolution mechanism is essential for avoiding enclosing the reaction interfaces during the dissolution.

Better understanding of the parameters influencing the kinetics of magnesium extraction is required for engineering design and the successful scale-up of the mineral carbonation technology. Hence, in the present study the kinetics of magnesium extraction from thermally activated serpentine under the CO_2-H_2O system, with a view to identifying the underlying rate-limiting mechanisms, is investigated. The effect of important variables on the dissolution reaction, including particle size, CO_2 partial pressure, reaction temperature, and saturation states, are systematically considered.

1.3 Dissertation Structure

The chapters in this study are arranged in the order of development from the underlying theoretical considerations to the experimental results. In Chapter 2, the literature relevant to the dissolution of crystalline silicate minerals (mostly under acidic conditions) is surveyed. Also, a review of the phase equilibria under the carbonic acid system is provided. The experimental apparatus and procedure are described in Chapter 3, and the results of the objective investigations are presented in Chapter 4. In Chapter 5, the experimental results are discussed and interpreted based on the underlying thermodynamics, kinetics analysis for the equilibrium adsorption of protons and bicarbonate ligands, and physical properties of the post-leached particles. Finally, the conclusion is derived, and suggestions concerning the direction of future research are proposed.

Chapter 2. Current Understanding of the Silicates Dissolution

2 Introduction

This chapter provides a brief review of the current findings regarding the chemical and physical fundamentals of silicates dissolution[1]. Serpentine dissolves under the action of acid according to the overall reaction shown schematically in (R 2.1),

$$3\ MgO.2SiO_2.(2\text{-}x)H_2O\ (s) + 6\ H^+\ (aq) \rightleftharpoons 3\ Mg^{2+}\ (aq) + 2\ SiO_2\ (s) + (5\text{-}x)\ H_2O\ (aq) \qquad \text{(R 2.1)}$$

Under stoichiometric dissolution, magnesium and silica release into solution with a molar ratio of 3:2. Selective removal of magnesium from the outer surface can account for greater magnesium release for a period of time. This trend results in the accumulation of a silica surface layer. The leached layer may form under at least two circumstances. First, the released silica precipitates as an amorphous surface layer induced by local supersaturation. Second, the chemical affinity for dissolution may reach an adequate level, enabling a new lower-entropy surface phase form through rearrangement of the remaining elements on the surface (Bales et al., 1985). Depending on the conditions, the chemical and structural properties of the leached layer may also involve several complex phenomena, such as ion exchange, precipitation of the diffusing magnesium species, and polymerisation of silica (Dran et al., 1986). Berner (1978) observed that there is a relation between the solubility of a mineral and the rate-controlling mechanism by which it dissolves. Minerals with solubilities in

---

[1] Here it is worth noting that the information provided in this chapter is basis on the surveyed literature that mostly covers the dissolution of crystalline silicates, since most kinetics studies have focused on the dissolution of crystalline minerals. However, the ultimate objective of the present study is to investigate kinetics of magnesium extraction from thermally activated serpentine (almost amorphous) under the carbonic acid system, for which the relevant literature is provided in Chapter 3.

the order of 10^{-3} (ml L^{-1}) dissolve at a rate limited by their surface reaction mechanism, while more soluble minerals are more likely to be restricted by the transport mechanism (Berner, 1978). As stressed by previous studies, such as Stumm and Wollast (1990), dissolution of minerals typically proceeds as a combination of chemical and physical reaction steps. If precipitation of the diffusing magnesium species occurs through the reaction interfaces, it likely induces another rate-limiting step. It is thus imperative to attain an inclusive understanding of the fundamental concepts of the silicate dissolution process (e.g., chemical affinity, dissolution mechanism, and pH) under different circumstances.

2.1 General Rate Law: Dissolution Rate & Chemical Affinity

The driving force of a reaction, ΔG, controls whether a mineral dissolves or precipitates under a given set of conditions. It is postulated that the rates of mineral hydrolysis reactions in nature are primarily controlled by the chemical affinities of the reactions (Aagaard and Helgeson, 1982).

ΔG is defined as,

$$\Delta G = RTln(\Omega), \tag{2.1}$$

where Ω is the ratio of the reaction activity quotient, ($Q = \prod_i a_i^{n_i}$) and the equilibrium constant, K_{eq}, for the reaction at the specified temperature and pressure ($\Omega = Q/K_{eq}$). The chemical affinity of the reaction is defined as being equal to $-\Delta G$, and has a value of zero at equilibrium. According to Lasaga (1998), the most general forms of the rate law applicable to mineral surface growth and dissolution reactions can be described by equation (2.2),

$$Rate_{net} = k_0 A e^{-E_a/RT} \prod_i a_i^{n_i} f(\Delta G), \tag{2.2}$$

where k_0 is a rate constant (mol m^{-2} s^{-1}), A is the reactive surface area of the mineral, E_a is the apparent activation energy of the overall reaction (kcal mol^{-1}), T is the temperature (K), R is the gas constant, a_i is the activity of species i, in the rate-determining reaction, and $Rate_{net}$ denotes the net rate of the reaction (rate = forward – reverse rate). Activation energy is an important parameter as it influences the reaction mechanism (Lasaga, 1981). The activation energies of a reaction, according to Lasaga et al. (1994), should be termed as apparent activation energies to signify the contributions of many terms, rather than a potential energy barrier of an elementary reaction. Casey and Sposito (1992) reported that dissolution activation energies vary greatly depending on solution pH. The temperature dependence of the rate law enters essentially through the Arrhenius equation for the rate constant, k,

$$k = k_0' e^{-E_a/RT} \tag{2.3}$$

where k_0' combines all of the other terms in equation (2.2). The final term in equation (2.2) introduces the dependence of the overall reaction rate on the saturation or undersaturation states of the system. This is expressed as a function of, f, the free-energy change of the growth or dissolution reaction. At equilibrium ($\Delta G = 0$), this function is equal to zero, and is where the kinetics are fully compatible with thermodynamics.

The behaviour of f away from equilibrium conditions is directly influenced by the kinetic mechanism. Based on common convention, an overall dissolution reaction is arranged with the reactants on the left and the products on the right; thus, ΔG of the spontaneous reaction is negative. The corresponding precipitation reaction is generally written from right to left; hence, ΔG of the reaction is positive. Therefore, it is important to attain an understanding from the $f(\Delta G)$ function in the interpretation of the kinetics data. The relation of the dissolution rate and ΔG, can be described with the aid of transition-state-theory for a rate-limiting elementary reaction, as derived by Lasaga (1981 & 1998), and Aagaard and Helgeson (1982) and shown by equation (2.4),

$$f(\Delta G) = -\big(1 - exp(\Delta G/RT)\big), \tag{2.4}$$

where ΔG is the Gibbs free energy of the overall reaction (kcal/mole), R is the gas constant, and T is the temperature (K). According to Lasaga (1998), highly under-saturated systems will have a negative ΔG, while highly saturated systems correspond to a large positive ΔG. According to the general principles, the dissolution rate moves to a limiting region termed the dissolution plateau when $\Delta G \rightarrow -\infty$. In this region, dissolution is constant with ΔG, and the reverse rate is negligible. Closer to equilibrium, dissolution reaction rates increase quite sharply with decreasing ΔG. Furthermore, near equilibrium the dissolution becomes slower and the rates become dependent on ΔG. Calculation of the precipitation rates presented by equation (2.4) show that the precipitation rates depend on ΔG over the entire saturation state. Through a complex reaction mechanism for composite reactions, the ΔG function can be determined by consideration of a rate-limiting single elementary reaction. Lasaga (1998) verified that, at certain undersaturation states the rate of the dissolution reaction will be independent of ΔG, and the reverse rate will become negligible – this is termed the far-from-equilibrium conditions (large negative ΔG). In this case, the rate of the dissolution reaction is controlled by the activity of the components (e.g., H^+) in the solution. Conversely, at near equilibrium the ΔG function of the overall reaction becomes linear and the dissolution rates are more dependent on ΔG. Therefore, equation (2.4) reduces to equation (2.5) for conditions close to equilibrium. In this instance, if the mineral dissolution and precipitation rates are controlled by the same elementary reaction at all saturation states, a linear function of ΔG can be derived for the dissolution and precipitation rates.

$$f(\Delta G) = -\Delta G/RT \qquad (2.5)$$

In dissolution/growth, the rate law becomes more complex as one deviates from equilibrium. In the case of precipitation (crystal growth) from aqueous solution, the growth process shows a strong dependence on the supersaturation state (Lasaga, 1998). In complex cases, the system may exhibit several phase transitions as ΔG changes. This type of behaviour could be responsible for deviation from the linear or near-linear rate laws evaluated with transition state theory. Therefore, the shape of the function, $f(\Delta G)$, provides useful information about the mechanism of the dissolution/growth of the minerals.

Rimstidt and co-workers expressed that the dissolution and precipitation rates of quartz obey the same linear function of ΔG, in the vicinity of equilibrium (Rimstidt and Barnes, 1980, Rimstidt, 2013). However, it is worth to note that the SiO_2-H_2O system is compositionally simple, and it is thus feasible to anticipate that a single reversible reaction mechanism might control both dissolution and crystal growth. However, in more complex compositional systems, the rate of the overall reaction may be a non-linear function of ΔG, at near equilibrium. In this case, different reaction mechanisms control the two separate dissolution and precipitation processes. Nagy et al. (1991) showed that the dissolution and precipitation rates of kaolinite ($Al_2Si_2O_5(OH)_4$) could not be expressed by the same linear function of ΔG in the vicinity of the equilibrium. Also, observation of the work conducted by (Shiraki and Brantley, 1995) indicated that there is almost no chance to evaluate the reaction rates of calcite ($CaCO_3$) over the full range of ΔG with one rate equation; rather, a series of rate curves is required to explain the dissolution and precipitation processes.

The most commonly accepted reason for the observed non-linear rate law is ascribed to the mechanism of controlling the dissolution process with relation to surface defects (Lasaga, 1983). Lasaga (1983) showed that a critical degree of undersaturation is required for the formation of crystal dislocation cores and etched pits on a mineral surface. Blum et al., (1990) suggested that crystal dislocations most likely have a more substantial effect on the bulk dissolution rates of quartz at saturation near equilibrium once microscopic etch pits should not form. The role of surface defects on mineral-water kinetics was predicted by Lasaga and Blum (1986) as a function of free energies. They expressed that mechanistic transition theory can explain a form of rate law (dissolution/crystal growth), that depends on surface defects (formation etch pits as the result of dislocation of cores) as a function of a critical saturation state, ΔG_{crit}, where a dislocation core can open up to form an etch pit.

This remarkable phenomenon is defined as the ability of mineral surfaces to undergo dramatic structural rearrangement as a function of ΔG. This hypothesis is supported through scanning electron microscopy analyses, where the post-leached mineral samples show significant morphological rearrangement (Nagy and Lasaga, 1992, Burch et al., 1993, Hellmann and Tisserand, 2006). Overall, the surveyed literature suggest that fast dissolution is associated with the formation of all sorts of etch pits on the surface, while slower dissolution rates at conditions closer to equilibrium are characterised by a lack of dislocation etch pitting. In this regard, Lasaga and co-workers suggested that complex surface transformations should be considered in the development of the rate equation of dissolution kinetics (Lasaga and Kirkpatrick, 1981, Lasaga, 1998).

2.2 Dissolution Mechanism for Silicate Mineral

The ultimate goal of this kinetic study is to understand the controlling mechanisms involved in the rate-limiting steps of the dissolution process. Some previous studies have revealed that reactions controlling mineral dissolution occur at the mineral surface. Lasaga (1984) demonstrated that, under acidic conditions, surface reactions proceed according to the rate of hydrogen ion exchange with cations, with a subsequent decomposition of the structure. Lasaga (1984) further argued that the cation-proton exchange process occurs at a relatively fast rate. However, transport of the dissolved products away from the mineral/solution interface becomes critical in controlling the dissolution as conversion could be limited in the vicinity of the reaction interface. The accomplishment of this transport process is defined as a diffusion process in the solution. Hence, Lasaga (1984) stated that if all the kinetic processes of the dissolution are fast relative to the diffusion rate, the dissolution should be termed as “diffusion-controlled”; otherwise, it is termed as “surface-controlled”[1]. Lasaga (1984) stressed that, in cases of diffusion-controlled dissolution, the surface concentration of a particular element is supposedly consistent with the solubility of the

---

[1] Throughout the literature, the rate expression corresponding to the diffusion-controlled reaction is known as the parabolic rate law; in contrast, the linear dissolution kinetics are compatible with the surface-controlled process (Helgeson, 1971).

mineral; thus, in the case of surface-controlled dissolution, the surface concentration should be equal to the concentration of the species in the bulk solution. Berner (1978) suggested that relatively fast dissolution reactions are related to the diffusion-controlled mechanism. Lasaga (1984) added that in any dissolution reaction, after some period, the rate of surface detachment becomes consistent with the rate of transport away from the surface. Determination of the two rate-limiting steps described above is possible via measurement of the final value of the solution composition and monitoring compatibilities of the reaction products with saturation indices (Helgeson, 1971).

According to Brantley (2008), transport-controlled dissolution can refer to slow transport that occurs either through the fluid boundary layer or across the altered layer on the mineral surface. Several studies suggest that, during silicate dissolution, silica is released as a form of dissolved monomers and is subsequently polymerised on the reaction interfaces (Casey et al., 1989, Casey et al., 1993b, Casey et al., 1993a, Velbel, 1993). Casey et al. (1993b) observed that the near-surface reaction interfaces are enriched in silicon and hydrogen but depleted in other cations. Such layers have been observed to develop on many dissolving silicates where the rate of Si release is less than the release rate of other cations. Brantley (2008) schematically expressed that, in silicates a number of bridging oxygen bonds are responsible for the degree of connectedness of silicon atoms to the surface layer[1], and that this number decreases from 4 (Q_4) to 3 (Q_3) to 2 (Q_2) to 1 (Q_1) before the silicon atoms released into the solution (Brantley, 2008). Pokrovsky and Schott (2000), reported the presence of a polymerised surface layer on forsterite (Mg_2SiO_4) after reaction under acidic conditions composed of a silica complex linked with hydrogen-bonded water molecules connected to the Mg octahedral deeper in the structure.

The forsterite structure involves individual silicon-oxygen tetrahedra linked by magnesium atoms, which are arranged in octahedral coordination. According to Brown (1980), an important structural feature of forsterite is the existence of serrated magnesium octahedral chains. Oelkers (2001a)

---

[1] In this notation of tetrahedral sites, Q_i was noted as sites having 4, 3, 2, or 1 bridging oxygen atoms.

showed that the dissolution mechanism of forsterite varies in proportion to the reaction rates of the Mg-O and Si-O bonds of the mineral structure. During the dissolution process, if the Si-O bonds connected to the mineral structure break faster than the octahedral Mg-O bonds, resulting in the liberation of Si (Oelkers, 2001a). This effect leads to a partially separated Mg octahedral that ultimately detaches. In this case, the Mg separation mechanism constitutes the rate-limiting precursor complex for the overall dissolution reaction. In contrast, if the Mg-O bonds in an octahedral chain break more rapidly than the Si-O bonds connected to atoms in the forsterite structure, this will lead to separation of Mg and be followed by liberation of Si tetrahedrals from the mineral structure. Rosso and Rimstidt (2000) suggested that the dissolution of forsterite involves hydronium ion adsorption to the forsterite surface. In this process, two of the three hydrogen atoms are associated with breaking the two Si-O-Mg bridging oxygen atoms that form the two H-O-Si bonds on the forsterite surface. This process was termed as a coordinated process where Mg-O bonds are displaced by the nucleophilic attack of the negative side of the water dipole. This process leads to leaving Si-O bonds with a negative charge on the surface, which could repel the negative side of the water dipole and limit the progress of the reaction. Thus, the bridging hydrogen ions from the solution handle balance the charge in the broken bonds. Rosso and Rimstidt (2000) postulated that under the coordinate reaction scenarios due to the high concentration of water molecules and the high mobility of the hydrogen ions, a relatively fast process should arise compared with the overall forsterite dissolution rate. Through molecular dynamic calculations, Rustad and Casey (2012) showed that the low-energy metastable configurations that form from the breaking of bonds between metals and coordinated oxygen atoms, surveyed by facile hydroxide, hydronium or water addition.

2.3 pH Dependence of the Dissolution Mechanism

Previous studies (such as Luce et al., 1972, Schott et al., 1981, Casey et al., 1993b, Blum and Lasaga, 1988) have demonstrated that the dissolution reaction under acidic conditions proceeds through the exchange of protons with metal ions, and thus maintaining the charge balance on the surface.

Casey and Westrich (1993) reported that the release rate of cations from olivine minerals correlates with the rate of exchange of water molecules between the bulk solution and the mineral surface. In this case, the absorption of protons at the surface is sufficient for the surface protonation to be faster than the detachment of metal species (Hachiya et al., 1984).

It is perceived from past studies that the influence of pH on the dissolution rate cab be explained by the contribution of the decomposition of activated complexes under different pH conditions (Helgeson et al., 1984, Chou and Wollast, 1985, Lasaga, 1984). On the basis of coordination chemistry applied to solid surfaces, Stumm et al. (1983) postulated that fractional orders of protons and ligands are compatible and dependent on the extent of surface protonation or the concentration of ligand surface complexes. Their proposal thus leads to the conclusion, that showing non-linear adsorption exchange isotherms would control the concentration of surface species. Blum and Lasaga (1988) suggested that the slope of the log rate versus pH curve should be approximately linear when the rate is proportional to the concentration of specific surface species (e.g., protons). Lasaga (1984) showed that the reaction is related to the dissolution of silicates by reaction (R 2.2),

$$mineral + nH^+ \rightarrow silica + cations + H_2O \qquad \text{(R 2.2)}$$

The rate of this reaction is expected to be dependent on the concentration of hydrogen ions or, equivalently, on the value of activity, a_{H^+}, under acidic conditions. Many attempts were made to determine the effect of pH on the rate constant, k_θ, of mineral dissolution. According to Lasaga (1984), at far-from-equilibrium conditions, the pH dependence of the rate constants can generally be summarised as,

$$k_\theta \propto (a_{H^+})^{n_\theta} \qquad 0 \leq n_\theta \leq 1 \qquad (2.6)$$

The values of n_θ vary depending on the governing kinetic mechanism. The most common value of the nonintegral, n_θ (based on the existence of a variety of surface sites with different adsorption and reaction energies) is reported between 0.5 and 1.0. A number of studies (such as Luce et al., 1972, Sanemasa et al., 1972, Blum and Lasaga, 1988, Pokrovsky and Schott, 2000, Rosso and Rimstidt, 2000, Wogelius and Walther, 1992, Hänchen et al., 2006, Chen and Brantley, 2000) have investigated the pH dependence of the dissolution rate for forsterite material at acidic conditions, at temperatures ranging from 298 to 338 K (except Hänchen et al. (2006), who used 363 to 423 K) and at ambient pressure (except Hänchen et al. (2006), who used 15 to 180 bar). An approximate reaction order of 0.5 for hydrogen ion activity in acid solution is consistently reported through the majority of studies concerning the dissolution rates of forsterite.

Comparatively, a limited number of experimental studies have investigated the dissolution kinetics of serpentine minerals (Bales et al., 1985, Daval et al., 2013a). Bales and Morgan (1985) determined the kinetics of the dissolution of chrysotile ($Mg_3(Si_2O_5)(OH)_4$) at a constant temperature of 298 K and a pH from 7-10. According to Bales and Morgan (1985), the release rate of magnesium occurred at a steady rate and was proportional to hydrogen ion activity with an order of 0.24. Daval et al. (2013a) investigated the kinetics of lizardite ($Mg_3Si_2O_5(OH)_4$) dissolution over a temperature range of 300 to 363 K and a pH from 3.2 to 6.2. They reported that the dissolution rate as a function of aqueous silica was proportional to the order of 0.5 for the hydrogen ion activity.

2.3.1 Proton-promoted Surface Complexation Model

The dissolution process includes a sequence of reversible reactions with a single chemical step in the overall sequence being rate-limiting. A rate equation is normally expressed from transition-state-theory where the reaction rate depends on the concentration of species that form the activated complex, equilibrium constants for the formation of activated complexes, and the overall free energy change of the reaction. Oelkers and co-workers provide a summary of the different dissolution scenarios applicable for a variety of silicates (Oelkers, 2001b, Oelkers and Schott, 1995, Oelkers, 1996)). In the case of a simple metal oxide (e.g., MgO in the absence of any

SiO_2 network related to the mineral structure), it is reasonable to assume that the dissolution rate at far-from-equilibrium conditions proceeds directly through the proton and metal cation exchange reaction. The equilibrium adsorption of protons into the reaction interfaces eventually controls the dissolution rate by the expression (2.7),

$$r_+ = k_+[P] = k_+\left(\frac{k' a_{H^+}^n}{1 + k' a_{H^+}^n}\right) \tag{2.7}$$

where k_+ denotes a rate constant consistent with the P precursor complex, $[P]$ stands for its concentration, k' denotes the equilibrium constant of the precursor complex (describing the exchange reaction between protons and metal cations), a_{H^+} denotes the activity of protons, and n stands for a stoichiometric coefficient (equal to the number of hydrogen atoms required to be absorbed to form one precursor complex). Under this condition, it is assumed that the precursor complex is in the equilibrium with the reactants (e.g., H^+) and, consequently, the variation in the concentration of reactants should be proportional to the rate of the reaction forming the active complex. However, such a simple proton-promoted surface complex model was deemed inadequate to explain the underlying mechanism for minerals containing mixed-oxides. In the case of silicate dissolution, the presence of the SiO_2 network in the mineral structure, generally leads to the formation of polymerised SiO_2 on the mineral surface. As a result, the exchange reactions appear to be inhibited by restricted access to the metal-oxide bonds deep in the mineral core. Several research groups expressed models that incorporate the effects of the released cations along with the effect of protons. Among those models, Oelkers and Schott's model was successfully used to predict the dissolution rate of a wide range of minerals. Based on this model, the dissolution rate varies with the activity of the liberated cations in the solution. A general kinetic rate model for the dissolution of silicates comprising M_i cations at far-from-equilibrium conditions, is illustrated in (2.8),

$$r_+ = k_+[P] = k_+ \left(\frac{k' \left(\frac{a_{H^+}^{v_i}}{a_{M_i}^{v_i}} \right)^s}{1 + k' \left(\frac{a_{H^+}^{v_i}}{a_{M_i}^{v_i}} \right)^s} \right) \tag{2.8}$$

where the parameters v_i and s are the stoichiometric coefficients for species appearing in the formation reaction for the precursor in the rate-limiting step. Accordingly, the dissolution rate of a multi-oxide mineral appears to depend not only on the activity of protons in solution, but also on the dissolved concentrations of cations. This model successfully describes the dissolution of several minerals (i.e., enstatite ($Mg_2Si_2O_6$), basaltic glass, and talc ($Mg_3Si_4O_{10}(OH)_2$) (Oelkers and Schott, 2001, Gislason and Oelkers, 2003, Saldi et al., 2007). However, studies focused on the dissolution of forsterite revealed that the dissolution rate was not affected by the released magnesium and silica concentrations in the solution and can be adequately explained by a proton-promoted mechanism (Oelkers, 2001a).

2.4 Carbonic Acid System

Carbon dioxide storage through the *ex situ* mineral carbonation process has great potential to address the drastic environmental consequences of climate change. This section aims, to provide insight into the phase equilibria and reaction pathways involved in the CO_2-H_2O environment. The carbonic acid system includes the chemical species including carbonate and bicarbonate (CO_3^{2-} and HCO_3^-) ions, undissociated carbonic acid (H_2CO_3), dissolved carbon dioxide CO_2 (aq), and in many instances carbon dioxide in a gas phase (Morse and Mackenzie, 1990). The sequence of the reactions from (R 2.3) to (R 2.6) indicates that the relationships among the various chemical species in the carbonic acid system. Among these chemical species, hydrogen ions (H^+) are recognised as especially important as they influence the buffer capacity of the carbonic acid system (Morse and Mackenzie, 1990).

$$CO_2\,(g) \rightleftharpoons CO_2\,(aq) \tag{R 2.3}$$

CO_2 *(aq)* + H_2O *(l)* $\rightleftharpoons$ H_2CO_3 *(aq)* (R 2.4)

H_2CO_3 *(aq)* $\rightleftharpoons$ HCO_3^- (aq) + H^+ *(aq)* (R 2.5)

HCO_3^- *(aq)* $\rightleftharpoons$ CO_3^{2-} *(aq)* + H^+ *(aq)* (R 2.6)

Conventionally, in the description of the carbonic acid system, the reaction steps (R 2.3 & R 2.4) are defined as a combined reaction. This action leads to the establishment of equilibrium between CO_2 (g) and H_2CO_3 (aq), such as the one expressed by Chen et al. (2006). However, this misleading definition of the equilibrium is associated with a difference of several orders of magnitude in the rate of the reaction of CO_2 (aq) to H_2CO_3 (aq) (Morse and Mackenzie, 1990, Lasaga, 1998). The reaction notation suggested by Plumber and Busenberg (1982) combines the reactions (R 2.4 & R 2.5). This evaluates the equilibrium more reasonably, as shown by reaction (2.7),

CO_2 *(aq)* + H_2O *(l)* $\rightleftharpoons$ HCO_3^- *(aq)* + H^+ *(aq)* (R 2.7)

In this study, the stages of the carbonic acid reactions are assumed in accordance with the modified reaction step (R 2.7), and the equilibrium of chemical species that are derived accordingly,

CO_2 *(g)* $\rightleftharpoons$ CO_2 *(aq)* $K_c = \frac{a_{CO_2}}{f_{CO_2}}\frac{f^o}{m^o}$ (R 2.8)

CO_2 *(aq)* + H_2O *(l)* $\rightleftharpoons$ HCO_3^- *(aq)* + H^+ *(aq)* $K_1 = \frac{a_{HCO_3^-}a_{H^+}}{a_{CO_2}a_{H_2O}}\frac{1}{m^o}$ (R 2.9)

HCO_3^- *(aq)* $\rightleftharpoons$ CO_3^{2-} *(aq)* + H^+ *(aq)* $K_2 = \frac{a_{CO_3^{2-}}a_{H^+}}{a_{HCO_3^-}}\frac{1}{m^o}$ (R 2.10)

H_2O *(l)* $\rightleftharpoons$ H^+ *(aq)* + OH^- *(aq)* $K_w = \frac{a_{OH^-}a_{H^+}}{a_{H_2O}}\frac{1}{(m^o)^2}$ (R 2.11)

in reactions (R 2.8) to (R 2.11), the respective dimensionless equilibrium constants were derived as K_c, K_1, K_2, K_3, K_w. In the equilibrium equations, f denotes the fugacity, m^o is the standard activity (1 mol kg^{-1} (same scale as that used to express concentration)), and f^o is the standard fugacity (at a pressure of one atm). The activity of species i in the aqueous solution can be calculated by using equation (2.9),

$$a_i = \gamma_i m_i \tag{2.9}$$

where m_i is the concentration, and γ_i is the activity coefficient of species a_i. By rearranging the equilibria derived from reactions (R 2.8, R 2.9, and R 2.10) activities of the aqueous carbon dioxide, bicarbonate, and carbonate species in terms of the carbon dioxide fugacity and hydrogen ion activity are as follows,

$$a_{CO_{2\,(aq)}} = K_c \frac{f_{CO_2}}{f^o}\, m^o \tag{2.10}$$

$$a_{HCO_{3\,(aq)}^-} = K_c K_1 \left(\frac{f_{CO_2} {m^o}^2 a_{H_2O}}{f^o a_H^+} \right) \tag{2.11}$$

$$a_{\,CO_{3\,(aq)}^{2-}} = K_c K_1 K_2 \left(\frac{f_{CO_2} {m^o}^3 a_{H_2O}}{f^o {a_H^+}^2} \right) \tag{2.12}$$

using equation (2.9) makes it possible to express equations (2.10, 2.11, and 2.12) in terms of concentrations through equations (2.13, 2.14, and 2.15),

$$m_{CO_{2\,(aq)}} = K_c \frac{f_{CO_2}}{f^o} \frac{1}{\gamma_{CO_{2\,(aq)}}}\, m^o \tag{2.13}$$

$$m_{HCO_{3\,(aq)}^-} = K_c K_1 \left(\frac{f_{CO_2} {m^o}^2 a_{H_2O}}{f^o a_H^+} \right) \left(\frac{1}{\gamma_{HCO_{3\,(aq)}^-}} \right) \tag{2.14}$$

$$m_{\,CO_{3\,(aq)}^{2-}} = K_c K_1 K_2 \left(\frac{f_{CO_2} {m^o}^3 a_{H_2O}}{f^o {a_H^+}^2} \right) \left(\frac{1}{\gamma_{CO_{3\,(aq)}^{2-}}} \right) \tag{2.15}$$

Now, for a dilute system, it is possible to approximate the activity of water as unity. In the carbonic acid system, the acid neutralisation capacity (alkalinity) of the solution in moles of proton per unit volume can be expressed as the alkalinity associated with the carbonic acid system A_c, and alkalinity of water A_w. This is demonstrated for a solution, in which the carbonic acid and water are the main contributing components, as total alkalinity is displayed by equation (2.16),

$$A_t = A_c + A_w \tag{2.16}$$

in such a solution based on the given partial pressure of CO_2, and an aqueous phase in equilibrium with other phases, the total alkalinity based on the proton concentration can be quantified by equation (2.17),

$$m_{H^+} = m_{HCO_3^-} + 2\, m_{CO_3^{2-}} + m_{OH^-} \tag{2.17}$$

equation (2.17) is written in terms of activities (α), as shown in (2.18),

$$\alpha_{H^+} = \alpha_{HCO_3^-} + 2\, \alpha_{CO_3^{2-}} + \alpha_{OH^-} \tag{2.18}$$

Observation of equations (2.17 & 2.18) indicates that the relative distribution of chemical species in the carbonic acid system can be represented as a function of pH. These equations demonstrate that a change in partial pressure of carbon dioxide (fugacity of CO_2) will lead to a change in the alkalinity of the carbonate system, but the total alkalinity of the system remains in balance. Chen et al. (2006) also showed that increase in the carbon dioxide partial pressure has led to a decrease in pH, as a result of the increase in hydrogen ion activity. They postulated that this phenomenon would facilitate the liberation of magnesium through the mineral carbonation process.

2.4.1 MgO-CO_2-H_2O System

The carbonic acid system becomes more complex in the presence of metal ions (e.g., Mg^{2+} from the dissolution of serpentine). This complexity is particularly seen through the work of Ellis and Wyllie (1980). The phenomenon of increased complexity can be explained by the formation of ion pairs, which result from changes in the ionic strength of the solution, and also the concentration of unpaired ions (De Visscher et al., 2012).

De Visscher et al. (2012) suggested a thermodynamic model for the solubility of a system containing a metal carbonate phase under the CO_2-H_2O system. Accordingly the equilibria defined as shown in reaction series of (R 2.12) to (R 2.14),

$$Mg^{2+}(aq)+OH^{-}(aq)\rightleftharpoons MgOH^{+}(aq)$$

$$K_{MgOH^+} = \frac{a_{MgOH^+}}{a_{Mg^{2+}}a_{OH^-}}m^o \tag{R 2.12}$$

$$Mg^{2+}(aq)+CO_3^{2-}(aq)\rightleftharpoons MgCO_3^{o}(aq)$$

$$K_{MgCO_3^0} = \frac{a_{MgCO_3^0}}{a_{Mg^{2+}}a_{CO_3^{2-}}}m^o \tag{R 2.13}$$

$$Mg^{2+}(aq)+HCO_3^{-}(aq)\rightleftharpoons MgHCO_3^{+}(aq)$$

$$K_{MgHCO_3^+} = \frac{a_{MgHCO_3^+}}{a_{Mg^{2+}}a_{HCO_3^-}}m^o \tag{R 2.14}$$

De Visscher et al. (2012) derived a polynomial relation showing that the proton activity in an aqueous solution (at a given condition) is proportional to the square root of the product of magnesium activity and CO_2 fugacity for the $MgCO_3$-CO_2-H_2O system where an aqueous phase is in equilibrium with the gas and solid phases.

In the MgO-CO_2-H_2O system there exists a variety of solid phases, including magnesium hydroxide (brucite ($Mg(OH)_2$)) and magnesium carbonates (magnesite ($MgCO_3$), nesquehonite ($MgCO_3{\cdot}3H_2O$), lansfordite ($MgCO_3{\cdot}5H_2O$), artinite ($MgCO_3{\cdot}Mg(OH)_2{\cdot}3H_2O$), and hydromagnesite ($4MgCO_3{\cdot}Mg(OH)_2{\cdot}4H_2O$)) (Bénézeth et al., 2011). Many studies have been dedicated to the thermodynamic modelling of the MgO-CO_2-H_2O system (e.g., Klein and Garrido, 2011). Magnesite is the most frequent and stable magnesium carbonate found in different geological environments (Königsberger et al., 1999). De Visscher et al. (2012) demonstrated that the equilibrium solubility of magnesium carbonate is the sum of the concentrations of the various magnesium ions and ion pairs in the solution, as shown in equation (2.19).

$$s = [Mg^{2+}] + [MgOH^{+}] + [MgHCO_3^{+}] + [MgCO_3^{0}] \tag{2.19}$$

Theoretically, magnesite precipitation requires the development of a certain degree of saturation in the solution. In the context of mineral carbonation, many studies have been attempted to explain the precipitation of magnesite in the MgO-CO_2-H_2O system (e.g., Hänchen et al., 2008, Bénézeth et al., 2011). The degree of saturation is typically described by the magnesite saturation index (Ω), which is the ratio of the aqueous ions activity product to the magnesite solubility product (K_{sp}). The magnesite solubility product is presumed to be a thermodynamic constant of the reaction (R 2.15),

$$MgCO_3\,(cr) \rightleftharpoons Mg^{2+}\,(aq) + CO_3^{2-}\,(aq) \qquad \text{(R 2.15)}$$

assuming magnesite to be pure and stoichiometric, its solubility product can be shown in accordance with (2.20),

$$K_{sp^0-mgs} = a_{Mg^{2+}} a_{CO_3^{2-}} \qquad (2.20)$$

where a_i represents the activity of the i^{th} ion. A large discrepancy regarding the equilibrium solubility of magnesite can be found in the literature – mostly reflecting the relative stability of the carbonate phases in the MgO-CO_2-H_2O system. The formation of magnesite is observed to be strongly kinetically controlled, as the sequence of transformation of the different compounds is dominated by kinetic constraints (Hänchen et al., 2008). Christ and Hostetler (1970) stated that the difficulty associated with the formation of magnesite from solution is related to the strong hydration characterisation of the aqueous magnesium cations. According to Hänchen et al. (2008), increasing the activity of the carbonate ions in the presence of the relatively low activity of magnesium leads the system towards the precipitation of magnesite. Hänchen et al. (2008) further discussed that the hydrated forms of magnesium carbonate precipitate much more easily than the anhydrous form. According to the Ostwald step rule, metastable phases progressively transform to more stable phases (Morse and

Casey, 1988) – thus magnesite formation is often the final product of transformation of hydromagnesite and/or other forms of hydrated carbonates. From the surveyed literature, one may perceive that an increasing temperature promotes the transformation of other carbonate species to magnesite (Wolf et al., 2004, Giammar et al., 2005, Hänchen et al., 2008). Bénézeth et al. (2011) carried out a series of experimental investigations to determine the magnesite solubility product at a temperature range from 323 to 473 K and P_{CO2} up to 30 bar in 0.1 molal NaCl solution. They derived an equation based on their experimental observations that can predict the solubility of magnesite as a function of temperature, as shown in equation (2.21). They further showed that magnesite solubility values predicted by using this equation are in a good agreement with the reported data in the literature.

$$log_{10}K_{sp^0-mgs} = a + \frac{b}{T(K)} + cT(K) \tag{2.21}$$

where the values of three coefficients are $a = 7.267$, $b = -1476.604$, and $c = -0.033918$. Under the carbonic acid system, carbonate precipitation is an important parameter that may influence the kinetics of the dissolution reaction. Wolf et al. (2004) adopted a fundamental approach to study the reaction processes that control CO_2 sequestration via mineral carbonation – using a micro-reaction system coupled with Synchrotron X-ray diffraction and Raman spectroscopy. The preliminary findings showed that, during the carbonation of thermally activated serpentine (activated at 913 K), magnesite was precipitated directly at a CO_2 partial pressure of 150 bar and the reaction temperature of 423 K. Through the work of O’Connor et al. (2005) it was demonstrated that magnesite is precipitated as separate small particles (< 10 μm) during the carbonation process. McKelvy et al. (2003) reported that the progress of the olivine dissolution reaction is directly affected by nucleation and intergrowth of magnesite through the interfacial reaction zones. According to McKelvy et al. (2003) and Andreani et al. (2009), the *in situ* formation of magnesite (nucleation and crystal growth) through the layers of the reaction zones can potentially apply another rate-limiting step to the extraction of magnesium. Overall, one may infer that knowledge of the thermodynamic properties of the $MgO-CO_2-H_2O$ system may be crucially important in identifying the rate-limiting steps involved in the extraction of magnesium from magnesium bearing silicates under the carbonic acid system.

2.5 Effect of CO_2 on Silicate Dissolution

Most of the available silicate dissolution experiments in the literature were performed in the absence of CO_2. However, some experiments were carried out with a higher amount of dissolved carbonate species either due to an equilibrated high-pressure CO_2 or additives of carbonate or bicarbonate salt. In this section, it is aimed to provide a brief review of the effect of CO_2 on the dissolution of silicates.

The direct impact of dissolved carbon dioxide on the dissolution kinetics of silicate minerals at neutral and acidic pH conditions has been investigated throughout many studies (Carroll and Knauss, 2005, Golubev et al., 2005, Pokrovsky and Schott, 2000, Wogelius and Walther, 1991). Wogelius and Walther (1991) reported that the presence of dissolved CO_2 at atmospheric pressure conditions resulted in an approximate ten-fold decrease in the dissolution rate of forsterite. Pokrovsky and Schott (2000) expressed that, in a mixed-flow reactor with a reaction temperature of 298 K and basic pH conditions ($pH \geq 9$), the dissolution rate of forsterite decreased with increasing carbon dioxide concentrations in the solution. They further explained that the rate reduction occurs as a result of the reaction between the liberated magnesium cations and carbonate ions – a magnesium surface complex containing carbon may form. Thus, the conclusion was that increasing CO_2 partial pressure inhibits the progress of forsterite dissolution. Carroll and Knauss (2005) investigated the dissolution kinetics of labradorite ($Na_{0.4}Ca_{0.6}Al_{1.6}Si_{2.4}O_8$) using a mixed-flow reactor at a temperature range of 303 to 403 K, a pH of 3.2, and a constant $m_{CO_2} \cong 0.6\ \text{mol kg}^{-1}$. The CO_2 molality was maintained by a correspondingly elevated CO_2 partial pressure – resulting in enhancement of the dissolution rate. This attribute was correlated with an increase in proton activity. In addition, Golubev et al. (2005) investigated the dissolution rates of forsterite and wollastonite using a mixed-flow reactor at a temperature of 298 K and a CO_2 partial pressure of one atm. The dissolution rates were not significantly affected by the presence of CO_2 at pH 4. A similar result was obtained by Hänchen et al. (2006) using a stirred-flow-through reactor. They reported that, at a low pH range (~2), the dissolution behaviour of forsterite is not affected by the presence of CO_2 and only depends on the solution pH – conversely at pH greater than 5, the presence of CO_2 resulted in a rapid decay of the apparent dissolution rate compared with CO_2-free cases. Giammar et al. (2005) showed that, during experiments performed using a batch reactor, elevated CO_2 partial pressure in the acidic solution resulted in an increase in the forsterite dissolution rate. This phenomenon was explained as an indirect result of the decrease in the solution pH. Daval et al. (2013a) measured the dissolution rate of lizardite in a continuously stirred flow-through reactor as a function of pH from 2.5 to 6.7 within a temperature range of 300 to 363 K in the presence of CO_2 ($40 \text{ bar} \leq P_{CO2} \leq 60 \text{ bar}$) and in the absence of CO_2. They reported that the dissolution rate increased by a factor of 5 at pH 5 in the presence of CO_2 compared with the CO_2 free solution. They concluded that, in addition to the proton-promoted mechanism, the dissolution reaction may be promoted by the bicarbonate ligands. In this regard, previous studies stated that ligand-promoted dissolution occurs in parallel with proton-promoted dissolution (Wogelius and Walther, 1991, Olsen and Rimstidt, 2008). Olsen and Rimstidt (2008) investigated the dissolution rate of forsterite in solutions of nitric and oxalic acid solutions over a pH range of 0–7 and at a temperature of 298 K. They discussed how proton-promoted and ligand-promoted dissolution mechanisms are simply two aspects of the same process. In addition, Wogelius and Walther (1991) suggested that ligand-promoted dissolution likely occurs in parallel with proton-promoted dissolution – hence the net rate of the dissolution reaction should be the sum of the two rates. Overall, most studies with regards to the effect of CO_2 on the dissolution rate of silicate minerals are in good agreement that the main controlling parameter is the solution pH. Under acidic conditions, the presence of CO_2 may facilitate proton-promoted mechanism; however, under alkaline conditions the formation of carbonate species may inhibit the progress of the dissolution reaction (Wogelius and Walther, 1992, Pokrovsky and Schott, 2000).

2.6 Evaluation of Passivating Properties of the Silica Layer

A number of studies focusing on mineral carbonation have shown the inhibiting effects of the amorphous secondary phase layer on the overall carbonation rate for forsterite and serpentine materials (Béarat et al., 2006, Jarvis et al., 2009). In this section, a review of the surface transformation of silicates during dissolution is provided.

Luce et al. (1972) studied the dissolution of magnesium silicate minerals (forsterite, enstatite, and lizardite) in aqueous solution over a relatively broad pH range of ~3 to 10. They reported that dissolution of magnesium silicates proceeded incongruently with respect to Mg:Si, resulting in the formation of surface phases. These surface phases act to slow dissolution by inhibiting the diffusion of reactants through the reaction layers. They concluded that the rate of dissolution decreased with time as the layer thickness increased. Grandstaff (1978) investigated the dissolution mechanism of forsterite in an acidic pH solution. Based on scanning electron microscope analysis carried out on forsterite grain surfaces (before and after dissolution), they detected no evidence of a thick or continuous residual of the precipitated layers on the mineral surface. They did observe overall surface area increase as a result of the formation of etch features on the surface. Despite this observed increase in surface area, the dissolution rate decreased; hence, the controlling dissolution mechanism was correlated with the rates of surface reaction (Grandstaff, 1978). Bales and Morgan (1985) examined the dissolution of chrysotile at pH values ranging from 7 to 10. They concluded that the liberation rate of magnesium is related to pH, and that the rate-limiting steps depend on the rates of the chemical reactions (Bales and Morgan, 1985). Schott et al. (1981) studied the dissolution of enstatite, diopside ($CaMg(Si_2O_6)$), and tremolite ($Ca_2Mg_5(Si_8O_{22})(OH)_2$) in aqueous solution at a low temperature and pH from 1 to 6. On the basis of high-magnification scanning electron microscopy and surface chemistry analysis, they stated that no continuous amorphous secondary phase was observed on the leached surface of the minerals. They assumed that, in case of the existence of an amorphous silica layer on the mineral surface, the structure would be unstable and it would rapidly break down and release silica into the solution. Therefore, it was concluded that surface chemical reactions control the rate of dissolution. In fact, this finding was supported by the observation of the relatively high activation energy, non-linear dependence of the dissolution rate on proton activity and the presence of etch pits (Schott et al., 1981). White and Brantley (1995) postulated that the dissolution mechanisms of most silicates are involved in the formation of alteration layers correlated with the surface condensation and reconstruction reactions. The dissolution mechanism of forsterite was studied in both acidic and basic solutions by Pokrovsky and Schott (2000). They reported that the rate-limiting step in the acidic solution is related to two stages: a) the ion-exchange mechanism of bridging metal-oxygen bonds, and b) decomposition of the protonated polymerised silica network linked to magnesium content deeper in the structure. The dissolution mechanism of forsterite was also characterised as a surface-controlled dissolution model by Hänchen et al. (2006). They proposed that the influence of the development of amorphous secondary layers on the availability of the reactive surface area be negligible. Nevertheless, it is worth to note that silica layers do form on the surface of post leached-feldspar mineral – but that the surface appears to be very permeable (Hellmann et al., 2003, Hellmann et al., 2004).

Daval et al. (2011) investigated the effect of the formation of an amorphous silica layer on the dissolution rate of forsterite. They observed that the formation of silica layers on the olivine surface resulted in the generation of a permeable structure that eventually became passivating as the reaction progressed. On this basis, they suggested that ignorance of the formation of amorphous silica layers has important consequences for the over-evaluation of dissolution rates (Daval et al., 2011). Furthermore, Cailleteau at al. (2008) suggested that the sharp reduction in the dissolution rate of silicates is directly related to the densification of the outer layers of the alteration film. Hellmann et al. (2012) used high-resolution and energy filtered transmission electron microscopy to conduct a comprehensive study of mineral-fluid reaction boundaries. Based on their examination of the surface chemistry and structure of large groups of laboratory-altered and field-weathered silicate materials, they demonstrated that nm-thick amorphous surface altered layers enriched in silica are found in silicate minerals, with a composition of hydrated amorphous silica. This observation suggests that a single dissolution mechanism based on interfacial dissolution-reprecipitation likely controls the dissolution mechanism of most silicate minerals (Hellmann et al., 2012).

Daval et al. (2013b) examined the interfacial zone between a bulk fluid and a common silicate mineral surface (diopside) to address the controversial question regarding the occurrence of the rate-determining step during the chemical weathering process. They proposed that the exchange of energy and matter occurring at the mineral surface involves both a) the inner interface, which is defined as the boundary between the original mineral and the amorphous silica-rich surface layer (ASSL), and b) the outer interface, where the bulk fluid contacts the ASSL (Daval et al., 2013b). They pointed out that, if ASSL does not act as a passivating layer, then the inner interface controls the dissolution kinetics. However, if the outer surface acts as a passivating layer (i.e., it is totally non-permeable), the outer interface inhibits contact of the bulk fluid with the unreacted material surface and controls the dissolution process. Daval et al. (2013b) concluded that unconstrained aqueous transport of cations is consistent with the mechanism suggested by Hellmann et al. (2003 & 2012) whereby interfacial dissolution-reprecipitation forms the ASSL. Hence, on the basis of the surveyed literature, silica appears to play a controversial role in the dissolution mechanism of silicate minerals.

2.7 Relation to Equilibrium in the Carbonic Acid System

The dissolution of a silicate may involve several elementary steps such as 1) mass transfer of dissolved reactants from the bulk solution to the mineral surface, 2) adsorption of solutes, 3) inter-lattice transfer of reacting species,

4) chemical reactions, 5) detachment of reaction products from the surface and, 6) mass transport into the bulk of the solution (Stumm and Wollast, 1990). The sequence of the dissolution reaction under hydrothermal carbonic acid conditions appears to be even more complex. Precipitation of secondary phases (i.e., amorphous silica and/or carbonates), which can act as passivating coatings, slows down the overall dissolution rates (Daval et al., 2009a, Daval et al., 2009b, Daval et al., 2010). According to Lasaga (1998), at a certain degree of saturation, nucleation spontaneously occurs on the surface of the pre-existing solid phase. If a precipitation reaction occurs in the porous substrate, diffusive transport of protons and mobility of the liberated magnesium are likely to be inhibited. This phenomenon leads to a decrease in porosity by clogging the pore throats. These influences can have profound effects on the natural weathering of silicate minerals.

According to many previous studies, chemical weathering reactions generally progress at slow rates as a consequence of taking place in the vicinity of equilibrium, unlike most laboratory studies (Swoboda-Colberg and Drever, 1993, White and Brantley, 1995, Hellmann and Tisserand, 2006). The weathering rates represent the sum of the dissolution and precipitation reactions occurring in environments with variable free energies. This phenomenon particularly holds true where the fluid-mineral interactions occur in micro-pores rather than in larger channels or macropores – resulting in mostly different fluid residence times involved in the reaction interfaces. Accordingly, the free energy of the dissolution reactions ($\Delta G_{micropore} \gg \Delta G_{macropores}$) gets closer to equilibrium (Swoboda-Colberg and Drever, 1993, Hellmann and Tisserand, 2006). Occurrence of this particular effect could also impact the progress of the dissolution reaction. Similarly, for the dissolution of silicates, the effect of saturation state appears to be more extremely where the reaction kinetics and fluid flow velocities are interdependent throughout the permeable substrate of the particles. The difference in saturation states of the bulk fluid and fluid flowing in the porous substrate may lead to disconnections in the pore spaces – thereby resulting in retardation of the dissolution rate.

2.8 Summary

Based on the surveyed literature, one may conclude that, under acidic conditions, the dissolution of metal silicates appears to advance through the exchange reaction of solutes (e.g., protons) with metal cations. The surface reactivity is known to be dependent on the surface species and its structural identity. The role of silica in the mineral structure seems to be controversial as it may influence the evolution of the rate-controlling step. The dissolution-reprecipitation mechanism likely occurs for most of the dissolving silicates. During the dissolution reaction of silicates, amorphous silica layers likely precipitate on the surface and result in the generation of a permeable surface – these may act as increasingly passivating layers as the reaction progresses.

Under the carbonic acid system, the occurrence of parallel reactions may lead to the formation of secondary carbonate phases. The occurrence of this interference step through the porous substrate of particles may further restrict any interdiffusion processes (between cations and protons). It is thus important to obtain a better understanding of the interaction effect of the governing phase equilibria in the carbonic acid system and the progression of the reaction interfaces on the dissolution rate.

Chapter 3. Methodology

3 Introduction

Previous studies showed that the slowest step in the mineral carbonation process is likely related to the digestion of magnesium from the natural magnesium silicate minerals (e.g., serpentine & olivine) (Schulze et al., 2004, Park and Fan, 2004, O'Connor et al., 2005). This fact is particularly true with serpentine due to its sheet silicate structure. Through various past studies (such as Schulze et al., 2004, O'Connor et al., 2005) the overall efficiency of carbonation process was observed to be improved by thermal pre-treatment of serpentine. Nonetheless, the lack of fundamental knowledge regarding the dissolution kinetics of thermally activated serpentine under the CO_2-H_2O system accounts for the main motivation for this study.

In this chapter, the experimental apparatus that was used for this study is described. In addition, the main analytical techniques that were employed to characterise the leachate and feedstock materials are introduced. The preliminary results for the effect of activation temperature on the magnesium availability of the research material are also presented. Lastly, a brief discussion over the reactor hydrodynamics is provided.

3.1 Theory of the Reaction Rate and Experimental Method

The chemistry involves in the heterogeneous reaction system is complex; hence, the bulk concentrations of dissolved species have been considered mainly as a descriptive parameter in many kinetic studies. Most of the mineral dissolution studies were conducted by using batch reactors where the concentrations of the dissolved species are measured as a function of time (Van Essendelft and Schobert, 2009a). These approaches often introduce difficulties in interpretation of the kinetics data as the concentration of the reactants and products may be influenced by the establishment of equilibrium. A number of other studies used a packed bed column to examine the dissolution kinetics; however, the extracted results were influenced by a strong concentration gradient across the column. In order to overcome these experimental difficulties, several past studies introduced a fluidised bed reactor or well mixed flow-through reactors to examine the dissolution kinetics of the minerals in the aqueous phase (Chou and Wollast, 1984, Dove and Crerar, 1990, Hänchen et al., 2006).

In the present study to measure the dissolution rate of thermally activated serpentine under the carbonic acid system, a three-phase fluidised bed reactor (i.e., (CO_2-H_2O-(MgO-SiO_2))) set-up was employed. Figure 3-1 shows a schematic view of the experimental apparatus. This reactor set-up was designed to operate at the high pressure and temperature, system pressure up to 170 bar and reaction temperatures up to 473 K. The reactor was enclosed in a fan forced oven equipped with a PID temperature control unit to maintain a uniform temperature environment. The reactor was built from stainless steel 3/8 ″ Swagelok fitting[1] into which a weighted amount of sample was charged prior to the experiment. The deposited mineral sample was held between two stainless steel Hollander weave meshes with filter rating of 5 μm.

The system is fed by two separately metered high-pressure streams[2] of H_2O and CO_2, delivered through a Waters 515 HPLC pump and an SFT-10 supercritical fluid pump (in a high-pressure mode), respectively. This configuration allowed regulating the superficial velocity of the two-phase reactive fluid passing through the reactor and also adjusting molality of the CO_2 in the system. In the present study, the residence time of the reactive fluid through the reactor (e.g., at a defined standard operating conditions, is 13 s) was adjusted with respect to the overall volumetric flow rate of the reactive fluid.

The individual streams of CO_2 and H_2O were mixed thoroughly before introducing into the reactor through a high pressure mixing tee with an *in*

---

[1] In this study for most of the conducted experiments the reactor consisted of stainless steel 3/8 ″ Swagelok union within a volume of $V_{Reactor} = 0.45$ cm^3; except for experiments with variable mass loadings – the reactor consisted from a stainless steel 3/8 ″ Swagelok bulkhead union within a volume of $V_{Reactor} = 1.14$ cm^3.

[2] The CO_2 was delivered as a liquid of ultra-high purity greater than 99.9 % from the dip tube CO_2 cylinder; water was supplied from Millipore ultrapure water tank.

situ titanium filter element. This step ensured that the reactive fluid reached complete saturation with respect to the equilibrium solubility of the CO_2 in the aqueous phase. The reactive fluid was preheated to the reaction temperature through along preheater coil (by using two metres of 1 mm ID capillary 316-SS tubing) prior to introducing into the reactor. A thermocouple (K-type) was located directly at the reactor inlet to monitor the temperature of the reactive fluid entering the reactor. The reactor effluent, (prior to the pressure drop across the back pressure regulator) was cooled to ambient temperature by passing through a counter-current flow heat exchanger. The pressure in the system was controlled by an ultra-low-flow Equilibar back pressure regulator. The back pressure regulator modulates the system pressure by using a reference gas pressure that acts in 1:1 ratio. A nitrogen line provides the reference pressure. Samples were collected for one minute at intervals chosen to capture the overall kinetics of the reaction – the samples were analysed for magnesium and silica content by using an inductively-coupled plasma optical emission spectrometry (ICP-OES). This analysis provides a direct insight into the elemental molalities of the reactor. In the present study, the magnesium and silica compounds of the aqueous effluent are selected to be monitored as the primary indicator of the elemental control for dissolution reactions. This strategy was adopted on the basis of the conducted overall scan by an ICP semi-quantitative method to determine the major elemental composition of the leachate samples[1].

The sampling was started from the first moment that the two-phase flow appears to be discharged from the sampling port. The entire volume of the system was measured by a tracer experiment as ~13 cm^3. It is estimated that ~70% of the total volume was associated with the volume of components and the reactor – and ~30% of the rest of total volume was due to the lines connect the reactor outlet to the sampling port.

3.1.1 Reaction Rate in a Well-mixed System

Steady-state conditions are accomplished for the solution composition as results of interaction of the inlet reactive-fluid with the deposited mineral in

---

[1] Other elements, such as Fe or Al, were not found in the detectable quantities.

the reactor cell; thus, the reactions rate can be defined in accordance with the assumption of the well-mixed system through equation (3.1).

$$r_i = \dot{m}_{water} \times C_i \tag{3.1}$$

where C_i is the difference between the molality of the component i between the outlet and inlet solutions (mol L^{-1}), $\dot{m}_{water}$ is the water mass flow rate (kg s^{-1}), and r_i is the reaction rate (mol s^{-1}). The residence time of the reactive fluid in the reactor ($\tau\ (s) = V_{Reactor}/\dot{V}_{mixtur\ flow}$) is calculated based on the ratio of volume of the reactor and the total volumetric flow rates. Furthermore, to investigate the saturation state at a constant residence time conditions a parameter is defined and termed as a mass loading factor τ_m (min), which is a ratio of the input solid mass versus the mass flow rate of water ($M_0/\dot{m}_{H_2O}$).

3.1.2 High Pressure and Low-Pressure Experimental Apparatus

Minor modifications were applied to the experimental apparatus introduced in the earlier work of (Mann, 2014), and it was utilised in the current study for measuring the dissolution rates under the high-pressure conditions, as shown in Figure 3-1. In addition, a low-pressure system was developed and used to monitor the kinetics of dissolution reaction under the relatively lower CO_2 partial pressure (gas phase), in which the CO_2 is delivered by using a calibrated mass flow controller. Further details of the experimental systems, either for the high-pressure set-up or the low-pressure set-up are provided in Appendix C.

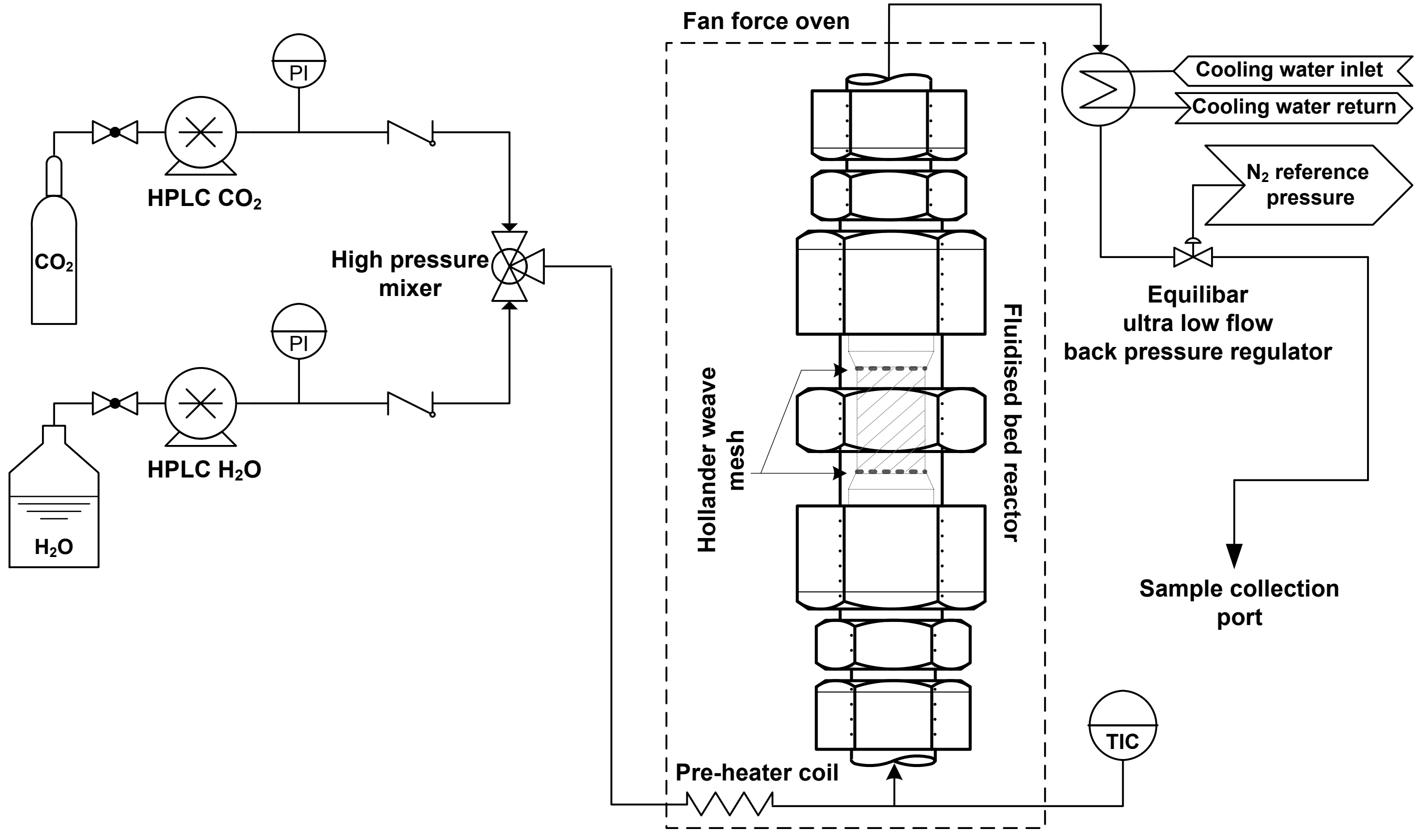

Figure 3-1. Simplified diagram of the experimental apparatus (in a high-pressure configuration) used to measure the kinetics of dissolution reactions reported in the present study.

3.2 Aqueous Sample Analysis

The dissolved elements in the aqueous solution were quantified by using the inductively coupled plasma with optical emission spectrometry (ICP-OES). In this technique, species are excited and ionised by high-temperature plasma, emitting photons that have particular energy characteristics that are identified by the quantised energy level structure of the atoms. Therefore, the wavelength of the emitted photons can be used to determine the elements from which they originated. The schematic diagram of an ICP-OES is shown in Figure 3-2.

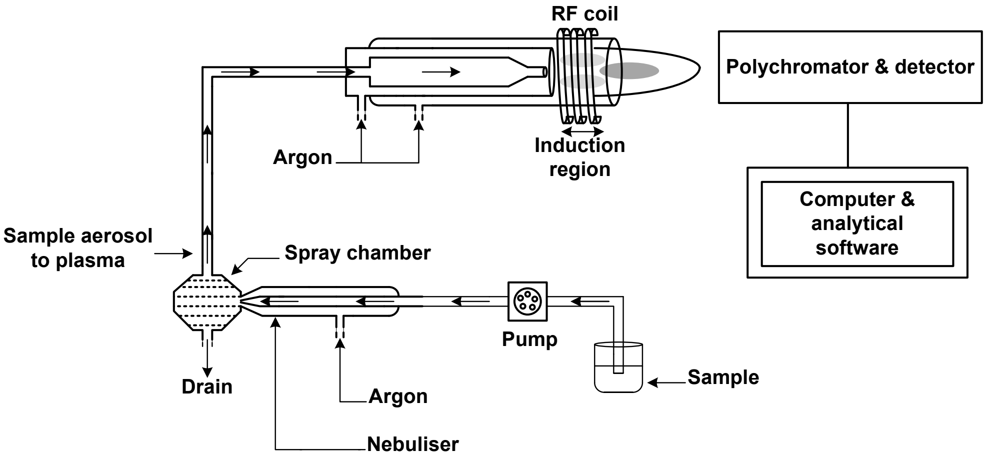

Figure 3-2. Schematic view of the ICP-OES system used for analysing the aqueous samples in this study.

In this study, the collected leachates from the experiments were diluted by using an auto diluter (Hamilton microlabs 600 series). Dilution was carried out to adjust the concentration in accordance with the range required by the ICP analysis. Subsequently, the aqueous samples were analysed for the total dissolved magnesium and silicon by using ICP-OES. The results were converted to molal concentration (molality (mol kg^{-1})) according to equation (3.2),

$$b_i = \frac{c_i}{\rho - \sum c_i \cdot M_i} \tag{3.2}$$

where b_i (or m_i) is the molality of the component i, c_i is the molar concentration of the component i, ρ is the solute density, and M_i is the molar mass of the constituent i. Solution densities were presumed to be equal to the density of pure water (at 298 K and 1 atm) as the aqueous samples at least were diluted by using Millipore water to a factor of 1:60. In the present study the method of semi-quantitative analysis was used to evaluate the elemental concentrations of a few number of studies. This analysis produced approximate results within the accuracy of ±30%; however, despite the associated systematic errors[1], the results were in the right order of magnitude. The majority of the experimental results presented in this study were acquired from the quantitative ICP analysis, otherwise indicated analysed through semi-quantitative method. In the quantitative method the relationship between the elemental concentration in the aqueous samples and the detected light intensity were converted to a set of intensity/concentration points for each element. A blank (Millipore water) was measured to identify the intensity of zero concentration. A set of standard solutions was measured to provide a set of intensities versus known concentration points (up to 16 mg L^{-1}) for magnesium and silicon. Linear regression functions were fitted to the points. The concentration of the dissolved elements in the aqueous samples was quantified by using the fitted functions. The associated errors within the quantitative analysis did not exceed ±7%.

3.3 Study of Material

In the present study, almost always the experimental investigations focused on the dissolution of thermally activated South West Oregon Lizardite (SWOL) material. This material was provided by National Energy Technology Laboratory (NETL). The details regarding the crystallinity of the serpentine mineral are beyond the scope of the present study; however, a

---

[1] In semi-quantitative technique the instrument was calibrated (up to 5 ppm) for a large number of elements. This calibration stored in the analytical section of the instrument and generally is being used for a long period of time. The results attained with this method of analysis are typically associated within systematic errors mainly due to the instrument drift, and differences reflected various sample matrixes.

brief review of past studies related to this topic is provided in the next section.

3.3.1 Literature Review for the Research Material

Knowledge of serpentine structural integrity is fundamental for improving the dissolution reaction rate and promoting the feasibility of the mineral carbonation process. According to Faust and Fahey (1962), the general structural formula for the serpentine group can be shown as $X_5Y_4O_{10}(OH)_8$[1], which represents the contents of a unit cell. The serpentine group consists of many species that share a common crystal structure (Clinkenbeard, 2005). The ordinary structures of serpentine minerals are phyllosilicates (organised in sheets or layers of silicates). According to Veblen and Wylie (1993), the primary structural unit of serpentine minerals is made from one tetrahedral sheet (SiO_4) bonded to one octahedral sheet ($MgO_2(OH)_4$). The tetrahedral and octahedral layers are connected by the sharing of non-bridging oxygen atoms, which results in the formation of a two-layer structure having the ideal formula of $Mg_3Si_2O_5(OH)_4$[2]. Due to the structural orientation, there is limited room for chemical substitution (e.g., Al, Fe) in the magnesium-serpentine minerals in which magnesium and silica normally reside. This substitution typically leads to the replacement of magnesium or silica with a small amount of another element such as iron or aluminium. According to Clinkenbeard (2005), the dimensions of an ideal (non-distorted) magnesium-occupied octahedral and silicon-occupied tetrahedral sheet are different, due to a misfit between the tetrahedral and octahedral sheets that leads to the formation of some stable trend in the serpentine tetrahedral-octahedral (t-o) layer. In general, there are three ways that serpentine structural accommodation occurs within subsequent structures represented by the three serpentine minerals; lizardite, chrysotile, and antigorite (Clinkenbeard, 2005). In lizardite, the misfit is accommodated by slight in-plane rotation of the tetrahedral within the planar structure of the layer. For Chrysotile, this occurs by the curling of the t-o layer into scrolls or hollow

---

[1] This general formula allows the substitution of atomic impurities (e.g., Al, Fe, Ni, or Cl) in the solid solution to occur in positions X or Y, as well as in the position allocated for (OH).

[2] Theoretically, it contains 43% MgO.

cylinders. In antigorite, in order to accommodate the misfit, alternating segments of curved layers are periodically inverted to create a wave-like or corrugated structure.

3.3.2 Serpentine Activation

In the context of mineral carbonation as noted by Goff and Lackner (1998a) due to the relative abundance and high magnesium content, serpentine material is a candidate for the mineral carbonation process. Among the serpentine groups, lizardite is the most abundant mineral (Wicks and O'Hanley, 1988). However, a number of studies have shown that serpentine dissolution rates are fairly slow (Daval et al., 2013a). This is mainly due to the existence of crystalline OH groups coordinated to Mg sites; thus, this material suffers from slow dissolution kinetics. Heat activation of lizardite contributes to the formation of meta-lizardite phase structures prior to complete dihydroxylation.

Despite the relatively high energy cost associated with the heat activation process, the thermal activation process has been the focus of several research groups for various applications (Brindley and Hayami, 1964, Brindley and Hayami, 1965, Martin, 1977, McKelvy et al., 2004, Brandenburg, 1940, Barnes et al., 1950, Hey and Bannister, 1948, Cajllère, 1936, Aruja, 1945). Thermal decomposition of serpentine is considered a dehydroxylation process in which structurally bound hydroxyls are removed in a form of liberated water vapour. During serpentine activation the crystal structure becomes disrupted, but recrystallisation of magnesium silicates may occur (Barnes et al., 1950, Hargreaves and Taylor, 1946, Hey and Bannister, 1948). Prolonging the dehydroxylation process at elevated temperatures leads to complete destruction of the crystal structure of the parent serpentine and subsequent formation of a final anhydrous product with a combination of forsterite and enstatite crystal orientation.

Extraction of magnesium from thermally activated serpentine was initially observed in the work of (Brandenburg, 1940). Brandenburg (1940) concluded that the extraction of magnesium from serpentine material is a function of the activation temperature. In addition, the high activation temperature was correlated with the primary reason for deactivation of the material. Later on, Barnes et al. (1950) conducted a study of the activation of Coal Creek serpentines. Barnes and co-workers showed that the activation of serpentine was a function of both time and temperature. They defined a graphical representation for the active area within a temperature range of ~873 to 1023 K. The low-temperature side of the defined area was represented for an under-activated material, while the activated area started to disappear for temperature above 1023 K. Therefore, the high-temperature region was termed the "dead burned" region (Barnes et al., 1950). Furthermore, they monitored changes in the crystal structure of the activated and non-activated material using X-ray diffraction patterns. The results indicated a gradual disappearance and dispersion of X-ray patterns[1] relative to the activation temperature. It was observed that, at an activation temperature of 873 K, the activated serpentine showed a nearly non-crystalline structure compared with untreated serpentine. Later on, this product of the activation process was termed "meta-serpentine" as recommended by McKelvy et al. (2004). Barnes and co-workers reported that changes in the crystalline character of serpentine were apparent again at temperatures above 873 K. This trend continued until a final product containing mostly olivine and enstatite was obtained at an activation temperature of 1273 K. In the context of mineral carbonation, during the development of the Albany NETL process, O'Connor and co-workers (2005) reported that the optimum reactivity of heat-treated serpentine occurs at a temperature range of 873 to 923 K. From the Albany NETL process, it is perceived that thermal activation of serpentine enhanced carbonation reactivity by an approximate factor of four. Henceforth, more studies have contributed to this field of research (e.g., McKelvy et al., 2004, Geerlings and Wesker, 2007, Boerrigter, 2010, Fedoročková et al., 2012, Dlugogorski and Balucan, 2014, Mann, 2014). All of these studies suggest that meta-serpentine material is formed as a product of an intermediate activation temperature, which is associated with the highest possible magnesium reactivity and has an amorphous-like structure.

---

[1] The Bragg peaks associated with the crystalline phase decreased in intensity along with the appearance of a broad diffuse peak denoted by the amorphous phase.

The kinetics of the dehydroxylation of South West Oregon Serpentine was investigated by Mann (2014) in great details. In this work, the rate of forsterite recrystallisation was probed through semi-quantitative and quantitative *ex situ* powdered X-ray diffraction (PXRD) using both conventional (CuK_{α}) and synchrotron (beamline 11-BM, APS, Argonne National Laboratory) radiation sources as a function of activation temperature. A constant residence time of two hours was employed across the analysis to obtain a temperature resolved series for the recrystallisation reaction of SWOL.

Semi-quantitative analysis was conducted on conventional powder XRD by monitoring the relative peak intensity (integrated peak area) of the forsterite 020, 021, and 120 diffraction indices as a function of activation temperature and plotting them against the scattering vector Q $(4\pi\, sin(\theta)/\lambda)$, which enabled direct comparison between the employed radiation sources (i.e., CuK_{α} and synchrotron). Across the entire temperature range, gradual forsterite formation was observed following the initial appearance at an activation temperature of 887 K through the trace presence related to the 021 diffraction index. At temperatures above 1063 K, rapid forsterite formation was observed, approaching its maximum concentration at 1221 K. It was also reported that rapid enstatite formation appears at temperatures above 1066 K through the trace diffraction lines of ~1.96 and 2.17 $Å^{-1}$, which gradually progress towards the maximum concentration at a temperature of 1221 K. A similar trend for the formation of forsterite and enstatite was observed under the investigations using a high resolution synchrotron radiation source, with the total phase content of forsterite approaching ~65 (wt. %) at 1221 K. The presence of enstatite was also accounted; therefore, the total phase content of the final activation product was equated to a conversion extent of ~0.98 with respect to initial the MgO content of the mineral. In this study, the associated error within the relative conversion extents was precisely determined for three indices, 020, 021, and 120, respectively. The error related to measurement was also identified as a maximum of 10%; this error is attributed to the use of the adsorption-diffraction method, which introduces error via primary issues with the preferred orientation and neglect of changes within the mass attenuation coefficient.

Comparison of this work with previous studies further point to the significance of forsterite formation is being initiated from amorphous serpentine. The PXRD patterns show that, during the initial stages of the activation process, dihydroxylation must occur before the formation of the amorphous medium. The optimum amorphous medium was observed at an activation temperature of 907 K, based on the relative extent of conversion of ~7% with respect to forsterite formation. The phase distribution of this material was quantified as ~5% forsterite, ~3% enstatite, and ~91% amorphous phase. The highly amorphous intermediate was called meta-serpentine, in which the MgO units are relatively loosely bound.

This property of the material is known to have a large influence on the overall performance of the mineral carbonation process. Thereby, in accordance with the objective of the present study, monitoring the magnesium extraction rate was viewed as an indication of magnesium availability in the activated SWOL as a function of temperature, and, thus, a series of preliminary study was carried out.

3.3.3 Effect of Activation Temperature on Magnesium Availability of Thermally Activated Serpentine

Preliminary studies were conducted to monitor trends in magnesium extraction rate with a view to identify maximum magnesium reactivity versus activation temperature. The research material (SWOL) was conventionally activated using a fluidised bed calciner reactor at a temperature range of 800 to 1250 K for two hours under an argon-fluidising medium.

Dissolution experiments were conducted at experimental conditions (T = 423 K and P_{CO2}= 100 bar) relevant to NETL conditions under the saturated CO_2-H_2O system using a constant mass loading of 250 mg of the treated material (the corresponding mass loading factor was set to 0.25 min). The continuous flow set-up outlined in the previous section was used, and the concentration of magnesium in the reactor effluent was determined through the semi-quantitative ICP analysis. Figure 3-3 shows the relative degree of completion[1] of magnesium extraction, X_{Mg}, as calculated in accordance with correlations (3.3) and (3.4),

$$\frac{dX_{Mg}}{dt} = \frac{MW_{Mg}}{M_0 Y_{Mg}|_0} r_{Mg} \tag{3.3}$$

$$X_{Mg} = \int_0^t \frac{dX_{Mg}}{dt} dt \tag{3.4}$$

where,

$Y_i\|_0$	mass fraction of element i in the feedstock
M_0	feed mass (kg)
MW_i	the atomic weight of element i (kg mol^{-1})
r_{Mg}	molar dissolution rate (mol s^{-1})

---

[1] The relative degree of conversion of magnesium was calculated based on the stoichiometric amount of total magnesium content in pure serpentine (~43 wt.%) with a chemical formula of $Mg_3Si_2O_5(OH)_4$. It is worth noting that, in fact, the material is not phase-pure and not all of the MgO content is available.

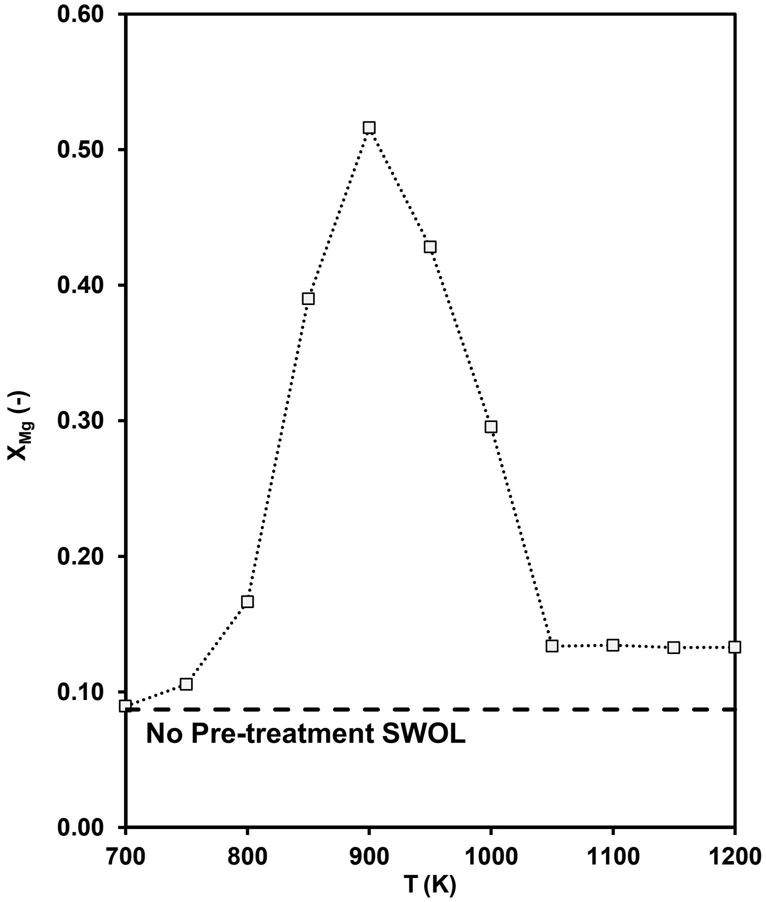

Figure 3-3. The fractional extent of magnesium conversion as a function of the activation temperature. The dissolution experiments were carried out at a reaction temperature of 423 K, P_{CO2} = 100 bar, and PSD = 63-75 μm over the reaction period of 60 minutes under the saturated CO_2-H_2O system.

The fractional extent of magnesium conversion displayed a sharp maximum for material activated at 900 K, which is approximately five times greater than achieved with untreated SWOL. This trend is consistently reported in several previous studies, such as Fouda et al., 1996, Li et al., 2009, Dlugogorski and Balucan, 2014, Werner et al., 2014b, and is in consensus with the finding reported by Mann (2014) concerning the formation of a nearly non-crystalline phase at an activation temperature of 900 K. Since then, based on these experimental results, an activation temperature of 900 K is selected for activation of the research material throughout this study.

3.3.4 Chemical Characterisation

In the present study, the chemical composition of the material is quantified through X-ray fluorescence (XRF) analysis performed at the University of NSW (see Appendix A). Table 3-1 shows the chemical composition of SWOL, and thermally activated SWOL (activated using a fluidised bed calciner reactor at conditions of 900 K for a period of 120 minutes under an argon-fluidising medium). The differences in the total elemental concentrations of thermally activated and non-activated material is originated from the amount of chemically bound water as percentages of LOI[1] (loss on ignition) are 3.97% and 16.96%, respectively.

Table 3-1. Chemical composition of the research materials – determined through the XRF analysis based on the average of seven times measurements.

Material	Major components (wt.%)						
	MgO	SiO_2	Fe_2O_3	Al_2O_3	CaO	Cr_2O_3	Mn_3O_4
SWOL	35.70	37.26	7.30	1.61	0.55	0.33	0.14
HT-SWOL*	41.39	43.06	8.63	1.83	0.49	0.42	0.15

**Activated at 900 K for 120 minutes*

Further determination of the magnesium content of the research material was carried out by digestion of the research materials in aqua regia solution, and subsequent ICP-OES analyses. This approach was adopted where the mass balance analysis required verification of the measured magnesium extraction rate.

3.3.5 Physical Characterisation of the Mineral Samples

The size distribution of the research materials was obtained using a combination of Retsch planetary ball mill (PM 400) and Retsch AS 200 digit vibratory sieving instruments. Prior to the wet milling process, the material was washed and sieved to <3 mm. The material was consistently distributed (125 g) in each grinding jars and milled for 1.5 minutes with 200 rpm of wheel spin. Size segregation was performed by using the Retsch AS

---

[1] The LOI values were determined through XRF analyses.

200 digit vibratory sieve shaker. This step was carried out according to the recommended procedure for standard wet sieving provided by the instrument manufacturer (Retsch). The ground material was size-fractionated by sieving at 20, 45, 63, 75, 90, 125, 150, 180, and 212 μm. The material was dried at 348 K in a drying oven overnight. Particle size analysis of the size-fractionated materials was performed by using a laser diffraction technique (Malvern Mastersizer 3000 within a range of 0.01-3500 μm) via the wet dispersion method. The particles were dispersed in water and agitated at 1000 rpm with ultrasonication before the analysis. Particle size analysis was carried out at a constant agitation speed of 1000 rpm until the particle size data were collected. Each specimen measurement consisted of an average of nine measurements. An initial record of the dispersant background before the addition of solid samples was acquired prior to each measurement. The solid samples were added until the maximum light obscuration[1] of 10% was achieved. Information obtained from the volume-weighted distribution analysis consisted of based particle size parameters including $d4,3$, $d3,2$, $d10$, $d50$, and $d90$. These parameters were defined as the volume mean diameter, Sauter mean diameter (defined as the diameter of a sphere with the same volume/surface area ratio), and particle diameters at 10, 50, and 90 percent of the cumulative distribution, respectively. The measured parameters are outlined in Table 3-2 for the South West Oregon Lizardite (SWOL) material.

The morphology and chemical composition of the individual sieved fractions are deemed to be uniform as the sensitivity study conducted by Mann (2014) showed no evidence of change in chemical composition for particle sizes < 20 μm up to 300 μm milling conditions covering 200 rpm for 20 min to 200 rpm for 1.5 min. Analysis of the powder XRD patterns of SWOL material as a function of three particle size distributions (< 20, 45-63, and 212-300 μm) confirms no broadening of the associated Bragg peaks with the crystalline phase.

---

[1] The interaction of light beams with particles passing through the photo-zone (sensing zone), results in light is being absorbed or refracted due to the physical properties of particles or being scattered at some oblique angle. The magnitude of this impulse depends on two parameters: the cross-sectional area of the particle and the physical principle of detection – either light scattering or light blocking (obscuration). The light obscuration method permits high resolution particle sizing.

Table 3-2. Summary of measured particle size parameters for the SWOL materials.

Material	SWOL						
d_p (μm)	< 20	20-45	45-63	75-90	90-125	125-150	150-180
$d_{3,2}$	6.49	39.60	65.80	102.00	127.00	164.00	208.00
$d_{4,3}$	21.60	45.70	73.00	111.00	138.00	180.00	225.00
d_{10}	2.73	25.50	45.00	73.70	91.20	116.00	149.00
d_{50}	13.10	42.60	69.70	107.00	133.00	172.00	216.00
d_{90}	35.80	70.70	107.00	154.00	192.00	256.00	313.00

3.4 Standard Dissolution Conditions

In the present study, on the basis of the Albany NETL process, selected experimental conditions are defined as the standard conditions. This strategy facilitates comparison of kinetics data throughout the study. The standard conditions employed were a reaction temperature of 423 K and P_{CO2} = 100 bar under the saturated CO_2-H_2O system (m_{CO2} ~3.7 mol kg^{-1}). These conditions contained 250 mg mass loading of thermally activated SWOL (activated at 900 K for 120 minutes) with a particle size distribution of 45-63 μm ($d_{3,2}$ = 62.9 μm). The overall volumetric flow rate of the reactive fluid set as 2.12 cm^3 min^{-1}. This volumetric flow rate corresponds to a reactor residence time of ~13 s and mass loading factor of 0.25 min.

3.5 Reactor Hydrodynamics

The calculation of the flow pattern in the reactor at the so-called standard conditions predicts that the state of the flow in the bed is similar to a moderately fluidised bed pattern, as described in Appendix C. The main advantage associated with this flow pattern is that it allows determination of the accurate kinetics of the dissolution reaction – due to the occurrence of homogeneous suspension where the solids and fluids are mixed well. However, the observatory experiment performed within a single flow of water passing through a transparent reactor set-up containing mineral particles in accordance with the standard loading factor at ambient pressure and temperature conditions showed contradictory results, indicating a stationary flow pattern. The implication of this observation is that the fluid merely percolates through the void spaces between the stationary particles –

accordingly, the reactor operates with the fixed bed conditions. To further investigate the effect of the reactor hydrodynamics on the measured rates, three sets of standard experiments were conducted with deliberately packed bed conditions (by using a homogeneous mixture of inert Al_2O_3 material and research material) versus the normal fluidised bed conditions. Figure 3-4 shows the results obtained under the identical flow and reactor conditions for magnesium concentration in the aqueous effluent. Despite the expectation of the concentration stratification being linked with the packed bed conditions, there is no apparent significant difference perceived for the packed bed versus the normal fluidised bed conditions.

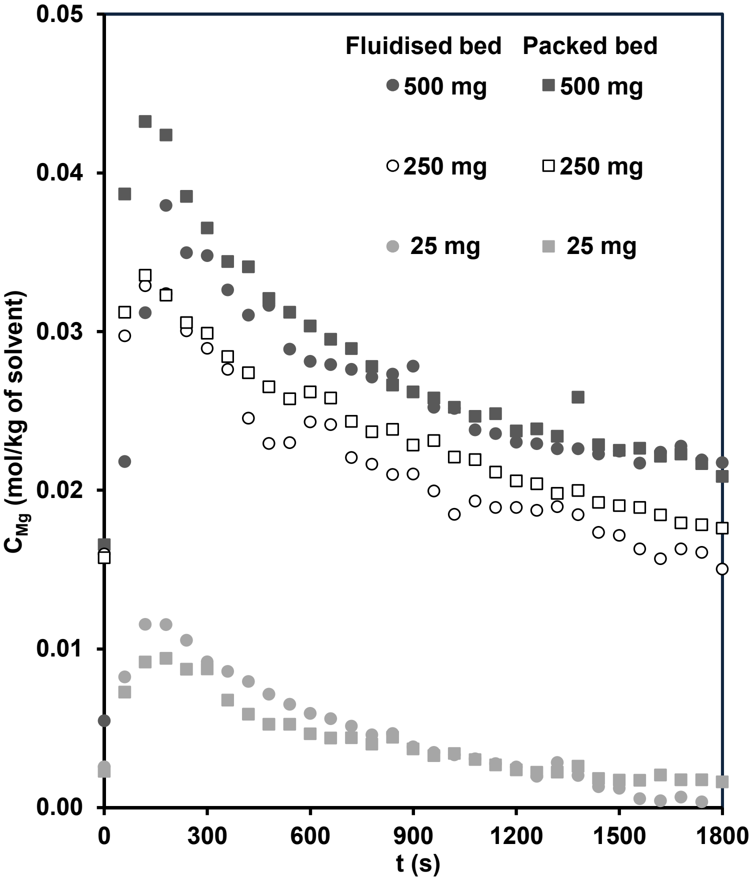

Figure 3-4. Magnesium concentration profiles for fluidised bed and packed bed conditions using different mass loadings of thermally activated SWOL (PSD = 45-63 μm) under the saturated CO_2-H_2O system, at P_{CO2} = 100 bar, T = 423 K, and 30 minutes reaction time.

To summarise, comparison of these observations suggests that the state of single-phase water flow in the bed does not seem to be fluidising – but in the presence of gas, it is expected that the flow pattern in the reactor complies with the fluidisation regime. On the other hand, the experimental results showed indistinguishable concentration profiles for packed versus fluidised bed conditions. On this basis, in the present study, it is presumed that the concentration of the measured components in the outlet stream is the same as the solution composition in the reactor cell.

3.6 Thermodynamics Prediction

Thermodynamics is a useful tool for elucidating reactions where equilibria are attained. However, many processes are controlled by reaction rates, and so can be explained merely by reaction kinetics. In the present study, to obtain insights into the evolution of the heterogeneous phase equilibria and reaction pathways during the dissolution reaction, thermodynamic modelling was conducted using OLI Analyser Studio 9.1 (OLI System Inc). The MSE (Mixed Solvent Electrolyte) thermodynamic framework, which is based on the Helgeson equation of state, was employed. In this model, aqueous activities (α) are determined through an extended Debye-Hückel limiting law. The activities of the aqueous species are calculated on the basis of the hypothetical standard state of one-molal (mol kg^{-1}). Performing calculations on a molal base makes the concentration definition independent of density and, therefore, temperature. The calculated equilibrium solubility of CO_2 under the CO_2-H_2O system was validated based on the well-established thermodynamic model for the solubility of CO_2 in water derived by Duan and Sun (2003), as presented in Appendix B.

3.6.1 Reaction Path Trajectories in MgO-CO_2-H_2O

In this study, thermodynamic modelling was used to calculate the equilibrium pH and magnesite saturation indices of the solution under experimental conditions. The pH of the system was calculated on the basis of the pressure, temperature, and total dissolved concentration of magnesium. *In situ* measurement of pH was not possible during the experiments as all of the reactions were performed under micro-scale hydrothermal conditions. The reaction path trajectories were calculated for the MgO-CO_2-H_2O system (using OLI-MSE under conditions similar to those used for the NETL process, as shown in Figure 3-5. As magnesium oxide dissolves, magnesium cations are released into the solution and, subsequently, protons are consumed (pH increases) –further progress in the dissolution of magnesium becomes inhibited since protons are the active species. The aqueous magnesium concentration increases until it is limited by the saturation limit of the secondary phase (solid $MgCO_3$). Under the utilised conditions (T_{reaction} = 423 K and P_{CO2} = 100 bar), the equilibrium solubility of magnesite was reached a molality of Mg ~0.0197 mol kg^{-1}. After the equilibrium point, the aqueous magnesium species must be transformed to solid magnesite[1] within the thermodynamic perspective. This phase transformation is also reflected in the evolution of the equilibrium pH. As the aqueous magnesium concentration increases, the corresponding proton concentration decreases (pH increases); this trend continues until the aqueous magnesium concentration reaches its phase transition threshold. Some possible magnesium ion pairs in solution were identified as $MgCO_3^{o}$ and $MgOH^{+}$. Table 3-3 shows the concentration of magnesium ion pairs along with the concentration of carbonate ions under saturation conditions.

---

[1] A distinction must be made between the kinetic rate constant and thermodynamic equilibrium constant. At given conditions, the transformation rate of aqueous magnesium compounds to solid magnesite might be affected by different operating parameters. Hence, throughout this study the equilibrium solubility of magnesite was used as an indication of the relevant concentration domain (saturated or under-saturated).

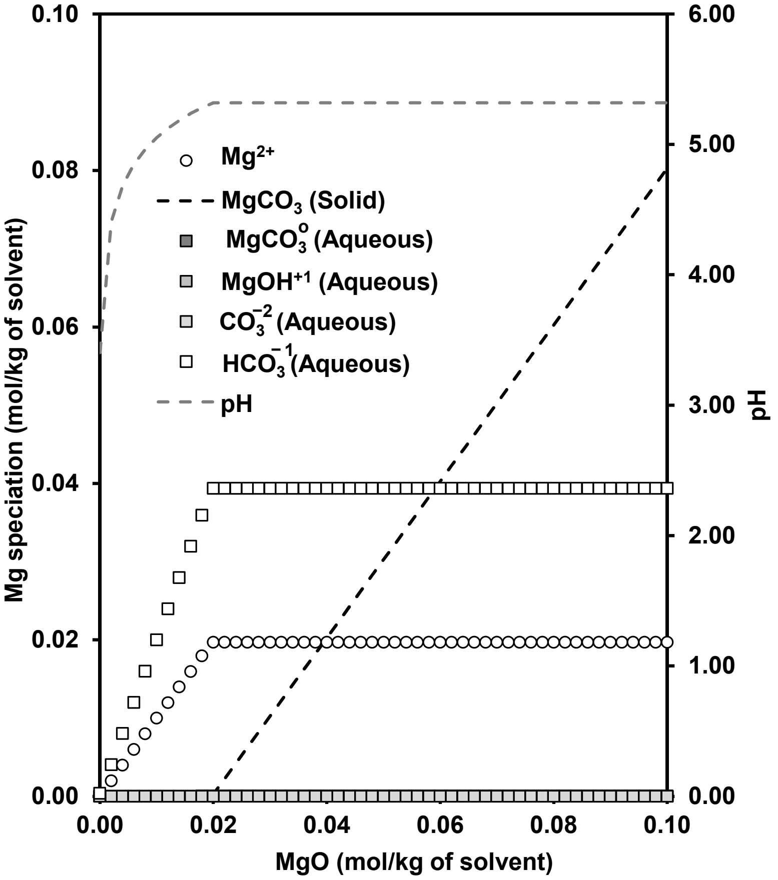

Figure 3-5. Distribution of magnesium speciation under the MgO-CO_2-H_2O system at P_{CO2} = 100 bar, T = 423 K, calculated using OLI-MSE at the saturated conditions ($m_{CO2} \cong 3.7$ molal). In OLI-MSE, H_2CO_3 and $CO_{2(aq)}$ are recognised as an equal and remained constant as simulations were performed at saturated conditions.

Table 3-3. Concentrations of carbonate ion and magnesium ion pairs at saturated conditions with respect to the solid $MgCO_3$ formation.

Species	Concentration (mol kg^{-1})
CO_3^{-2}	1.33×10^{-6}
$MgOH^{+1}$	1.45×10^{-5}
$MgCO_3^{\circ}$	3.87×10^{-5}

From this observation, it appears that the magnesium cation is a prevailing cation and the bicarbonate is the main anion in this system – in a ratio of $[HCO_3^-] = 2\,[Mg^{2+}]$. As shown in Chapter 2, the concentration of protons and bicarbonate ions are directly related to CO_2 fugacity in accordance with reaction (R 3.1),

$$CO_2\,(aq) + H_2O\,(l) \rightleftharpoons HCO_3^-\,(aq) + H^+\,(aq)$$

$$\frac{K_1 K_{CO_2} f_{CO_2} a_{H_2O}\,(m^o)^2}{f^o a_{HCO_3^-}} = a_{H^+} \tag{R 3.1}$$

it is thus reasonable to express that the $[H^+] \propto [HCO_3^-]^{-1} \propto [Mg^{2+}]^{-1}$ – the activity of protons can be shown proportional to the reciprocal of the activity of magnesium cations, in accordance with equation (3.5),

$$a_{H^+} \propto \frac{1}{a_{Mg^{2+}}} \tag{3.5}$$

Overall, the simulation of the reaction pathways has suggested that the extraction of magnesium in the carbonic acid system can be equilibrium limited under saturation conditions, as the parallel precipitation (combination of nucleation and growth steps) of magnesite influences the progress of the dissolution process. According to previous studies, formation of magnesite is thermodynamically dominated versus the other forms of magnesium carbonate species throughout most of the conditions. (Königsberger et al., 1999, Hänchen et al., 2008, Bénézeth et al., 2011). In this study, the equilibrium solubilities of magnesite were calculated using OLI-MSE under the corresponding experimental conditions. Magnesite solubility data obtained from the OLI-MSE database was also compared with the Bénézeth et al. (2011) model, as describe in Appendix B. This comparison suggested that the OLI-MSE calculations report the solubility product of magnesite to be an order of magnitude lower than the experimental value. One possible explanation for the observed discrepancy in the solubility data could be related to the crystallinity status of the magnesite (crystalline or amorphous). Here it is worth noting that the formation of other magnesium carbonate polymorphs which are explained in section (2.4.1) is possible under the reaction conditions; nevertheless, magnesite has the lowest solubility of the possible carbonate phases. The magnesium concentration profiles measured from the experiments are compared with the solubility product of magnesite to shed some light on the degree of saturation of the system. Determination of exact phases and crystallinity of all possible magnesium carbonate polymorphs formed during the dissolution reactions are not pursued in the current study.

3.6.2 Solubility of Silica in Aqueous Solution

Through the literature reviewed in section 2.6, silica is described as playing an important role in the dissolution process of silicates. The chemistry of the solution containing silica is known to be complex and difficult to predict. This phenomenon is particularly become important in the dissolution of magnesium silicates, as the exact form of the liberated silica will vary depending on several variables (e.g., crystal silicate structure[1] (see Appendix B)). Investigation of the detailed sequence associated with silica reactions in the aqueous phase is beyond the scope of this study; instead, the thermodynamics information relevant to this study is presented in this section.

The formation of free silica in aqueous solution depends on several factors including the silica solubility limit, solution pH, temperature, solution chemistry, and operating conditions (e.g., system pressure). Unlike for metal carbonate, an increase in temperature results in an increase in the solubility of silica (Chen and Marshall, 1982, Fournier and Rowe, 1977). Based on the experimental observations, several research groups have expressed that the solubility of amorphous silica increases with increasing temperature (Morey et al., 1964, Chen and Marshall, 1982). However, they also reported that the opposite trend occurs when salts are present in the solution (e.g., magnesium sulphate, magnesium chloride), as higher salt concentrations increase supersaturation (Makrides et al., 1980). Furthermore, other researchers, such as Fournier and Rowe (1977), demonstrated that the effect of pressure at elevated temperature on the solubility of amorphous silica is less significant than the temperature effect. Measuring silica concentration in an aqueous solution thus requires an understanding of silica equilibrium chemistry and its heterogeneous chemistry. Amorphous silica can be found in an aqueous solution in different forms, a) dissolved (or reactive), b)

---

[1] In this study the calculated solubility of amorphous silica was used for comparison of the measured silica concentration profiles, as the examined material nearly has non-crystalline structure.

polymerised (reacts slowly), c) colloidal (or unreactive), and d) suspended (or particulate) (Iler, 1979). According to Iler (1979), when the solid phase of silica makes contact with water, a small amount of silica dissolves and enters the aqueous phase. Two chemical reactions govern the dissolution of silica in water, hydration and dehydration catalysed by OH^- ions (at pH above 3), which are shown by reaction (3.2),

$$(SiO_2)_x(s)+2H_2O(l) \underset{k_-}{\overset{k_+}{\rightleftharpoons}} H_2SiO_4(aq) \underset{k_-}{\overset{k_+}{\rightleftharpoons}} (SiO_2)_{x-1}(s)+Si(OH)_4(aq), \qquad \text{(R 3.2)}$$

where k_+ denotes for equilibrium with hydration step and indicates k_- equilibrium of dehydration step. Carman (1940) postulated that in reaction (R 3.2) a single layer of water molecules adsorbs at a silica surface; this effect is regarded as surface hydration and, as a result, surface hydroxyl groups (e.g., the monomer “soluble silica” or $Si(OH)_4$) are formed. Furthermore, Iler (1979) stated that the formed hydroxyl groups had a weak inclination to dissociate and release hydrogen ions. In contrast, these hydrated silica groups are highly instable, and have a tendency to undergo an irreversible condensation. Therefore, depending on the saturation status and pH of the solution, the formed Si(OH) groups could rapidly change and grow particles, and subsequently transferred to colloidal silica. In general, under heavy supersaturation conditions, condensation (nucleation and growth) between primary colloidal particles leads to the formation of silica gels (Carman, 1940, Weres et al., 1981, Alexander et al., 1954). The associated reaction may be expressed by reaction (3.3),

$$\text{-Si-OH + HO-Si-} \rightleftharpoons H_2O + \text{-Si-O-Si-} \qquad \text{(R 3.3)}$$

Under supersaturation conditions with respect to anhydrous nonporous amorphous SiO_2, the equilibrium concentration of $Si(OH)_4$ at 298 K corresponds to 70 ppm as SiO_2; however, the common types of amorphous silica, such as those containing small porous, exhibit a marginally higher solubility 100-130 ppm (Iler, 1979). Here it is worth noting that the pH of the solution significantly influences the solubility of amorphous silica; as such, Iler (1979) reported that at pH above 10 and 298 K, the solubility of amorphous silica reaches ~800 ppm. Nevertheless, under acidic conditions the variation in the solubility of silica is minor. The OLI-MSE calculations under the standard conditions (e.g., T = 423 K and P_{CO2} = 100 bar) show that in going from pH 3.4 to 5.4, the solubility of amorphous silica changes insignificantly (~9%). In the present study, the pH of the solution is always tied to acidic conditions.

The reactions (dissolution and condensation) of the silica content of silicate minerals, when exposed to an aqueous phase, are complex and could influence the extraction mechanisms of metal cations. This phenomenon becomes more complex at the local reaction conditions. For instance, in the case of dissolution of magnesium silicate (e.g., serpentine) under moderately acidic conditions (pH above 3) at a particular reaction site, as the magnesium content of the mineral is extracted, the local pH changes towards more basic conditions. The change in pH, depending on local saturation levels, typically gives rise to condensation of the released silica groups at the local site. In this regards, Makrides et al. (1980) reported that, from pH 4-6 the rate of disappearance of monomers (condensation of silica nuclei) increases by a factor of approximately 10 for each pH unit from a solution saturated with silicic acid.

In the present study, the solubility of amorphous silica was simulated using OLI-MSE for the SiO_2-H_2O-CO_2 system[1], as shown in Figure 3-6, in which SiO_2 (aqueous) is referred to the monomeric units in the solution. The dissolution of silica hardly affects the solution pH under acidic conditions. According to OLI-MSE thermodynamic modelling, other possible silicic acid ion associations (e.g., $H_3SiO_4^{-2}$) may be found in negligible concentrations, as shown in Table 3-4. Under the employed experimental conditions (T_{reaction} = 423 K and P_{CO2} = 100 bar), the equilibrium solubility of amorphous SiO_2 was reached a molality of ~0.011 mol kg^{-1}. This value is in close agreement with previous studies investigate the solubility of

---

[1] In aqueous solutions that are adequately saturated with dissolved silica, the excess silica might be converted to colloidal amorphous silica – thus the term "silica" here refers to amorphous silica rather than crystalline silica.

amorphous silica in the aqueous phase (Chen and Marshall, 1982). Theoretically, the concentration of aqueous silica compounds increases until it is limited by saturation limit of the amorphous SiO_2.

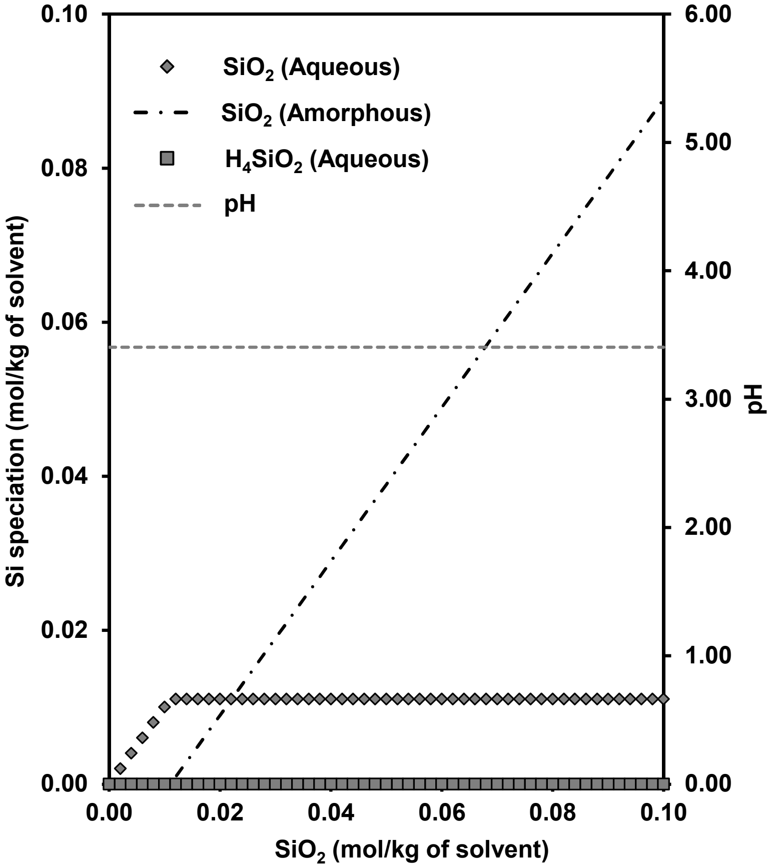

Figure 3-6. Distribution of silica speciation under the SiO_2-CO_2-H_2O system at P_{CO2} = 100 bar, T = 423 K, calculated using OLI-MSE at the saturated conditions ($m_{CO2} \cong 3.7$ molal).

Table 3-4. Concentrations of silicic acid, hydrogen metasilicate ion and dihydrogen orthosilicate ion at saturated conditions with respect to amorphous silica saturation.

Species	Concentration (mol kg^{-1})
H_4SiO_4	1.57×10^{-126}
$HSiO_3^{-1}$	4.22×10^{-8}
$H_2SiO_4^{-2}$	5.31×10^{-16}

In the present study, the measured silica dissolution rates are reported and compared with the equilibrium solubility of the amorphous silica.

Chapter 4. Experimental Results

4 Introduction

Prior studies of mineral carbonation (e.g., O’Connor et al., 2005) have not addressed the kinetics of fundamental steps (i.e., dissolution and precipitation) involved in mineral carbonation in any detail. In this study, this gap was addressed with the objective of elucidating the kinetics of magnesium extraction from thermally activated serpentine by carbonic acid under conditions relevant to *ex situ* mineral carbonation. The experimental results shown in this chapter examine variables that influence the overall form of the rate law related to the mineral-water dissolution and surface growth reactions. Measured rates and thermodynamics are qualitatively compared through calculation of the governing phase equilibria. This approach is essential in the interpretation of the reaction kinetics in the vicinity of the equilibrium solubility of $MgCO_3$. The results presented in this chapter are discussed in detail in Chapter 5.

4.1 Dissolution of Thermally Activated SWOL under the CO_2-H_2O System

Experiments were carried out to assess the kinetics (reaction rates) of magnesium and silica extraction from thermally activated SWOL using the experimental approaches described in Chapter 3. Throughout this process, water operates as a reactant and as a transporting agent of dissolved components. The nominal volumetric flow setting of the pumps were evaluated by measuring the discharge flow rate of the system, at a constant pressure of 100 bar and pump flow rates (H_2O: 1 mL min^{-1} and CO_2: 0.2 mL min^{-1}), as shown in Figure 4-1. These results indicate that the amount of aqueous phase discharges from the sampling port essentially remains identical to the liquid phase pumped into the system.

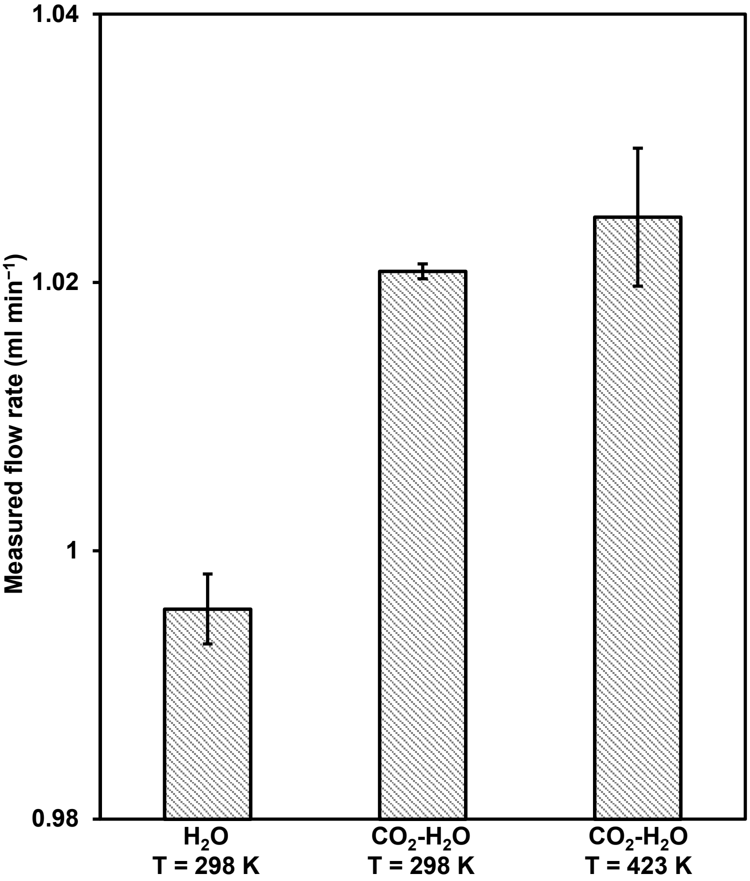

Figure 4-1. Measured discharge flow rate of the aqueous phase for the indicated flow conditions (all the measurements were conducted at a system pressure of 100 bar). The error bars denoted the standard deviation with three replicate experiments.

Typical results are shown in Figure 4-2 (expressed in molar concentration scale to facilitate comparison with the equilibrium solubilities of magnesite and silica). In this study, the molar dissolution rate (r_i) and the fractional extent of conversion (X_i) of the dissolved elements were calculated by using equation (4.1) to equation (4.3), respectively.

$$r_i = -\frac{dN_i}{dt} = \dot{m}_{Aqueous} \times C_i \tag{4.1}$$

conversion rates,

$$\frac{dX_i}{dt} = r_i \times \frac{1}{N_i|_0} \tag{4.2}$$

the fractional extent of extraction X_{Mg},

$$X_i = \int_0^t \frac{dX_i}{dt} dt \tag{4.3}$$

where,

$\dot{m}_{Aqueous}$	water mass flow rate (kg s^{-1})
C_i	molality of the dissolved elements (e.g., Mg) (mol kg^{-1})
r_i	molar dissolution rate (mol s^{-1})
$N_i\|_0$	initial total number of moles of element i, in the reactor (mol)[1]

The molar dissolution rates (r_i) are directly determined through the individual magnesium and silica molalities by using equation (4.1). The degrees of conversion are determined according to equation (4.2), where X_i is expressed as the amount of element i leached relative to the initial amount of i in of the mineral.

Observation of the concentration profiles of the aqueous magnesium and silicon moieties (abbreviated as Mg and Si in Figure 4-2) shows that magnesium was released relatively faster compared with silica. The concentration of magnesium reached a maximum[2] of ~0.03 mol kg^{-1} approximately after 4 minutes from the starting time. Beyond the peak, the magnesium concentration decreased steadily until the termination of the reaction. Initially, the magnesium concentration exceeded its calculated saturation value corresponding to the conditions in the reactor but after ~27 minutes the dissolution continued in undersaturated conditions. Under the saturated conditions, it is possible that some $MgCO_3$ precipitated in the reactor and was trapped there. However, TPD[3] (Temperature Programmed Desorption) analysis of the residual solids removed from the reactor showed that there was no significant carbonate present. The aqueous concentrations are therefore taken to represent the actual rate of magnesium extraction from the mineral phase.

---

[1] Determined using the XRF data presented in Table 3-4.

[2] This delay could be related to the lag time associated with flow from the reactor outlet to the point of sample collection.

[3] No evidence for peaks corresponding to $MgCO_3$ was detected and the amount of deposited carbonate was less than 1%. This observation implies that the form of the deposited MgCO3 within the particles may be non-crystalline, as no other phases of carbonate (those with higher solubilities) were also found.

Aqueous silica[1] (abbreviated as Si) was released more slowly than magnesium. The concentration was relatively constant throughout, approaching ~0.007 mol kg^{-1}.

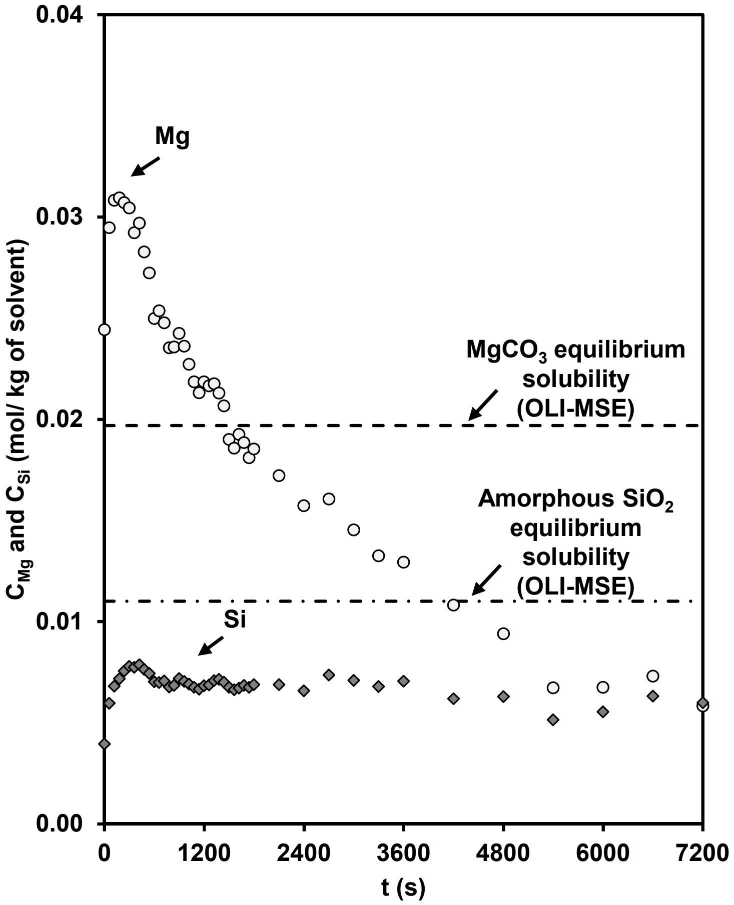

Figure 4-2. Magnesium and silica concentration profiles acquired from the dissolution of thermally activated SWOL (PSD = 45-63 μm) under the saturated CO_2-H_2O system, at P_{CO2} = 100 bar, T = 423 K, and 120 minutes reaction time. The equilibrium solubilities of the $MgCO_3$ & SiO_2 were calculated by using OLI-MSE. Results were analysed using quantitative ICP-OES.

The corresponding silica conversion rates and the evolution of the degrees of conversion for magnesium and silica are presented in Figure 4-3 and Figure 4-4, respectively.

---

[1] In this study a term of "aqueous silica" was used and referred to overall silica phases in the aqueous solution. It must be noted that the release rate of cations reflect the global dissolution process, and are not always equal to true intrinsic rate of detachment from the original mineral structure.

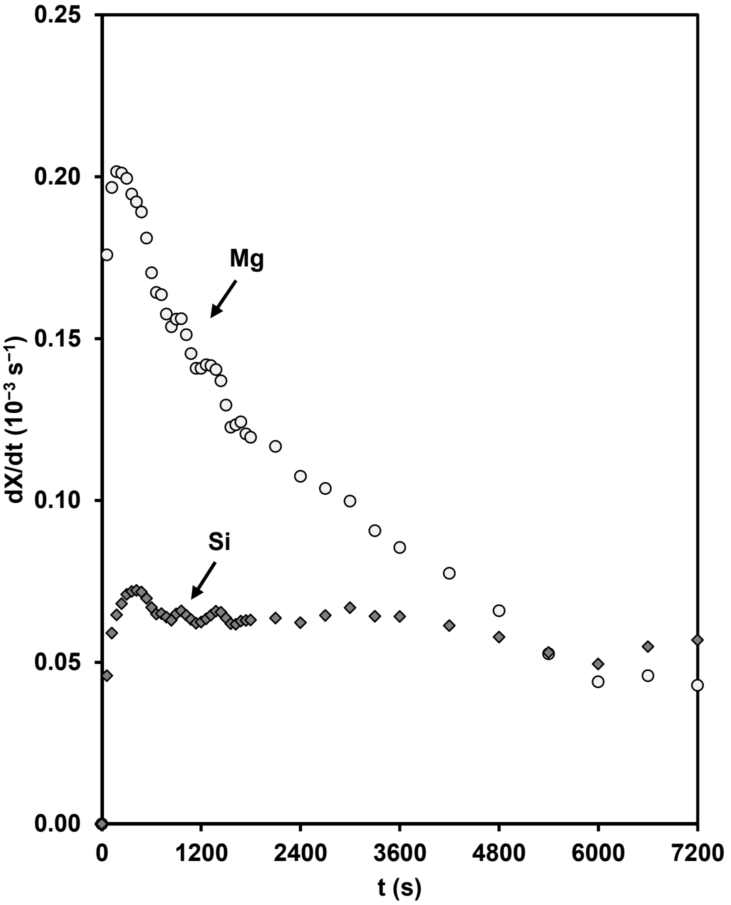

Figure 4-3. Magnesium and silica conversion rates, acquired from the dissolution of thermally activated SWOL (PSD = 45-63 μm) under the saturated CO_2-H_2O system, at $P_{CO2} = 100$ bar, $T = 423$ K, and 120 minutes reaction time.

During the initial stage, the conversion rate of magnesium was approximately three-fold greater than the corresponding rate for silica but the rates become comparable after longer reaction times when the relative extraction rate for magnesium slows relative to the approximately steady rate for silica. The extent of cumulative conversion of magnesium and silica reached 66% and 43%, respectively, over the reaction period of 120 minutes, as shown in Figure 4-4.

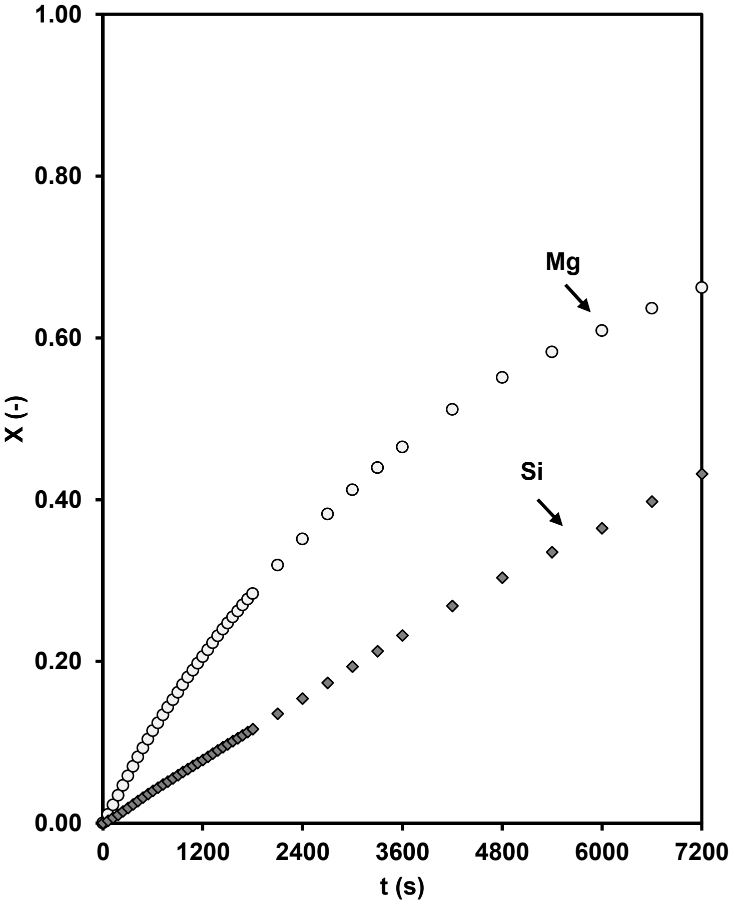

Figure 4-4. Degree of completion of magnesium and silica extraction, acquired from the dissolution of thermally activated SWOL (PSD = 45-63 μm) under the saturated CO_2-H_2O system, at P_{CO2} = 100 bar, T = 423 K, and 120 minutes reaction time.

In the literature, mineral dissolution is described as congruent if elements are released at the stoichiometric ratios of the parent mineral. The ratio of magnesium versus silica release rate, illustrated in Figure 4-5, shows the instantaneous ratios of the molar dissolution rates for magnesium versus silica for the experiment reported in Figure 4-2. For comparison, the theoretical stoichiometric ratio was quantified as ~1.43, with respect to elemental quantities determined through XRF analysis. As described above, the initial extraction rate of magnesium is relatively faster than that of silica. On this basis, it is expected that the residual mineral is correspondingly depleted in magnesium and enriched in silica. It appears however that, at ~80 minutes reaction time, the Mg:Si extraction ratio approached that for congruent dissolution but this is probably of no particular significance because the ratio continues to decrease smoothly beyond this point.

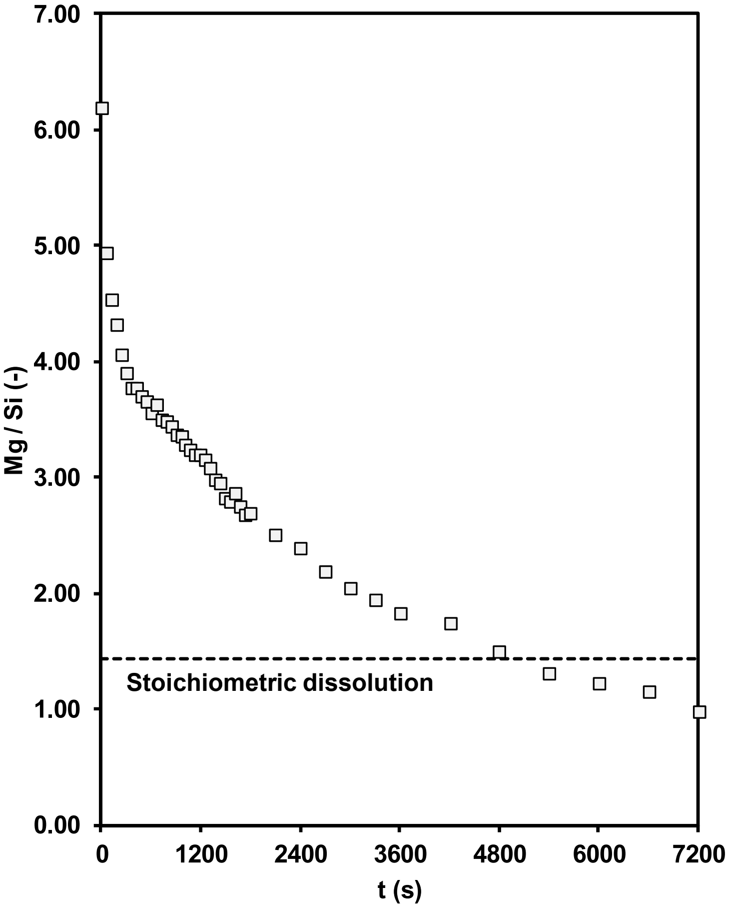

Figure 4-5. Magnesium-silica molar ratio obtained from the dissolution profiles presented in Figure 4-2 (showing an initial preferential release of magnesium), the dashed line represents the stoichiometric dissolution.

In order to investigate further the behaviour of the dissolution profiles, the experiment was repeated for a longer period (4 hours), as summarised in Figure 4-6 and Figure 4-8. As the reaction proceeded, similar to what was observed in Figure 4-2, the extraction rate of magnesium decreased.

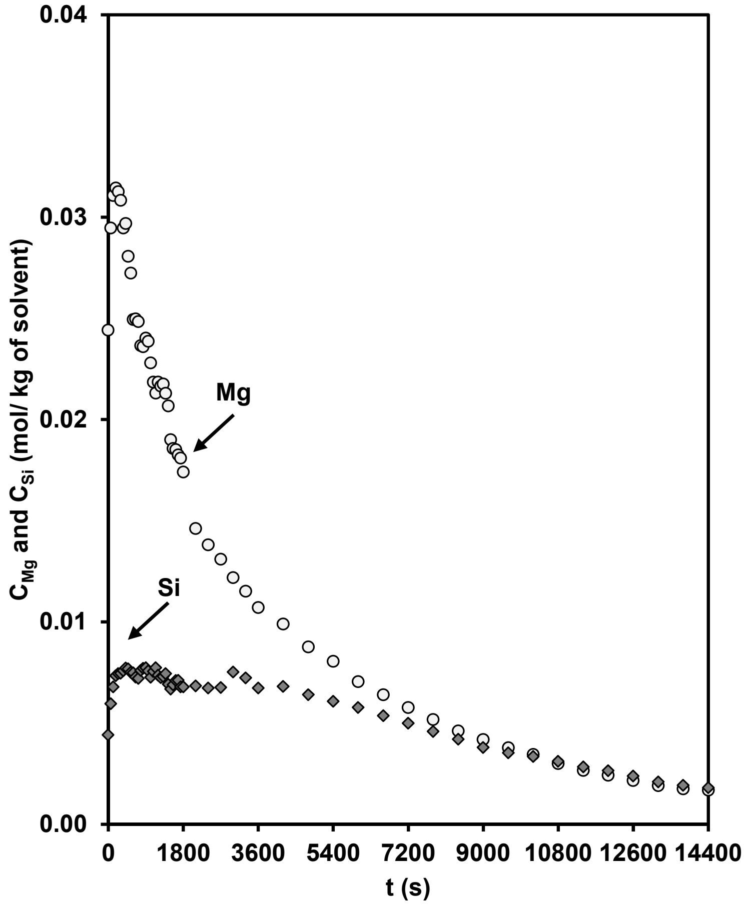

Figure 4-6. Magnesium and silica concentration profiles acquired from the dissolution of thermally activated SWOL (PSD = 45-63 μm) under the saturated CO_2-H_2O system, at P_{CO2} = 100 bar, T = 423 K, and 240 minutes reaction time.

While it is not the objective of this thesis to investigate the ultimate extents of extraction achievable, it is interesting to note that the fractional conversion of Mg after 4 hours is 78%, as shown in Figure 4-7, with every sign that the process will continue to completion, although at diminishing rate. The extent of extraction of silica reaches 65% after 4 hours – clearly much of the original mineral has been solubilised.

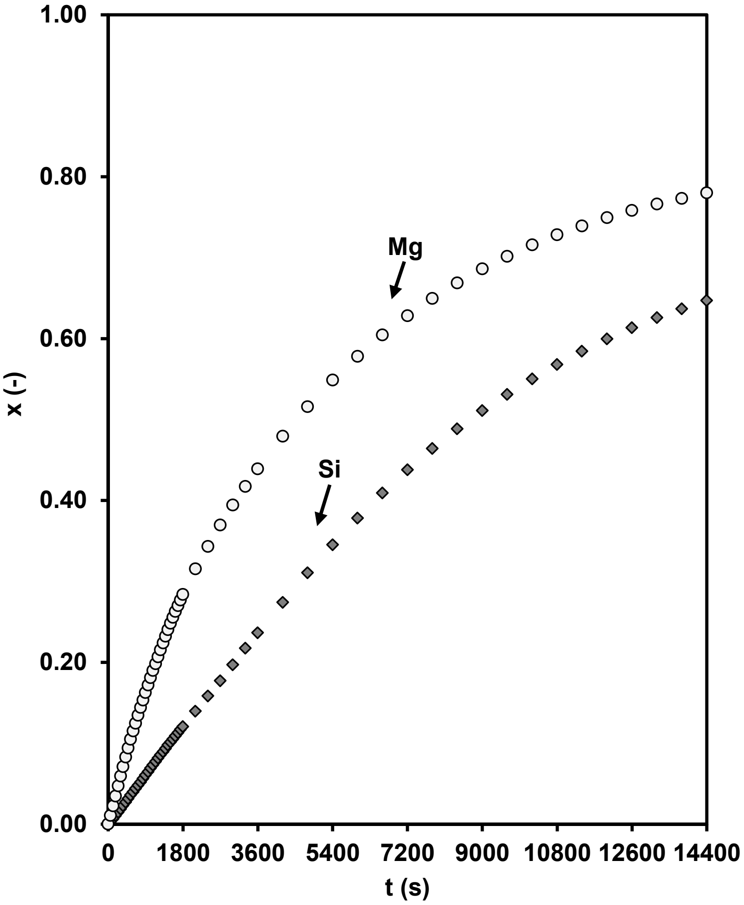

Figure 4-7. Degree of completion of magnesium and silica extraction, acquired from the dissolution of thermally activated SWOL (PSD = 45-63 μm) under the saturated CO_2-H_2O system, at P_{CO2} = 100 bar, T = 423 K, and 240 minutes reaction time.

Now from Figure 4-8, it is apparent that the relative extraction Mg:Si falls below that for congruency; at the same time, this ratio does appear to approach an asymptotic limit, in this case corresponding to approximately equimolar rates of dissolution.

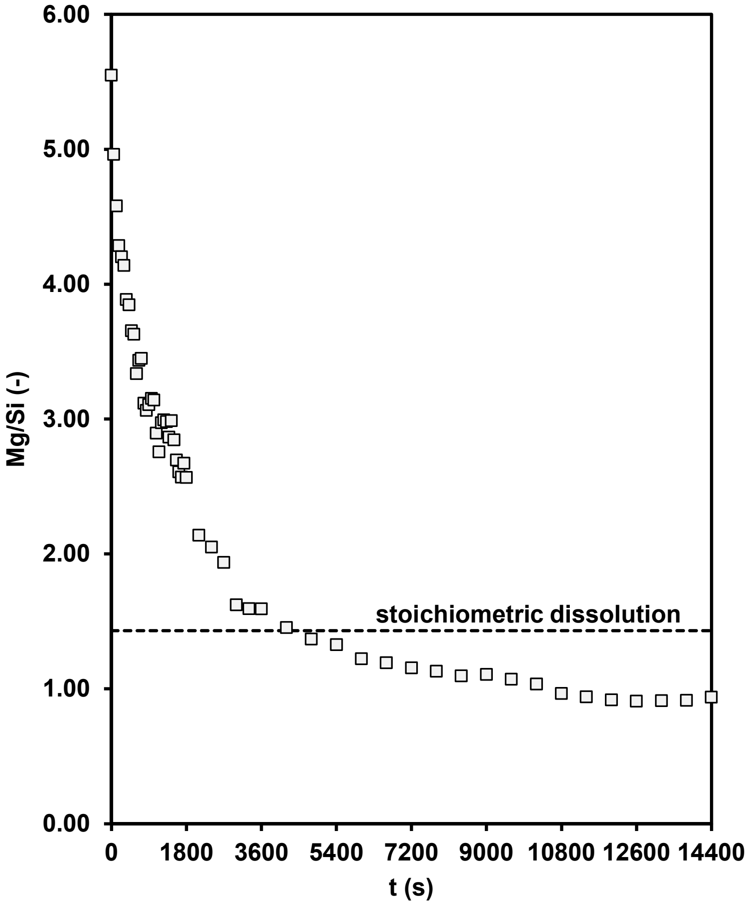

Figure 4-8. Magnesium-silica molar ratio obtained from the dissolution profiles presented in Figure 4-6 (showing an initial preferential release of magnesium), the dashed line represents the stoichiometric dissolution.

4.1.1 Reproducibility and Mass Balance Closure

A mass balance analysis was carried out on the system based on the data attained from seven standard dissolution experiments[1]. The leachates analysis along with the compositional analysis of the residual solids in the reactor indicated that the extent of uncertainties associated with the extraction rate was roughly ±5%. Figure 4-9 shows the results obtained from identical flow and reactor conditions for the magnesium and silica concentrations in the aqueous effluent and Figure 4-10 illustrates the corresponding evolution of the degree of conversions for the magnesium and silica, X(-).

---

[1] Results were analysed using quantitavive ICP-OES.

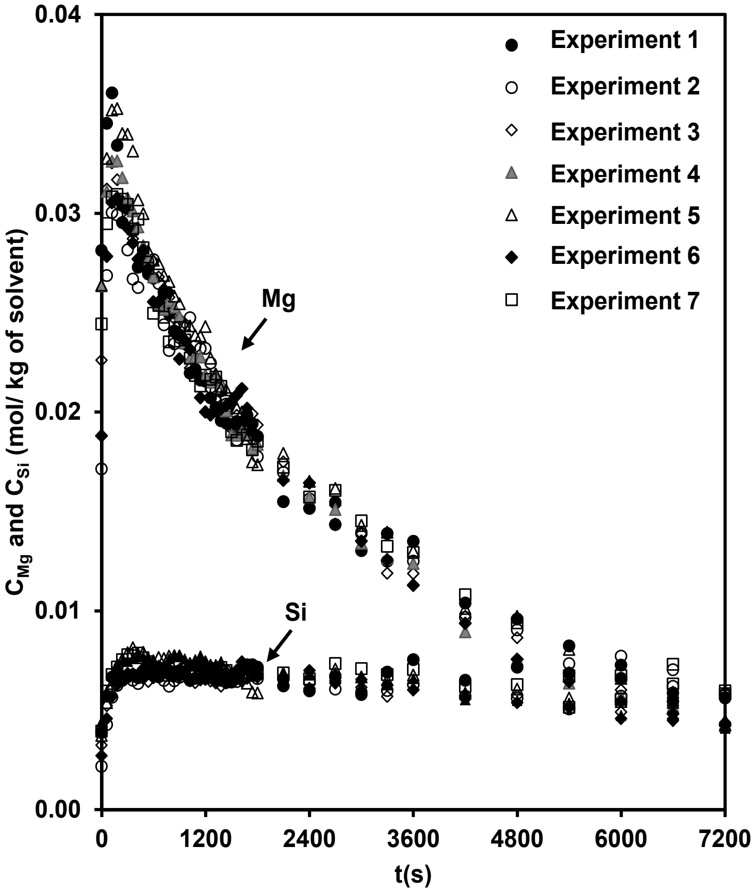

Figure 4-9. Concentration profiles of magnesium and silica acquired from the dissolution of thermally activated SWOL (PSD = 45-63 μm) under the saturated CO_2-H_2O system, at P_{CO2} = 100 bar, T = 423 K, and 120 minutes reaction time for seven replicate experiments.

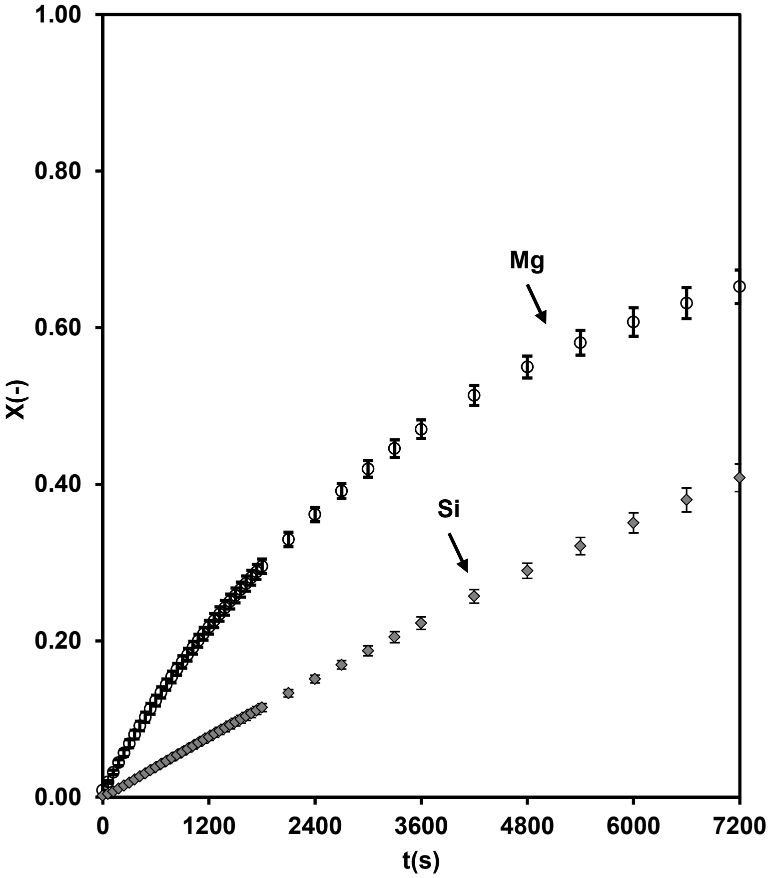

Figure 4-10. Degree of completion of magnesium and silica extraction of magnesium and silica acquired from the dissolution of thermally activated SWOL (PSD = 45-63 μm) under the saturated CO_2-H_2O system, at P_{CO2} = 100 bar, T = 423 K, and 120 minutes reaction time. The error bars are denoted the standard deviation obtained with seven replicate experiments.

Table 4-1 provides a summary of the mass distribution after the dissolution experiments. This fractional loss of mass from the initial solid was approximately 37%. The chemical composition of the consolidated residual from seven experiments was determined by XRF analysis, as shown in Table 4-2.

Table 4-1. Percentage of reduction in the loaded mineral mass after 120 minutes dissolution under the saturated CO_2-H_2O system, activated SWOL (900 K, 120 minutes), P_{CO2} = 100 bar, T = 423 K. Variability in the average quantities corresponds to the ±standard deviation.

Experiment	Mass-in (mg)	Solid residue (mg)	Mass reduction (%)
1	252.04 ±0.25	146.20 ±0.02	41.99
2	251.53 ±0.01	150.69 ±0.15	40.08
3	251.30 ±0.03	159.04 ±0.02	36.71
4	251.92 ±0.03	167.00 ±0.06	33.71
5	251.45 ±0.04	166.61 ±0.14	33.74
6	250.75 ±0.05	167.41 ±0.02	33.23
7	252.27 ±0.10	152.19 ±0.12	39.67
Average	251.61 ±0.51	158.50 ±8.85	37.02 ±3.59

Table 4-2. The chemical composition of the consolidated residue from seven experiments at standard operation conditions (P_{CO2} = 100 bar, T = 423 K, and 120 minutes reaction time) determined through XRF analysis.

Material	Major components (wt.%)						
	MgO	SiO_2	Fe_2O_3	Al_2O_3	CaO	Cr_2O_3	Mn_3O_4
Solid residue	25.07	39.81	13.09	2.88	0.61	0.62	0.16

The elemental mass balance results for the consolidated data are shown in Table 4-3. The overall mass balances for the magnesium and silica contents of the material were closed within approximately 5% and 2%, respectively. In addition to confirming the good mass balances for the major components, Table 4-3 verifies the earlier observation that negligible iron is extracted under the experimental conditions. Approximately 30% of the calcium in the parent sample is apparently extracted – the failure to detect any calcium in the aqueous product stream clearly relates to the low average concentration that this loss represents over the lifetime of the experiment ($< 10^{-4}$ mol kg^{-1}); the same holds for the apparent loss of ~30% of the manganese content of the initial solid.

Table 4-3. Summary of mass balance for 120 minutes dissolution experiments under the saturated CO_2-H_2O system, 45-63 μm activated SWOL (900 K, 120 minutes), P_{CO2} = 100 bar, T = 423 K.

Major components	Input (mg)	Solid Residue (mg)	Extracted (mg)	Unaccounted (mg)
MgO	100.94	39.72	66.97	-5.8
SiO_2	105.33	63.08	43.91	-1.7
CaO	1.56	0.97	-	0.6
Cr_2O_3	0.93	0.98	-	<0.1
Al_2O_3	4.56	4.56	-	<0.1
Fe_2O_3	20.65	20.74	-	-0.1
Mn_3O_4	0.38	0.25	-	0.1

4.2 Effect of Particle Size on the Extraction of Magnesium and Silica

The identification of factors contributing to the slow rate of the mineral carbonation process was a principal motivation for this study. Several pre-treatment methods have been investigated to enhance the reaction rate and conversion including heat activation (e.g., McKelvy et al., 2004), grinding (e.g., Summers et al., 2005), the use of additives in reactive fluid, and implementation of the elevated pressure and temperature schemes (e.g., O'Connor et al., 2005). The effect of grinding is mainly to change the character of material by reducing the particle size and increasing the overall surface area. Hence, a series of experimental studies conducted to evaluate the effect of particle size distribution on the extraction rate of magnesium and silica from thermally activated SWOL. The SWOL material was comminuted using the stainless steel ball mill under a wet milling procedure, as explained in Chapter 3. The milled material was size-segregated through the wet sieving scheme to achieve discrete sieve size fractions. A laser-based particle sizer (Malvern Mastersizer 3000) was used to determine the mean particle size and particle size distribution, as presented in Chapter 3. The size-fractionated SWOL samples were thermally activated in a fluidised bed calciner reactor at a temperature of 900 K for 120 minutes under an argon fluidising medium. Dissolution experiments were carried out under the defined standard experimental conditions (input mass = 250 mg, mass loading factor of 0.25 min, T =

423 K and P_{CO2} = 100 bar) under the saturated (m_{CO2} ~3.7 mol kg^{-1}) CO_2-H_2O system. Dissolution experiments were performed through the continuous flow set-up as described in Chapter 3. Figure 4-11 shows the concentration profile of magnesium in the aqueous effluent, obtained at identical flow and reactor conditions. The results here had to be analysed using a semi-quantitative ICP-OES and have been rescaled using calibrated reference data[1].

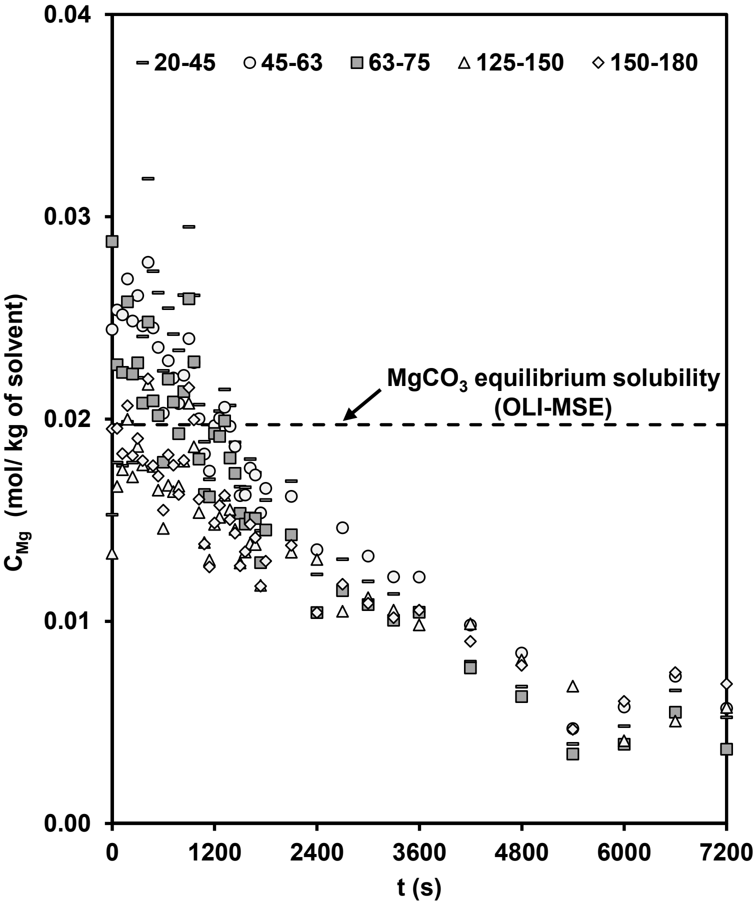

Figure 4-11. Magnesium concentration profiles for the range of particle size distributions (as indicated in the figure), acquired from the dissolution of thermally activated SWOL (PSD = 45-63 μm) under the saturated CO_2-H_2O system, at P_{CO2} = 100 bar, T = 423 K, and 120 minutes reaction time.

---

[1] The results of the standard dissolution experiment was rescaled with the data attained through quantitative analysis (Figure 4-2), this has used as a basis for other data series presented in Figure 4-11. Thus, the noise in data is likely attributed to the intrastic error associated with the semi-quantitative method, as it is explain in Chapter3.

It is apparent from Figure 4-11 that magnesium extraction rates were only weakly dependent on particle size over the range examined. In particular, there is no evidence of mechanical activation or production of fines in the wet milling procedure. Overall, it is concluded that the external surface area of the particles has little effect on the rate of extraction of magnesium. This attribute can also be seen through the cumulative extent of magnesium conversion profiles, as shown in Figure 4-12. As also found in Section 4.1, there is no evidence of homogeneous formation of carbonate phases.

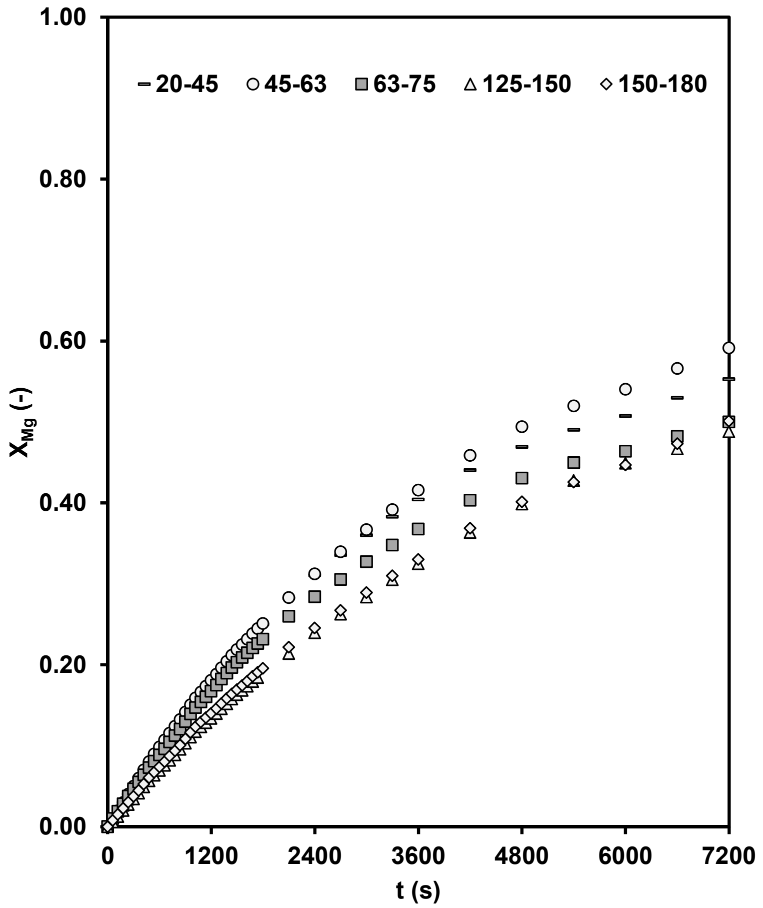

Figure 4-12. Degree of completion of magnesium extraction for the range of particle size distributions (as indicated in the figure), acquired from the dissolution of thermally activated SWOL (PSD = 45-63 μm) under the saturated CO_2-H_2O system, at P_{CO2} = 100 bar, T = 423 K, and 120 minutes reaction time.

Figure 4-13 illustrates the concentration profile of silica in the aqueous effluent, obtained at identical flow and reactor conditions and Figure 4-14 shows the corresponding cumulative extent of silica conversion, X_{Si}.

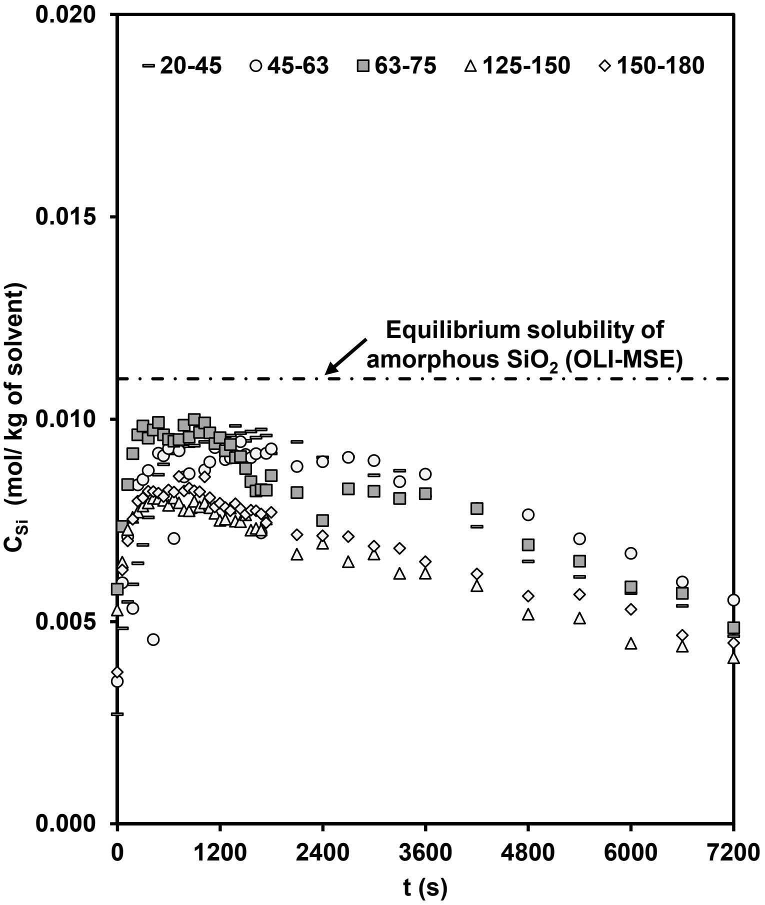

Figure 4-13. Silica concentration profiles for the range of particle size distributions (as indicated in the figure), acquired from the dissolution of thermally activated SWOL (PSD = 45-63 μm) under the saturated CO_2-H_2O system, at P_{CO2} = 100 bar, T = 423 K, and 120 minutes reaction time. The presented results are rescaled with reference to the calibrated data.

From Figure 4-13 the silica extraction rates similar to magnesium extraction rates not significantly influenced by the examined range of particle size. This behaviour is also observable through the cumulative extent of silica conversion profiles. It is noteworthy that silica concentrations initially proceeded in the vicinity of the equilibrium solubility of the amorphous silica and decreased gradually over the lifetime of the experiments.

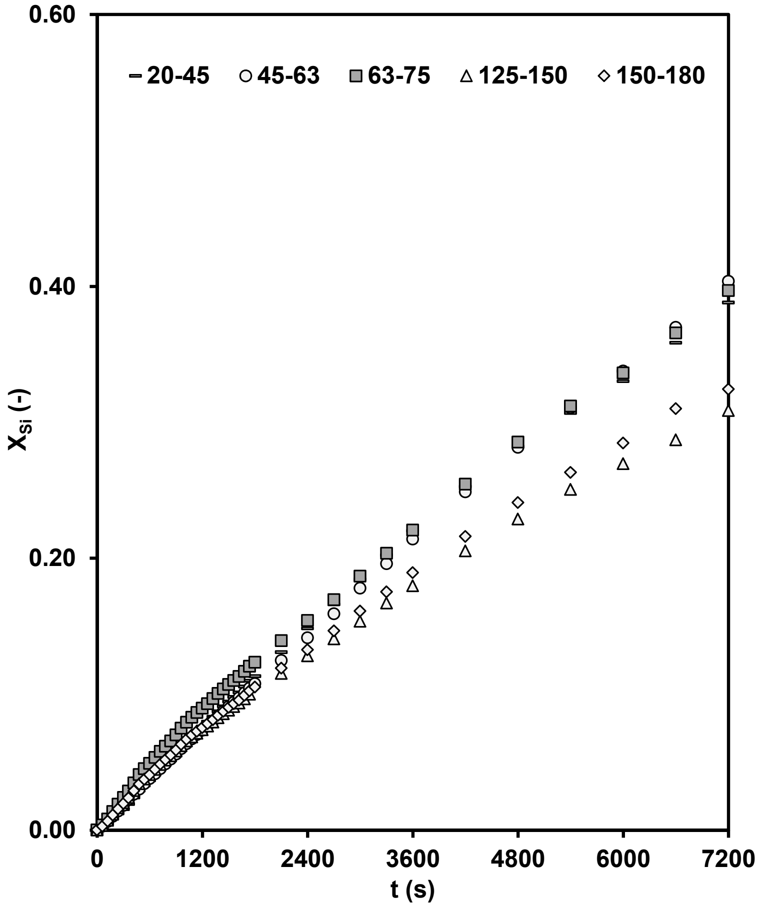

Figure 4-14. Degree of completion of silica extraction for the range of particle size distributions (as indicated in the figure), acquired from the dissolution of thermally activated SWOL (PSD = 45-63 μm) under the saturated CO_2-H_2O system, at P_{CO2} = 100 bar, T = 423 K, and 120 minutes reaction time.

Figure 4-15 shows the magnesium-silica molar ratio, as also evident from the dissolution profiles presented in Figure 4-11 and Figure 4-13 the incongruent extraction of magnesium appears for a period of ~80 minutes. After ~80 minutes the Mg:Si ratios continue under the theoretical stoichiometric ratio, indicating the preferential release rate of silica.

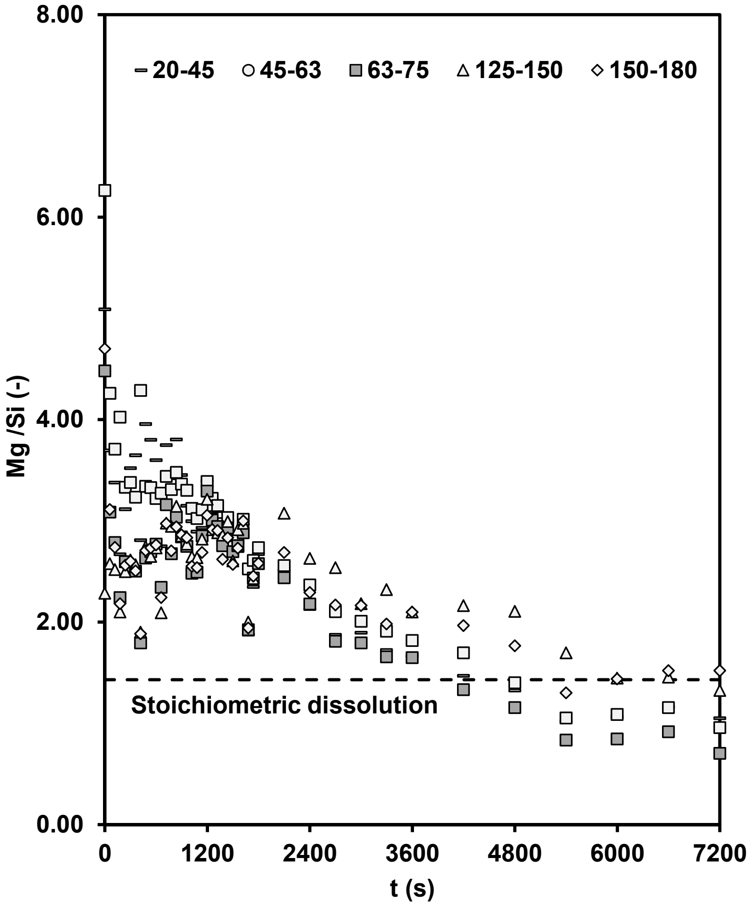

Figure 4-15. Magnesium-silica molar ratio for the range of particle size distributions (as indicated in the figure), obtained from the dissolution profiles presented in Figure 4-11 & Figure 4-13, the dashed line represents the stoichiometric dissolution.

4.3 Effect of Pressure on the Extraction of Magnesium and Silica

The carbonic acid system, including carbonate mineral solubility and the distribution of the carbonic acid chemical species, is significantly affected by pressure (Guthrie et al., 2001). In the development of the Albany NETL process, it was demonstrated that the effect of raising the pressure was associated with the increase in the activity of CO_2 and greater overall efficiency of the carbonation process. Previous studies (e.g., Sabirzyanov et al., 2003) showed that the solubility of CO_2 in water increased substantially at higher pressure. In order to evaluate the effect of pressure on the dissolution rate of thermally activated SWOL under the carbonic acid system, experiments were performed at a constant reaction temperature of 423 K under conditions where a separate CO_2-rich gas phase is present. The experiments were carried out using the continuous flow system described in Chapter 3 and results were analysed using quantitative ICP-OES. The basic conditions in all runs were the same as those in Section 4.1: mass loading of 250 mg of the activated SWOL (PSD = 45-63 μm); temperature 423 K. The experiments also all employed the same relative mass flows as previously (m_{CO2} ~3.7 mol kg^{-1}) but the total flow rate was adjusted to achieve the same volumetric flow rate (i.e., same velocity and same residence time) of the reactive fluid through the reactor at each pressure condition (see Appendix C). Table 4-4 shows the total mass flow rates employed in the experiments from 10 to 160 bar; it also shows the saturation (with respect to precipitation of solid $MgCO_3$ and amorphous silica, calculated via OLI-MSE) concentrations of aqueous magnesium and silica species for each condition.

Table 4-4. Summary of total mass flow rates, mass loading factors and equilibrium saturation concentrations of the aqueous magnesium and silica for the conditions where pressure was varied within a range of 10 to 160 bar, and at a reaction temperature of 423 K.

P (bar)	160	150	140	130	120	110	100	90	80	70	20	10
Mass Loading Factor (min)	0.20	0.20	0.21	0.22	0.22	0.24	0.25	0.27	0.29	0.32	0.25	0.25
τ(s)	13.00	13.00	13.00	13.00	13.00	13.00	13.00	13.00	13.00	13.00	13.00	13.00
Total Mass Flow Rate (g min^{-1})	1.49	1.45	1.41	1.35	1.30	1.23	1.17	1.09	1.01	0.92	1.03	1.01
Equilibrium Solubility of $MgCO_3$ (mol kg^{-1})*	0.023	0.022	0.022	0.021	0.021	0.020	0.020	0.019	0.018	0.018	0.010	0.007
Equilibrium Solubility of SiO_2 (mol kg^{-1})*	0.012	0.012	0.011	0.011	0.011	0.011	0.011	0.011	0.011	0.011	0.010	0.009

**Calculated by OLI-MSE*

Figure 4-16 shows the results for magnesium leachate concentrations obtained over the range of pressures accessible with the liquid-delivery apparatus, from 70 to 160 bar. The concentration profiles are very similar in all cases, especially for the first 30 minutes of reaction – during this period; the concentrations are again at or above their saturation values for $MgCO_3$ precipitation. The profiles for individual runs fall below their respective saturation lines and become more distinct after extended periods, with somewhat higher concentrations arising from the lower pressures. As previously, there was no evidence, in any of these the experiments, for the homogeneous formation of carbonate phases.

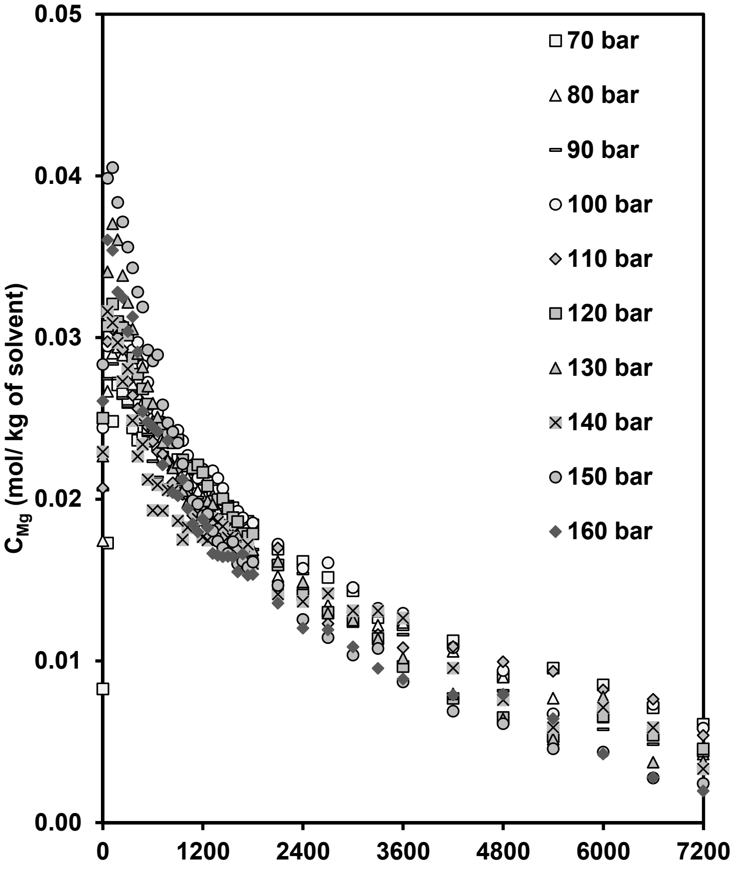

Figure 4-16. Magnesium concentration profiles for experiments with different CO_2 partial pressures (as indicated in the figure), acquired from the dissolution of thermally activated SWOL (PSD = 45-63 μm) under the saturated CO_2-H_2O system, $T = 423$ K, and 120 minutes reaction time. All runs had the same residence time in the reactor (13 s) and the same CO_2 molality (~3.7 mol kg^{-1}). Further clarifications of the presented data are provided in Appendix D.

When the concentration profiles are converted to conversion profiles (Figure 4-17) using Eq. 4.2 and 4.3, the different water flow rates employed in the individual experiments now come into play. It is apparent that, for the highest pressures (100 to 160 bar), the conversion profiles are very similar throughout the experiment. At lower pressures, however, the conversion at any time falls as the pressure decreases. Thus, the tendency to produce more concentrated leachates after long reaction times at lower pressures is more than offset by the lower water flow rates under these conditions.

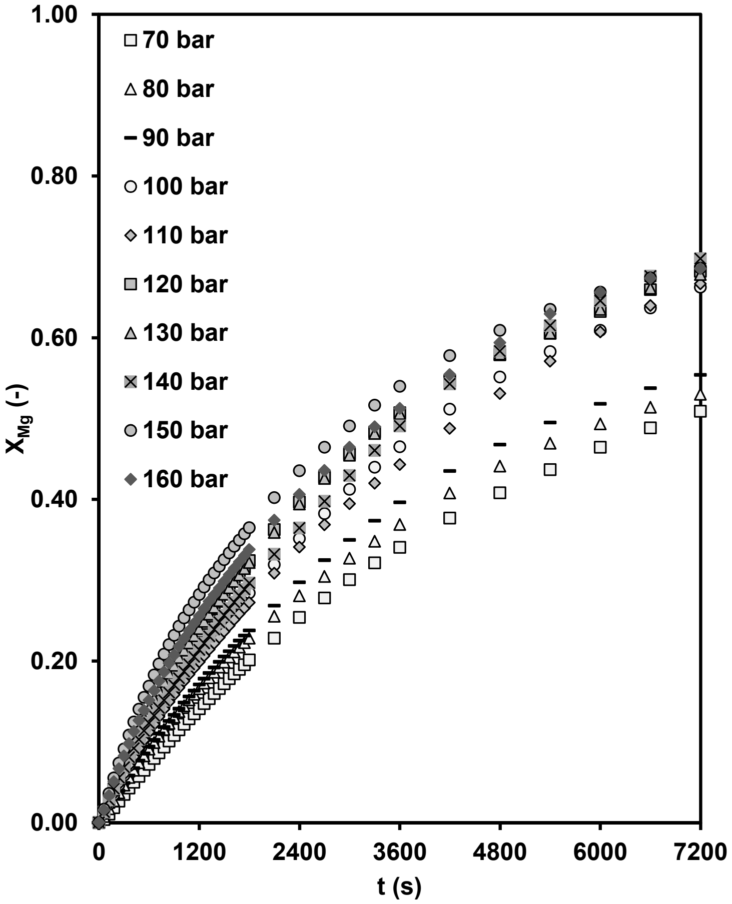

Figure 4-17. Degree of completion of magnesium extraction for experiments with different CO_2 partial pressures (as indicated in the figure), acquired from the dissolution of thermally activated SWOL (PSD = 45-63 μm) under the saturated CO_2-H_2O system, T = 423 K, 120 minutes reaction time. All runs had the same residence time in the reactor (13 s) and the same CO_2 molality (~3.7 mol kg^{-1}).

The concentration profiles of silica in aqueous effluent are shown in Figure 4-18. The concentration profiles are quite similar in all cases[1]. It appears that the silica concentrations in the reactor are close to their saturation values for amorphous silica precipitation.

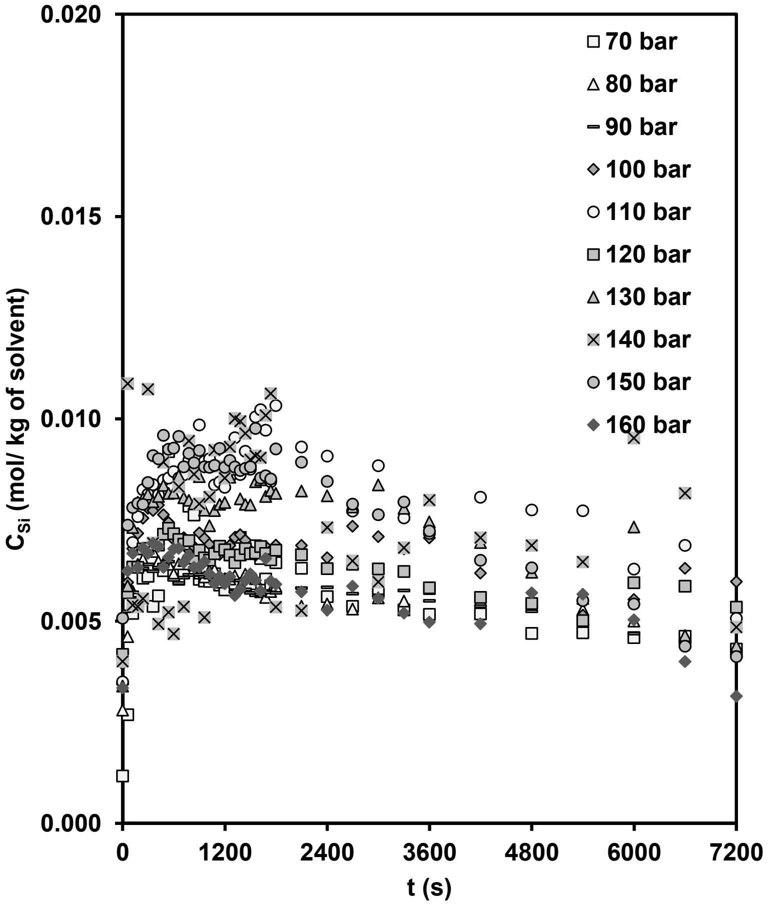

Figure 4-18. Silica concentration profiles for experiments with different CO_2 partial pressures (as indicated in the figure), acquired from the dissolution of thermally activated SWOL (PSD = 45-63 μm) under the saturated CO_2-H_2O system, $T = 423$ K, and 120 minutes reaction time. All runs had the same residence time in the reactor (13 s) and the same CO_2 molality (~3.7 mol kg^{-1}).

The corresponding cumulative extent of the silica conversions is shown in Figure 4-19. The effect of different water flow rates used in this series of the study also appears on the silica conversion profiles.

---

[1] Further clarifications of the presented data are provided in Appendix D.

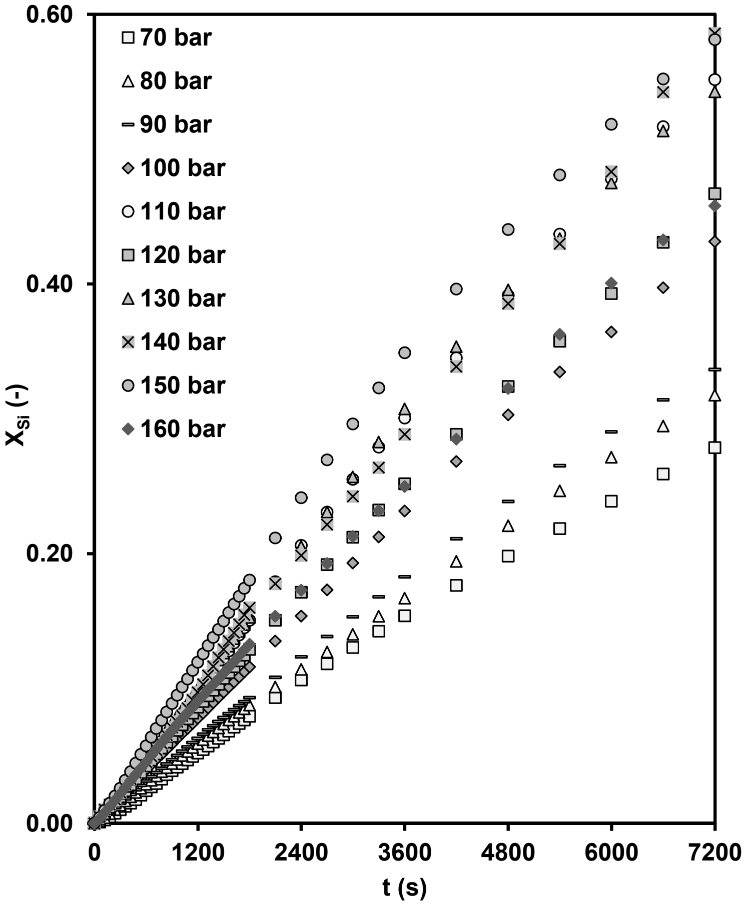

Figure 4-19. Degree of completion of silica extraction for experiments with different CO_2 partial pressures (as indicated in the figure), acquired from the dissolution of thermally activated SWOL (PSD = 45-63 μm) under the saturated CO_2-H_2O system, T = 423 K, 120 minutes reaction time. All runs had the same residence time in the reactor (13 s) and the same CO_2 molality (~3.7 mol kg^{-1}).

Figure 4-20 illustrates the magnesium-silica molar ratio for the dissolution profiles presented in Figure 4-16 and Figure 4-18, indicating to the initial incongruent extraction of magnesium. As the dissolution experiments advanced Mg:Si ratios change towards the theoretical stoichiometric ratio and, therefore, preferential silica release rate[1].

---

[1] Further clarifications for the presented data are provided in Appendix D.

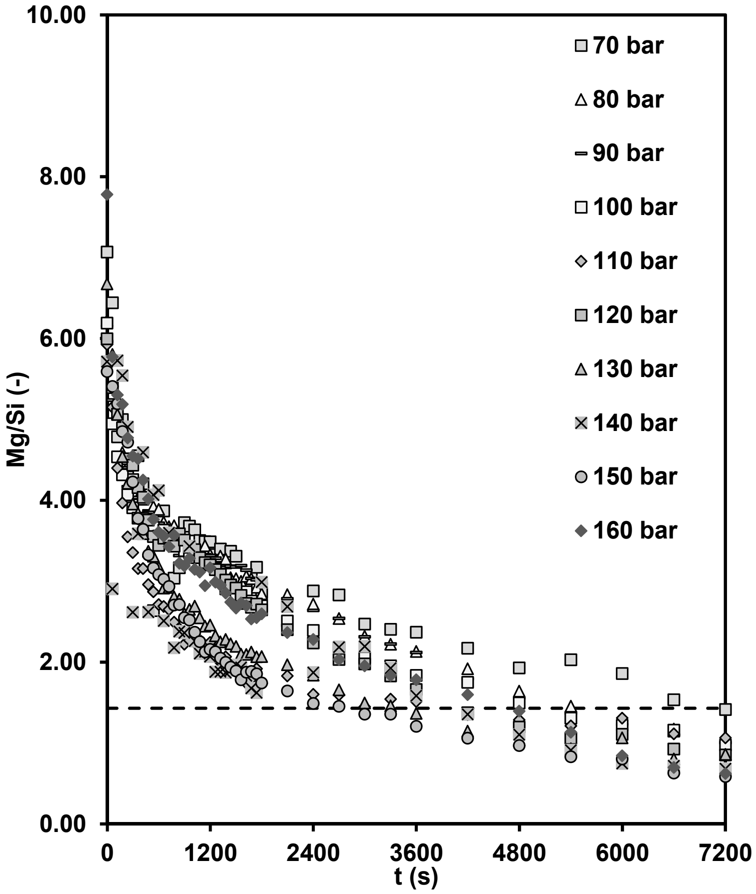

Figure 4-20. Magnesium-silica molar ratio for experiments with different CO_2 partial pressure (as indicated in the figure), obtained from the dissolution profiles presented in Figure 4-16 & Figure 4-18, the dashed line represents the stoichiometric dissolution.

In order to extend these investigations to lower pressure, the CO_2 delivery system was modified to meter gaseous CO_2 up to a maximum pressure ~20 bar. Figure 4-21 shows the leachate concentration profiles[1] obtained at 10 and 20 bar, together with the results from the liquid-feed system at 100 bar. The observed trends and scattering of the data in the early stages of the experiment at 10 bar are believed to be the result of the slow system response and the difficulty of controlling the flow after the CO_2 was first initiated under these conditions (see the employed flow rates illustrated in Table C-11 of Appendix C).

---

[1] Results were analysed using quantitative ICP-OES.

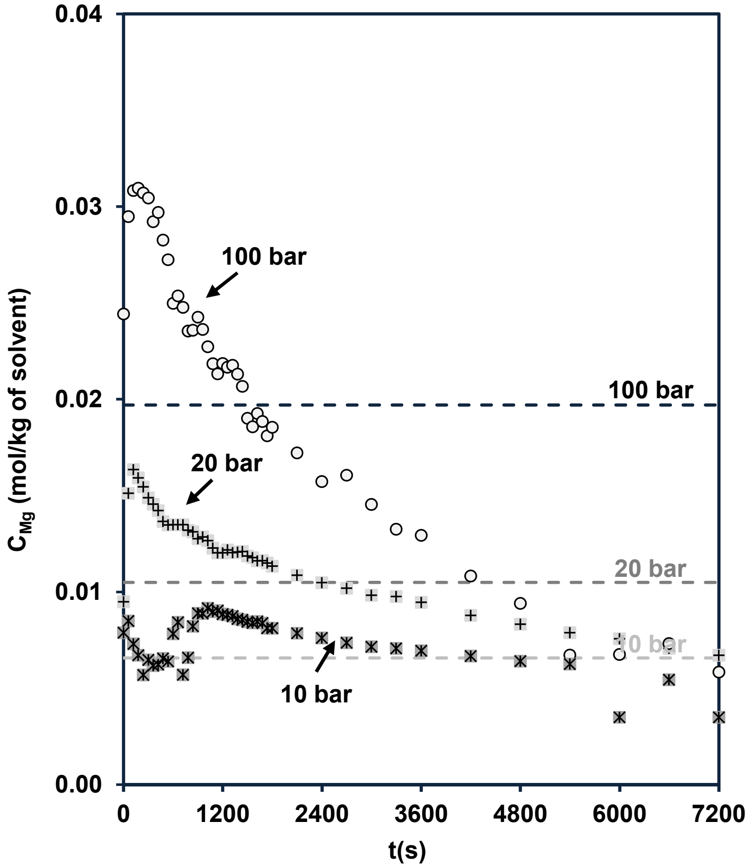

Figure 4-21. Magnesium concentration profiles acquired from the dissolution of thermally activated SWOL (PSD = 45-63 μm) under the saturated CO_2-H_2O system, P_{CO2} = 10, 20, and 100 bar, T = 423 K, and 120 minutes reaction time. All runs had the same residence time in the reactor (13 s) as those in Figure 4-16. The dashed lines represent equilibrium solubilities of $MgCO_3$, calculated by OLI-MSE.

It is apparent that the concentration of magnesium is significantly lower at 10 and 20 bar than at the reference condition (P_{CO2} = 100 bar). However, in terms of relationship to saturation, all curves show more-or-less similar behaviour, proceeding from an initial saturated to under-saturated concentrations after a period of reaction. The differences between the leachate concentrations after prolonged reaction are much less than they were initially but, as shown in Figure 4-22, the extents of reaction at this point are also very different.

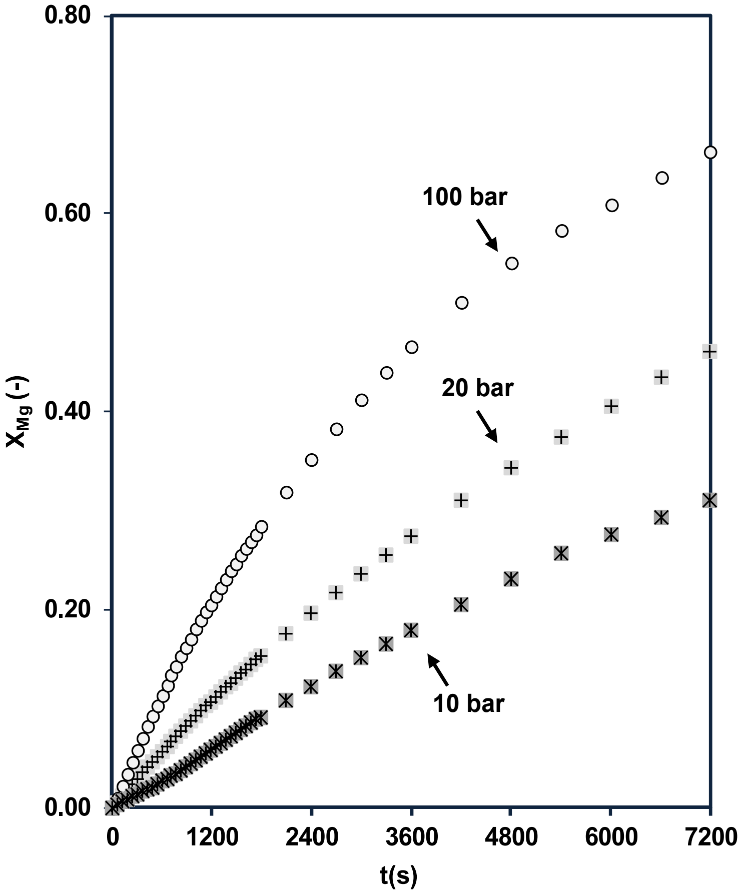

Figure 4-22. Degree of completion of magnesium extraction acquired from the dissolution of thermally activated SWOL (PSD = 45-63 μm) under the saturated CO_2-H_2O system, P_{CO2} = 10, 20, and 100 bar, T = 423 K, and 120 minutes reaction time. All runs had the same residence time in the reactor (13 s) as those in Figure 4-16.

Overall, comparison of Figure 4-17 and Figure 4-22 reveals that the effect of pressure on the rate of extraction of magnesium in the saturated CO_2-water system is quite limited: in going from 160 bar to 10 bar, the ultimate extent of extraction decreases only ~50% in the system[1]. Under the conditions studied, the high initial rate of extraction appears to be tied to the saturation condition for precipitation of $MgCO_3$, thus apparently accounting for the greater part of the effect of pressure.

In contrast with the near-equilibrium concentrations of aqueous silica species observed at higher pressures (Figure 4-18), extractions at 10 and 20

---

[1] Here it is worth noting that the pressure was varied within the factor of 16; however, the change in pressure was associated with ~50% drop in conversion rate which is significant, but not relative to the ratio of change in pressure.

bar gave rise to significantly lower, under-saturated concentrations throughout the reaction period, as shown in Figure 4-23.

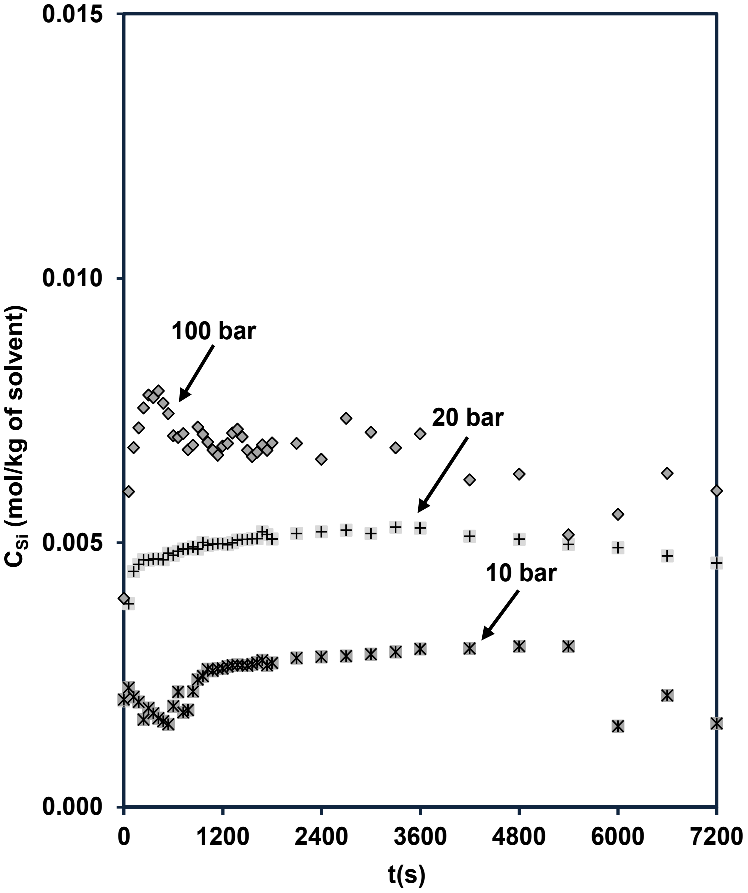

Figure 4-23. Silica concentration profiles acquired from the dissolution of thermally activated SWOL (PSD = 45-63 μm) under the saturated CO_2-H_2O system, P_{CO2} = 10, 20, and 100 bar, T = 423 K, and 120 minutes reaction time. All runs had the same residence time in the reactor (13 s) as those in Figure 4-16.

The corresponding cumulative silica conversion profiles are illustrated in Figure 4-24. The fractional extent of silica extractions can be seen to be marginally influenced by reducing the pressure from 100 to 20 bar. However in the case of 10 bar, the conversion rate of silica appears to be suppressed by ~50%. Considering the similar mass loading factor employed for all the presented instances in Figure 4-24 and predominate under-saturated conditions for 10 bar run; the apparent extraction rate of silica is clearly reduced. Overall, the effect of pressure seems to be not profound compared with the effect of equilibrium on silica dissolution rates from going 100 to 20 bar.

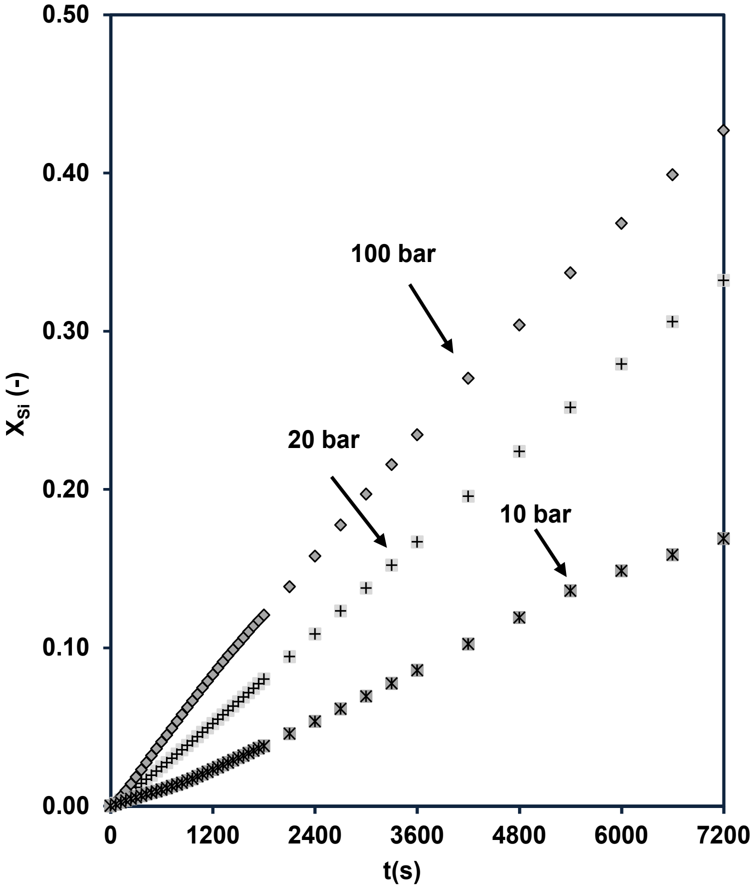

Figure 4-24. Degree of completion of silica extraction acquired from the dissolution of thermally activated SWOL (PSD = 45-63 μm) under the saturated CO_2-H_2O system, P_{CO2} = 10, 20, and 100 bar, T = 423 K, and 120 minutes reaction time. All runs had the same residence time in the reactor (13 s) as those in Figure 4-16

The relatively low release rate of silica (as presented in Figure 4-23) from the lower pressure runs compared with the corresponding concentration profiles of magnesium (in the vicinity of the thermodynamic saturation limit) point to an incongruent dissolution, as shown in Figure 4-25.

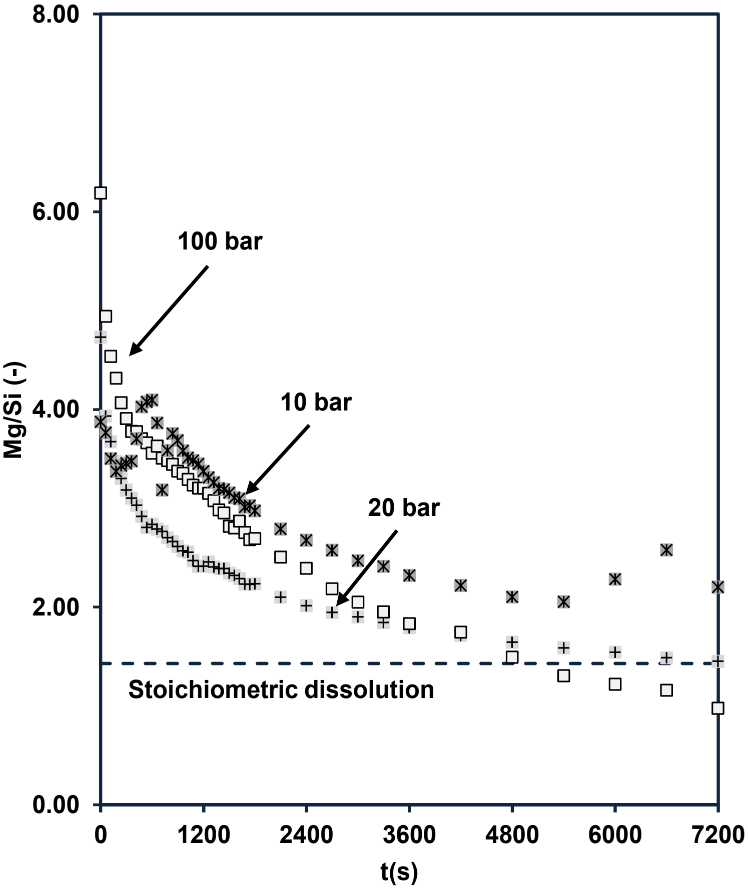

Figure 4-25. Magnesium-silica molar ratio obtained from the dissolution of thermally activated SWOL (PSD = 45-63 μm) under the saturated CO_2-H_2O system, at P_{CO2} = 10, 20, and 100 bar, T = 423 K, and 120 minutes reaction time, the dashed line represents the stoichiometric dissolution.

4.3.1 Effect of CO_2 Molality

The provision of CO_2 beyond its requirement for saturation of the system should have no impact on the aqueous chemistry arising if the carbonic acid system is thermodynamically equilibrated[1]. This expectation was tested experimentally by modifying the conditions employed to explore the effect of pressure on the system. Now, the water flow rate is kept constant at the standard condition and only the CO_2 flow rate is adjusted as the pressure is varied so as to give the same total volumetric flow rate (and residence time) as obtained at the standard condition (and in the foregoing discussion). As

---

[1] Here it is worth to note that addition of extra CO_2 at higher pressures leads to solubility of higher amount of CO_2 into the aqueous phase, meaning lower pH as it is presented in Table C-9 of Appendix C. Nevertheless, once the system reaches equilibrium regardless of how much extra CO_2 is provided, pH of the CO_2-H_2O system will no longer change.

shown in Table 4-5, this constraint gave rise to a range of CO_2 molality from 2.50 to 6.22 mol kg^{-1} as the pressure was varied in the range 70 to 160 bar – under all conditions, the supply of CO_2 was vastly in excess of the requirements for equilibration of the carbonic acid equilibria. As previously, the experiments employed a constant mass loading of 250 mg of the activated SWOL (PSD = 45-63 μm) and results were analysed using quantitative ICP-OES.

Table 4-5. Summary of total mass flow rates, mass loading factors and equilibrium saturation concentrations of the aqueous magnesium and silica for the experiments with variable molalities performed within pressure a range of 70 to 160 bar, and at a reaction temperature of 423 K.

P (bar)	160	150	140	130	120	110	100	90	80	70
m_{CO2} (mol kg^{-1})	6.22	5.85	5.40	5.00	4.55	4.10	3.70	3.30	2.90	2.50
Mass Loading Factor (min)	0.25	0.25	0.25	0.25	0.25	0.25	0.25	0.25	0.25	0.25
τ (s)	13	13	13	13	13	13	13	13	13	13
Total Mass Flow Rate (g min^{-1})	1.28	1.25	1.24	1.22	1.20	1.19	1.17	1.15	1.13	1.11
Equilibrium Solubility of $MgCO_3$ (mol kg^{-1})*	0.023	0.022	0.022	0.021	0.021	0.020	0.020	0.019	0.018	0.018
Equilibrium Solubility of SiO_2 (mol kg^{-1})*	0.012	0.012	0.011	0.011	0.011	0.011	0.011	0.011	0.011	0.011

**Calculated by OLI-MSE*

Figure 4-26 illustrates the concentration of aqueous magnesium in effluent obtained for the identical flow and reactor conditions[1]. These results confirm the equilibrium expectation and thus suggest that the carbonic acid system is indeed close to equilibrium in these experiments. The corresponding magnesium cumulative conversion profiles are illustrated in Figure 4-27. The also point again to the importance of the saturation of the leachate with magnesium in the early, high-rate period – a higher water flow removes more magnesium from the solid during this period than a lower water flow.

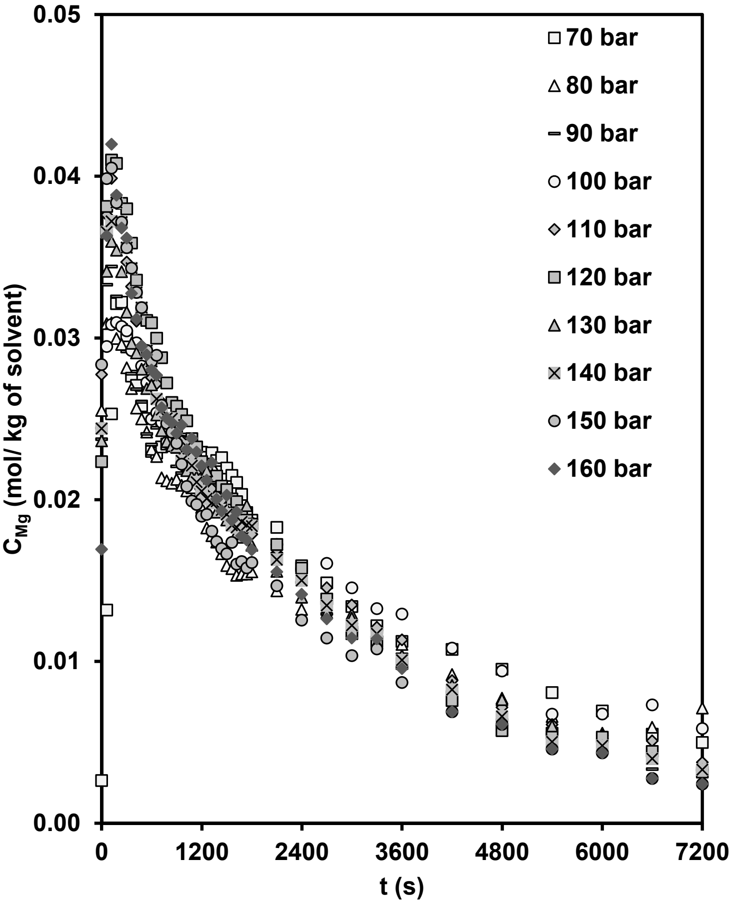

Figure 4-26. Magnesium concentration profiles for experiments with different CO_2 partial pressures (70 to 160 bar), acquired from the dissolution of thermally activated SWOL (PSD = 45-63 μm) under the saturated CO_2-H_2O system (variable molalities), *T* = 423 K, and 120 minutes reaction time. All runs had the same residence time in the reactor as (13 s) and variable molaities as shown in Table 4-5.

---

[1] Further clarifications for the presented data are provided in Appendix D.

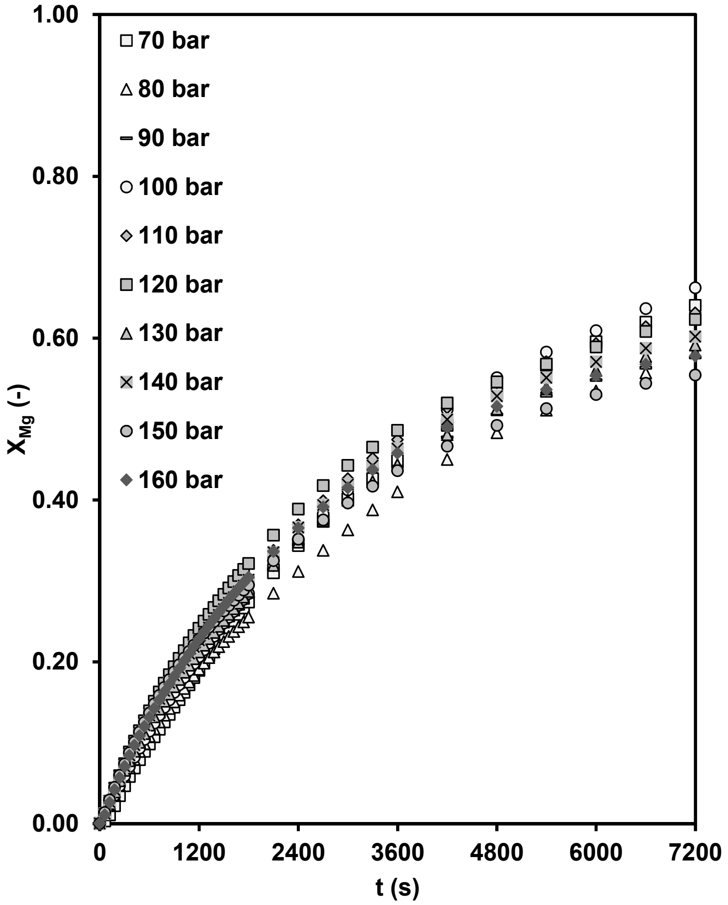

Figure 4-27. Degree of completion of magnesium extraction for experiments with different CO_2 partial pressures (70 to 160 bar), acquired from the dissolution of thermally activated SWOL (PSD = 45-63 μm) under the saturated CO_2-H_2O system (variable molalities), T = 423 K, and 120 minutes reaction time. All runs had the same residence time in the reactor as (13 s) and variable molaities as shown in Table 4-5.

Figure 4-28 illustrates the concentration profiles of silica in the aqueous effluent, obtained at identical flow and reactor conditions. The concentration profiles are almost similar in all cases – initially continue close to the saturation limit of amorphous SiO_2 precipitation and decrease slightly until the termination point. The corresponding cumulative conversion profiles are illustrated in Figure 4-29.

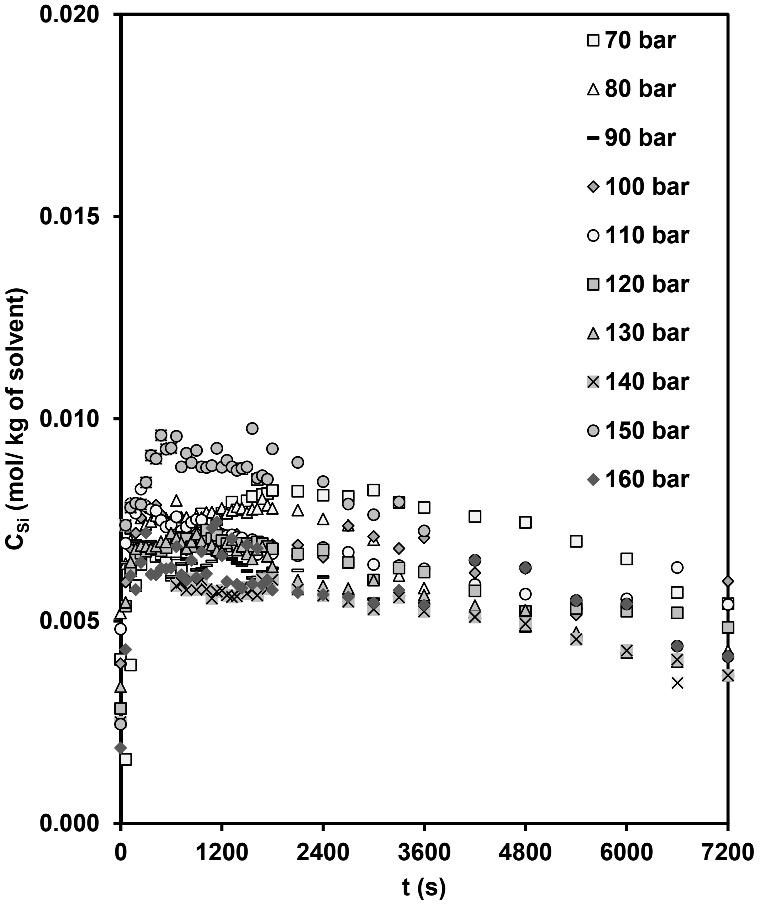

Figure 4-28. Silica concentration profiles for experiments with different CO_2 partial pressures (70 to 160 bar), acquired from the dissolution of thermally activated SWOL (PSD = 45-63 μm) under the saturated CO_2-H_2O system (variable molalities), T = 423 K, and 120 minutes reaction time. All runs had the same residence time in the reactor as (13 s) and variable molaities as shown in Table 4-5.

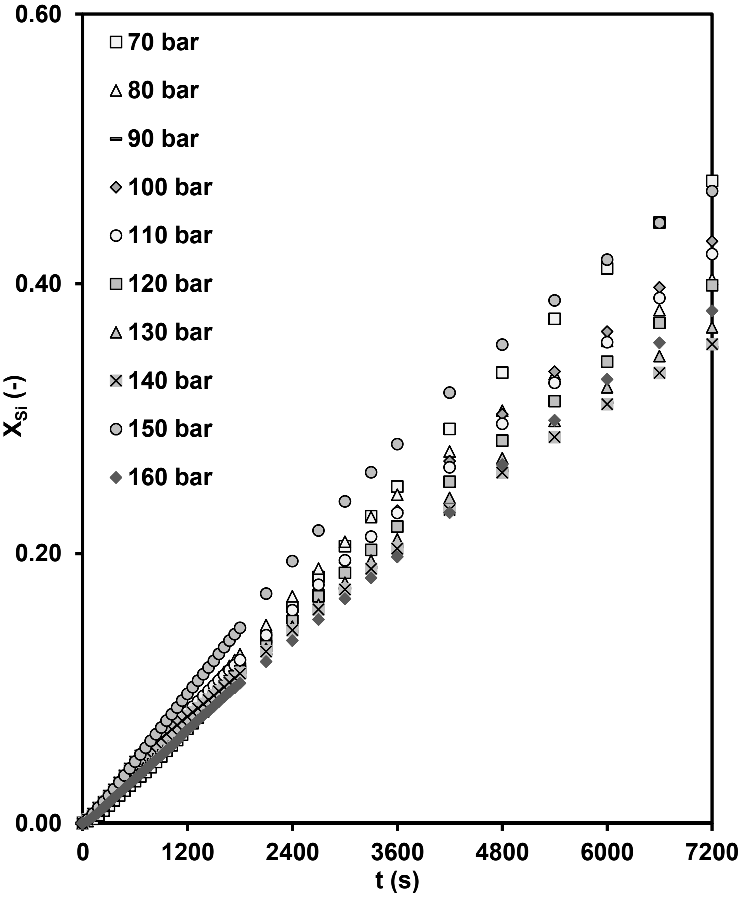

Figure 4-29. Degree of completion of silica extraction for experiments with different CO_2 partial pressures (as indicated in the figure), acquired from the dissolution of thermally activated SWOL (PSD = 45-63 µm) under the saturated CO_2-H_2O system, T = 423 K, 120 minutes reaction time. All runs had the same residence time in the reactor (13 s) and variable molaities as shown in Table 4-5.

Overall, considering the reported effect of pressure in section 4.3 and the offset influence of constant water flow rates employed in this series of the experiment as expected the silica conversion profiles are very similar, especially in the first 30 minutes of the reaction period. The corresponding magnesium-silica molar ratios are shown in Figure 4-30; confirm the initial preferential magnesium release rate over a period of reaction, with an approaching trend towards a congruent dissolution. The overall trend transformed to silica preferential release rate after ~80 minutes.

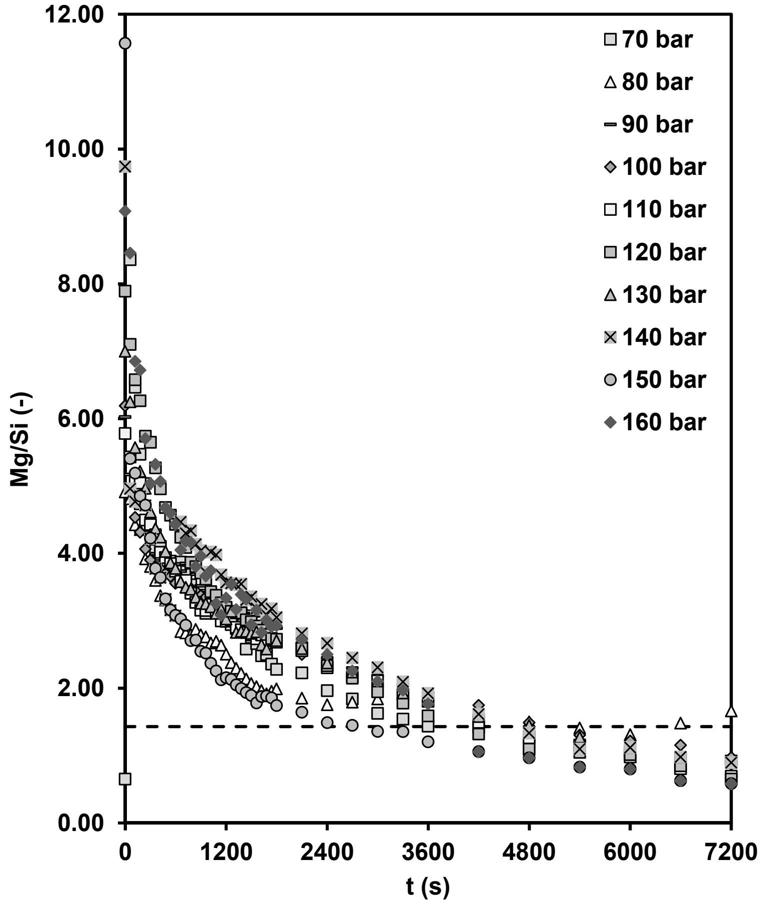

Figure 4-30. .Magnesium-silica molar ratio for experiments with different CO_2 partial pressure (as indicated in the figure), obtained from the dissolution profiles presented in Figure 4-28 & Figure 4-26 the dashed line represents the stoichiometric dissolution.

It is believed that only small amount of hydrated aqueous CO_2 exists in the form of carbonic acid (Lasaga, 1984). Thus, the effect of hydration rate of CO_2 on proton delivery seems to be essential for extraction of magnesium, which was further investigated by performing an experiment under the saturated (m_{CO2} ~3.7 mol kg^{-1}) CO_2-H_2O system – leading to the measurement of the relative extraction rate of magnesium along the reactor depth. All conditions corresponded to standard conditions (input mass = 250 mg, T = 423 K, P_{CO2} = 100 bar, and mass loading factor of 0.25 min). The mineral particles were distributed evenly through the reactor within the three distinct sections in a packed bed configuration. The relative extent of extraction of magnesium over the reactor depth was evaluated after 30 minutes reaction, as shown in Figure 4-31. It appears that as magnesium was accumulated in the aqueous phase (here it is worth noting that the system was supersaturated with CO_2), the concentration of protons was diminished along the depth of reactor.

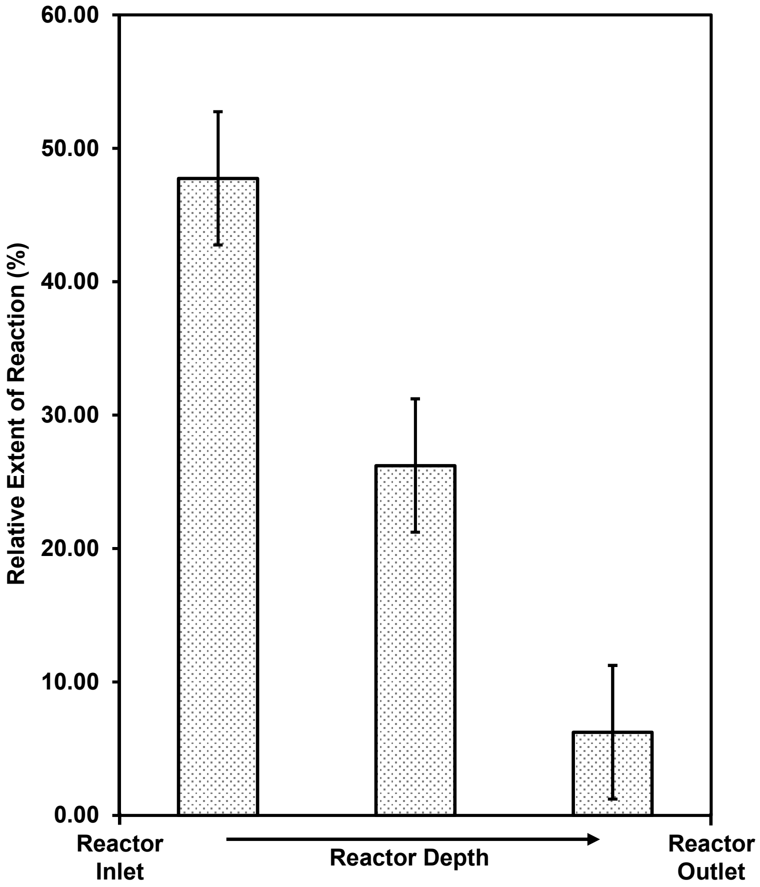

Figure 4-31. Relative extent of magnesium extraction along the reactor depth is denoting to the kinetic of decay of the protons. The error bars denote to the extent of uncertainties associated with the presented analysis.

From this observation, it is apparent that due to the mineral dissolution, the demand for protons is relatively greater than the reproduction rate of protons by the hydration of CO_2 into the aqueous phase.

4.4 Effect of Reaction Temperature on the Extraction of Magnesium and Silica

The reaction temperature is expected to be an important factor in optimisation of the mineral carbonation process since this parameter influences the dynamics and the extent of dissolution reaction. Gerdemann et al. (2002) reported that increasing in the reaction temperature from ambient temperature up to 458 K was associated with the significant enhancement of the overall carbonation rate of olivine in the carbonic acid system. In addition, they observed that raising the temperature was accompanied by a decrease in the activities of the carbon dioxide species in the solution. Werner at al. (2014 b) observed that, at CO_2 partial pressure of ~2 bar, the dissolution rate of thermally activated serpentine under the carbonic acid system was enhanced by increasing the reaction temperature from 303 up to 393 K. Considering the reported literature, evaluating the temperature-dependence of the extraction rate clearly involves both kinetics and thermodynamics considerations.

In this section, the effect of reaction temperature on the magnesium and silica extraction rates is studied. Experiments were performed using the standard liquid-delivery, high-pressure continuous flow system described previously and results were analysed using quantitative ICP-OES. All conditions except temperature corresponded to the standard settings – P_{CO2} = 100 bar, a constant mass loading of 250 mg of thermally activated SWOL (PSD = 45-63 μm) under the saturated CO_2-H_2O system where m_{CO2} ~3.7 mol kg^{-1} (see Appendix C). Table 4-6 provides the reaction temperatures, total mass flows and calculated equilibrium solubility of magnesium carbonate (magnesite) for the individual runs that covered the temperature range from 303 to 468 K.

Table 4-6. Summary of total mass flow rates, mass loading factors and equilibrium saturation concentrations of the aqueous magnesium and silica for the experiments with variable reaction temperatures within the range of 303 to 468 K and P_{CO2} = 100 bar.

T (K)	303	333	363	393	423	438	453	468
Mass Loading Factor (min)	0.14	0.18	0.20	0.23	0.25	0.26	0.28	0.29
τ (s)	13	13	13	13	13	13	13	13
Total Mass Flow Rate (g min^{-1})	2.06	1.65	1.42	1.28	1.17	1.11	1.06	1.00
Equilibrium Solubility of $MgCO_3$ (mol kg^{-1})*	0.725	0.286	0.116	0.047	0.020	0.013	0.008	0.005
Equilibrium Solubility of SiO_2 (mol kg^{-1})*	0.003	0.004	0.006	0.008	0.011	0.013	0.014	0.016

**Calculated by OLI-MSE*

Figure 4-32 displays the results obtained for the concentration of aqueous magnesium in the leachate. The saturation concentrations of magnesium are also shown with respect to the formation of $MgCO_3$, from Table 4-6. Overall, it is apparent that the highest initial rates occur at lower temperatures, and that extraction of magnesium is severely inhibited at the highest temperatures studied. The corresponding conversion profiles presented in Figure 4-33 show more clearly that the overall extents of extraction are similar for temperatures from 303 to 393 K and then the conversion profiles decrease at temperatures above ~400 K, this effect being more pronounced with each increase in temperature.

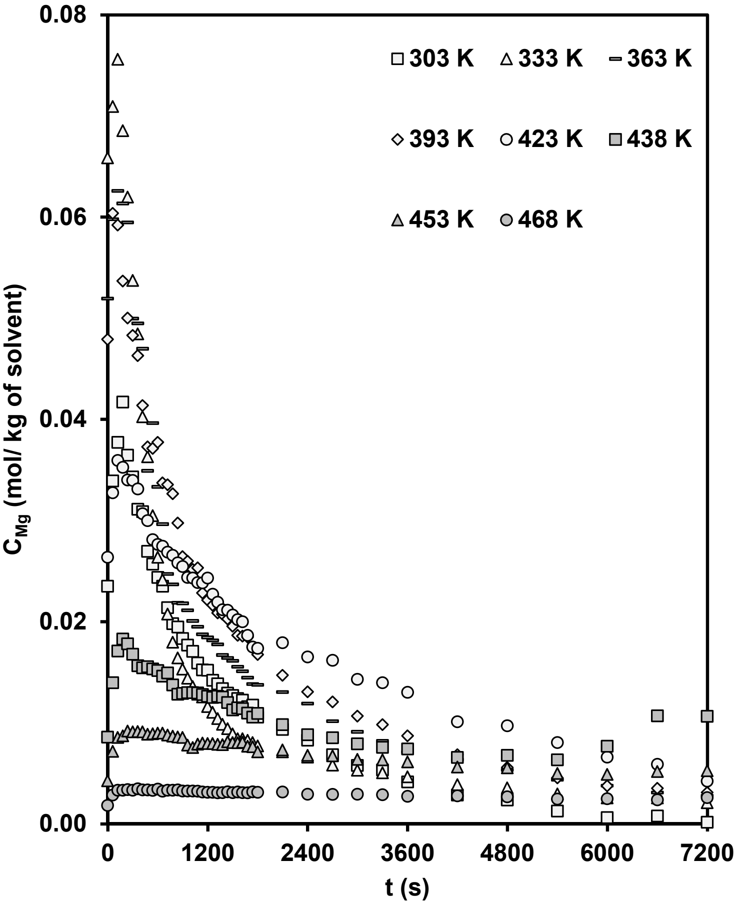

Figure 4-32. Magnesium concentration profiles acquired from the dissolution of thermally activated SWOL (PSD = 45-63 μm) under the saturated CO_2-H_2O system as a function of the indicated reaction temperatures, P_{CO2} = 100 bar, and 120 minutes reaction time. All runs had the same residence time in the reactor (13 s).

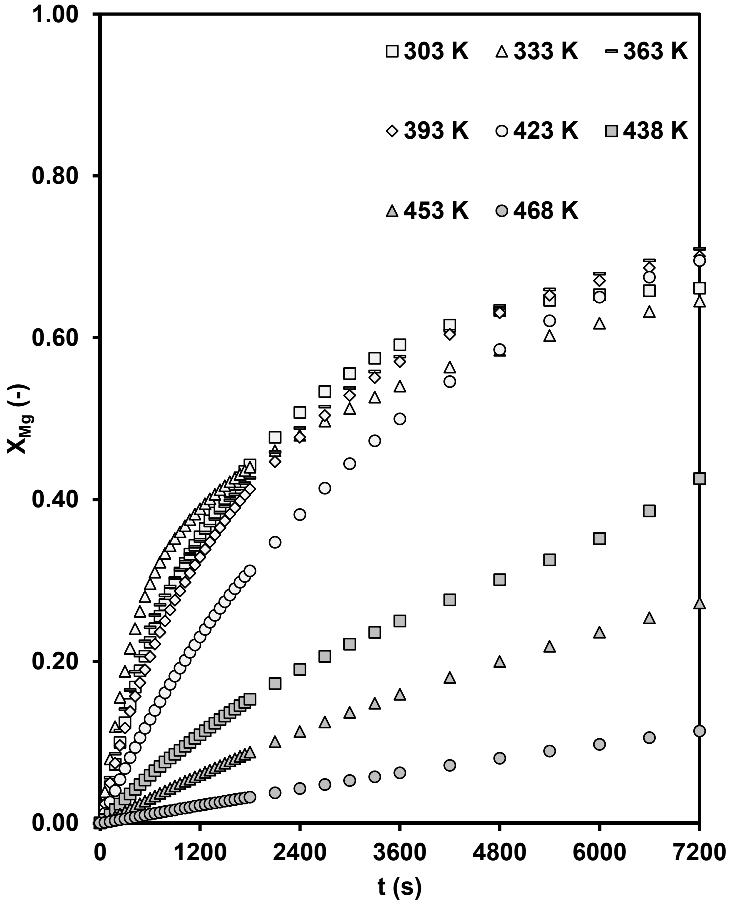

Figure 4-33. Degree of completion of magnesium extraction for dissolution of thermally activated SWOL (PSD = 45-63 μm) under the saturated CO_2-H_2O system as a function of the indicated reaction temperatures, P_{CO2} = 100 bar, and 120 minutes reaction time. All runs had the same residence time in the reactor (13 s).

Qualitatively, it is apparent that the general trend of the overall rate for reaction follows that for the saturation magnesium concentration shown in Table 4-6. The solubility of $MgCO_3$ increases significantly at lower temperature with the result that the leachate concentrations of magnesium remain distinctly below the solubility limit at all times in the runs at 303, 333 and 363 K; at 393 K, the equilibrium solubility is exceeded slightly at the very earliest times but the concentrations thereafter are well below equilibrium. At higher temperatures, the initial concentrations are increasingly suppressed, and the profiles become flatter, more-or-less following the equilibrium trends. At the highest temperature of 468 K, there is no initial peak and the extraction rate remains approximately constant throughout the experiment.

Figure 4-34 shows the silica concentration profiles in the aqueous effluent for the identical flow and reactor conditions. It seems that the higher silica initial release rates occur at the relatively lower reaction temperatures – after the peak the corresponding dissolution profiles continue close to the saturation limit of SiO_2 precipitation.

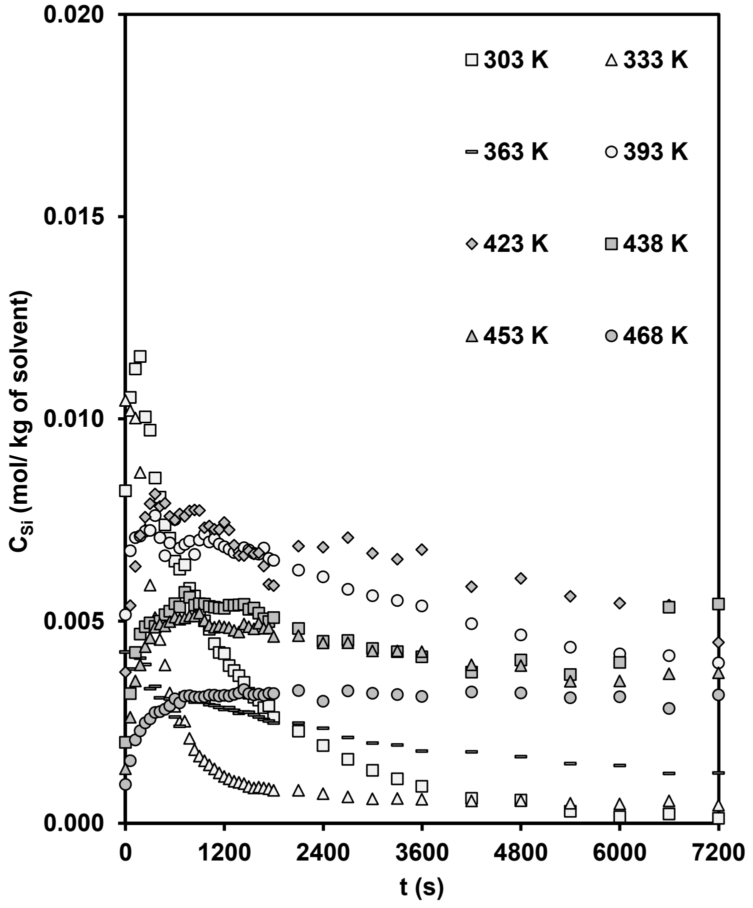

Figure 4-34. Silica concentration profiles acquired from the dissolution of thermally activated SWOL (PSD = 45-63 μm) under the saturated CO_2-H_2O system as a function of the indicated reaction temperatures, P_{CO2} = 100 bar, and 120 minutes reaction time. All runs had the same residence time in the reactor (13 s).

The solubility of SiO_2 increases with increasing temperature, as shown in Table 4-6. The corresponding concentration of silica in leachate increases proportional to rise in temperature up to 423 K. However, at temperatures above ~423 K the apparent silica concentration in the aqueous effluent decreased sharply – thus progressing at the undersaturated conditions. This behaviour is also perceptible from the coincident fractional extent of silica extraction profiles, as shown in Figure 4-35. The relatively high silica extraction rate at a temperature of 303 K is likely influenced by the artefact of water content employed for that experiment. However, the general trend of the overall rates follow the corresponding to saturation limit of amorphous silica – expect at reaction temperatures above 423 K, where the conversion rates dropped while the solubility of amorphous silica increased.

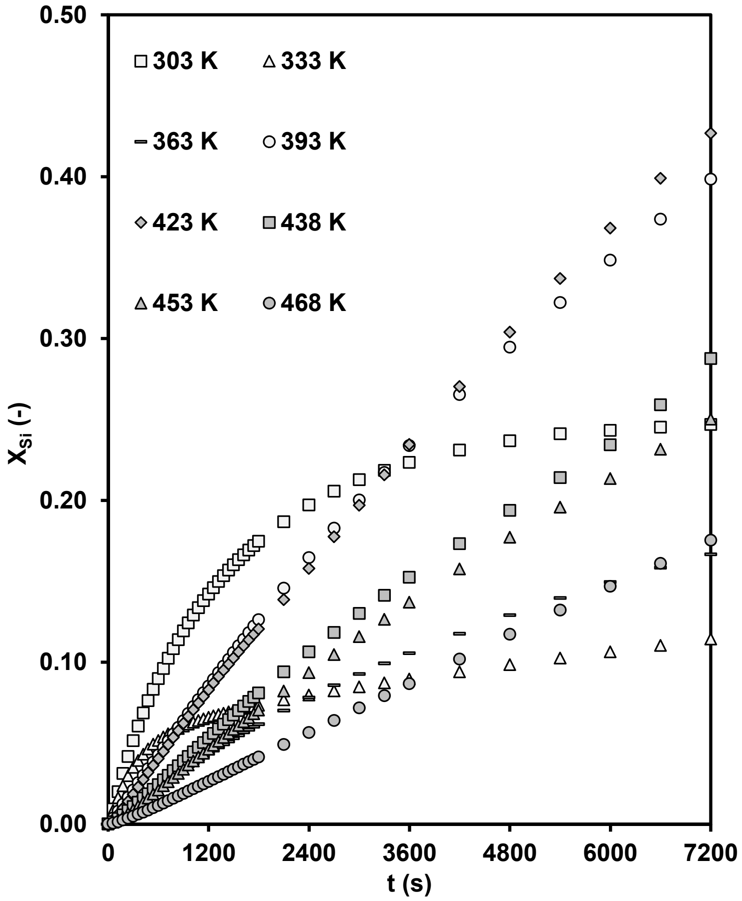

Figure 4-35. Degree of completion of silica extraction for dissolution of thermally activated SWOL (PSD = 45-63 μm) under the saturated CO_2-H_2O system as a function of the indicated reaction temperatures, P_{CO2} = 100 bar, and 120 minutes reaction time. All runs had the same residence time in the reactor (13 s).

Figure 4-36 provides the magnesium-silica molar ratio. Dissolution becomes more stoichiometric at the elevated temperature. It is also appreciable to note that by increasing the temperature from 303 to 363 K, an overall trend of initial magnesium extraction rates increase – then it decreases at temperatures above 363 K, progressively.

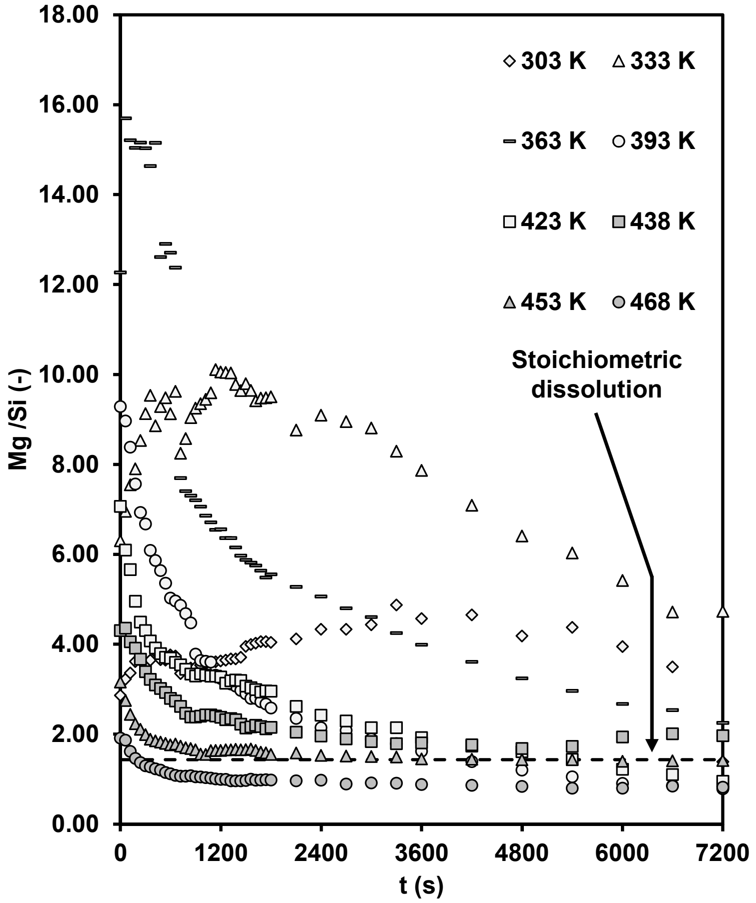

Figure 4-36. Magnesium-silica molar ratio for experiments with different CO_2 partial pressure (as indicated in the figure), obtained from the dissolution profiles presented in Figure 4-34 & Figure 4-32 the dashed line represents the stoichiometric dissolution.

The relationship between $MgCO_3$ and SiO_2 solubility and leachate concentrations was explored in more detail in a series of experiments that employed half the standard flow rate in order to induce the system towards saturation. The pressure was held at 100 bar, and the mass loading was 250 mg, summary of the used experimental conditions are provided in Table 4-7.

Table 4-7. Summary of the mass loading factors, total mass flow rates, reactor residence times, and the equilibrium saturation concentration for the aqueous silica for the experiments with variable reaction temperatures in the range of 373 to 473 K and P_{CO2} = 100 bar.

T (K)	373	398	423	448	473
Mass Loading Factor (min)	0.50	0.50	0.50	0.50	0.50
Total Mass Flow Rate(g min^{-1})	0.66	0.66	0.66	0.66	0.66
τ (s)	20	18	16	15	13
Equilibrium Solubility of SiO_2 (mol kg^{-1})*	0.007	0.009	0.011	0.014	0.016

**Calculated by OLI-MSE*

Figure 4-37 illustrates the results obtained for the concentration of aqueous magnesium in the effluent for different reaction temperatures. The highest extraction rate of magnesium was associated with a reaction temperature of 373 K where the dissolution proceeded in the under-saturated region with respect to the equilibrium solubility of magnesite. From 398 K, the initial high rate period is suppressed in accordance with the equilibrium expectation; beyond the initial period, the profiles are increasingly flattened and follow a trend corresponding to approximately two times the saturation concentration.

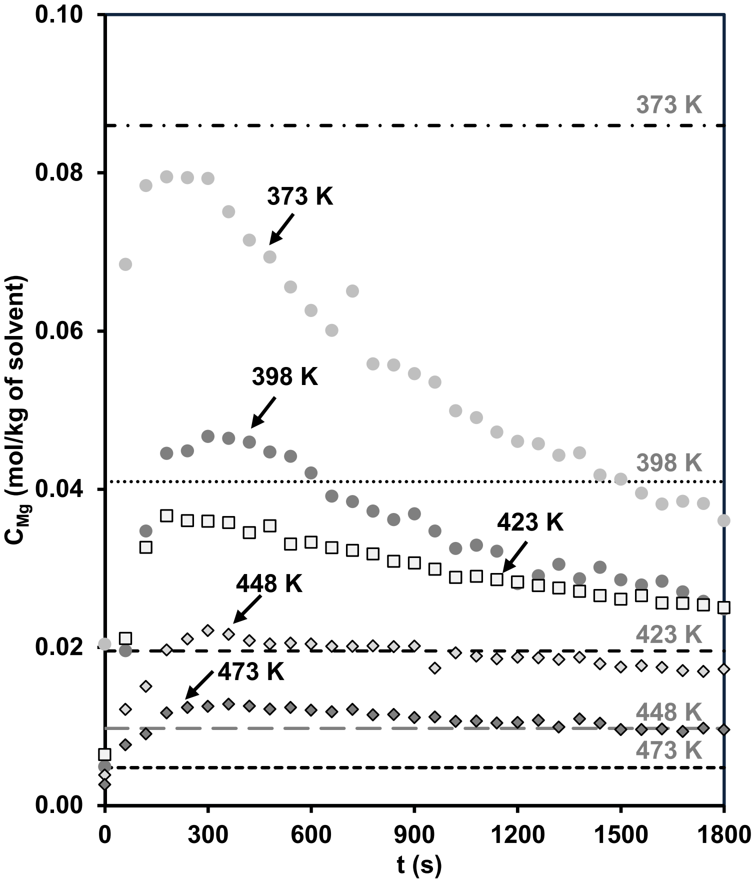

Figure 4-37. Magnesium concentration profiles for different reaction temperatures (as indicated in the figure) attained from the dissolution of thermally activated SWOL (PSD = 45-63 μm) under the saturated CO_2-H_2O system, at P_{CO2} = 100 bar, and 30 minutes reaction period. The equilibrium solubility of $MgCO_3$ was calculated by using OLI-MSE under identical experimental conditions and shown by the dashed lines for each reaction temperature.

Although the leachate concentrations do appear to be governed by $MgCO_3$ solubility, TPD analysis verified that for the elevated reaction temperatures, the solids collected from the reactor contain only insignificant (corresponded to ~2% of the magnesium) amounts of magnesium carbonate. In addition, the difference in the measured extracted magnesium and the analysed amount of magnesium left in the solid residual together accounted for the initial magnesium content of the solids fed to the reactor, is not exceeded ±5%, as provided in Table 4-8.

Table 4-8. Summary of mass balance closure for 30 minutes dissolution experiments conducted under the saturated CO_2-H_2O system, P_{CO2} = 100 bar, and mass loading factor = 0.5 min.

Exp	MgO Input (mg)	Solid Residue (mg)	Extracted (mg)	Differences (±%)
373	105.06	70.02	33.61	1.36
423	108.28	93.19	18.85	3.47
473	103.88	98.69	5.19	0.00

Regardless of its basis, the overall effect of this link between the extraction rate and the saturation concentration of magnesium is profound. Operation at 373 K extracted approximately six times the amount of magnesium extracted at 473 K, as in shown in Figure 4-38. At the same time, under equilibrium-limited conditions, the quantity of magnesium extracted is fixed, independent of the mass loading of the reactor – comparing the degrees of extraction after 30 min at 423 K, the higher mass loading factor in Figure 4-38 gave rise to 17% extraction versus 31% in Figure 4-33.

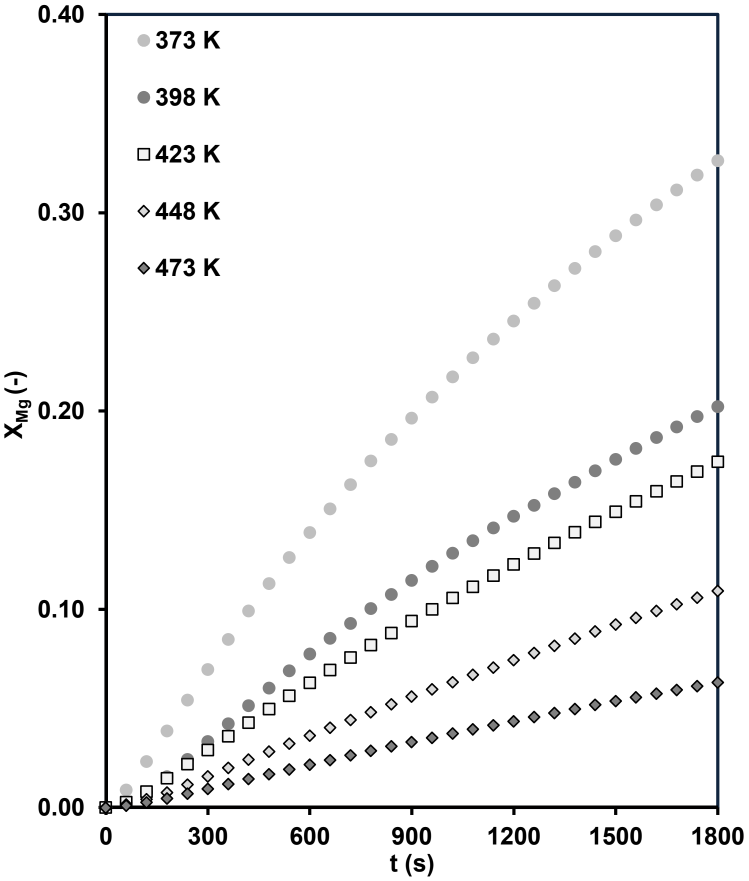

Figure 4-38. Degree of completion of magnesium extraction as a function of the reaction temperature (as indicated in the figure) obtained from the dissolution of thermally activated SWOL (PSD = 45-63 μm) under the saturated CO_2-H_2O system, at P_{CO2} = 100 bar, and 30 minutes reaction time.

Figure 4-39 shows aqueous silica concentrations in the effluent for identical flow and reactor conditions. Similar to what was observed in Figure 4-34, silica concentration profiles below/or at a reaction temperature of 423 K were advanced in the vicinity of the amorphous SiO_2 equilibrium solubilities that shown Table 4-7. Overall, the silica extraction rates appear to follow the equilibrium-limited conditions. Nonetheless, as it is evidenced by the identical dissolution profiles for reaction temperatures of 448 and 473 K, the concentration of silica in leachates declines progressively by increasing in temperature. This attribute can be seen in the corresponding cumulative silica conversion profiles as displayed in Figure 4-40.

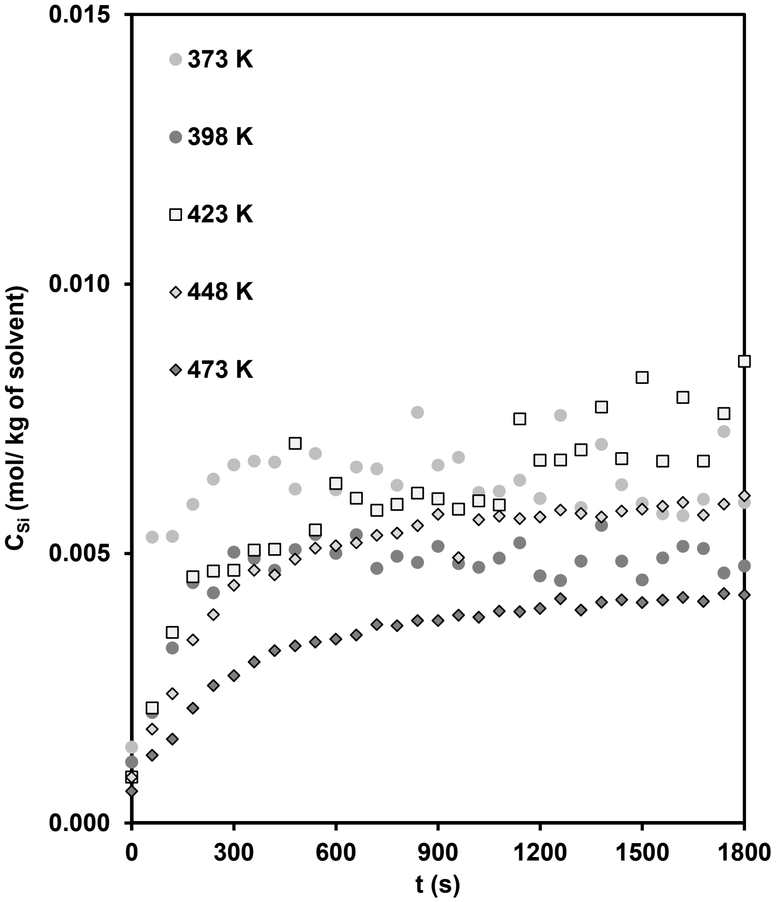

Figure 4-39. Silica concentration profiles for different reaction temperatures (as indicated in the figure) attained from the dissolution of thermally activated SWOL (PSD = 45-63 μm) under the saturated CO_2-H_2O system, at P_{CO2} = 100 bar, and 30 minutes reaction period.

From the results presented in Figure 4-34 and Figure 4-39, one may perceive that the extraction rates of silica at temperatures lower than 423 K depend only weakly on the mass loading factor and follow more-or-less the equilibrium solubility of amorphous SiO_2. On the other hand, above the reaction temperature of 423 K, despite the increase in the solubility of amorphous silica, it appears that the apparent silica concentration decreases with increasing the temperature. This observation implies that at elevated temperatures likely other mechanisms interplay/influence on the apparent silica dissolution process rather than only the equilibrium-limited attribute. On the basis of this observation, one may conclude that the silica extraction is very sensitive to the reaction temperature.

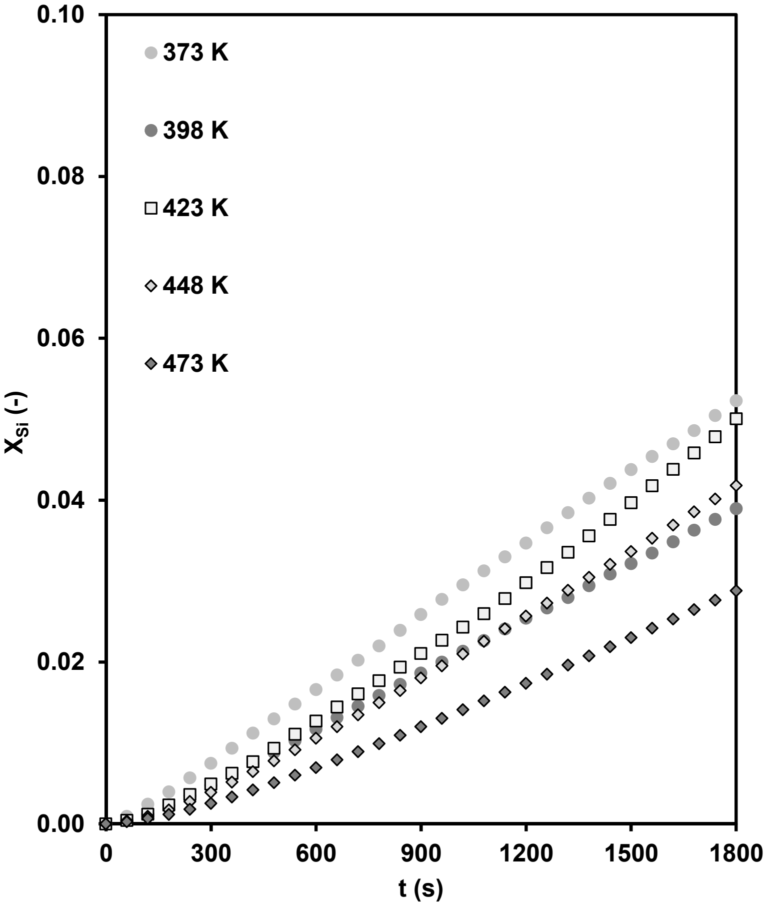

Figure 4-40. Degree of completion of silica extraction as a function of the reaction temperature (as indicated in the figure) obtained from the dissolution of thermally activated SWOL (PSD = 45-63 μm) under the saturated CO_2-H_2O system, at P_{CO2} = 100 bar, and 30 minutes reaction time.

In Figure 4-41 the molar ratio of magnesium-silica is plotted. Similar to what was observed in Figure 4-36, the dissolution reactions do appear to commence with the preferential release of magnesium – and then this trend is transferred towards more stoichiometric at higher temperatures.

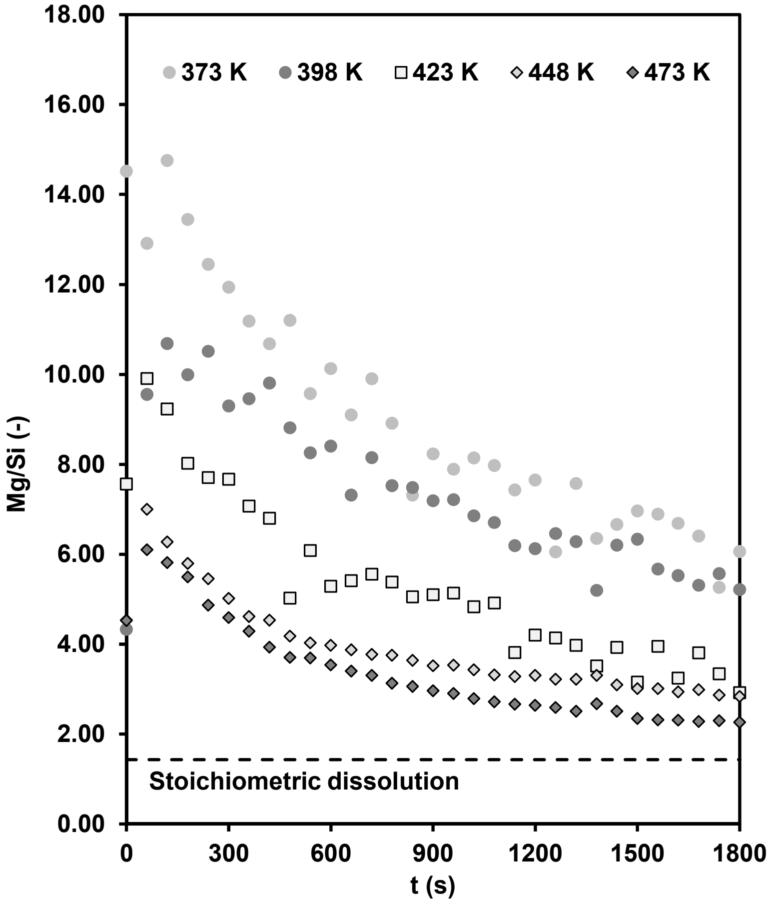

Figure 4-41. Magnesium-silica molar ratio for experiments with different CO_2 reaction temperatures (as indicated in the figure), obtained from the dissolution profiles presented in Figure 4-37 & Figure 4-39, the dashed line represents the stoichiometric dissolution.

4.4.1 Comments on the Experimental Results

It is worth noting that silica concentration profiles almost always proceed in the vicinity of the equilibrium solubility of the amorphous silica; nonetheless, no appreciable evidence for solid silica particles has been found within the reactor or leachates. It is believed that the solubility of silica is higher at elevated reaction temperatures than at ambient conditions; thus, the silica compounds in the reactor effluent were expected to precipitate at ambient conditions. However immediately after the reactions, no evidence of silica condensation was observed within the reactor effluent. The silica particles did grow within a few days (e.g., four days) and were visible under TEM examination (see Appendix E); depending on ambient conditions, such as temperature this period may be different. Since the silica dissolution profiles are typically tied within the equilibrium of amorphous silica – the dissolution of silica appears to be equilibrium-limited. Certainly no concrete comments regarding the governing kinetics can be extracted from this behaviour of the curves.

In the present study, it appears that the extraction of magnesium generally advances in accordance with the pseudo first order rate characteristic, such as that shows in Figure 4-2. Nevertheless, the behaviour of the curves seems to change to apparent zero-order reaction rates as the concentration profiles proceed in the supersaturated region. This apparent change in the form of the curves (under supersaturated conditions) is attributed to the equilibrium-limited behaviour[1]. Although relatively less soluble magnesium carbonate polymorphs might be present under the reaction conditions, no evidence for solid magnesium carbonate was observed within the leachates or the reactor.

4.5 Effect of Fluid Residence Time on the Extraction of Magnesium and Silica

Reactions at mineral-water interface are greatly influenced by transport properties of the system. The alternation process at reaction interface varies on the basis of the rate at which transport of solute away from the reaction zones. Under different volumetric flow rate circumstances, the solution might approach its thermodynamic saturation limit. Previous studies (e.g., Weyl, 1958) revealed that in the solid-liquid system at given conditions the rate at which saturation (with respect to a particular phase) is reached depends on the flow velocity of the aqueous phase and the size of the pore spaces. Holland (1978) expressed a variety of plots which denoted that, the concentration of dissolved elements in river waters changed inversely with the overflow conditions. Holland (1978) justified that these changes are indicating to insufficient chemical reaction rates, which would offset the shorter contact times with rocks. Lasaga (1984) proposed that the rate law must be corrected for the effect of chemical interaction rates as a function of

---

[1] The equilibrium dependence of the rate is likely correlated with the equilibrium constant as, $K_{eq} = k_{forward}/k_{reverse}$, therefore the rates tend to become constant and called as a equilibrium-limited.

flow rate for a given time and space in the locality. According to Nagy and Lasaga (1992) and Nagy et al. (1991), the effect of flow rate is important as the rates of dissolution and precipitation reactions are interfering each other and varied as a function of saturation states.

In this section, experiments are described in which the reactor mass loading factor has been varied by changes in the volumetric flow of water and CO_2. Apart from the flow rates, all other parameters were kept according to the standard conditions: P_{CO2} = 100 bar, temperature of 423 K; mass loadings 250 mg of the activated SWOL (PSD = 45-63 μm); m_{CO2} = 3.7 mol kg^{-1}. Results were analysed using quantitative ICP-OES. The total volumetric flow rate and mass loading factors, as well as the corresponding residence times of the reactive fluid in the reactor, were varied as presented in Table 4-9.

Table 4-9. Summary of the mass loading factors, the total volumetric flow rates and the residence times of the reactive fluid in the reactor.

Volumetric flow rate (cm^3 min^{-1})	τ (s)	Mass Loading Factor (min)
8.50	3.30	0.06
4.20	6.50	0.13
2.10	13.00	0.25
1.20	22.50	0.50
1.00	30.00	1.00

Figure 4-42 illustrates the results obtained for the concentration of aqueous magnesium in the reactor effluent.

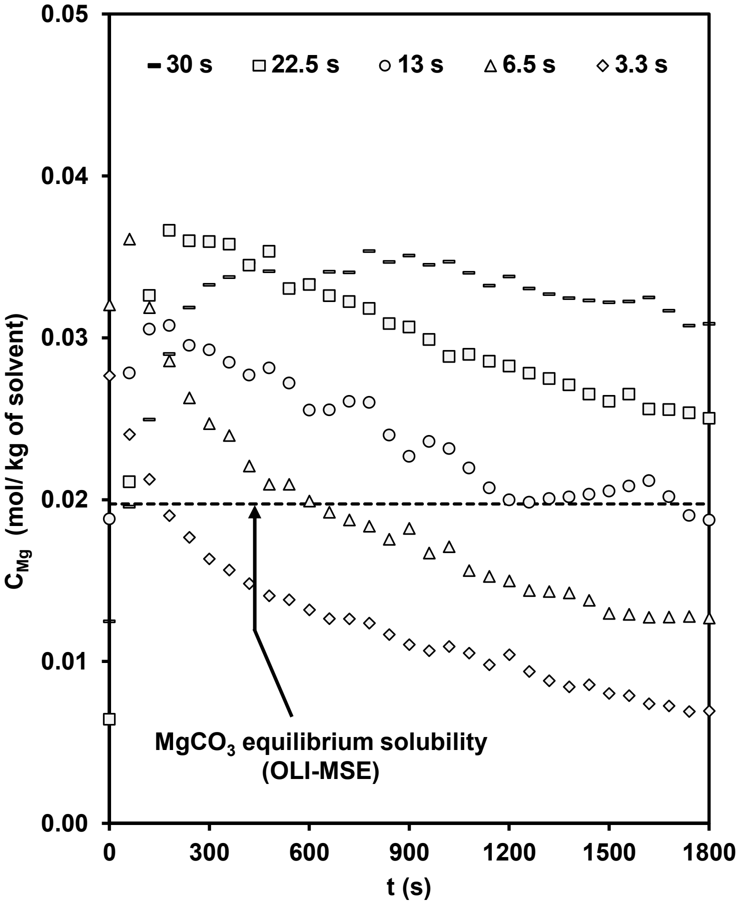

Figure 4-42. Magnesium concentration profiles acquired from the dissolution of thermally activated SWOL (PSD = 45-63 μm) under the saturated CO_2-H_2O system, at P_{CO2} = 100 bar, T = 423 K, and 30 minutes reaction time, for the indicated fluid residence times. The equilibrium solubility of magnesite was calculated by using OLI-MSE under identical experimental conditions.

Figure 4-43 shows the corresponding cumulative extent of magnesium conversion profiles, X_{Mg} for different residence times. Ideally for irreversible kinetics, the different curves in Figure 4-42 and Figure 4-43 should scale as the load factor or residence time. However, it is clear that this is not achieved in these experiments with the concentrations (Figure 4-42) tend to grouped around that corresponding to the equilibrium solubility of $MgCO_3$. Only at the lowest load factor are the concentrations below the saturation value for all but the first few points. Doubling the load factor sees higher concentrations emerging but not in proportion to the change in load factor – accordingly, the extent of magnesium extraction after 30 minutes decreases, by about 40%. As the load factor is further increased, the leachate concentrations change even less and the extent of extraction falls relatively faster. The magnesium extraction rate from the experiment conducted at the shortest residence time (3.3 s) is approximately six times greater than for the experiment performed with the longest residence time (30 s). At the lowest examined volumetric flow rate (1 cm^3 min^{-1}) there is a relatively long transient before the concentration of magnesium approaches a plateau value. This transient apparently arises because the residence time of the fluid in this case (30 seconds) plus the delay time in the delivery system becomes signficant relative to the observation time. However, once the plateau is reached, the effluent concentration remains remarkably steady at 0.035, 1.8 times the calculated sauration value.

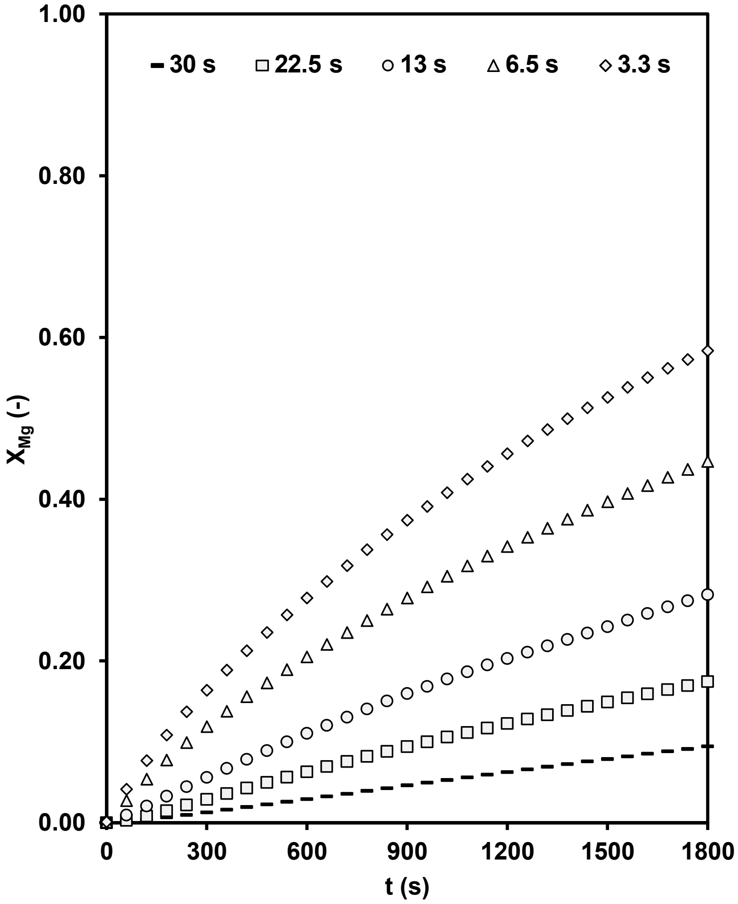

Figure 4-43. Degree of conversion of magnesium acquired from the dissolution of thermally activated SWOL (PSD = 45-63 μm) under the saturated CO_2-H_2O system, at P_{CO2} = 100 bar, T = 423 K, and 30 minutes reaction time, for the indicated fluid residence times.

Figure 4-44 illustrates the results obtained for identical flow and reactor conditions for the silica concentration in the aqueous effluent and Figure 4-45 shows the corresponding evolution for the degrees of conversion, X_{Si}. In all cases the apparent concentration of silica in the solution did not exceed the saturation limit (~0.01 molal the equilibrium solubility of amorphous silica). At the highest volumetric flow rate the concentration of silica shows a slight decay trend relative to the reaction progress. However, at the lowest volumetric flow rate the concentration of silica gradually increased and reached apparent steady state conditions in the vicinity of the thermodynamic saturation limit for amorphous silica.

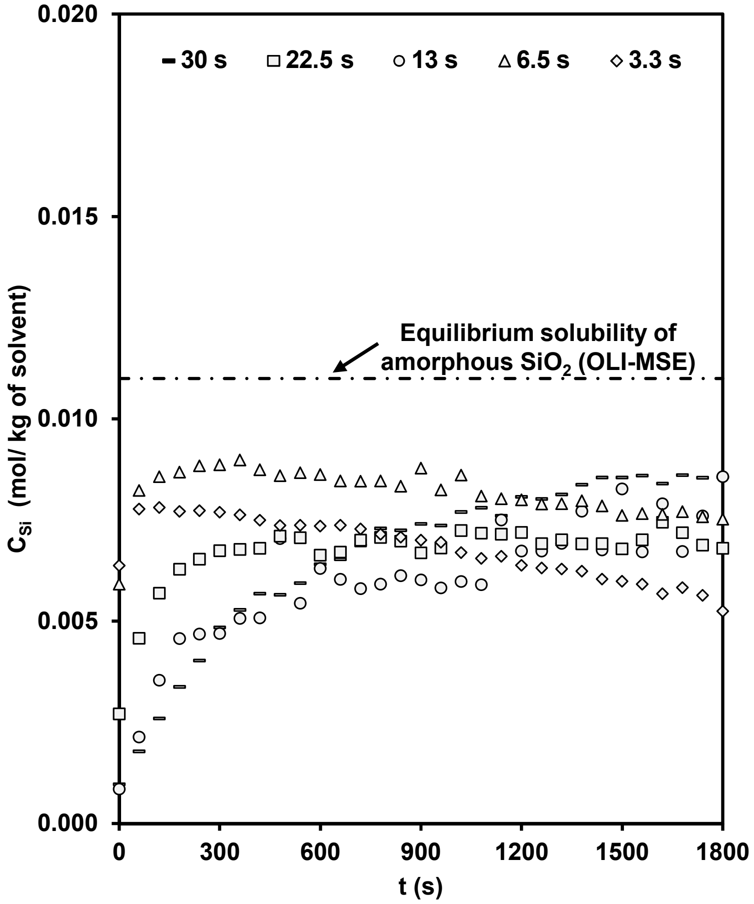

Figure 4-44. Silica concentration profiles acquired from the dissolution of thermally activated SWOL (PSD = 45-63 μm) under the saturated CO_2-H_2O system, at P_{CO2} = 100 bar, T = 423 K, and 30 minutes reaction time, for the indicated fluid residence times.

As expected the coincident fractional extent of silica conversions display subsequent slower extraction rates for cases with the relatively lower volumetric flow rates. However, with the higher volumetric flow rates, the higher degrees of completion of silica extraction are achieved. The extraction rate of silica is ~15 times greater for the experiment performed with the highest volumetric flow rate compared with the one carried out at the lowest volumetric flow rate.

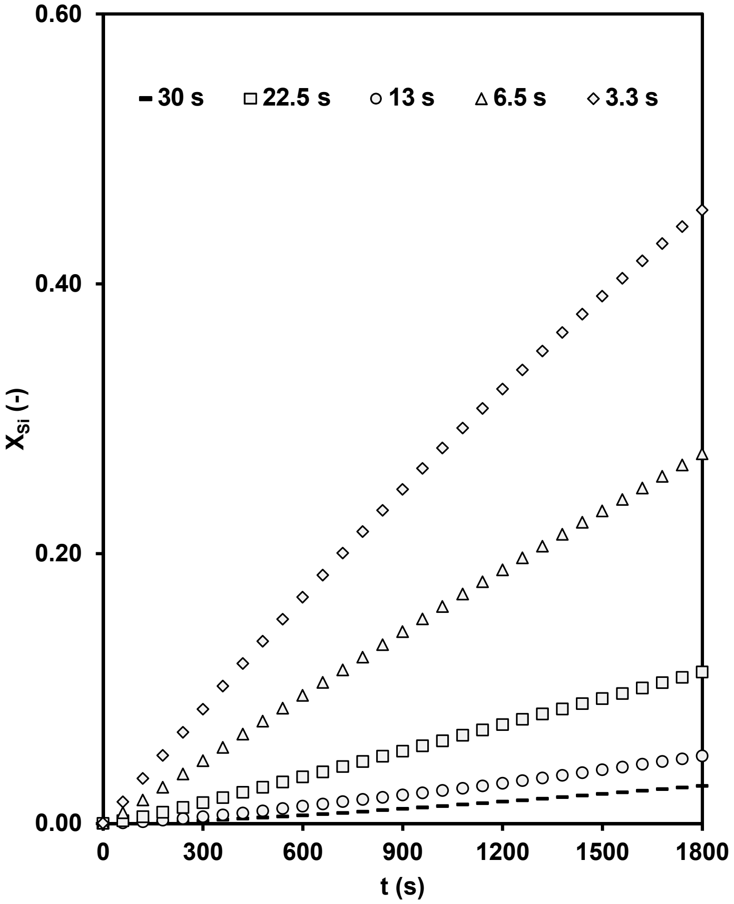

Figure 4-45. Degree of conversion of silica acquired from the dissolution of thermally activated SWOL (PSD = 45-63 μm) under the saturated CO_2-H_2O system, at P_{CO2} = 100 bar, T = 423 K, and 30 minutes reaction time, for the indicated fluid residence times.

In Figure 4-46 the molar ratio of magnesium-silica is illustrated. All the curves indicate the initial preferential release of magnesium, with a tendency towards dissolution stoichiometric, as the reactions progress. The dissolution stoichiometric appears to be stabilised relatively faster within a discernible rate for cases with the relatively higher flow rates.

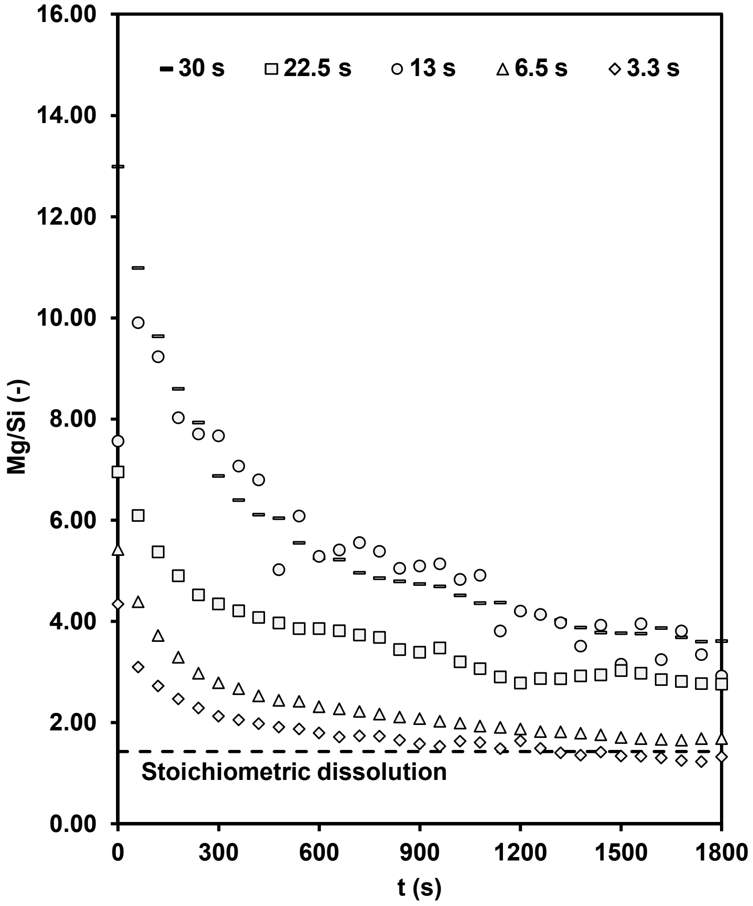

Figure 4-46. Magnesium-silica molar ratio for experiments with different fluid residence times (as indicated in the figure), obtained from the dissolution profiles presented in Figure 4-42 & Figure 4-44, the dashed line represents the stoichiometric dissolution.

4.6 Effect of Varying the Mass Loading on the Extraction of Magnesium and Silica

Another way to change the load factor is to change the mass loading of the particles in the reactor. This approach has the advantage of not changing the gross hydrodynamics in the reactor while at the same time allowing a wider range of variation than can be achieved by changing the flow rate. In this section, results are reported for a series of experiments in which the particle loading has been varied from 25 to 1000 mg. The reaction conditions were otherwise standard: T = 423 K, P_{CO2} = 100 bar, m_{CO2} =3.7 mol kg^{-1}, volumetric flow = 2.12 cm^{3} min^{-1}. Results were analysed using quantitative ICP-OES. Table 4-10 illustrates the mass loading and corresponding mass loading factor for each of the experiments.

Table 4-10. Summary of different mass loading factors for corresponding mass loadings.

Mass Loading (mg)	Mass Loading Factor (min)
25	0.03
50	0.05
100	0.10
150	0.15
250	0.25
500	0.50
1000	1.00

The experiments were carried out through the continuous flow system as it was outlined in Chapter 3 under the saturated CO_2-H_2O system (m_{CO2} ~3.7 mol kg^{-1}). In this series of the experiments, the reactor was operated according to a packed-bed configuration[1], consisted of stainless steel 3/8 ″ Swagelok bulkhead union. However, as described in Chapter 3, this strategy would not have any apparent significant effect on the kinetics implications of the obtained data. It is worth to note that since the volume of the reactor in this series of the experiment is larger than the standard reactor, employment of the standard volumetric flow rate – resulting in the artefact on the increase of fluid residence time to ~32 s.

Figure 4-47 shows results obtained under the identical flow and reactor conditions for the magnesium concentration in the aqueous effluent. Increasing the solids loading in the reactor has led to a higher concentration of magnesium in the aqueous effluent and induced the system towards saturation (with respect to the equilibrium solubility of magnesite). However, this increase in leachate concentration is not consistent with the order of increasing the mass loadings.

---

[1] It was experimentally observed that there was no apparent difference between the packed-bed and fluidised-bed conditions used in this study.

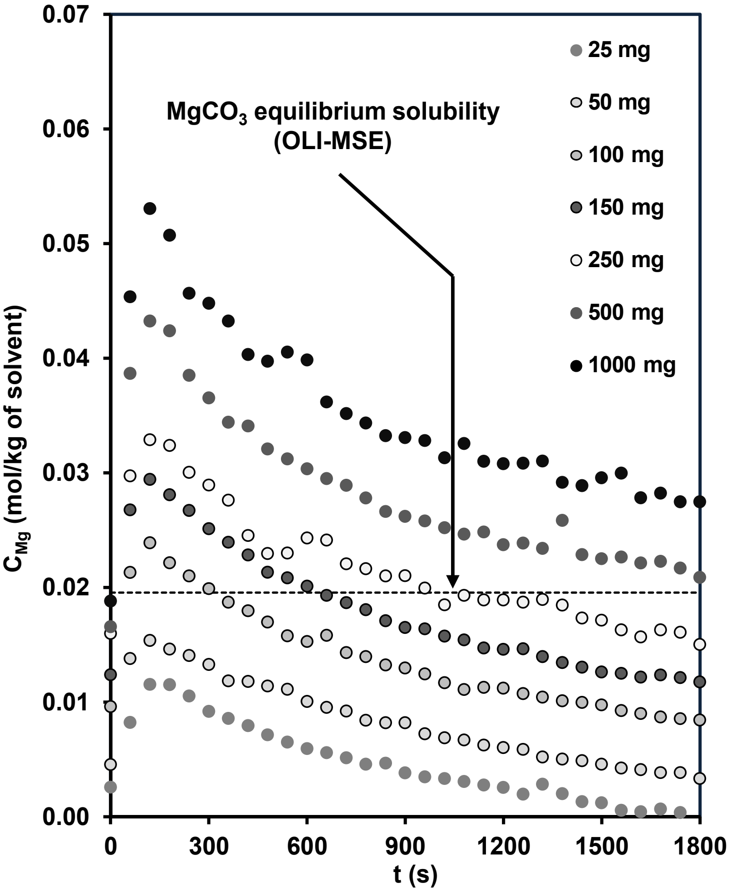

Figure 4-47. Magnesium concentration profiles for different mass loadings acquired from the dissolution of thermally activated SWOL (PSD = 45-63 μm) under the saturated CO_2-H_2O system, at P_{CO2} = 100 bar, T = 423 K, and 30 minutes reaction time. The solubility of the $MgCO_3$ was calculated by using OLI-MSE under identical experimental conditions.

Figure 4-48 displays the corresponding evolution of the degrees of magnesium conversion, shown as X_{Mg}. The degrees of completion become lower correlated with higher mass loadings. This effect can be clearly seen through the comparison of the experiment with 1000 mg mass loading and the experiment with standard mass loading (250 mg). The degree of completion of magnesium is dropped by order of ~2 as a result of four times higher mass loading. In addition, it appears that dissolution reaction identical to 25 mg mass loading almost tends to stop after 30 minutes reaction period. Overall, one may suggest that the overall conversion of dissolution reactions is correlated with the available reactant (proton) concentration proportion to the abundant of the reactive surface area, where it declines through higher mass loading conditions.

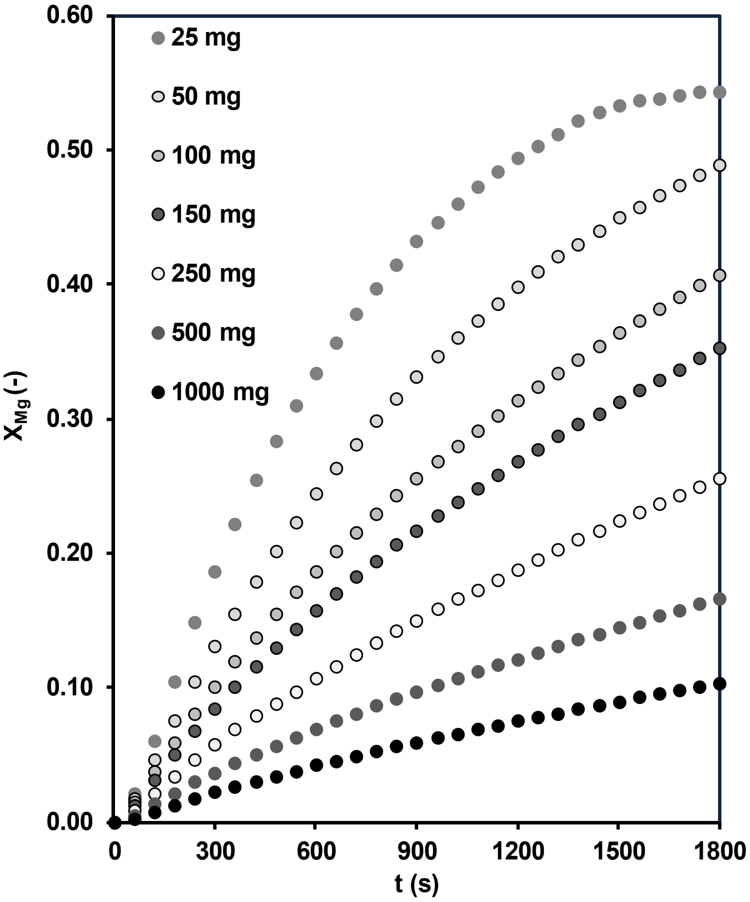

Figure 4-48. Degree of completion of magnesium extraction for different mass loadings obtained from the dissolution of thermally activated SWOL (PSD = 45-63 μm) under the saturated CO_2-H_2O system, at P_{CO2} = 100 bar, T = 423 K, and 30 minutes reaction time.

Figure 4-49 shows results obtained under the identical flow and reactor conditions for silica concentration in the aqueous effluent. Figure 4-50 displays the corresponding degrees of silica completion as X_{Si}. Increasing the solids mass loading in the reactor has led to a higher concentration of silica in the aqueous effluent until the apparent concentration of silica approached saturation limit of the amorphous silica. This attribute can be seen clearly through the silica concentration profiles associated with the higher mass loadings (i.e., 250 mg, 500 mg, and 1000 mg). The observed level of saturation is in a good agreement with the solubility limit of amorphous silica. The corresponding degrees of completion of silica are lower for higher mass loadings as expected.

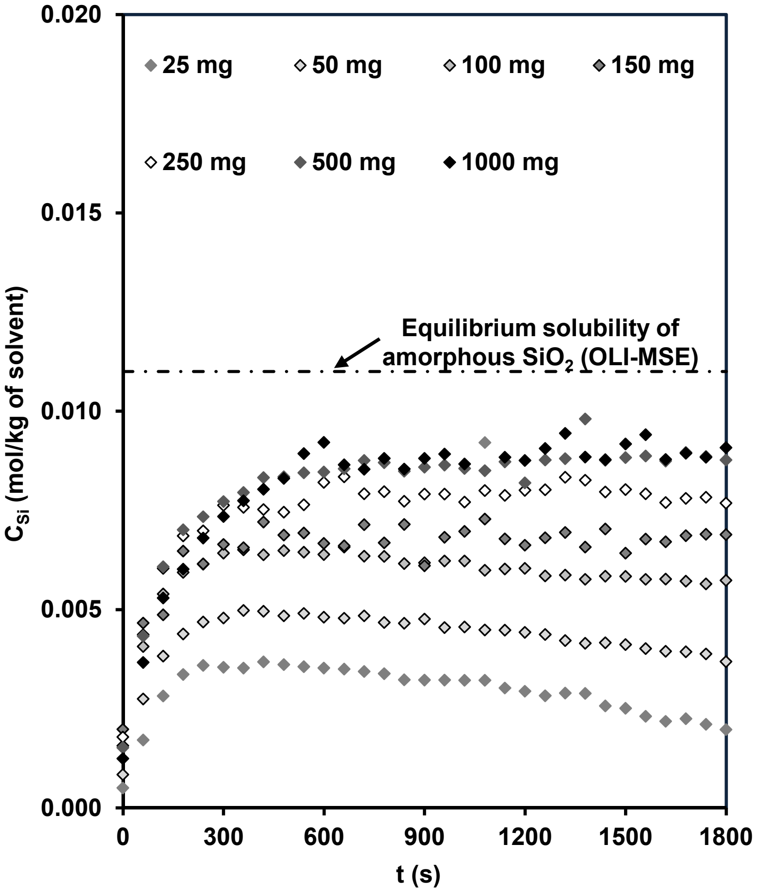

Figure 4-49. Silica concentration profiles for different mass loadings acquired from the dissolution of thermally activated SWOL (PSD = 45-63 μm) under the saturated CO_2-H_2O system, at P_{CO2} = 100 bar, T = 423 K, and 30 minutes reaction time.

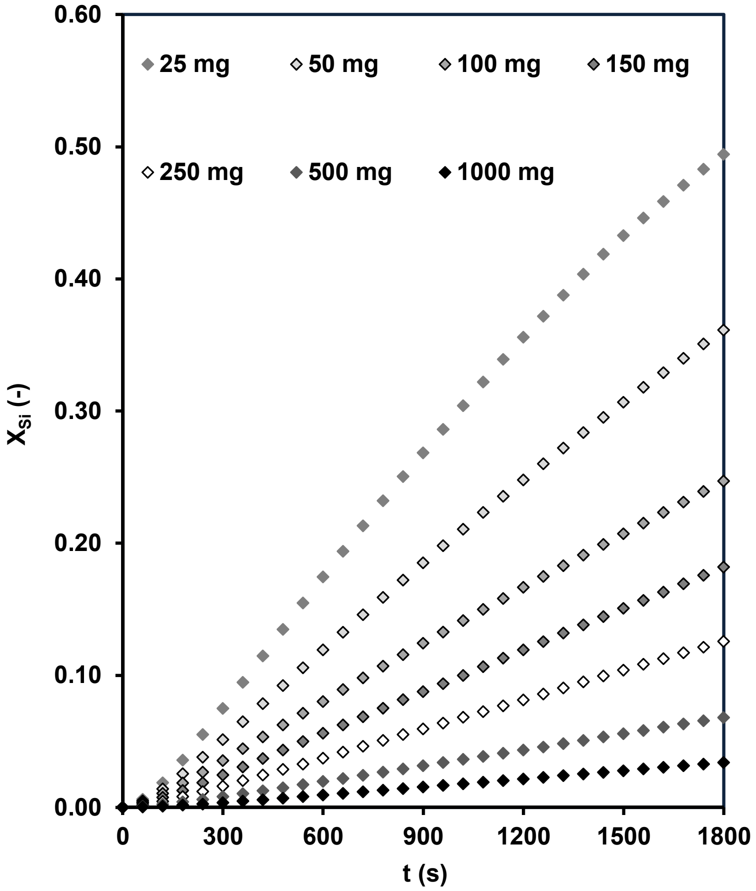

Figure 4-50. Degree of completion of silica extraction for different mass loadings obtained from the dissolution of thermally activated SWOL (PSD = 45-63 μm) under the saturated CO_2-H_2O system, at P_{CO2} = 100 bar, T = 423 K, and 30 minutes reaction time.

Figure 4-51 shows the corresponding molar ratio of magnesium-silica. It is apparent that all the reactions start with the initial preferential release of magnesium – as reactions progress, ratios incline towards the dissolution stoichiometric. Although the extraction of magnesium from the reaction with 25 mg mass loading seems to be halted after 30 minutes, the corresponding Mg/Si ratio indicates the extraction of silica continues.

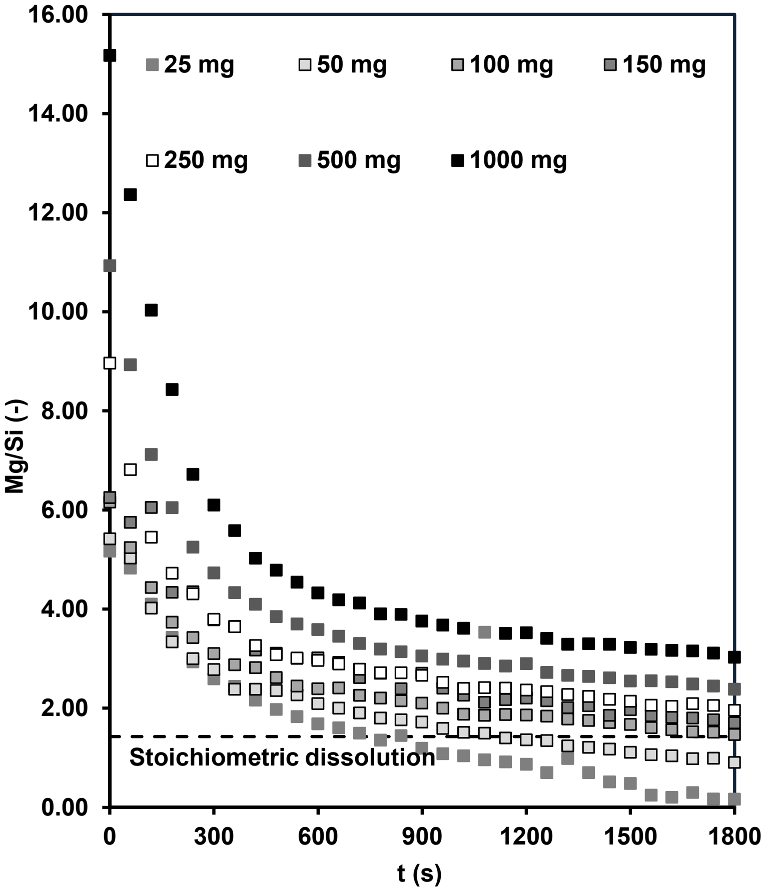

Figure 4-51. Magnesium-silica molar ratio for experiments with different CO_2 partial pressure (as indicated in the figure), obtained from the dissolution profiles presented in Figure 4-47 & Figure 4-49 the dashed line represents the stoichiometric dissolution.

4.7 Summary of Results

The solubility of magnesium species in the aqueous phase reduces proportional to increasing temperature; while, silica is relatively more soluble at the elevated temperatures, and vice versa at the lower temperatures. The silica dissolution is almost always tied to the equilibrium solubility of amorphous SiO_2. Nevertheless, no evidence of solid silica was found within the reactor or effluent of the reactor, suggesting dissolution/reprecipitation may proceed on the particle surface.

In the early stages, magnesium concentrations are limited by equilibrium – there is some overshoot, but the actual concentration achieved are still tied to the equilibrium behaviour. The magnesium concentrations achieved in the leachate may fall below the equilibrium values, where the mass loading factor is low and/or at extended reaction times. Although the magnesium levels seem to be set by equilibrium, there is no evidence confirms the formation of homogenous $MgCO_3$ throughout the system. Now the mystery is reflected the equilibration mechanism – perhaps carbonates species formed in/on the particles. The kinetic implications of the magnesium extraction and subsequent potential surface phenomena are discussed in Chapter 5. The counterparts between magnesium and silica extraction with regards to the development of reactive interfaces are also debated.

Chapter 5. Discussion of Results

5 Introduction

As outlined in the Chapter 1 several studies have been dedicated to characterisation of the dissolution behaviour of both natural and activated serpentine by using various chemicals and additives (Park et al., 2003, Park and Fan, 2004, Teir et al., 2007, Teir et al., 2009, Van Essendelft and Schobert, 2009a, Van Essendelft and Schobert, 2009b, Van Essendelft and Schobert, 2010, Fedoročková et al., 2012, Daval et al., 2013a). In the present study, the extraction rates of magnesium and silica from thermally activated SWOL under the CO_2-H_2O system have been measured under different experimental circumstances, with a view to identifying the underlying rate-limiting mechanisms, as reported in Chapter 4. The equilibrium chemistry of the carbonic acid speciation plays a critical role in controlling the reaction rates. It is believed that magnesium (as MgO in the activated rock) is liberated by the protons associated with the carbonic acid equilibria according to reactions (R 5.1 & R 5.2),

$$H_2O(aq) + CO_2(g) \rightleftharpoons H_2CO_3(aq) \rightleftharpoons HCO_3^{-}(aq) + H^{+}(aq) \qquad \text{(R 5.1)}$$

$$MgO(s) + 2H^{+}(aq) \rightleftharpoons Mg^{2+}(aq) + H_2O(l) \qquad \text{(R 5.2)}$$

while precipitation of $MgCO_3$ is governed ultimately by the equilibrium of the reaction (R 5.3),

$$Mg^{2+}(aq) + CO_3^{2-}(aq) \rightleftharpoons MgCO_3(s) \qquad \text{(R 5.3)}$$

this is known to be a complex process under hydrothermal conditions. If such a precipitation occurs through the porous substrate within the particles, diffusive transport of reactant and product (e.g., protons & magnesium) will be further inhibited.

In Chapter 4 the dependence of the dissolution kinetics on participating elementary reactions is reported based on the concentrations of reactants (i.e., Mg^{2+}) in the effluent[1]. From these results, it is apparent that the extraction rate of magnesium is greatly influenced by the equilibrium of magnesium carbonate as the concentrations approach the corresponding saturation limits. One implication that can be extracted is related to the occurrence of *in situ* precipitation of carbonate phases through the porous substrate of particles – this may reduce the permeability of the reacted zones. On the other hand, it is worth noting that dissolution is a multi-step process involving redistribution of components in a reaction zone by diffusion and chemical reactions at the solid-liquid interfaces. These changes facilitate the flux of active components across the reaction interfaces. Oelkers and co-workers showed that in the aqueous solution the surface chemistry of multi-oxide silicates is very different from that of simple oxides (Oelkers et al., 2009). They further discussed that at acid conditions due to the preferential metal exchange reactions the surface contacting the fluid becomes enriched with silica. Several other authors expressed the view that this surface transformation leads to the generation of altered porous layers on the mineral surface (Hellmann et al., 2003, Hellmann et al., 2004, Hellmann et al., 2015). Commonly the porous silica layers eventually become thicker as dissolution proceeds (Morgan et al., 1973).

Hence, it appears that the precise interpretation of the measured rates requires studying both the effect of pH on the dissolution rate along with the complex evolution of the reactive surface area. In this chapter, the dependence of the measured kinetics on pH is examined with a view to elucidating the underlying mechanism of the extraction of magnesium from thermally activated SWOL under the carbonic acid system. In an attempt to quantify the complexities of the reaction occurring at fluid-mineral interfaces, the surface properties of the post leached particles are investigated. As a result, some light is shed on the connection between the measured kinetics and the evolution of the reaction interfaces.

---

[1] The implicit assumption is the measurable aqueous species are in equilibrium with reactive surfaces and reflect the actual reactant that participating in rate-controlling steps.

5.1 Kinetic Analysis

The kinetic implications of the extraction of magnesium in previous studies focusing on the dissolution of forsterite and serpentine (e.g., Blum. and Lasaga., 1988, Hänchen et al., 2006, Daval et al., 2013a) were explained through the normalising of the experimental dissolution rates versus the measured pH. The majority of the available data in the literature have been in agreement with the reaction order of 0.5 for hydrogen ions – it is presumed that the surface concentration of protons stems from their adsorption on a surface and the likely role of silica layers in the rate-controlling mechanism are not considered. However, several changes in the reaction mechanisms may occur as the pH varies; including the changes in the chemistry, structure, and transport properties of the leached silicate surfaces.

One can only infer the nature of magnesium silicates dissolution under the acid conditions is the preferential removal of the magnesium cations from the reactive surface area coupled with proton consumption (as discussed in Chapter 2 and shown through the thermodynamic simulations in Chapter 3). In addition, reviewing the surveyed literature suggests that a rate law that could explain underlying reaction mechanisms should consider both physical and chemical properties of both fluid and solid (Nagy et al., 1991).

The dissolution rates of minerals can be interpreted within the framework of the general rate law (as outlined in Chapter 2) that incorporates the effects of temperature (Arrhenius behaviour, for the most kinetic reactions), catalysing or inhibiting species, a variation of surface area, and reaction affinity (Lasaga, 1998). Nonetheless, it should be noted that the general form of rate law is applicable for a system with no limits for the interfacial area between the reacting solid and the aqueous solution. Under the far-from-equilibrium conditions (ΔG is large and negative) the rate of the dissolution reaction is presumed to be independent of magnitude of the chemical affinity. Hence, the dissolution rate would be a function of the distinct reactive surface species (e.g., protons) and available interfacial area between the phases.

In the present study by consideration of dissolution under the proton attack conditions along with the potential variation in the reaction interfaces, the general form of rate law can be expressed according to equation (5.1) – under the far-from-equilibrium conditions. In this equation, the change in the reaction interface is presumed to progress as a function of the fractional extent of conversion and shown as $f(X)$.

$$r_{Mg} = ke^{-E_a/RT}C_{reactant}^{n} f(X) \tag{5.1}$$

where k is an intrinsic rate constant, incorporates the controlling step in the dissolution process, $f(X)$ is a function of the amount of reactive surface area, $C_{reactant}$ is the bulk aqueous concentration of reactant, and n is the apparent overall reaction order which incorporates both the equilibrium isotherm for surface adsorption of the reactive intermediate and the surface reaction order.

At this point, to appreciate the associated pH dependence and the evolution of reaction interfaces – it is worth reviewing how the rate data are extracted from the experiments, in the present study. The total rate of extraction of magnesium is obtained directly from the measurement of the reactor effluent concentration according to equation (5.2),

$$r_{Mg} = -\frac{dN_{Mg}}{dt} = \dot{m}_{water} \times C_{Mg} \tag{5.2}$$

$$\therefore \frac{dX_{Mg}}{dt} = \frac{-1}{N_{Mg}\big|_0}\frac{dN_{Mg}}{dt} = \frac{\dot{m}_{water}MW_{Mg}C_{Mg}}{M_0 Y_{Mg}|_0} \tag{5.3}$$

$$\therefore \frac{dX_{Mg}}{dt} = \frac{\dot{m}_{water}}{M_0}\frac{MW_{Mg}}{Y_{Mg}|_0}C_{Mg} \tag{5.4}$$

in equations (5.3) and (5.4) the ratio $\dot{m}_{water}/M_0$ is the inverse mass loading factor, τ_m^{-1} which is specific to a particular experiment. As previously described, the initial mass fraction of magnesium in the sample is

$Y_{Mg}|_0 = 24.8\%$ in all cases. The dimensionless rate is related to the reaction behaviour of the sample via the assumed form shown with equation (5.5),

$$\frac{dX_{Mg}}{dt} = k_{reactant}\, C_{reactant}^{n} f(X) \qquad (5.5)$$

where $k_{reactant}$ is an intrinsic rate constant for the controlling step in the dissolution process (containing also the particle size). We seek to identify the functional form $f(X)$ by equating the rate equation with the measured rate in accordance to equation (5.6),

$$k_{reactant}.f(X) = \frac{1}{C_{reactant}^{n}} \frac{dX_{Mg}}{dt} = \frac{1}{\tau_m} \frac{MW_{Mg}}{Y_{Mg}|_0} \frac{C_{Mg}}{C_{reactant}^{n}} \qquad (5.6)$$

According to the objective of this study, to evaluate the extraction rate of magnesium, it is assumed that at the molecular level the kinetics of the dissolution reaction are directly correlated with the exchange rate of the protons absorbed into the Mg-O bonds in the activated mineral. This process results in the transformation of solid species and the release of magnesium cations into the solution. The concentration of this activated complex should be proportional to the extent of proton adsorption at the surface of MgO sites in a mineral matrix. For reaction controlled by proton attack, the functional form $f(X)$ is shown in accordance with equation (5.7),

$$\frac{1}{C_{H^+}^{n}} \cdot \frac{dX_{Mg}}{dt} = \frac{1}{\tau_m} \cdot \frac{MW_{Mg}}{Y_{Mg}|_0} \cdot \frac{C_{Mg}}{C_{H^+}^{n}} \qquad (5.7)$$

Now, as discussed previously in Chapter 3, for given conditions of (T and p), we know that it is approximately the case that $C_{H^+} \propto C_{Mg}^{-1}$, so the kinetic plot behaves as,

$$\frac{1}{C_{H^+}^{n}} \cdot \frac{dX_{Mg}}{dt} \sim K_{expt} \cdot C_{Mg}^{1+n} \qquad (5.8)$$

where K_{expt}[1] is a constant (incorporating equilibrium and experimental properties) specific for the conditions of a given experiment. Therefore for proton attack, to the extent that C_{Mg} varies, the experiments return useful kinetic information regarding n and $f(X)$. The bulk concentration of C_{H^+} is determined as a function of pH (10^{-pH})[2]. In the present study, experimental measurement of the pH at the reaction conditions was not possible; hence, the pH is calculated by using OLI-MSE Analyser Studio 9.2 (for the MgO-CO_2-H_2O system for the reaction sets of 2.8 to 2.11 as well as 5.2 & 5.3 including a large number of other magnesium species). Whilst the proposed kinetic analysis is only valid for data related to the far-from-equilibrium conditions[3], it was employed to investigate the kinetic implications of all the measured extraction rates of magnesium, presented in Chapter 4.

Figure 5-1 shows the experimental conversion rates of magnesium computed by using equation (5.3) – Figure 5-2 and Figure 5-3 illustrate the shape of the rate function $f(X)$ on the basis of the normalised experimental conversion rates of magnesium by half and first order proton dependence, respectively. In these figures points obtained under conditions which the magnesium concentration is below its expected equilibrium value are represented by open symbols; whereas, supersaturation conditions are represented by filled symbols.

---

[1] $K_{expt} = \frac{1}{C_{H^+}^{n} C_{Mg}^{n}} \cdot \frac{1}{\tau_m} \cdot \frac{MW_{Mg}}{Y_{Mg}|_0}$

[2] This strategy provides the active concentrations of proton with reference to solution composition corresponded to specific experimental conditions.

[3] Far-from-equilibrium & near-equilibrium conditions identical to the undersaturated conditions.

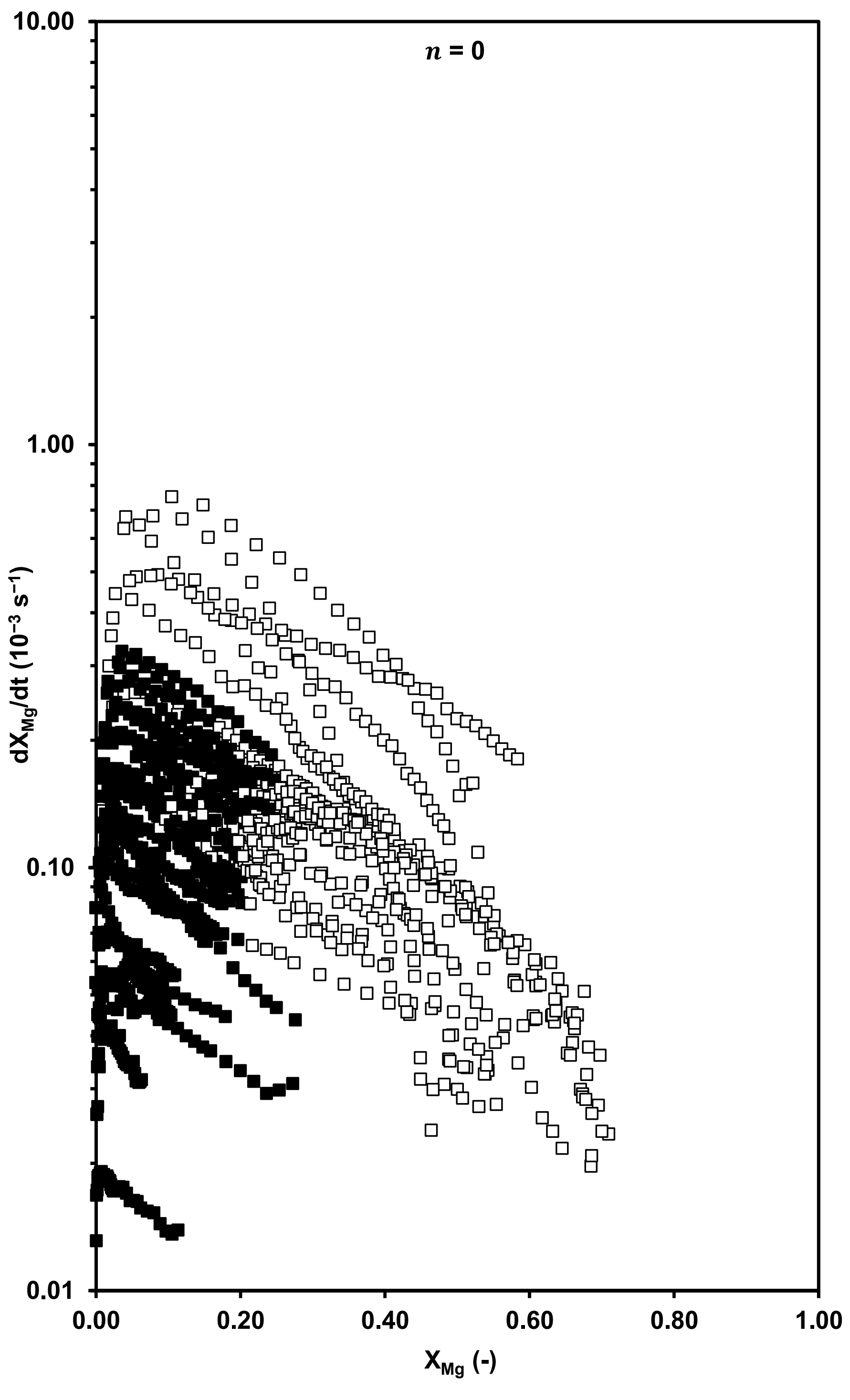

Figure 5-1. Experimental conversion rates of magnesium plotted against the fractional extent of magnesium extraction, for all the experiments, covering different reaction temperatures from 303 to 473 K, pressures from 10 to 160 bar, mass loadings from 25 to 1000 mg, particle sizes from 20 to 180 μm, and residence times from 3.3 to 30 s. The filled symbols (■) indicate conditions saturated with respect to the solid $MgCO_3$ formation; unfilled symbols (□) indicate under saturated conditions.

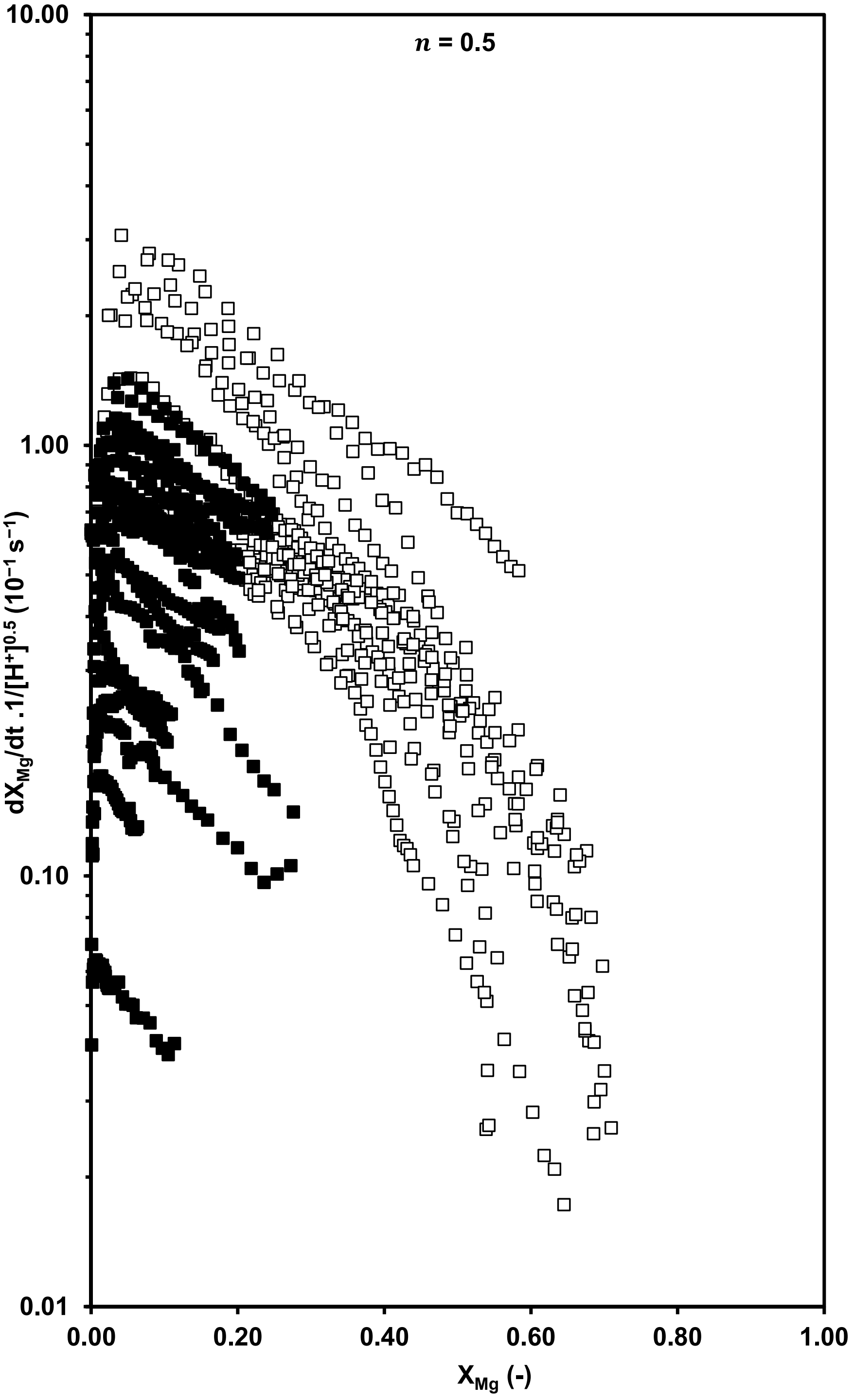

Figure 5-2. Experimental conversion rates of magnesium normalised by the local equilibrium proton concentration (n = 0.5) plotted against the fractional extent of magnesium extraction, for all the experiments, covering different reaction temperatures from 303 to 473 K, pressures from 10 to 160 bar, mass loadings from 25 to 1000 mg, particle sizes from 20 to 180 μm, and residence times from 3.3 to 30 s. The filled symbols (■) indicate conditions saturated with respect to the solid $MgCO_3$ formation; unfilled symbols (□) indicate under saturated conditions.

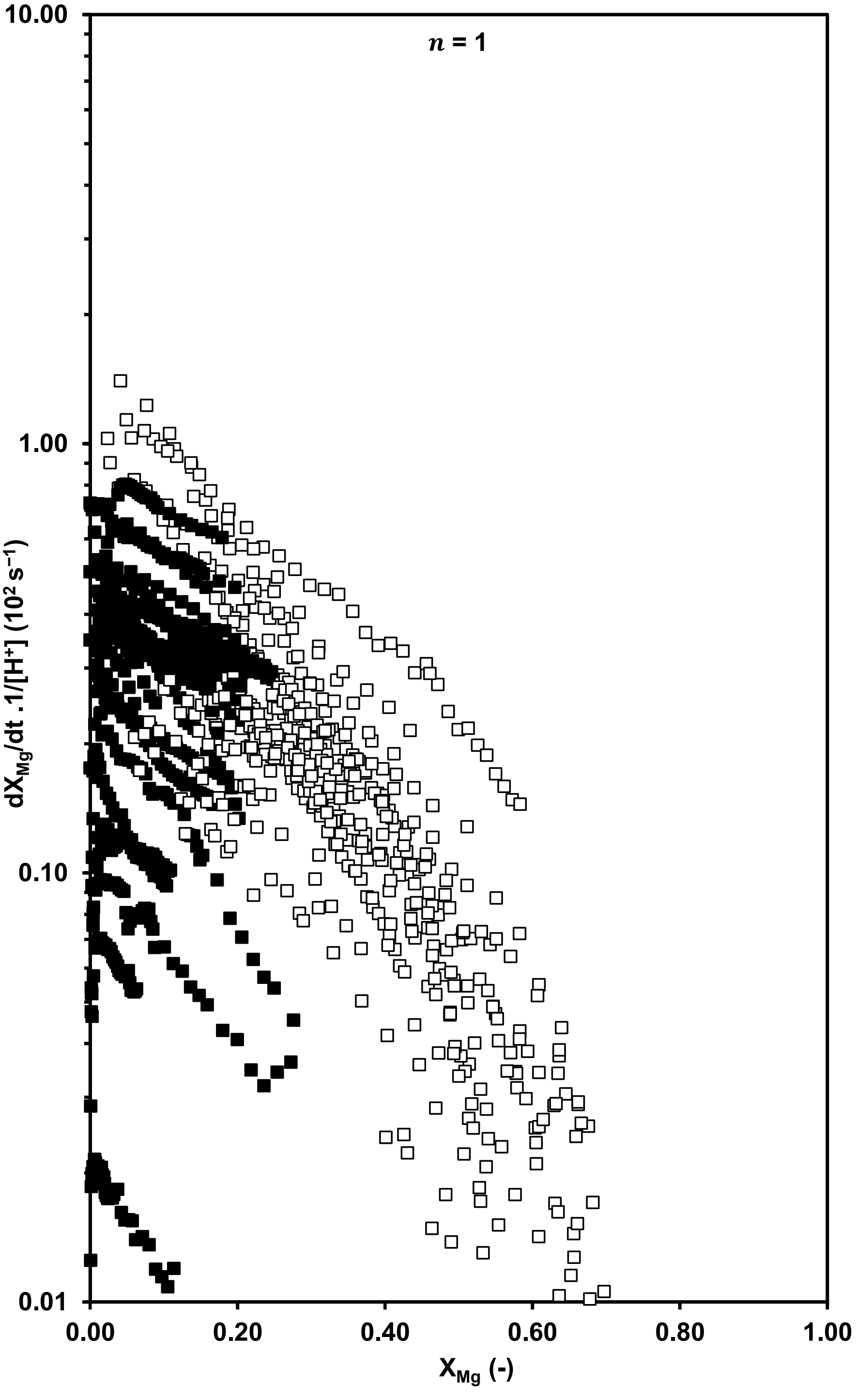

Figure 5-3. Experimental conversion rates of magnesium normalised by the local equilibrium proton concentration (n = 1) plotted against the fractional extent of magnesium extraction, for all the experiments, covering different reaction temperatures from 303 to 473 K, pressures from 10 to 160 bar, mass loadings from 25 to 1000 mg, particle sizes from 20 to 180 μm, and residence times from 3.3 to 30 s. The filled symbols (■) indicate conditions saturated with respect to the solid $MgCO_3$ formation; unfilled symbols (□) indicate under saturated conditions.

Comparing Figure 5-1 with Figure 5-2 and Figure 5-3 confirm that correlations of the undersaturated data have improved by incorporating the proton concentration dependence– it can also be seen that the undersaturated data are more tightly clustered with $n = 1$. In order to investigate the reaction order with respect to protons as a reactant – the relative standard deviations of the unsaturated normalised experimental rates at X_{Mg} ~0.25 versus the values of n are plotted, as shown in Figure 5-4. The scatter in the data is minimised in the vicinity of n equal to 1 to 1.25 – thus, in the current study it is presumed that $n = 1$ which appears to give the best overall representation of kinetics.

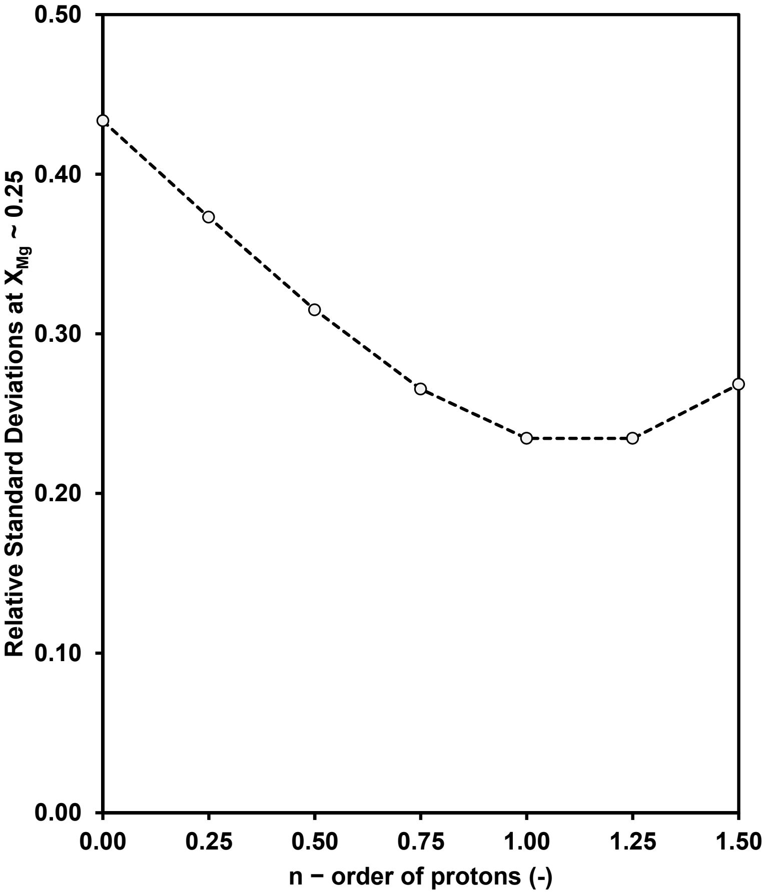

Figure 5-4. Relative standard deviations of the normalised curves at X_{Mg} ~0.25 for experiments proceed at undersaturated conditions plotted versus the order of the protons.

Here it is worth to remind that dissolution rates typically depend on surface speciation. The dissolution reaction under acid conditions needs protons, which come to be bonded to the surface oxides ions and weaken the critical bonds; therefore, detachment of the metal species into the solution results – the consumed protons replaces the metal ions, leaving the solid surface and thus maintaining the charge balance (Furrer and Stumm, 1986, Stumm and Wollast, 1990). Under steady state conditions, one may generalise that the original surface sites are regenerated completely after the detachment step (under the assumption that surface protonation equilibria are maintained and kept constant by the solution pH). The adsorption isotherms of the protons indeed have been found to be sufficiently faster than the detachment of the metal species (Hachiya et al., 1984); hence, it can be presumed that the concentration of protons at the surface is in equilibrium with the solution. As explained in Chapter 2, throughout several past studies that investigated dissolution of crystalline mixed oxides (like forsterite) the value of n (apparent overall order of reaction that could be related to the equilibrium isotherm and/or to the reaction kinetics) has been interpreted typically between 0 and 0.5. However, current observation suggests n should be equal to one – this discrepancy may reflect the fact that thermally activated serpentine contains amorphous-like structure rather than crystalline.

Observation of Figure 5-3 indicates that while there is a significant scatter, the data for undersaturated conditions are clearly clustered and show a common trend – here it must be remembered that the experimental conditions cover a vast range of conditions as described in Chapter 4. In this context, the correlation of the rate data is quite remarkable and suggests the existence of a relatively simple, unifying rate behaviour. In contrast to these data, the data for supersaturated conditions are clearly distinct, corresponding to the fact that the rate in these cases is strongly influenced by the equilibrium transport capacity of the aqueous phase. Under some circumstances (e.g., Figure 4-2), the early (low X) extraction conditions are supersaturated but the rate soon falls below the saturation limit – it is these cases that produce the filled symbols in Figure 5-3 that follow the general trend of the undersaturated data. This suggests that the demarcation between saturated and undersaturated conditions is not precise, perhaps because of kinetic effects; or because the degree of supersaturation needed to induce kinetic effects (such as precipitation of carbonate in the pores) is not precisely defined; or because the equilibrium saturation conditions predicted by OLI-MSE are not exact.

In order to investigate the rate-controlling step for conditions not influenced by equilibrium (unsaturated), the average trend of the rates for undersaturated conditions are compared to standard rate equation models for the reaction of solids of constant external size in Figure 5-5. The models considered are volumetric reaction control, shrinking core with chemical reaction control, and shrinking core with product layer diffusion control. Table 5-1 shows the form of the rate function ($f(X)$ in equation (5.7)). For the purposes of this comparison, the experimental conversion range is rescaled so that complete conversion ($X_{apparent} = 1$) is taken to occur at the measured conversion value of $X = 0.7$ – this is consistent with the ultimate level of extraction achievable in the experiments and the fact that the rate of extraction goes to zero at this measured conversion level. Furthermore, in order to facilitate the comparison with the data, the model curves are scaled to coincide with the mean experimental rate at $X_{apparent} = 0.2$.

Table 5-1. Forms of the rate function based on the rate equation models, i.e., volumetric reaction control, shrinking core with chemical reaction control, and shrinking core with product layer diffusion control, adopted from (Levenspiel, 1999). The $C_{constant}$ for the presented models are provided in Appendix G.

Model	Equation
Volumetric reaction control	$\frac{dX_{Mg}}{dt} = (1 - X) \times C_{constant}$
Chemical reaction control	$\frac{dX_{Mg}}{dt} = (1 - X)^{2/3} \times C_{constant}$
Product layer diffusion control	$\frac{dX_{Mg}}{dt} = \frac{C_{constant}}{((1 - X)^{-1/3} - 1)}$

Comparison of the mean kinetic curve with the predicted profiles using the employed models indicates that the product layer diffusion model captures the overall experimental trend while the other models are clearly inappropriate. Considering the product layer diffusion shrinking core model control, the measured rate under some undersaturated conditions (e.g.,

Figure 4-47), at relatively low X_{Mg} is lower than expected – this might indicate a poor model match. However, it could also be due to time constants of the measurements and of the mixing conditions in the reactor; it could also result of a limited supply of protons, either because (a) the carbonic acid equilibria are not being maintained at high rates occurring here or (b) external mass transfer limitations.

The value of $C_{constant}$ in Table 5-1 for product layer diffusion control varies with particle size as $1/\bar{d}^2$ and results obtained with different particle sizes would not be expected to fall on a common curve in plots such as Figure 5-3. In fact, the results presented in Figure 4-11 and Figure 4-12 indicate that the reaction rates appear to not depend on the external surface area of the particles, even as the particle size was varied within a factor of nine. This is an unexpected result and quite inconsistent with a shrinking core model. One complicating factor in the data presented in Figure 4-11 is that the initial reaction gave rise to saturated effluent and that deposition of $MgCO_3$ in the pores of particles may have determined the subsequent kinetics results. It is noted, however, that as the extractions continue to undersaturated conditions, the rates follow in a consensus of the clustered undersaturated data.

It is clear that product layer diffusion can not control the kinetics of the overall reaction in its simplest form as expressed in Table 5-1 because of the observed lack of sensitivity to particle size. Of the models in Table 5-1, only volumetric reaction (i.e., fast diffusion throughout the particle) would be expected to proceed independently of particle size. However, the kinetic form for this model matches the data very poorly, as shown in Figure 5-5. An alternative model is a diffusion-plus-reaction mechanism suggested by Pigford and Sliger (1973) for the reaction between a gas and solid. In this model, a particle of solid is presumed to be made up of many spherical particles of solid active reaction sites similar to the grain model introduced by Szekely and Evans (1970). According to the diffusion-plus-reaction mechanism theory, the reactant must diffuse through the pores separating the sub-particles and react with their surfaces. The rate of reaction is likely dictated by the thickness of a solid reaction product that forms on the surface of the sub-particles. The product layer thickness is, in turn, determined by the whole time history of the local concentration of the product. Hence, one may postulate that under various particle sizes the composite particles reacted with the same extent of reaction where principally the reaction rate has been controlled either by the diffusion of reactant (e.g., protons) through the pores between the grain and/or by diffusion through the developing layers of the reaction product. The dependence of the rate on particle size in this model depends on the balance between diffusion and reaction, but mixed control does significantly reduce the sensitivity to particle size.

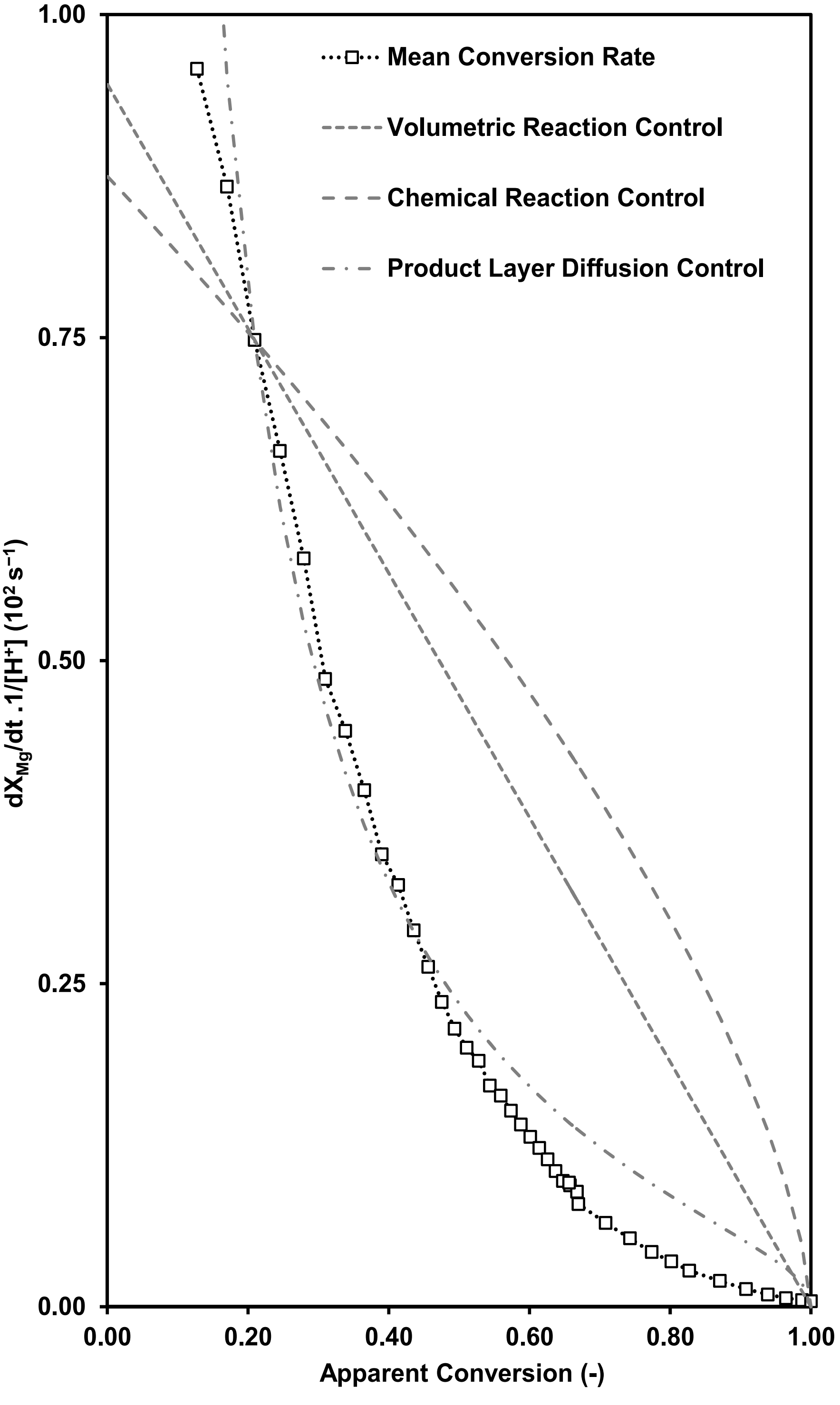

Figure 5-5. Average trend of the rates for under saturated conditions plotted versus the apparent conversion – compared with the rate equation models presented in Table 5-1 as indicated in the figure.

In this regard, it is worth to note that the correct form of kinetics correlation almost certainly does not exist since the particle size and morphology are changing significantly as the dissolution reaction is progressed. In the context of mineral dissolution, it is important to understand which part of the reaction interfacial zone (inner vs. outer interface) plays the major role in the rate-limiting process. Scanning Electron Microscopy (SEM) is used to visualise the unreacted particles along with the post-leached particles attained from the standard dissolution conditions, as shown in Figure 5-6. Despite the average mass loss of ~37% during the 120 minutes dissolution reaction (as shown in Table 4-1), the external shape of the particles appears not to change dramatically corresponding to the measured mass loss. The ~37% mass loss that occurred during the dissolution experiments would correspond to ~15% change in the particles diameter at constant density. In fact, this observation suggests a significant restructuring should occur within the particles as they react.

Observation of Figure 5-6 (c) indicates that a cluster of secondary phase partially covers the surface of the reacted particles. Furthermore, the crystal structures of residual solids attained from the standard dissolution reactions were examined by X-ray diffraction analysis (see Appendix E); results show no appreciable changes occurred regarding crystal structure of the residual solids. Indeed, this observation suggests the generated surface layers are either very thin or may comprise an amorphous phase. The BET measurement for the overall surface area of the post-leached particles[1] indicated that the overall surface area increased by ten-fold compared with the unreacted material (see Appendix H), indicating the surface of the post-leached particles become relatively permeable. This quality of the surface of particles has been attributed through a number of prior studies with the dissolution-reprecipitation mechanism, in which silica species first dissolve and then reprecipitated on the mineral surface – this is also indicated through the measurement of the chemical composition of the reacted particles by using SEM-EDS technique for different reaction times, as presented in Appendix E. These results show that as the reaction progresses

---

[1] Acquired from the standard reaction conditions for a period of 30 minutes reaction.

the corresponding solid residues become depleted in magnesium, but still relatively rich in silica.

In this respect, Hellmann et al. (2012) on the basis of TEM examination of reaction interfaces for a range of hydrolysed silicate minerals suggested that the surface layers must be permeable to inward and outward fluxes of solution and product species, respectively. On the other hand, Daval et al. (2011) discussed that during the carbonation reaction of olivine, surface reaction layers generated by dissolution-reprecipitation mechanism are first permeable and eventually become passivating with further progress of the reaction. In this regard, Cailleteau at al. (2008) suggested that the sharp reduction in the dissolution rate of silicates with time, arises from the densification of the outer layers of the alteration film, perhaps leading to pore closure in the reaction interfaces.

Considering the surveyed literature, under the undersaturated conditions (not affected by equilibrium solubility of magnesite) dissolution mechanism may be eventually influenced by the evolution of the surface reaction layers. However, it must be noted that the activated material used in the present study is not crystalline – may not follow the same dissolution pathways as the crystalline silicates. In the context of a grain dissolution model, as the dissolution of the activated sites (e.g., MgO) on the particle surface is progressed, this process may generate internal branches that contribute to the development of surface area – nonetheless at the same time the saturated dissolving silica species is still able to reprecipitate on the reaction surfaces and result in clogging the generated pathways. Therefore, the controlling reaction interfacial zone could be related to the internal interfacial area or/and the external particles surface area.

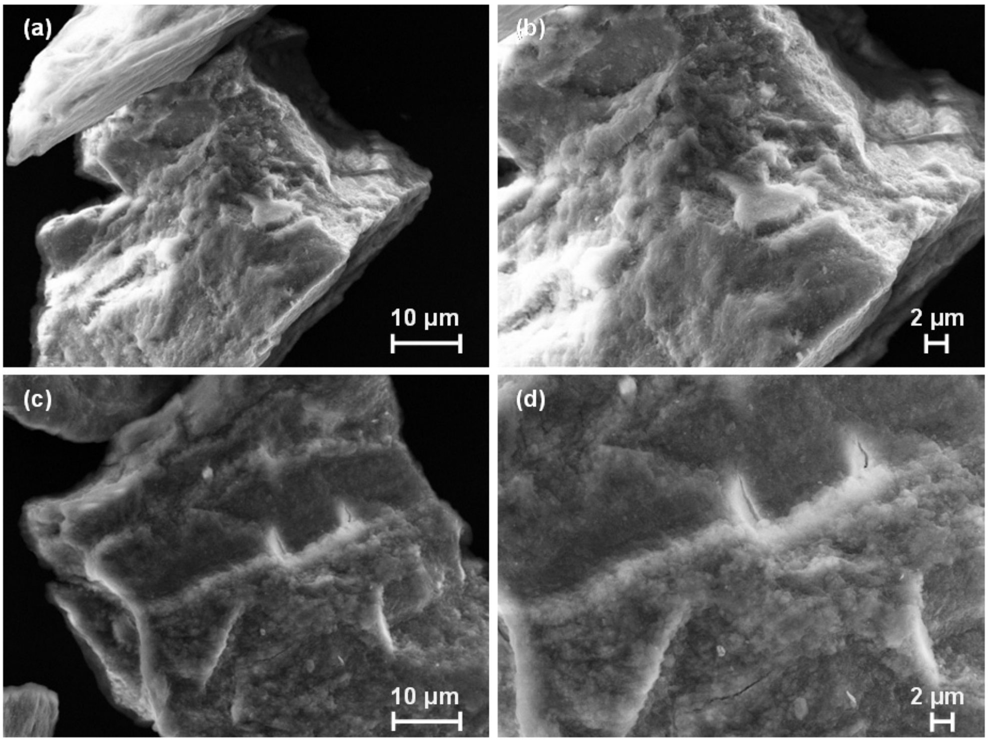

Figure 5-6. Scanning electron micrographs of, (a & b) unreacted heat-treated SWOL (2 hours, 900 K), (c & d) post-leached particles obtained from dissolution reaction conducted under the saturated CO_2-H_2O system, at $P_{CO2} = 100$ bar, $T = 423$ K, and 120 minutes reaction time. At higher magnification precipitation of secondary clusters on the mineral surface is apparent. Images obtained using Zeiss EVO/Qemscan instruments at an acceleration voltage of 15 kV.

5.1.1 Evidence for Role of Bicarbonate Ion

In the previous studies, it has been suggested that the dissolution reaction may be promoted by the presence of the bicarbonate ligands (Olsen and Rimstidt, 2008, Daval et al., 2013a). If the ligand-promoted and proton-promoted dissolution reactions occur in parallel; henceforth, the overall expression rate can be expressed in accordance with the sum of the organic-free rate and organic-promoted rate (Wogelius and Walther, 1992). Thus, in order to obtain the kinetics implications under conditions that the controlling reactant are bicarbonate ions – the possible role of bicarbonate ions as reactants is examined by applying equation (5.6). As noted in Chapter 3, $C_{HCO3^-} \approx 2\, C_{Mg}$, and thus the kinetic plot behaves as,

$$\frac{1}{C^{q}_{HCO3^-}} \cdot \frac{dX_{Mg}}{dt} \sim K_{expt} \cdot C^{1-q}_{Mg} \tag{5.9}$$

if the apparent order is $q = 1$, then the kinetic analysis returns a constant value for $k.f(X)$ for any run – indeed this equation contains no kinetic information whatsoever. The implication that can be extracted from a constant value for $k.f(X)$ is the method of analysis, is invalid when $C_{reactant} \propto C_{Mg}$ – since the functional form of $f(X)$ is actually determined by the nature of the reaction, and it cannot be a constant. This attribute can be seen through the shape of the rate function normalised by the first order bicarbonate, as shown in Figure 5-7; where the data obtained under conditions that the magnesium concentration is below its expected equilibrium value are represented by open symbols; while, supersaturation conditions are represented by filled symbols.

Despite a few scatter data for specific experiments (e.g., mass loading factor $\leq$ 0.06 min), the normalised curves return to almost constant – essentially it is a pre-ordained result that contains no kinetic information.

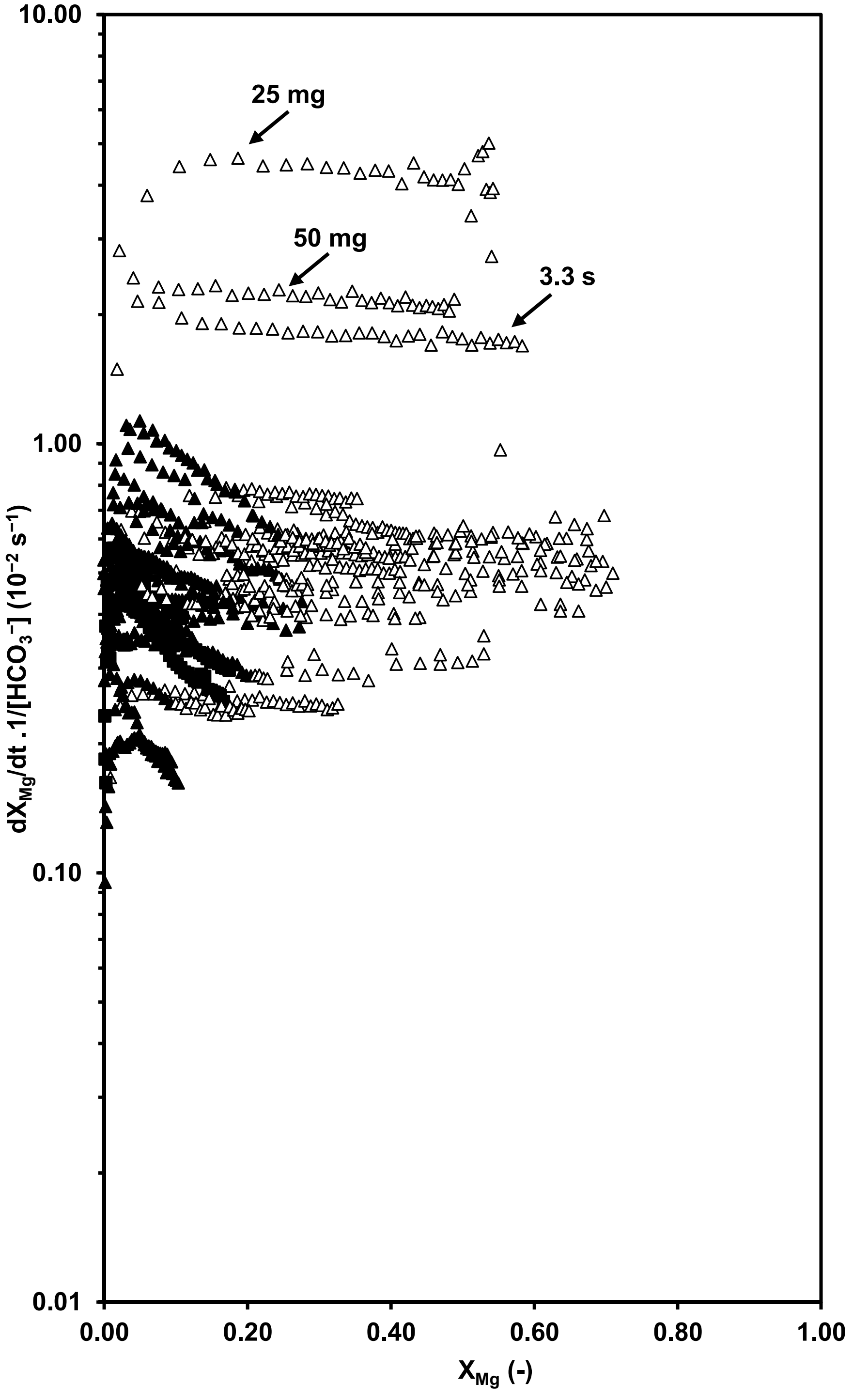

Figure 5-7. Experimental extraction rates of magnesium normalised by the local equilibrium bicarbonate concentration plotted against the fractional extent of magnesium extraction, for all the experiments, covering different reaction temperatures from 303 to 473 K, pressures from 10 to160 bar, mass loadings from 25 to 1000 mg, particle sizes from 20 to 180 μm, and residence times from 3.3 to 30 s. The filled symbols (▲) indicate conditions saturated with respect to the solid $MgCO_3$ formation; unfilled symbols (△) indicate under saturated conditions.

5.1.2 Summary and Significance

The remarkable consensus of the rates for undersaturated data under the proton attacked conditions signified that the extraction rate of magnesium is more-or-less proportional to the bulk equilibrium proton concentration in the solution. In addition, the convergence of the undersaturated curves implied that the activation energy linked to the rate law is almost negligible (indicated through the clustered curves for experiments with different reaction temperatures). Also, the calculation of apparent activation energy points to the similar conclusion (see Appendix F). The mean trend of the rates is also seen to be relatively in good agreement with the shrinking core product layer diffusion control model. However, further comparison of the rates acquired from variable particle size indicates a need for a more complex model, such as the grain models that can explain nonlinear reaction rate while also having little dependence on the particle size. This holds true for most of the cases that the build-up of the reaction products insides the reaction interfaces reduces the driving force, or the accumulation of a reaction product increases the interdiffusion resistance. In the upcoming sections, the implications of silica dissolution rate along with the effect of partially saturated and fully saturated conditions on the extraction of magnesium are discussed.

5.1.3 Associations of the Silica Dissolution Rates and Alteration of the Reaction Surface Layers

In the context of magnesium silicate dissolution, through the vast majority of experimental studies, silicate dissolution rates have been determined under conditions of far-from-equilibrium. Under such circumstances, dissolved silica concentrations have no effect on dissolution rates. Moreover, equilibrium calculations through thermodynamic packages usually do not allow for the influence of a silica-rich layer on the overall silicate dissolution rates, with silica being treated as individual, separate phases. The assumption of dissolution at far-from-equilibrium is implied that at given experimental conditions, saturation of the dissolved elements in the fluid is not influenced by the silicate mineral dissolution reaction rate (as the Gibbs free energy of the system not approaching the equilibrium). As a result of these factors, the existence of silica-rich layer has been dismissed, or it has been concluded that any such layers must be highly porous. Correspondingly, conclusions regarding the rate-limiting steps did not include processes at the silicate/water interface. However, according to the recent experimental studies conducted by Hellmann et al. (2012) and Daval et al. (2013b), these assumptions are not always correct; and the effect of silica reactions on the dissolution rates should be considered more accurately. Hellmann et al. (2012) suggested that silica surface layers formed on the mineral surfaces could be correlated with the elevated degree of hydration of the dissolving surface. They further explained that the properties of the fluid including pH, bulk fluid saturation level, chemical composition, and the reaction temperature are vitally influenced the final thickness of the polymerised silica on the mineral surface. According to Iler (1979), the solubility of the silica is influenced by several orders of magnitude by incorporation of foreign ions, particularly Al, and Mg.

During the hydrolysing reaction of magnesium silicates, as a result of proton exchange and breaking of the Mg-O bonds depending on the mineral structure, a SiO-H bond can be released as an aqueous silica species, as described in the surveyed literature in Chapters 3. It is possible that the separated Si(OH) groups rapidly link to the parent mineral and generate a silica network, or form colloidal silica particles and then liberated along with the magnesium compound into the aqueous phase.

According to solubility predictions provided by OLI-MSE at relatively lower temperature, the decrease in the solubility of silica causes increasing supersaturation that leads to an increase in the precipitation rate – this phenomenon is consistently observed in the current study through the particles growth from the leachate (see Appendix E). At elevated temperatures, the solubility of the amorphous silica increases, meaning the higher amount of aqueous silica compounds can be released in the solution. On the other hand, the increase in the local pH associated with extraction of magnesium also may give rise to the condensation of silica compounds. The final effects of all these parameters on silica reaction rates can be transformed to the extraction rate of metal cation, as a result of dynamic change in thickness of the silica layers on reactive surfaces.

In the present study, the extraction rate of silica is observed to be relatively fast compared with what is estimated for the dissolution rates of vitreous silica. Almost all the measured rates for silica proceed in the vicinity of the equilibrium solubility of amorphous silica, except those related to elevated reaction temperatures, i.e., higher than 423 K (e.g., Figure 4-34, and Figure 4-39), and low mass loading (e.g., 25 & 50 mg) as shown in Figure 4-49. The saturation of silica in the aqueous leachate implies to the possibility of precipitation of the released silica compounds on the reaction interfaces during the reactions.

According to Putnis (2002), the transformation of the porous substrate and subsequent densification of the generated surface layers is variably depending on the relative amount of the phases dissolving and precipitating. Thus, the overall thickness of the silica layer at any point during the experiment should essentially be a function of the amount of silica released into the solution. Hellmann et al. (2012) further suggested that nanoscale surface evolution can potentially have a retarding effect on the progress of the chemical weathering process. Based on their diffusion model, they stated that the interdiffusion mechanism is inconsistent with the moderate to thick surface layers. This inconsistency introduced a step-like jump in cation concentration through the depth of the altered zone. In this study, the exact details of the physical processes concerning the generation of the surface layers were not investigated. However, the thickness of the silica-rich layers appears to increase with the progress of the reactions. The declining trend of the normalised rates for undersaturated experiments in Figure 5-3 reflects how the dissolution reaction slows as magnesium is extracted – one possible explanation could be correlated with an increase in the thickness of silica-rich layers either on the internal reaction pathways or on the outer surface of the reacting particles. Hellmann et al. (2015) also discussed that in the mineral-fluid reaction the hydration rate of the pristine mineral reduces proportionally to the progress of the dissolution reaction.

At relatively elevated temperatures, despite the competing effect of silica solubility, higher reprecipitation of silica species on the reaction interfaces may contribute to the observed reduction in the silica extraction rate (e.g., Figure 4-34, and Figure 4-39). If such rapid reprecipitations occur, it may restrict the fluid pathways – however there is no concrete evidence available in the present study. Observation of Mg:Si ratios show that in almost all the cases reported in Chapter 4, dissolution reactions are initially incongruent, and then eventually continue towards the vicinity of the dissolution stoichiometric. At the elevated reaction temperatures; however, it seems the congruent dissolution is established (e.g., Figure 4-36 and Figure 4-41) relatively faster, which suggesting extraction of magnesium and silica proceeded with a more-or-less similar rate. The associated changes to the reaction interfaces of silicate minerals relative to temperature have been attributed in past studies (e.g., Petit et al., 1987). Petit et al. (1987) observed that hydrogen ion penetration depth on the surface of diopside reacting in an acidic solution is reduced for samples hydrolysed at elevated temperatures. Overall, it appears that the interfacial changes are strongly related to the parallel extraction of silica with magnesium and the subsequent reprecipitation of silica through the reaction interfaces.

5.1.4 Influence of Partially Saturated Conditions on Extraction Rate of Magnesium and its Association with Reaction Interfaces

As reported in Chapter 4, and also as the discussion above in relation to kinetic analysis presented in Figure 5-3, some data were obtained under partially saturated conditions (e.g., Figure 4-2, Figure 4-11, and Figure 4-16) in which an initially (super)saturated product stream gives way to undersaturation. It is possible that the kinetics observed under these circumstances should not be compared with those where bulk saturation is not seen at any stage – however as the extraction continues under undersaturated conditions, the kinetics do clearly follow the clustered trend for completely undersaturated extractions. In order to further investigate this phenomenon, the dissolution profile at the so-called standard conditions which started above the saturation limit of magnesite and continued within the undersaturated conditions is considered. The initial nonstoichiometric quality of the dissolution profile is apparent through the observation of the measured rates, as presented in Figure 4-5. Brantley (2008) discussed that during the hydrolysing of silicates, the stoichiometric ratio potentially provides critical information about the alteration process of the silica layers on the reactive surface area. The more rapid release rate of the cations (e.g., magnesium) compared with silica commonly leads to the production of a leached layer on the mineral surface. This phenomenon is reported by many authors, such as Weissbart and Rimstidt (2000), who investigated wollastonite dissolution rate in acid solutions (pH in a range of 2 to 6) using a mixed flow reactor.

The Scanning Electron Microscopy coupled with the Energy Dispersive analysis (SEM-EDS) technique has been employed to examine the development of reaction layers and the composition of the post-leached grains obtained from standard dissolution conditions. The leached particles were embedded in an epoxy mould, cut and polished to allow for a cross-sectional view of the leached surface of the grains. Finally, all samples were carbon-coated with a thickness of 20-25 nm and analysed using scanning electron microscopy (SEM) in backscatter mode[1] to assess the compositional phases, along with energy dispersive spectroscopy (EDS) to measure the chemical composition. Figure 5-8 and Figure 5-9 demonstrate SEM images and the qualitative EDS analysis for the unreacted and post-leached particles, respectively. According to this analysis, the unreacted material has a uniform composition corresponding to unreacted thermally activated serpentine. However, zones closer to solid-fluid interfaces for the post-leached particles are relatively depleted in magnesium cation, and correspondingly enriched in silica. At the centre of the particle, the composition is seemingly unchanged from that found for the unreacted particles. It is noteworthy here that magnesium concentrations remained appreciable throughout the particles, which clearly suggests that the classical shrinking-core model with the rate controlled by product diffusion is indeed not the correct model for the rate of magnesium extraction.

---

[1] BSE (Secondary electrons are low energy electrons (< 50 eV) emitted due to the inelastic collisions between the beam electrons and the specimen electrons) was used to detect compositional differences, if the differences arise from a change in the atomic number.

In addition, spectrum (c) in Figure 5-9 provides additional evidence for the deposition of carbonate species close to the solid-fluid interfaces. Nevertheless, no apparent changes in the XRD profiles of the reacted particles were found (expect some apparent growth in the shoulder at 2θ ~60°, which certainly are not related to $MgCO_3$, as presented in Appendix E) suggesting that carbonate species could be deposited within an amorphous phase. Such a deposition may likely further impact the progress of the dissolution reaction by blocking the porosity and reducing the permeability features of the reaction/diffusion zones. On this basis, it is therefore plausible to postulate that the deposited carbonate phases in between the silica network may generate an apparent physical disjunction through the reaction interfaces – which could be responsible for the observed inconsistency in the normalised rates in the vicinity of the equilibrium, as shown in Figure 5-3.

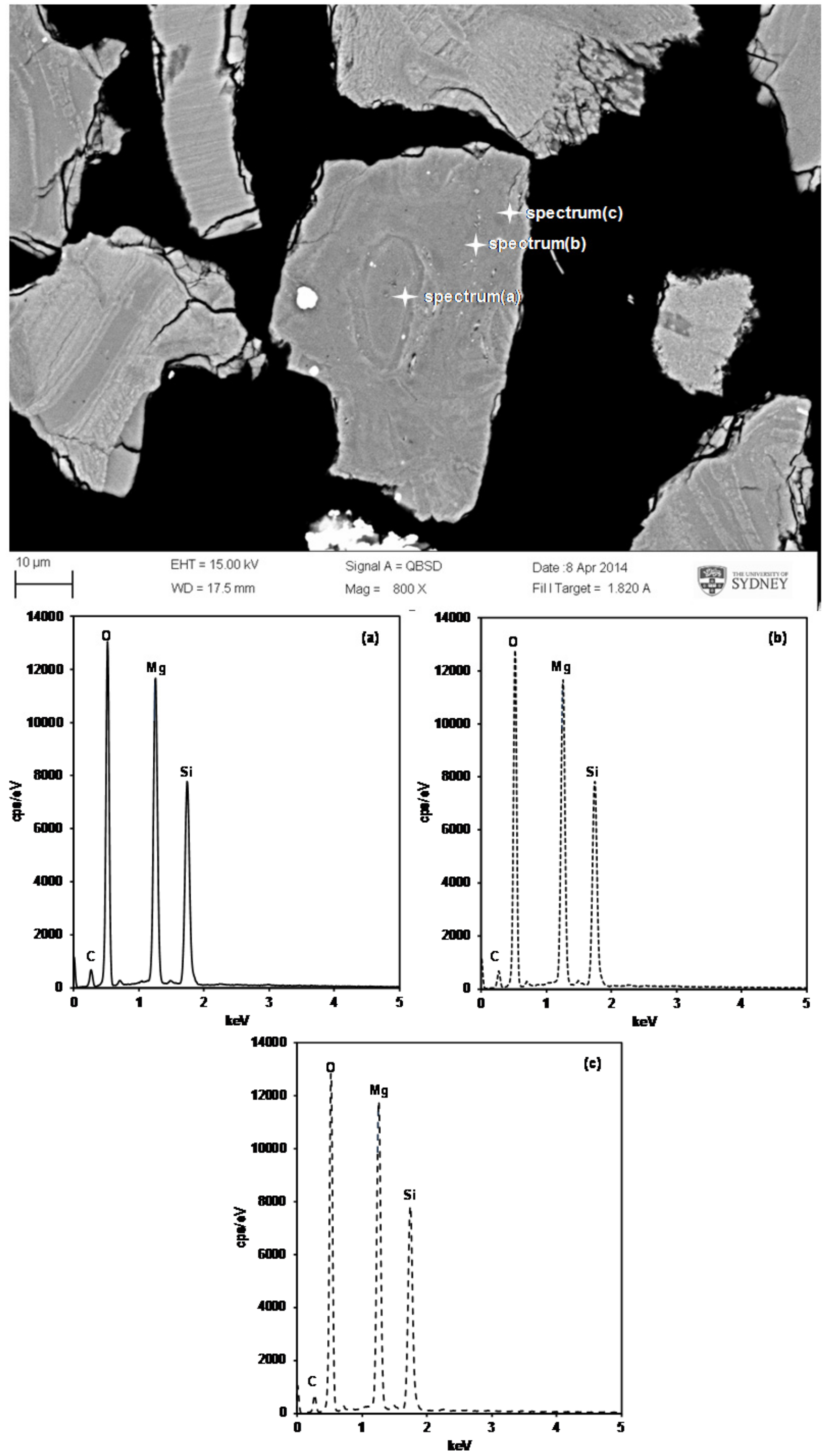

Figure 5-8. SEM micrograph (backscattered electron) and the corresponding EDS spectrums (a, b, and c) indicating to the elemental compositions of a polished section of an unreacted grain of activated SWOL (900 K, 120 minutes), attained by using Zeiss EVO/Qemscan instrument integrated with Oxford Instruments AZtec. There was no compositional gradient detected as indicated by EDS spectrums.

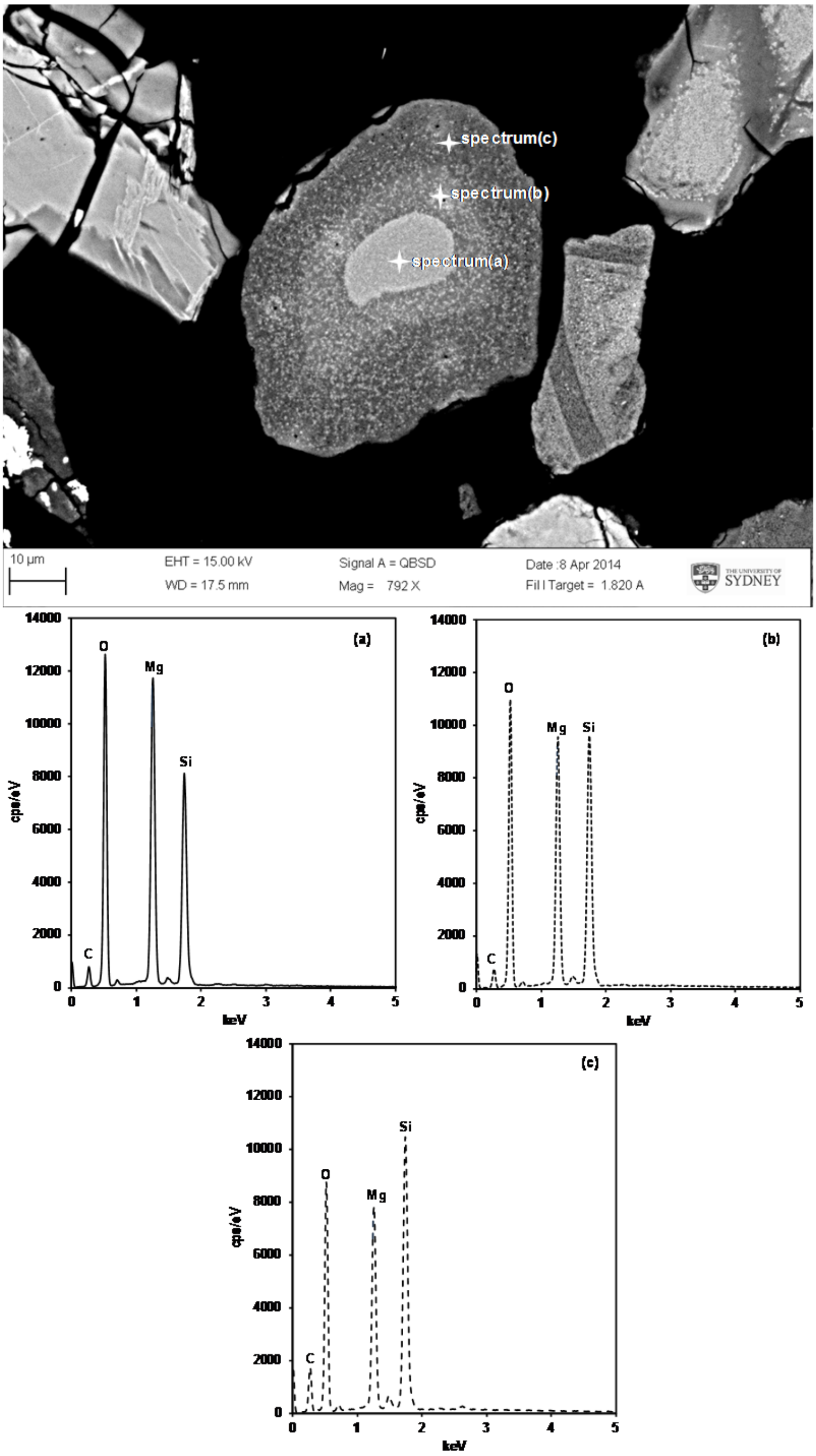

Figure 5-9. SEM micrograph (backscattered electron) and the corresponding EDS spectrums (a, b, and c) pointing to the elemental compositions of polished section of a post-leached grain (activated SWOL reacted under saturated CO_2-H_2O system at P_{CO2} = 100 bar, 423 K, 120 minutes), attained by using Zeiss EVO/Qemscan instrument. The darker outer-interface was relatively rich in silica as indicated by EDS spectrum (c).

5.1.5 Influence of Highly Saturated Conditions on Extraction Rate of Magnesium

Figure 5-3 demonstrates the influence of saturation on the rate of magnesium extraction[1] – as the degree of saturation increases, the extraction rate is highly suppressed (as indicated in Figure 5-3 by filled symbols). The effect of equilibrium appears across a broad range of the experimental conditions in Chapter 4 (e.g., relatively high mass loading in Figure 4-47). The relation between equilibrium and the fractional degree of magnesium extraction can be most directly seen through the experiments with variable mass loadings, as shown in Figure 5-10. In fact, it should be noted that the presented values for the degree of saturation in Figure 5-10, likely point to the typical heterogeneous saturation index rather than the homogeneous saturation of $MgCO_3$ – since the saturation index of pure magnesite in the solution is expected to hold a higher value. One may explain this phenomenon could be related to the uncertainties in the OLI-MSE prediction of the equilibrium solubility of magnesite, or it could be related to the local saturation index in the porosity of the particles rather than the saturation index in the bulk solution. Overall, the increase in the level of saturation is directly correlated with the decrease in the fractional extraction rate – this trend continues up to a point where the rise in saturation ratio nearly plateaus, and then this effect transfers to the rate, also appearing to follow with a more-or-less constant trend.

---

[1] At a selective degree of conversion of $X_{Mg} = 0.05$.

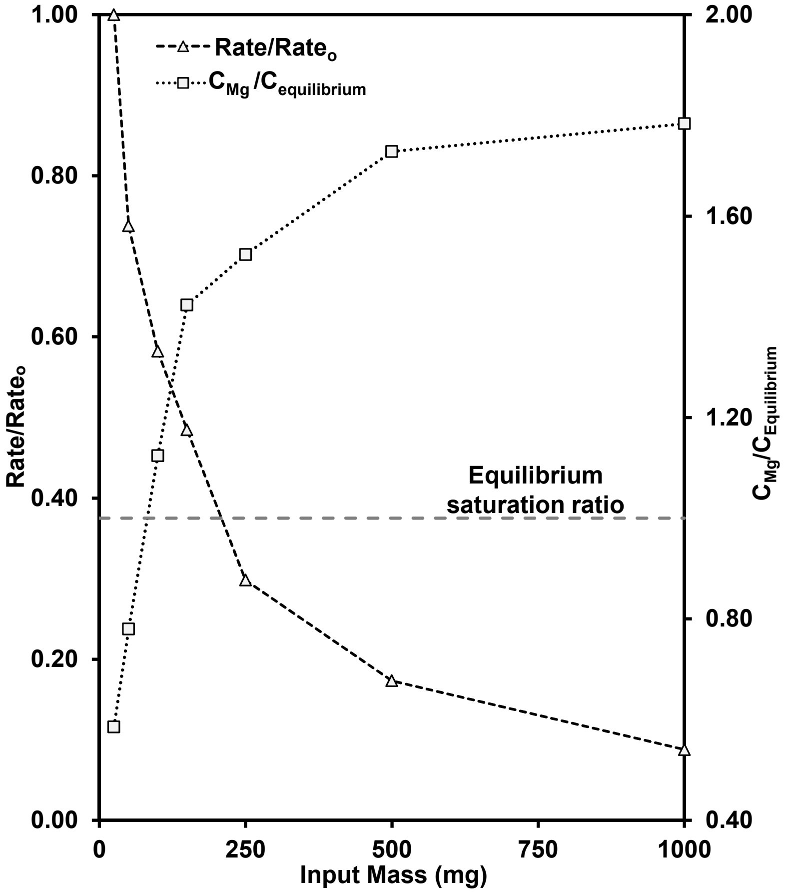

Figure 5-10. Variation of $C_{Mg}/C_{equilibrium}$ at $X_{Mg} = 0.05$, and $Rate/Rate_0$ ($Rate_0$ is related to the experiment with 25 mg mass loading) plotted against the variation of reactor mass loadings in the reactor – corresponding to mass loading factor from 0.03 to 1 min, as shown in section 4.6.

The slowest dissolution rate is, in fact, related to the highest mass loading (1000 mg) for which the fractional conversion is almost ten times slower than in the fastest case (25 mg). The inhibition effect of operating near saturation is also apparent through the experiments with variable reaction temperatures, as shown in Figure 5-11 and Figure 5-12. At reaction temperatures higher than 373 K, the concentration of magnesium in the aqueous leachate proceeds in the vicinity of the equilibrium saturation limit of $MgCO_3$ – this corresponds to the progressive decline in the fractional extent of magnesium extraction, as illustrated in Figure 5-12.

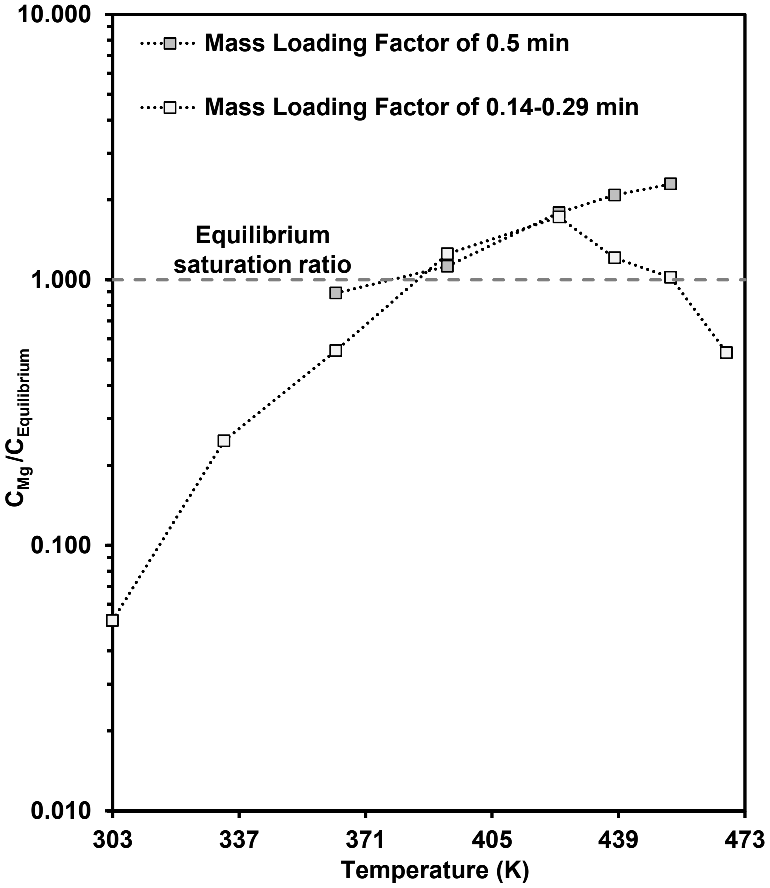

Figure 5-11. Variation of $C_{Mg}/C_{equilibrium}$ at $X_{Mg} = 0.05$ plotted against the different reaction temperatures for two sets of experiments with a constant mass loading factor of 0.5 min, and variable mass loading factors from 0.14 to 0.29 min, as shown in section 4.4.

At highly saturated conditions, the fractional extent of magnesium extraction is ~9 times lower compared with the experiments carried out at undersaturated conditions. As the dissolution reactions proceed at/or close to supersaturated conditions, the reduction in the fractional extent of conversion likely results from the decrease in the incentive driving forces for further leaching of magnesium cations as the solution has already become supersaturated with aqueous magnesium species – therefore increasing the chance of formation of some stable magnesium carbonates. However, no evidence for such homogeneous formation of carbonate species has been found.

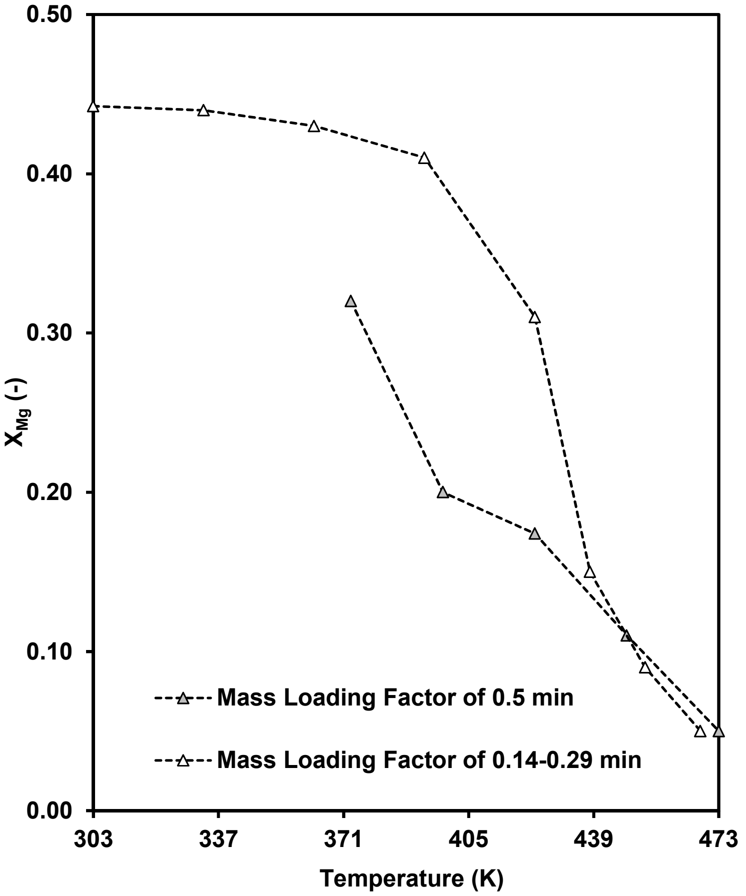

Figure 5-12. Variation of X_{Mg} (t = 1800 s) plotted against the different reaction temperatures for two sets of experiments with a constant mass loading factor of 0.5 min, and variable mass loading factors from 0.14 to 0.29 min, as shown in section 4.4.

Previous studies of forsterite carbonation (e.g., Giammar et al., 2005) have also attributed the decrease in the apparent aqueous magnesium concentration is related to the phase transformation of the aqueous magnesium compounds to stable solid magnesite. Similary, Mann (2014) postulated that, under the carbonic acid system, the reduction in the extraction rate of magnesium at relatively high-temperature conditions is correlated with the phase transformation of aqueous magnesium to stable solid carbonates. However in the present study, TPD analyses of the residual solids after extraction at supersaturated conditions verified that the mass of such carbonate is very small. On the other hand, the SEM-EDS spectra in Figure 5-9 show a clear evidence of carbon (presumably as carbonate) near the surface of the extracted mineral. In order to further evaluate this effect, a series of static dissolution experiments for residual solids acquired from the experiments under supersaturated conditions was carried out using high purity water under nitrogen at room temperature – since samples which had not been leached gave up no magnesium under these conditions, it is presumed that any magnesium entering the solution from leached particles is in a more-or-less soluble form i.e., as magnesium carbonate species into the porous substrate of particles. After the equilibrium period of 10 days, analysis of the obtained leachate indicated that ~1% of the unextracted magnesium content of the reacted particles under supersaturated conditions was deposited in the form of magnesium carbonate species through the porous substrate within the particles.

In order to extract a feasible conclusion from these observations, it is worth reviewing the available literature in this context. Giammar et al. (2005) conducted a series of batch experiments of acid digestion that simultaneously exposed a reacting forsterite mineral with water, and a supercritical CO_2 phase at pressures up to 100 bar and temperature up to 368 K. They observed that despite the highly saturated conditions, after a period of 14 days magnesite precipitation was not achieved in the solution, rather than discrete crystals associated with the forestrite surface. The reluctance of magnesium carbonate to form in the solution can be attributed to the strong hydration properties of small magnesium ions (Sayles and Fyfe, 1973). Giammar et al. (2005) reported that the rate-limiting step in the formation of magnesite in the solution is related to the initiation of the nucleation process. The precipitation of the solid phase consists of the two separate processes of nucleation and growth. Nucleation may occur homogeneously in the solution or heterogeneously at the mineral-water interface. This process is highly influenced by the degree of saturation of the solution with respect to a particular phase (e.g., $MgCO_3$); accordingly, many authors (e.g., Nancollas and Purdie, 1964, Steefel and Van Cappellen, 1990) stated that at supersaturation conditions, it would be theoretically possible for precipitation to initiate and overcome of all the nucleation and growth barriers.

In this regard, Nielson (1964) argued that the presence of a foreign surface could be employed for greater control over nucleation, since the interfacial energy between a crystal nucleus and a solid substrate is usually lower compared with crystal formation from the solution (Nielsen, 1964). Thus, the formation of stronger bonds with those in the substrate compared with the bonds of solvation is anticipated. Also, De Yoreo and Vekilov (2003) explained that nucleation initiates through the formation of small nuclei of the new phase, inside of the relatively larger volume of the old phase. At the same time, the strength of bonding at the interface is highly dependent on the structure and chemistry of the substrate surface (De Yoreo and Vekilov, 2003).

In the context of mineral-fluid dissolution, the development of porosity is assumed to follow the dissolution-reprecipitation mechanism. This mechanism may allow saturated fluids, with respect to certain phases, to be transported through rock without crystallising until the branched porosities are connected. According to Putnis and co-workers, the threshold saturation state (K_{sp}) required for nucleation and growth in the bulk fluid is usually higher than the fine porosities (Putnis et al., 1995, Putnis and Mauthe, 2001, Mukai et al., 2014). Hence, increasing the saturation level induces crystallisation/precipitation in fine porous media. In this respect, Daval et al. (2009b) reported that during the carbonation process of wollastonite under the carbonic acid system, due to the occurrence of *in situ* carbonation products in the wollastonite-silica interfacial region along with generation of carbonation coating on particles the reaction layers become passivating. Kwak et al. (2011) investigated the reaction layers of the reacting forsterite under a supercritical CO_2-H_2O system using TEM and NMR techniques. Likewise, they reported that at the saturation conditions, a layer comprising magnesite and amorphous silica is formed on forsterite reaction layers. The rate-limiting feature of *in situ* precipitation of stable carbonate species during the carbonation of forsterite has also been reported in other studies (e.g., McKelvy et al., 2003, Andreani et al., 2009) where carbonation products created a physical disjunction through the reaction interfaces.

Comparing the surveyed literature and the present experimental observations suggests that, in spite of the relatively insignificant amount of *in situ* carbonates precipitation on the residual solids in the reactor (confirmed by TPD analysis), the nucleation of magnesite most likely occurs through the porous substrate under the supersaturated conditions. If such reactions occur, it would be associated with a number of implications. First, the plateau behaviour of the measured rates (identical to the supersaturation conditions, such as those presented in Figure 4-37) is likely attributed to the equilibrium of carbonation products deposited (as results of both nucleation and crystal growth of carbonate phases) into the porous substrate within the particles. In addition, at the saturation conditions the deviation of the shape of the rate function $f(X)$ from the proposed pH dependence mechanism (as indicated by the filled symbols in Figure 5-3) would be correlated with a physical interference – since *in situ* formation of carbonates may likely render physical barriers through the reaction interfaces. These effects would influence the properties of the reaction interfaces and their corresponding volumes.

Structural Properties of Post-leached Particles

Studying changes in the properties (chemical and physical) of the mineral surface is important for understanding the dissolution process. This approach can potentially provide information about the alteration process occurring throughout the reaction interfaces. The SEM-EDS technique was used to visualise the solid particles and examine the chemical composition of the particles surfaces. The post-leached products from the undersaturated and supersaturated experiments were collected and air-dried. The solid samples were mounted on an aluminium stud using double-sided sticky tape and then carbon coated to a thickness of 20-25 nm. Backscattered electron (BSE) images for the unreacted particles (thermally activated SWOL), residual solid obtained from the experiment carried out at 373 K corresponding to undersaturated conditions, and residual solids from the experiment performed at 473 K corresponding to supersaturated conditions are shown in Figure 5-13, Figure 5-14, and Figure 5-15, respectively.

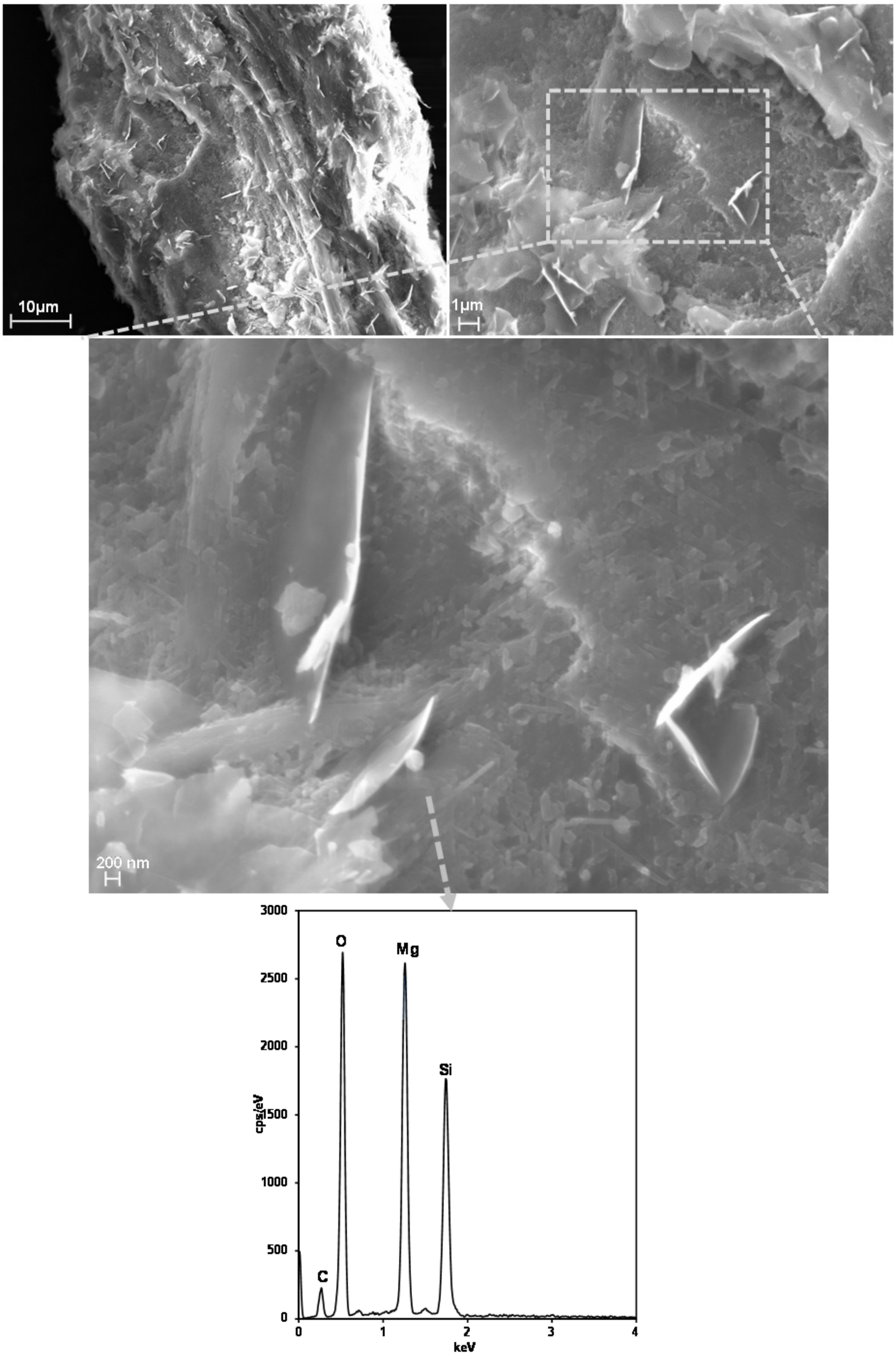

Figure 5-13. SEM micrograph (backscattered electron) and the corresponding EDS spectrums indicating to the chemical compositions of the surface of a thermally activated SWOL grain, attained by using Zeiss Ultra Plus instruments at an accelerating voltage of 15 kV.

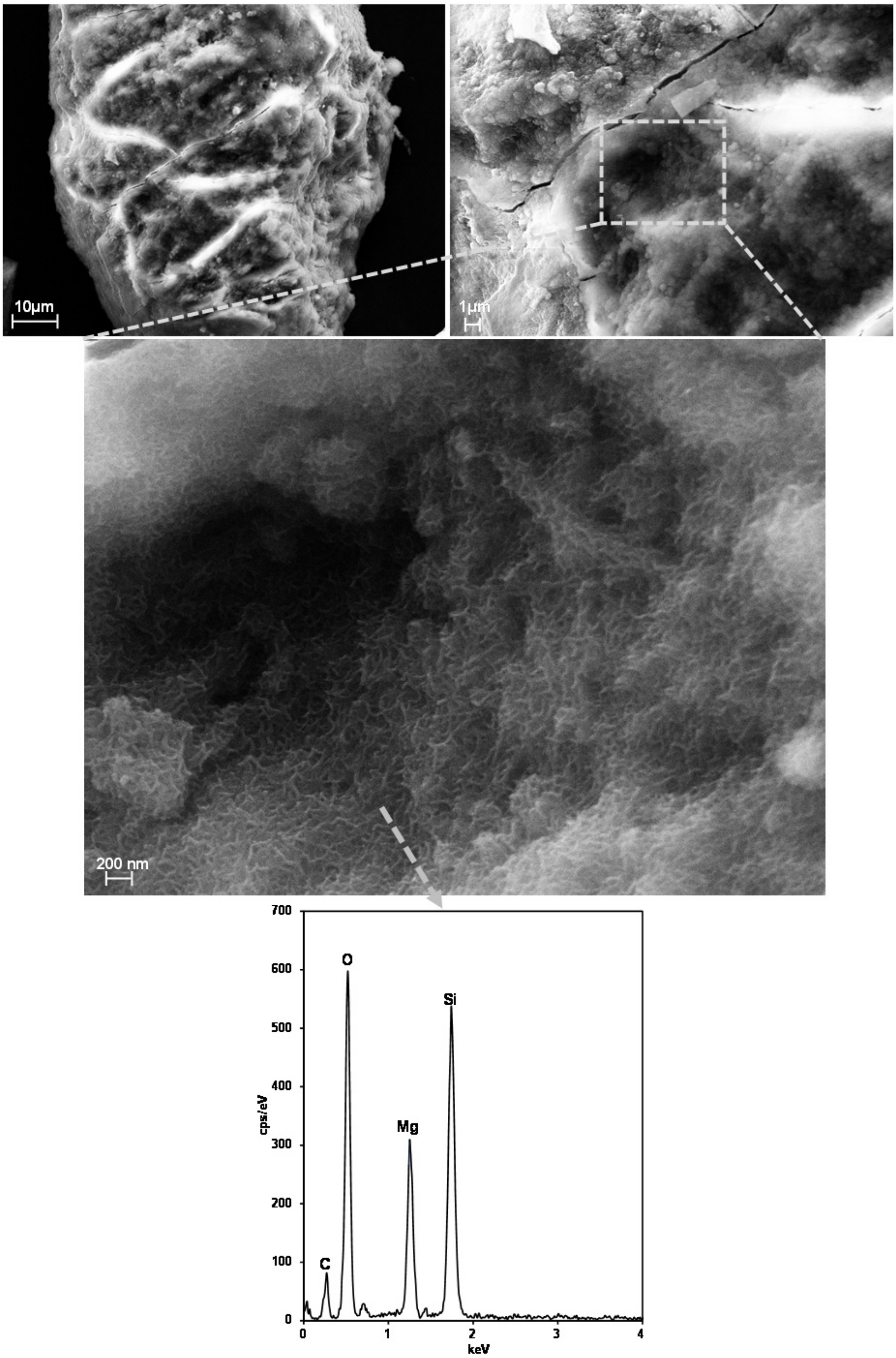

Figure 5-14. SEM micrograph (backscattered electron) and the corresponding EDS spectrums indicating to the chemical compositions of the surface of a post-leached grain (activated SWOL reacted under P_{CO2} = 100 bar, T = 373 K, 30 minutes) corresponding to undersaturated conditions, attained by using Zeiss Ultra Plus instruments at an accelerating voltage of 15 kV.

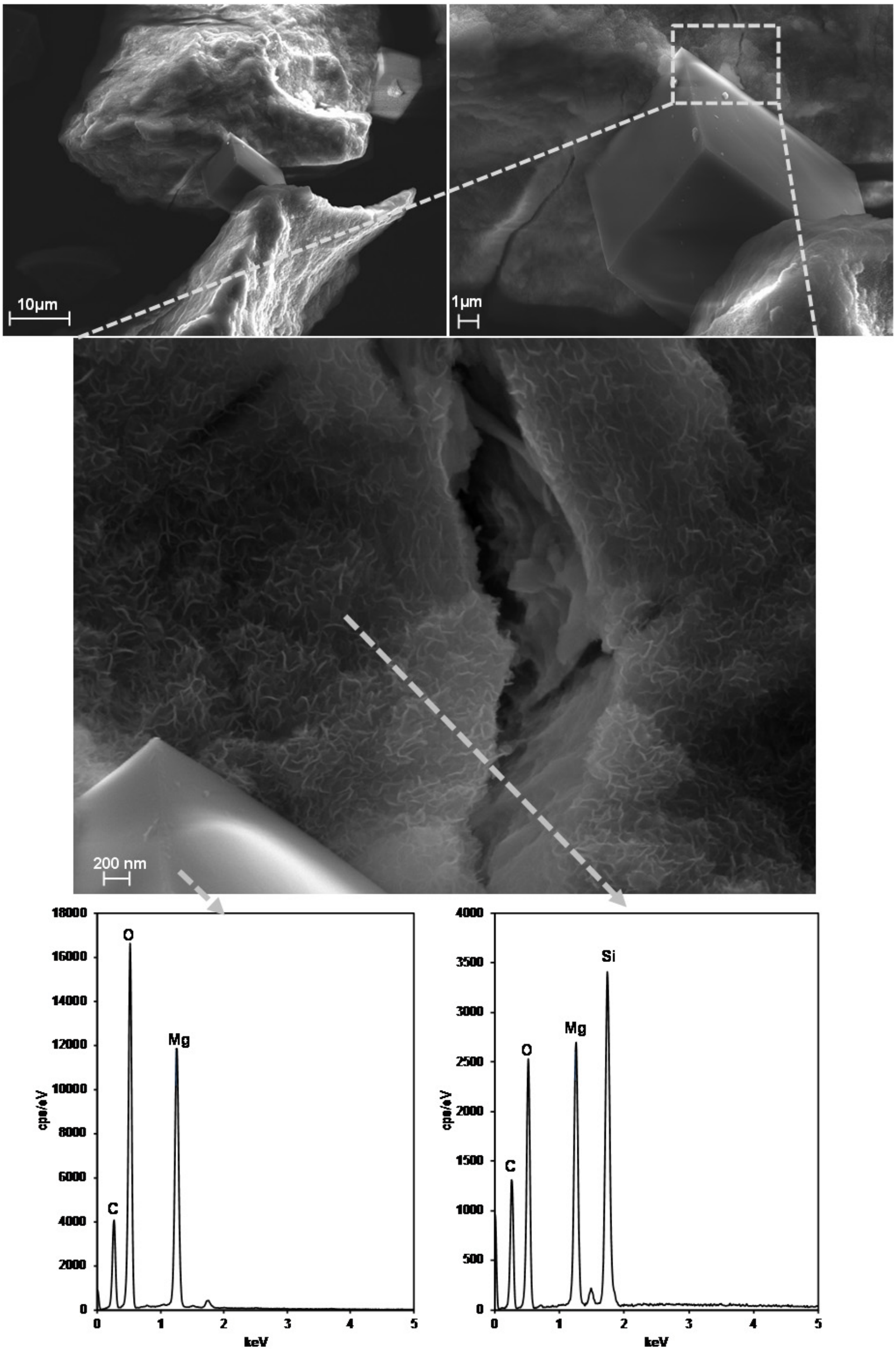

Figure 5-15. SEM micrograph (backscattered electron) and the corresponding EDS spectrums indicating to the chemical compositions of the surface of a post-leached grain (activated SWOL reacted under P_{CO2} = 100 bar, T = 473 K, 30 minutes) corresponding to supersaturated conditions, attained by using Zeiss Ultra Plus instruments at an accelerating voltage of 15 kV. The strong Mg and O signals are associated with the product crystals (magnesite), whereas a strong Si and O are related to the composition of the surface layer.

Comparison of surfaces of the particles indicates that after the dissolution reaction the surfaces were transformed into sponge-like structures, containing various pores in a nanometre scale. This analysis once more showed that the surface of the post-leached particles is relatively rich in silica and depleted of magnesium. The surfaces of the particles under both saturated and undersaturated conditions show cracks and opened etch pits. The undersaturated conditions produced relatively small etch pit development, consisting of etch pits up to ~5 μm in diameter; no evidence for surface precipitation of magnesite is noted. In contrast, the exclusive surface feature of the particles reacted under the supersaturation conditions indicates the occurrence of a new phase throughout its structure. Separate crystals with a different chemical composition corresponding to magnesite (high Mg and O signals) appear to have formed which seemingly become entrapped through the silica layers. In addition, it appears that the shape of newly growth crystals is very similar to the morphology of magnesite. Under the supersaturated conditions deposition of carbonate phases through the silica surface layers is also evidenced by the relatively higher carbon spectrum in Figure 5-15.

Observations of these morphological alterations imply that the status of saturation should significantly influence the overall volume associated with the reaction interfaces of the particles. Hence, a series of porosimetry analyses were carried out to evaluate the effect of saturation state on reaction interfaces associated with the porosity of the substrates, as shown in Table 5-2. These analyses were performed by using the multipoint BET method[1]. In this method, N_2 adsorption and desorption isotherms were measured at the temperature of liquid N_2 (77 K) by employing a surface area analyser (Quantachrome Autosorb-1). The samples were degassed at a temperature of 423 K for 12 hours under vacuum (~10^{-3} Torr) prior to each analysis.

---

[1] The presented measurements were accurate up to ±10%.

Table 5-2. Summary of BET, porosimetry measurements of the surface area, total pore volume and average pore size, and fractional degree of magnesium and silica extraction for the unreacted mineral (thermally activated SWOL), and residual solids obtained under the indicated experimental conditions.

Material	Surface area ($m^2\ g^{-1}$)	Total Volume ($cm^3\ g^{-1}$)	Average Pore Size (Å)	X_{Mg}	X_{Si}
Unreacted*	11.96	0.02	69.45	-	-
Partially Saturated**	128.35	0.11	34.30	0.28	0.12
Saturated**	90.78	0.07	32.15	0.17	0.05
Supersaturated***	44.25	0.03	31.39	0.06	0.03

**Activated SWOL (900 K, 2 hours)*

***Post-leached Particles acquired from 30 minutes dissolution reactions at* P_{CO2} *=100 bar, and T = 423 K; mass loading factor of 0.25 and 0.5 min, for partially saturated (* $C_{Mg} \geq C_{equlibrium}$*) and saturated experiments (*$C_{Mg} > C_{equlibrium}$*), respectively.*

****Post-leached Particles acquired from 30 minutes dissolution reactions at* P_{CO2} *= 100 bar, and T = 473 K, mass loading factor of 0.5 min (*$C_{Mg} \gg C_{equlibrium}$*).*

This analysis shows that pore volume seems to be directly related to the extent of extraction of magnesium and silica – this attribute can be seen through the almost linear relation of pore development to the fractional degrees of extraction of magnesium and silica, as shown in Figure 5-16. In addition, the trend of pore development can be seen in the pore size distribution curves presented in Appendix H. Under the supersaturated conditions, reprecipitation of leached magnesium could inhibit the progress of the reaction at the very early stages – which could result in the pores not opening up.

On the other hand, under the conditions where the extraction of magnesium appears to be relatively higher, (e.g., partially saturated conditions), concurrent dissolution-reprecipitation of silica into the generated reaction pathways may ultimately contribute to the blocking of the porous substrate. Considering both scenarios, one may conclude that the deposition of any carbonate phases at the initial stage of the dissolution reaction through the pore pathways or/on the reaction sites of the particles can significantly influence the extraction of both magnesium and silica.

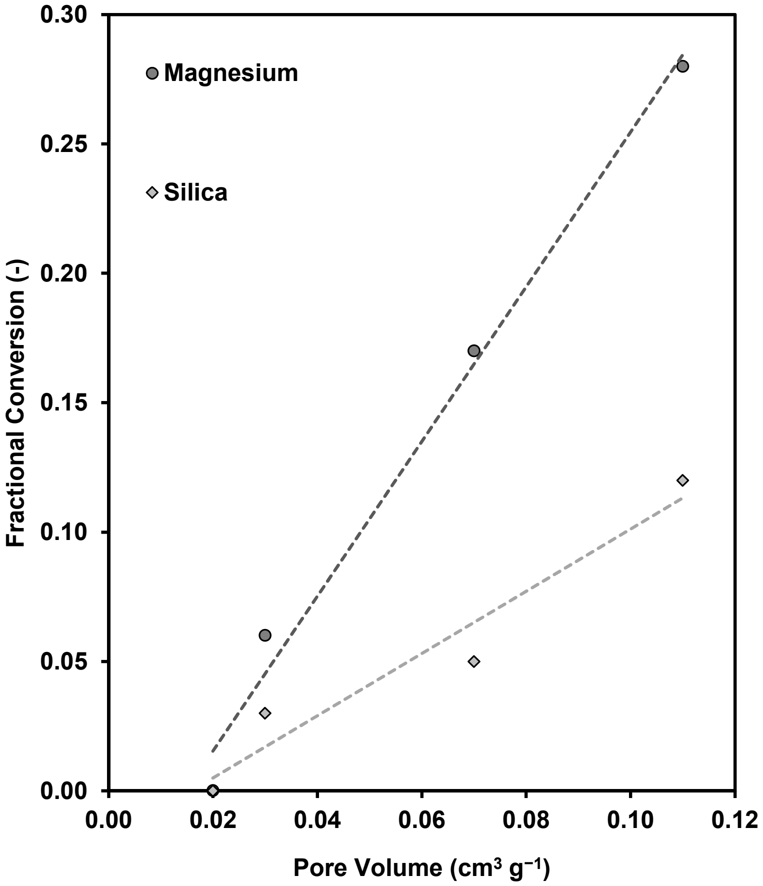

Figure 5-16. Variation of particles pore volume plotted against the fractional extent of magnesium and silica extraction for the experiments indicated in Table 5-2, the dashed lines represent the linear least square curve fit showing the correlation of magnesium and silica data points, respectively.

Combining these observations with the SEM images in Figure 5-15, further supports the suggestion that the nucleation and growth of magnesium carbonate species throughout the reaction zones are likely responsible for the reduction in the extraction rates – possibly restricting the interdiffusion of reactants and reaction products across the reaction interfaces. In this study, *in situ* determination of the associated carbonate phases is not pursued. Nonetheless, the important lesson from the present analysis is to distinguish the thermodynamic limitations between the different dissolution regimes.

5.2 Summary of Discussion

In the context of the mineral carbonation process, these observations underline that the kinetics of magnesium extraction under the carbonic acid system is very sensitive to equilibria involved in the system and highly inhibited under the supersaturated conditions. Whilst one may emphasise that the extraction of magnesium is favourable at undersaturated conditions (far-from-equilibrium). The unification of undersaturated data normalised by the local equilibrium concentration suggests that the reaction rate is more-or-less proportional to the bulk concentration of the protons in the solution. The declining trend in the undersaturated rates, which reflects how the liberation of magnesium slows as the reactions progress, is likely correlated with reconstruction of the reaction interfaces by reprecipitation of silica species. The average form of the rate function appears to be in agreement with the product layer diffusion control shrinking core model – however the lack of sensitivity to particle size accounts as a strong contrary evidence. Perhaps an alternative model should be similar to the grain models that can describe nonlinear reaction rates while also having little dependence on particle size.

Chapter 6. Conclusions and Recommendations for Future Work

6 Conclusion

The understanding of the dissolution characteristic of thermally activated serpentine under the carbonic acid system is perceived to play a significant role in the success of the serpentine-based mineral carbonation process. The present study set to investigate the kinetics of magnesium extraction from thermally activated serpentine under the additive-free carbonic acid system, with a view to elucidating the underlying mechanism.

The equilibria in the carbonic acid system become more complex in the presence of metal cations. The magnesium content of the activated mineral is leached by the protons associated with the $MgO-CO_2-H_2O$ equilibria. The availability of protons is inhibited by the accumulation of magnesium in the aqueous phase, as the extraction proceeds. Thus, the extraction of magnesium from this system can be termed a self-inhibited process. From the OLI-MSE thermodynamic modelling, it was found that this trend prevails up to the saturation of the solution with respect to the equilibrium solubility of $MgCO_3$, beyond which there would be no change in the equilibrium pH. The simulated reaction pathways in the $MgO-CO_2-H_2O$ system showed that under the standard reaction conditions (T = 423 K and P_{CO2} = 100 bar), the predicted equilibrium molal solubility of magnesite is C_{Mg} ~0.0197 mol kg^{-1} and the corresponding pH is 5.3. It should be noted that, from the surveyed literature, $MgCO_3$ was considered as the most stable carbonate phase forming in the $MgO-CO_2-H_2O$ system.

The detailed concentration profiles of the extraction rates for magnesium and silica were measured using a continuous fluidised bed reactor under the saturated CO_2-H_2O system. The composition of the solution at discrete kinetic intervals was measured and compared with the corresponding saturation states of the solution in which new phases will be produced (rendered by OLI-MSE calculations). Also, the detailed profiles of the extraction rates as a function of the extent of conversions were obtained. Although reporting the fractional conversion of extraction is not accounted as a conclusive objective of the current study – it is worth noting that under the standard reaction conditions (T = 423 K, P_{CO2} = 100 bar, and τ_m = 0.25 min), the degrees of completion of magnesium and silica were found to be approximately 65% and 40%, respectively, within a 120 minutes reaction period.

Experiments were carried out over a wide range of conditions, covering different reaction temperatures (from 303 to 473 K), pressures (from 10 to 160 bar), mass loading factors (from 0.03 to 1 min), and particle sizes (from 20 to 180 μm). The higher concentrations of magnesium in the effluent corresponded to higher rates of extraction in the reactor. However, at sufficiently high rates, concentrations were found to be limited by the equilibrium solubility of $MgCO_3$ – although no evidence for $MgCO_3$ particles in the effluent or/in the reactor was found. It was, therefore, concluded that the corresponding solid magnesium carbonate species must be associated with the mineral particles rather than with the homogeneous formation of solid carbonates from the solution. The kinetic implications of the entire set of experimental data for magnesium extraction were evaluated through a pH-dependent expression that is expected to be valid for far-from-equilibrium conditions, given by expression (6.1),

$$\frac{dX_{Mg}}{dt} = k_{H^+}\,[H^+]^n e^{-E_a/RT} f(X) \tag{6.1}$$

From these analyses, three distinct regimes were identified – undersaturated, partially saturated, and supersaturated conditions.

6.1 Kinetic Implications

The kinetic implications of the measured rates were expressed through master plots showing the form of the rate function $f(X)$ versus the fractional extent of conversion. For the undersaturated conditions, the rates at a particular value of X_{Mg} ~0.25 showed a minimum standard deviation with $n \cong 1$ and also implied that $E_a \approx 0$ – suggesting that the rates at undersaturated conditions are directly proportinal to the bulk aqueous activity of protons, and more importantly, regardless of the specific experimental conditions, the consensus of the undersaturated data indicated negligible activation energy. This result differs from prior findings for the dissolution of crystalline serpentinite (e.g., $n \cong 0.53$ and $E_a \approx 10$ kcal mol^{-1} (Daval et al., 2013a)), perhaps reflecting the fact that the activated material used in this study is amorphous rather than crystalline.

Partially saturated conditions were defined as those in which the concentration of magnesium in the effluent at early stages of the reaction reached or even exceeded that corresponding to the saturation of $MgCO_3$. In these cases, there was an apparent disjunction between data obtained above and below the calculated equilibrium solubility of $MgCO_3$. At sufficiently high values of the effluent magnesium concentration relative to the equilibrium solubility (~1.5-2 times), the extraction rate is limited by the equilibrium solubility not only in the early phases of reaction, but also at greater extents of conversion. These "fully saturated" reaction conditions appear to be associated with a very different rate-limiting mechanism.

6.2 Implications for the Dissolution Model

Comparison of the mean form of rate functions $f(X)$ for undersaturated data with the classical shrinking core models indicated that the product layer diffusion control shrinking core model seems to provide a relatively good description. However, due to the lack of sensitivity to particle size, it was concluded that this model cannot be correct. In fact, the results presented for the variation of particles size (within a factor of nine), suggesting a surprising outcome as the reaction rates appeared to be independent of the external surface area of the particles. An additional complex factor in the interpretation of the data was related to the initial saturation state of many reactions – since deposition of the carbonate species through the pores of the particles may have determined the subsequent kinetics results. It was noted, however, that as the extractions continued and proceeded at the undersaturated conditions, the rates followed with the common clustered for all the undersaturated data.

Hence, an alternative model was suggested; a grain model incorporating diffusion of the reactant through the internal spaces between the grain boundaries, with the reaction occurring at the individual grains. Such a reaction pathway should lead to the development of internal porosity as the reaction proceeds (and silica is also extracted), but the solids, in fact, develop very little pore volume. This gave rise to the idea that a significant restructuring process was probably involved during the dissolution of the particles. The observation of the post-leached particles acquired from the standard dissolution reaction through SEM images further indicated the existence of surface restructuring phenomenon.

The dissolution and reprecipitation of the silica inside the internal reaction interfaces and/or on the outer surface of the particles were considered to be responsible for the surface restructuring process. The dissolution profiles of silica indeed provide sufficient implications to support interfacial evolution. The relatively high concentration of silica in the aqueous leachate observed for numerous experimental cases implied that the amorphous silica was reprecipitated on the reacting surfaces – similar to the dissolution-reprecipitation mechanism outlined and stressed by Hellmann et al. (2015) and Putnis (2015).

On the other hand, under the supersaturated conditions (with respect to equilibrium solubility of $MgCO_3$), the dissolution and reprecipitation of the leached magnesium further inhibited the extraction of magnesium. This was considered the basis for the magnesium concentration being limited by equilibrium. The SEM-EDS analyses verified the formation of magnesite species through the silica-rich layers at the mineral surface. Depositions of stable carbonates likely rendered physical barriers through the reaction zones – thus play an important role in restructuring the reaction surfaces.

On the whole, this study investigated the kinetics of magnesium extraction at a broad range of conditions including far-from-equilibrium and close to equilibrium. Under the supersaturated (close to equilibrium) conditions, parallel precipitation and deposition of carbonate species through the reaction interfaces of the solid/fluid inhibit the process of magnesium extraction. As a result, interdiffusion of the reactant and reaction products through the network of the porous substrate within the particles is expected to be significantly restricted. In addition, it is understood that the reactions associated with the dissolution and reprecipitation of silica species further influence the extraction of magnesium at undersaturated conditions by limiting the transport of active aqueous species between the reaction interfaces and the external fluid.

6.3 Recommendations for Future Research

While this study has attempted to contribute and elucidate the underlying mechanisms involved in the extraction of magnesium from thermally activated serpentine under the carbonic acid system, there are areas that require further investigation. The following sections provide suggestions for future work.

6.3.1 Dissolution under Non-equilibrium Conditions

The presented experimental results and kinetic analysis have motivated additional questions regarding the understanding and quantification of several reactions and factors (e.g., the effect of pressure, temperature and particle size) influenced by the equilibrium conditions. In fact, non-equilibrium behaviour seems interesting as the potential complicating effects of stable carbonate interactions during the dissolution process are simplified – this could be an important subject for further studies. In this regard, obtaining detailed knowledge of the transition behaviour of the dissolving surfaces along with the precipitation of the reaction products could also be pursued in future research – utilisation of *in situ* spectroscopic techniques (e.g., Raman and Infrared Spectroscopy) could potentially provide additional information regarding the surface-association and nucleation of secondary carbonate phases throughout the porosity features of reacting minerals under the carbonic acid system. The formation of reaction intermediates and final products such as magnesite could be identified as function reaction conditions (e.g., temperature and pressure).

6.3.2 Surface Characterisation

In a first instance, the dissolution reaction is believed to initiate from the surface coordination of the reactants (e.g., protons) which polarise and weaken the metal-oxide bonds on the reactive surfaces of the particles surface. In almost all cases, the non-congruent dissolution reaction has been observed with respect to magnesium components. After a period of some time, this trend readjusts itself towards more stoichiometric dissolution. This may explain why, as the thickness of the surface layers seemingly increase – thus, the rate of hydration of the unreacted mineral is likely reduced. The presented experimental results under the undersaturated conditions (not influenced by equilibrium conditions) thus provide evidence for this quality of the surface. Nevertheless, the preceding dissolution leaves little hesitation that a decrease in the diffusional transport of the aqueous reactant through the possible thick surface layers leads to the decline, and ultimately, the stop of the extraction of magnesium.

Further insight into the importance of reaction interfaces could be determined by studying the associated dissolution and reprecipitation reactions of silica – such an approach may also provide useful data for elucidating the reaction mechanism. The results presented in this study provide indirect evidence as to how the rate of magnesium extraction declines with time, perhaps as the silica surface layers become thicker and disconnect the network of reaction interfaces. The present analysis of the post-leached surfaces appear partially concurs with the universal dissolution-reprecipitation mechanism, as regions close to the solid/fluid surfaces were relatively enriched in silica. However, according to the prior research, the dissolution-reprecipitation behaviour is associated with the generation of high porosity; whereas this was not found within the considerable extent in the current observations. In the context of a grain model, such a reprecipitation of amorphous silica into the interfacial reaction pathways render them passivating. On the other hand, highly saturated conditions of silica in the aqueous leachate may further complicate the interpretation of the measured rates as they almost always indicate to the simultaneous reprecipitation of silica.

Therefore, it is recommended that as a first step the rate and extent of silica dissolution should be determined under well-controlled conditions with respect to parameters (e.g., temperature) that influence the equilibrium solubility of amorphous silica. Further characterisation of the physical and chemical properties of the altered surface layers of the particles via techniques such as secondary ion mass spectrometry (SIMS) along with advanced high-resolution transmission electron microscopy (HRTEM) would also shed some light on the mechanisms of the reactions involved in the dissolution process.

6.3.3 Hydration Rate of CO_2

In the present study, the effect of CO_2 molality is experimentally evaluated on magnesium extraction rates. It was found that the presence of an extra amount of supercritical CO_2 phase did not have any considerable effect on the kinetics of magnesium extraction, and, in fact, the carbonic acid system appeared always behave according to equilibrium expectations. Many studies have been dedicated to the investigation of the rate-limiting step involved in the dissolution of CO_2 in the aqueous solution, which is applicable to various fields of science (e.g., Khalifah, 1971). In the context of mineral carbonation, the rate-limiting characteristic of CO_2 hydration in the aqueous phase examined by Smithson and Bakhshi (1973) – who found that this step is rate-limiting for carbonation of MgO slurries at a reaction temperature of 311 K (Smithson and Bakhshi, 1973). Furthermore, Lasaga (1984) stated that the slow hydration rate of carbonic acid appears to be a rate-limiting factor throughout the weathering process. The present results show that the reduction in the relative extent of reaction throughout the depth of reactor in the presence of extra CO_2 may indicate the slow hydration rate of CO_2 in the aqueous phase. It is thus suggested that additional research in this area would be useful for the future application of the mineral carbonation process.

References

AAGAARD, P. & HELGESON, H. C. 1982. Thermodynamic and kinetic constraints on reaction rates among minerals and aqueous solutions; I, Theoretical considerations. *American journal of Science,* 282**,** 237-285.

ALEXANDER, G. B., HESTON, W. & ILER, R. K. 1954. The solubility of amorphous silica in water. *The Journal of Physical Chemistry,* 58**,** 453-455.

ANDREANI, M., LUQUOT, L., GOUZE, P., GODARD, M., HOISE, E. & GIBERT, B. 2009. Experimental study of carbon sequestration reactions controlled by the percolation of CO_2-rich brine through peridotites. *Environmental Science & Technology,* 43**,** 1226-1231.

ARUJA, E. 1945. An X-ray study of the crystal structure of antigorite. *Mineralogical Magazine,* 27**,** 65-74.

BACHU, S., BONIJOLY, D., BRADSHAW, J., BURRUSS, R., HOLLOWAY, S., CHRISTENSEN, N. P. & MATHIASSEN, O. M. 2007. CO_2 storage capacity estimation: methodology and gaps. *International Journal of Greenhouse Gas Control,* 1**,** 430-443.

BALES, R. C. & MORGAN, J. J. 1985. Dissolution kinetics of chrysotile at pH 7 to 10. *Geochimica et Cosmochimica Acta,* 49**,** 2281-2288.

BALES, R. C., MORGAN, J. J. & ANDREW, W. 1985. *Surface chemical and physical behavior of chrysotile asbestos in natural waters and water treatment.* California Institute of Technology.

BARNES, V. E., SHOCK, D. A. & CUNNINGHAM, W. A. 1950. *Utilization of Texas Serpentine,* Austin, Univ. of Texas.

BÉARAT, H., MCKELVY, M. J., CHIZMESHYA, A. V. G., GORMLEY, D., NUNEZ, R., CARPENTER, R. W., SQUIRES, K. & WOLF, G. H. 2006. Carbon Sequestration via Aqueous Olivine Mineral Carbonation: Role of Passivating Layer Formation. *Environmental Science & Technology,* 40**,** 4802-4808.

BÉNÉZETH, P., SALDI, G. D., DANDURAND, J.-L. & SCHOTT, J. 2011. Experimental determination of the solubility product of magnesite at 50 to 200°C. *Chemical Geology,* 286**,** 21-31.

BERNER, R. A. 1978. Rate control of mineral dissolution under earth surface conditions. *American journal of Science,* 278**,** 1235-1252.

BERNER, R. A., LASAGA, A. C. & GARRELS, R. M. 1983. The carbonate-silicate geochemical cycle and its effect on atmospheric carbon dioxide over the past 100 million years. *Am. J. Sci,* 283**,** 641-683.

BLENCOE, J. G., PALMER, D. A., ANOVITZ, L. M. & BEARD, J. S. 2012. Carbonation of metal silicates for long-term CO_2 sequestration. Google Patents.

BLUM, A. E., YUND, R. A. & LASAGA, A. C. 1990. The effect of dislocation density on the dissolution rate of quartz. *Geochimica et Cosmochimica Acta,* 54**,** 283-297.

BLUM., A. & LASAGA., A. 1988. Role of surface speciation in the low-temperature dissolution of minerals. *Nature,* 331**,** 431-433.

BOERRIGTER, H. 2010. *Process for preparing an activated mineral.* US20100282079

BRANDENBURG, H. R. 1940. *Process for recovering magnesium oxide*.

BRANTLEY, S. L. 2008. Kinetics of mineral dissolution. *Kinetics of water-rock interaction.* Springer.

BRENT, G. F. & PETRIE, J. G. 2008. CO_2 sequestration by mineral carbonation in the Australian context.

BRINDLEY, G. & HAYAMI, R. 1964. Kinetics and mechanisms of dehydration and recrystallization of serpentine: I. *Clays Clay Miner,* 12**,** 4-35.

BRINDLEY, G. & HAYAMI, R. 1965. Mechanism of formation of Jbrsterite and enstatite from serpentine.

BROWN, G. 1980. Olivines and silicate spinels. *Reviews in Mineralogy and Geochemistry,* 5**,** 275-381.

BURCH, T., NAGY, K. & LASAGA, A. 1993. Free energy dependence of albite dissolution kinetics at 80 C and pH 8.8. *Chemical Geology,* 105**,** 137-162.

CAILLETEAU, C., ANGELI, F., DEVREUX, F., GIN, S., JESTIN, J., JOLLIVET, P. & SPALLA, O. 2008. Insight into silicate-glass corrosion mechanisms. *Nat Mater,* 7**,** 978-983.

CAJLLÈRE, M. S. 1936. 40 SECTION DES SCIENCES. *Comptes rendus: Section des sciences***,** 40.

CARMAN, P. C. 1940. Constitution of colloidal silica. *Transactions of the Faraday Society,* 36**,** 964-973.

CARROLL, S. A. & KNAUSS, K. G. 2005. Dependence of labradorite dissolution kinetics on CO_2 (aq), Al (aq), and temperature. *Chemical Geology,* 217**,** 213-225.

CASEY, W. H., HOCHELLA, M. F. & WESTRICH, H. R. 1993a. The surface chemistry of manganiferous silicate minerals as inferred from experiments on tephroite (Mn_2SiO_4). *Geochimica et Cosmochimica Acta,* 57**,** 785-793.

CASEY, W. H. & SPOSITO, G. 1992. On the temperature dependence of mineral dissolution rates. *Geochimica et Cosmochimica Acta,* 56**,** 3825-3830.

CASEY, W. H., WESTRICH, H. R., BANFIELD, J. F., FERRUZZI, G. & ARNOLD, G. W. 1993b. Leaching and reconstruction at the surfaces of dissolving chain-silicate minerals. *Nature,* 366 253-256.

CASEY, W. H., WESTRICH, H. R., MASSIS, T., BANFIELD, J. F. & ARNOLD, G. W. 1989. The surface of labradorite feldspar after acid hydrolysis. *Chemical Geology,* 78**,** 205-218.

CHEN, C.-T. A. & MARSHALL, W. L. 1982. Amorphous silica solubilities IV. Behavior in pure water and aqueous sodium chloride, sodium sulfate, magnesium chloride, and magnesium sulfate solutions up to 350°C. *Geochimica et Cosmochimica Acta,* 46**,** 279-287.

CHEN, Y. & BRANTLEY, S. L. 2000. Dissolution of forsteritic olivine at 65°C and $2< pH< 5$. *Chemical Geology,* 165**,** 267-281.

CHEN, Z.-Y., O'CONNOR, W. K. & GERDEMANN, S. J. 2006. Chemistry of aqueous mineral carbonation for carbon sequestration and explanation of experimental results. *Environmental Progress,* 25**,** 161-166.

CHOU, L. & WOLLAST, R. 1984. Study of the weathering of albite at room temperature and pressure with a fluidized bed reactor. *Geochimica et Cosmochimica Acta,* 48**,** 2205-2217.

CHOU, L. & WOLLAST, R. 1985. Steady-state kinetics and dissolution mechanisms of albite. *Am. J. Sci,* 285**,** 963-993.

CHRIST, C. L. & HOSTETLER, P. B. 1970. Studies in the system MgO-SiO_2-CO_2-H_2O (II); the activity-product constant of magnesite. *American Journal of Science,* 268**,** 439-453.

CLINKENBEARD, J. P. Guidelines for geologic investigations of naturally occurring asbestos in California. Geological Society of America Abstracts with Programs, 2005. 97.

DAVAL, D., HELLMANN, R., CORVISIER, J., TISSERAND, D., MARTINEZ, I. & GUYOT, F. 2010. Dissolution kinetics of diopside as a function of solution saturation state: macroscopic measurements and implications for modeling of geological storage of CO_2. *Geochimica et Cosmochimica Acta,* 74**,** 2615-2633.

DAVAL, D., HELLMANN, R., MARTINEZ, I., GANGLOFF, S. & GUYOT, F. 2013a. Lizardite serpentine dissolution kinetics as a function of pH and temperature, including effects of elevated P_{CO2}. *Chemical Geology,* 351**,** 245-256.

DAVAL, D., HELLMANN, R., SALDI, G. D., WIRTH, R. & KNAUSS, K. G. 2013b. Linking nm-scale measurements of the anisotropy of silicate surface reactivity to macroscopic dissolution rate laws: new insights based on diopside. *Geochimica et Cosmochimica Acta,* 107**,** 121-134.

DAVAL, D., MARTINEZ, I., CORVISIER, J., FINDLING, N., GOFFÉ, B. & GUYOT, F. 2009a. Carbonation of Ca-bearing silicates, the case of wollastonite: experimental investigations and kinetic modeling. *Chemical Geology,* 265**,** 63-78.

DAVAL, D., MARTINEZ, I., GUIGNER, J.-M., HELLMANN, R., CORVISIER, J., FINDLING, N., DOMINICI, C., GOFFÉ, B. & GUYOT, F. 2009b. Mechanism of wollastonite carbonation deduced from micro-to nanometer length scale observations. *American Mineralogist,* 94**,** 1707-1726.

DAVAL, D., SISSMANN, O., MENGUY, N., SALDI, G. D., GUYOT, F., MARTINEZ, I., CORVISIER, J., GARCIA, B., MACHOUK, I. & KNAUSS, K. G. 2011. Influence of amorphous silica layer formation on the dissolution rate of olivine at 90°C and elevated P_{CO2}. *Chemical Geology,* 284**,** 193-209.

DE VISSCHER, A., VANDERDEELEN, J., KOENIGSBERGER, E., CHURAGULOV, B. R., ICHIKUNI, M. & TSURUMI, M. 2012. IUPAC-NIST solubility data series. 95. alkaline earth carbonates in aqueous systems. part 1. introduction, Be and Mg. *Journal of Physical and Chemical Reference Data,* 41**,** 013105-013105-67.

DE YOREO, J. J. & VEKILOV, P. G. 2003. Principles of crystal nucleation and growth. *Reviews in mineralogy and geochemistry,* 54**,** 57-93.

DLUGOGORSKI, B. Z. & BALUCAN, R. D. 2014. Dehydroxylation of serpentine minerals: Implications for mineral carbonation. *Renewable and Sustainable Energy Reviews,* 31**,** 353-367.

DOVE, P. M. & CRERAR, D. A. 1990. Kinetics of quartz dissolution in electrolyte solutions using a hydrothermal mixed flow reactor. *Geochimica et Cosmochimica Acta,* 54**,** 955-969.

DRAN, J.-C., PETIT, J.-C. & BROUSSE, C. 1986. Mechanism of aqueous dissolution of silicate glasses yielded by fission tracks.

DUAN, Z. & SUN, R. 2003. An improved model calculating CO_2 solubility in pure water and aqueous NaCl solutions from 273 to 533 K and from 0 to 2000 bar. *Chemical Geology,* 193**,** 257-271.

ECCLES, J. K., PRATSON, L., NEWELL, R. G. & JACKSON, R. B. 2009. Physical and economic potential of geological CO_2 storage in saline aquifers. *Environmental science & technology,* 43**,** 1962-1969.

ED DLUGOKENCKY & PIETER TANS. NOAA/ESRL (www.esrl.noaa.gov/gmd/ccgg/trends/).

ELLIS, D. E. & WYLLIE, P. J. 1980. Phase relations and their petrological implications in the system $MgO\text{-}SiO_2\text{-}H_2O\text{-}CO_2$ at pressures up to 100 kbar. *American Mineralogist,* 65**,** 540-556.

FAUST, G. T. & FAHEY, J. J. 1962. *The serpentine-group minerals*, US Government Printing Office.

FEDOROČKOVÁ, A., HREUS, M., RASCHMAN, P. & SUČIK, G. 2012. Dissolution of magnesium from calcined serpentinite in hydrochloric acid. *Minerals Engineering,* 32**,** 1-4.

FOUDA, M. F. R., AMIN, R. E.-S. & ABD-ELZAHER, M. M. 1996. Extraction of Magnesia from Egyptian Serpentine Ore via Reaction with Different Acids. II. Reaction with Nitric and Acetic Acids. *Bulletin of the chemical society of Japan,* 69**,** 1913-1916.

FOURNIER, R. & ROWE, J. 1977. Solubility of amorphous silica in water at high temperatures and high pressure. *Am. Mineral.;(United States),* 62.

FURRER, G. & STUMM, W. 1986. The coordination chemistry of weathering: I. Dissolution kinetics of δ-Al_2O_3 and BeO. *Geochimica et Cosmochimica Acta,* 50**,** 1847-1860.

GAILLARDET, J., DUPRÉ, B., LOUVAT, P. & ALLÈGRE, C. J. 1999. Global silicate weathering and CO_2 consumption rates deduced from the chemistry of large rivers. *Chemical Geology,* 159**,** 3-30.

GEERLINGS, J. J. C. & WESKER, E. 2007. *A process for sequestration of carbon dioxide by mineral carbonation*. WO2007060149.

GERDEMANN, S. J., O'CONNOR, W. K., DAHLIN, D. C., PENNER, L. R. & RUSH, H. 2007. Ex situ aqueous mineral carbonation. *Environmental Science & Technology,* 41**,** 2587-2593.

GIAMMAR, D. E., BRUANT, R. G. & PETERS, C. A. 2005. Forsterite dissolution and magnesite precipitation at conditions relevant for deep saline aquifer storage and sequestration of carbon dioxide. *Chemical Geology,* 217**,** 257-276.

GISLASON, S. R. & OELKERS, E. H. 2003. Mechanism, rates, and consequences of basaltic glass dissolution: II. An experimental study of the dissolution rates of basaltic glass as a function of pH and temperature. *Geochimica et Cosmochimica Acta,* 67**,** 3817-3832.

GOFF, F. & LACKNER, K. S. 1998a. Carbon Dioxide Sequestering Using Ultramaf ic Rocks. *Environmental Geosciences,* 5**,** 89-102.

GOFF, F. & LACKNER, K. S. 1998b. Carbon dioxide sequestering using ultramafic rocks. *Environmental Geosciences,* 5**,** 89-101.

GOLUBEV, S. V., POKROVSKY, O. S. & SCHOTT, J. 2005. Experimental determination of the effect of dissolved CO_2 on the dissolution kinetics of Mg and Ca silicates at 25°C. *Chemical Geology,* 217**,** 227-238.

GRANDSTAFF, D. 1978. Changes in surface area and morphology and the mechanism of forsterite dissolution. *Geochimica et Cosmochimica Acta,* 42**,** 1899-1901.

GUTHRIE, G., CAREY, J. W., BERGFELD, D., BYLER, D., CHIPERA, S., ZIOCK, H.-J. & LACKNER, K. Geochemical aspects of the carbonation of magnesium silicates in an aqueous medium. NETL Conference on Carbon Sequestration, 2001. 1-14.

HACHIYA, K., SASAKI, M., SARUTA, Y., MIKAMI, N. & YASUNAGA, T. 1984. Static and kinetic studies of adsorption-desorption of metal ions on a. gamma.-alumina surface. 1. Static study of adsorption-desorption. *The Journal of Physical Chemistry,* 88**,** 23-27.

HÄNCHEN, M., PRIGIOBBE, V., BACIOCCHI, R. & MAZZOTTI, M. 2008. Precipitation in the Mg-carbonate system—effects of temperature and CO_2 pressure. *Chemical Engineering Science,* 63**,** 1012-1028.

HÄNCHEN, M., PRIGIOBBE, V., STORTI, G., SEWARD, T. & MAZZOTTI, M. 2006. Dissolution kinetics of fosteritic olivine at 90–150°C including effects of the presence of CO_2. *Geochimica et Cosmochimica Acta,* 70**,** 4403-4416.

HARGREAVES, A. & TAYLOR, W. 1946. An x-ray examination of decomposition products of chrysotile (asbestos) and serpentine. *Mineralogical Magazine,* 27**,** 204-216.

HAUG, T. A., KLEIV, R. A. & MUNZ, I. A. 2010. Investigating dissolution of mechanically activated olivine for carbonation purposes. *Applied Geochemistry,* 25**,** 1547-1563.

HELGESON, H. C. 1971. Kinetics of mass transfer among silicates and aqueous solutions. *Geochimica et Cosmochimica Acta,* 35**,** 421-469.

HELGESON, H. C., MURPHY, W. M. & AAGAARD, P. 1984. Thermodynamic and kinetic constraints on reaction rates among minerals and aqueous solutions. II. Rate constants, effective surface area, and the hydrolysis of feldspar. *Geochimica et Cosmochimica Acta,* 48**,** 2405-2432.

HELLMANN, R., COTTE, S., CADEL, E., MALLADI, S., KARLSSON, L. S., LOZANO-PEREZ, S., CABIÉ, M. & SEYEUX, A. 2015. Nanometre-scale evidence for interfacial dissolution–reprecipitation control of silicate glass corrosion. *Nature materials*.

HELLMANN, R., PENISSON, J.-M., HERVIG, R., THOMASSIN, J.-H. & ABRIOUX, M.-F. 2003. An EFTEM/HRTEM high-resolution study of the near surface of labradorite feldspar altered at acid pH: evidence for interfacial dissolution-reprecipitation. *Physics and Chemistry of Minerals,* 30**,** 192-197.

HELLMANN, R., PENISSON, J., HERVIG, R., THOMASSIN, J. & ABRIOUX, M. 2004. Chemical alteration of feldspar: a comparative study using SIMS and HRTEM/EFTEM. *Water rock interaction. AA Balkema, Rotterdam*.

HELLMANN, R. & TISSERAND, D. 2006. Dissolution kinetics as a function of the Gibbs free energy of reaction: An experimental study based on albite feldspar. *Geochimica et Cosmochimica Acta,* 70**,** 364-383.

HELLMANN, R., WIRTH, R., DAVAL, D., BARNES, J.-P., PENISSON, J.-M., TISSERAND, D., EPICIER, T., FLORIN, B. & HERVIG, R. L. 2012. Unifying natural and laboratory chemical weathering with interfacial dissolution–reprecipitation: a study based on the nanometer-scale chemistry of fluid–silicate interfaces. *Chemical Geology,* 294**,** 203-216.

HEY, M. & BANNISTER, F. 1948. A note on the thermal decomposition of chrysotile. *Mineralogical Magazine,* 28**,** 333-337.

HOLLAND, H. D. 1978. *The chemistry of the atmosphere and oceans*.

HUIJGEN, W. J., COMANS, R. N. & WITKAMP, G.-J. 2007. Cost evaluation of CO_2 sequestration by aqueous mineral carbonation. *Energy Conversion and Management,* 48**,** 1923-1935.

HUIJGEN, W. J. J. & COMANS, R. N. J. 2005. Carbon dioxide sequestration by mineral carbonation. Literature review update

2003-2004. Energy research Centre of the Netherlands ECN, Petten (Netherlands).

ILER, R. K. 1979. *The chemistry of silica: solubility, polymerization, colloid and surface properties, and biochemistry*.

INTERNATIONALENERGYAGENCY 2014. CO_2 EMISSIONS FROM FUEL COMBUSTION.

JARVIS, K., CARPENTER, R., WINDMAN, T., KIM, Y., NUNEZ, R. & ALAWNEH, F. 2009. Reaction mechanisms for enhancing mineral sequestration of CO_2. *Environmental Science & Technology,* 43**,** 6314-6319.

JOS G.J. OLIVIER, GREET. JANSSENS-MAENHOUT, MARILENA. MUNTEAN & JEROEN. A.H.W. PETERS 2014. Trends in global CO_2 emissions: 2014 Report.

JULCOUR, C., BOURGEOIS, F., BONFILS, B., BENHAMED, I., GUYOT, F., BODÉNAN, F., PETIOT, C. & GAUCHER, É. C. 2015. Development of an attrition-leaching hybrid process for direct aqueous mineral carbonation. *Chemical Engineering Journal,* 262**,** 716-726.

KHALIFAH, R. G. 1971. The carbon dioxide hydration activity of carbonic anhydrase I. Stop-flow kinetic studies on the native human isoenzymes B and C. *Journal of Biological Chemistry,* 246**,** 2561-2573.

KLEIN, F. & GARRIDO, C. J. 2011. Thermodynamic constraints on mineral carbonation of serpentinized peridotite. *Lithos,* 126**,** 147-160.

KÖNIGSBERGER, E., KÖNIGSBERGER, L.-C. & GAMSJÄGER, H. 1999. Low-temperature thermodynamic model for the system $Na_2CO_3-MgCO_3-CaCO_3-H_2O$. *Geochimica et Cosmochimica Acta,* 63**,** 3105-3119.

KWAK, J. H., HU, J. Z., TURCU, R. V., ROSSO, K. M., ILTON, E. S., WANG, C., SEARS, J. A., ENGELHARD, M. H., FELMY, A. R. & HOYT, D. W. 2011. The role of H_2O in the carbonation of forsterite in supercritical CO_2. *International Journal of Greenhouse Gas Control,* 5**,** 1081-1092.

LACKNER, K. S. 2002. Carbonate chemistry for sequestering fossil carbon. *Annual review of energy and the environment,* 27**,** 193-232.

LACKNER, K. S., WENDT, C. H., BUTT, D. P., JOYCE JR, E. L. & SHARP, D. H. 1995. Carbon dioxide disposal in carbonate minerals. *Energy,* 20**,** 1153-1170.

LASAGA, A. Kinetics of silicate dissolution. Fourth International Symposium on Water-Rock Interaction, 1983. Misasa Japan, 269-274.

LASAGA, A. C. 1981. Rate laws of chemical reactions. *Rev. Mineral.;(United States),* 8.

LASAGA, A. C. 1984. Chemical kinetics of water‐rock interactions. *Journal of Geophysical Research: Solid Earth (1978‐2012),* 89**,** 4009-4025.

LASAGA, A. C. 1998. *Kinetic theory in the earth sciences*, Princeton University Press.

LASAGA, A. C. & BLUM, A. E. 1986. Surface chemistry, etch pits and mineral-water reactions. *Geochimica et Cosmochimica Acta,* 50**,** 2363-2379.

LASAGA, A. C. & KIRKPATRICK, R. J. 1981. *Kinetics of geochemical processes*, Mineralogical Society of America Washington DC.

LASAGA, A. C., SOLER, J. M., GANOR, J., BURCH, T. E. & NAGY, K. L. 1994. Chemical weathering rate laws and global geochemical cycles. *Geochimica et Cosmochimica Acta,* 58**,** 2361-2386.

LEVENSPIEL, O. 1999. Chemical reaction engineering. *Industrial & engineering chemistry research,* 38**,** 4140-4143.

LI, W., LI, W., LI, B. & BAI, Z. 2009. Electrolysis and heat pretreatment methods to promote CO_2 sequestration by mineral carbonation. *Chemical Engineering Research and Design,* 87**,** 210-215.

LITTLE, M. G. & JACKSON, R. B. 2010. Potential impacts of leakage from deep CO_2 geosequestration on overlying freshwater aquifers. *Environmental science & technology,* 44**,** 9225-9232.

LUCE, R. W., BARTLETT, R. W. & PARKS, G. A. 1972. Dissolution kinetics of magnesium silicates. *Geochimica et Cosmochimica Acta,* 36**,** 35-50.

MAKRIDES, A. C., TURNER, M. & SLAUGHTER, J. 1980. Condensation of silica from supersaturated silicic acid solutions. *Journal of Colloid and Interface Science,* 73**,** 345-367.

MANN, J. P. 2014. *Serpentine Activation for CO_2 Sequestration.* University of Sydney.

MARTIN, C. 1977. The thermal decomposition of chrysotile. *Mineralogical Magazine,* 41**,** 453-459.

MAZZOTTI, M., ABANADES, J. C., ALLAM, R., LACKNER, K. S., MEUNIER, F., RUBIN, E., SANCHEZ, J. C., YOGO, K. & ZEVENHOVEN, R. 2005. Mineral carbonation and industrial uses of carbon dioxide. *IPCC special report on carbon dioxide capture and storage***,** 321-338.

MCKELVY, M. J., BEARAT, H., CHIZMESHYA, A. V. G., NUNEZ, R. & CARPENTER, R. W. 2003. Understanding olivine CO_2 mineral sequestration mechanisms at the atomic level: Optimizing reaction process design. *Other Information: PBD: 1 Aug 2003.*

MCKELVY, M. J., CHIZMESHYA, A. V. G., DIEFENBACHER, J., BÉARAT, H. & WOLF, G. 2004. Exploration of the Role of Heat Activation in Enhancing Serpentine Carbon Sequestration Reactions. *Environmental Science & Technology,* 38**,** 6897-6903.

METZ, B., DAVIDSON, O., DE CONINCK, H., LOOS, M. & MEYER, L. 2005. IPCC, 2005: IPCC special report on carbon dioxide capture and storage. Prepared by Working Group III of the Intergovernmental Panel on Climate Change. *Cambridge, United Kingdom and New York, NY, USA, 442 pp.*

MÖLLER, P. 1989. *Magnesite: geology, mineralogy, geochemistry, formation of Mg-carbonates*, Lubrecht & Cramer Ltd.

MOREY, G., FOURNIER, R. & ROWE, J. 1964. The solubility of amorphous silica at 25°C. *Journal of Geophysical Research,* 69**,** 1995-2002.

MORGAN, A., LALLY, A. & HOLMES, A. 1973. Some observations on the distribution of trace metals in chrysotile asbestos. *Annals of Occupational Hygiene,* 16**,** 231-240.

MORSE, J. W. & CASEY, W. H. 1988. Ostwald processes and mineral paragenesis in sediments. *American Journal of Science,* 288**,** 537-560.

MORSE, J. W. & MACKENZIE, F. T. 1990. *Geochemistry of sedimentary carbonates*, Elsevier.

MUKAI, H., AUSTRHEIM, H., PUTNIS, C. V. & PUTNIS, A. 2014. Textural evolution of plagioclase feldspar across a shear zone: Implications for deformation mechanism and rock strength. *Journal of Petrology***,** egu030.

NAGY, K., BLUM, A. & LASAGA, A. 1991. Dissolution and precipitation kinetics of kaolinite at 80^{o}C and pH 3; the dependence on solution saturation state. *American Journal of Science,* 291**,** 649-686.

NAGY, K. & LASAGA, A. 1992. Dissolution and precipitation kinetics of gibbsite at 80^{o}C and pH 3: The dependence on solution saturation state. *Geochimica et Cosmochimica Acta,* 56**,** 3093-3111.

NANCOLLAS, G. & PURDIE, N. 1964. The kinetics of crystal growth. *Quarterly Reviews, Chemical Society,* 18**,** 1-20.

NIELSEN, A. E. 1964. *Kinetics of precipitation*, Pergamon Press Oxford.

O'CONNOR, W. K., DAHLIN, D. C., RUSH, G. E., GERDEMANN, S. J., PENNER, L. R. & NILSEN, D. N. 2005. FINAL REPORT AQUEOUS MINERAL CARBONATION: Mineral Availability, Pretreatment, Reaction Parametrics, And Process Studies National Energy Technology Laboratory.

OELKERS, E. & SCHOTT, J. 1995. The dependence of silicate dissolution rates on their structure and composition. *Water Rock Interaction***,** 153-156.

OELKERS, E. H. 1996. Summary and review of the physical and chemical properties of rocks and fluids. *Rev. Miner.,* 34**,** 131-191.

OELKERS, E. H. 2001a. An experimental study of forsterite dissolution rates as a function of temperature and aqueous Mg and Si concentrations. *Chemical Geology,* 175**,** 485-494.

OELKERS, E. H. 2001b. General kinetic description of multioxide silicate mineral and glass dissolution. *Geochimica et Cosmochimica Acta,* 65**,** 3703-3719.

OELKERS, E. H., GOLUBEV, S. V., CHAIRAT, C., POKROVSKY, O. S. & SCHOTT, J. 2009. The surface chemistry of multi-oxide silicates. *Geochimica et Cosmochimica Acta,* 73**,** 4617-4634.

OELKERS, E. H. & SCHOTT, J. 2001. An experimental study of enstatite dissolution rates as a function of pH, temperature, and aqueous Mg and Si concentration, and the mechanism of pyroxene/pyroxenoid dissolution. *Geochimica et Cosmochimica Acta,* 65**,** 1219-1231.

OLSEN, A. A. 2007. *Forsterite dissolution kinetics: applications and implications for chemical weathering.* Virginia Polytechnic Institute and State University.

OLSEN, A. A. & RIMSTIDT, D. J. 2008. Oxalate-promoted forsterite dissolution at low pH. *Geochimica et Cosmochimica Acta,* 72**,** 1758-1766.

PACHAURI, R. K., ALLEN, M., BARROS, V., BROOME, J., CRAMER, W., CHRIST, R., CHURCH, J., CLARKE, L., DAHE, Q. & DASGUPTA, P. 2014. Climate Change 2014: Synthesis Report. Contribution of Working Groups I, II and III to the Fifth Assessment Report of the Intergovernmental Panel on Climate Change.

PARK, A.-H. A. & FAN, L.-S. 2004. CO_2 mineral sequestration: physically activated dissolution of serpentine and pH swing process. *Chemical Engineering Science,* 59**,** 5241-5247.

PARK, A.-H. A., JADHAV, R. & FAN, L.-S. 2003. CO_2 Mineral Sequestration: Chemically Enhanced Aqueous Carbonation of Serpentine. *The Canadian Journal of Chemical Engineering,* 81**,** 885-890.

PETIT, J.-C., MEA, G. D., DRAN, J.-C., SCHOTT, J. & BERNER, R. 1987. Mechanism of diopside dissolution from hydrogen depth profiling.

PIGFORD, R. & SLIGER, G. 1973. Rate of diffusion-controlled reaction between a gas and a porous solid sphere-reaction of SO_2 with

$CaCO_3$. *Industrial & Engineering Chemistry Process Design and Development,* 12, 85-91.

PLUMBER, L. & BUSENBERG, E. 1982. The solubilities of calcite, aragonite and vaterite in CO_2–H_2O solutions between 0 and 90°C, and an evaluation of the aqueous model for the system $CaCO_3$–CO_2–H_2O. *Geochim. et Cosmochim. Acta,* 46, 1011-1040.

POKROVSKY, O. S. & SCHOTT, J. 2000. Kinetics and mechanism of forsterite dissolution at 25°C and pH from 1 to 12. *Geochimica et Cosmochimica Acta,* 64, 3313-3325.

PRIGIOBBE, V., COSTA, G., BACIOCCHI, R., HÄNCHEN, M. & MAZZOTTI, M. 2009. The effect of CO_2 and salinity on olivine dissolution kinetics at. *Chemical Engineering Science,* 64, 3510-3515.

PUTNIS, A. 2002. Mineral replacement reactions: from macroscopic observations to microscopic mechanisms. *Mineralogical Magazine,* 66, 689-708.

PUTNIS, A. 2015. Glass corrosion: Sharpened interface. *Nat Mater,* 14, 261-262.

PUTNIS, A. & MAUTHE, G. 2001. The effect of pore size on cementation in porous rocks. *Geofluids,* 1, 37-41.

PUTNIS, A., PRIETO, M. & FERNANDEZ-DIAZ, L. 1995. Fluid supersaturation and crystallization in porous media. *Geological Magazine,* 132, 1-13.

RIMSTIDT, J. D. 2013. *Geochemical Rate Models: An Introduction to Geochemical Kinetics*, Cambridge University Press.

RIMSTIDT, J. D. & BARNES, H. 1980. The kinetics of silica-water reactions. *Geochimica et Cosmochimica Acta,* 44, 1683-1699.

ROSSO, J. J. & RIMSTIDT, J. D. 2000. A high resolution study of forsterite dissolution rates. *Geochimica et Cosmochimica Acta,* 64, 797-811.

RUSTAD, J. R. & CASEY, W. H. 2012. Metastable structures and isotope exchange reactions in polyoxometalate ions provide a molecular view of oxide dissolution. *Nature materials,* 11, 223-226.

SABIRZYANOV, A., SHAGIAKHMETOV, R., GABITOV, F., TARZIMANOV, A. & GUMEROV, F. 2003. Water solubility of carbon dioxide under supercritical and subcritical conditions. *Theoretical Foundations of Chemical Engineering,* 37**,** 51-53.

SALDI, G. D., KÖHLER, S. J., MARTY, N. & OELKERS, E. H. 2007. Dissolution rates of talc as a function of solution composition, pH and temperature. *Geochimica et cosmochimica acta,* 71**,** 3446-3457.

SANEMASA, I., YOSHIDA, M. & OZAWA, T. 1972. The dissolution of olivine in aqueous solutions of inorganic acids. *Bulletin of the Chemical Society of Japan,* 45**,** 1741-1746.

SAYLES, F. & FYFE, W. 1973. The crystallization of magnesite from aqueous solution. *Geochimica et Cosmochimica Acta,* 37**,** 87-99.

SCHOPKA, H. H., DERRY, L. A. & ARCILLA, C. A. 2011. Chemical weathering, river geochemistry and atmospheric carbon fluxes from volcanic and ultramafic regions on Luzon Island, the Philippines. *Geochimica et Cosmochimica Acta,* 75**,** 978-1002.

SCHOTT, J., BERNER, R. A. & SJÖBERG, E. L. 1981. Mechanism of pyroxene and amphibole weathering-I. Experimental studies of iron-free minerals. *Geochimica et Cosmochimica Acta,* 45**,** 2123-2135.

SCHULZE, R. K., HILL, M. A., FIELD, R. D., PAPIN, P. A., HANRAHAN, R. J. & BYLER, D. D. 2004. Characterization of carbonated serpentine using XPS and TEM. *Energy Conversion and Management,* 45**,** 3169-3179.

SEIFRITZ, W. 1990. CO_2 disposal by means of silicates. *Nature,* 345**,** 486-486.

SHIRAKI, R. & BRANTLEY, S. L. 1995. Kinetics of near-equilibrium calcite precipitation at 100^{o}C: An evaluation of elementary reaction-based and affinity-based rate laws. *Geochimica et Cosmochimica Acta,* 59**,** 1457-1471.

SMITHSON, G. L. & BAKHSHI, N. 1973. Kinetics and mechanism of carbonation of magnesium oxide slurries. *Industrial & Engineering Chemistry Process Design and Development,* 12**,** 99-106.

STEEFEL, C. I. & VAN CAPPELLEN, P. 1990. A new kinetic approach to modeling water-rock interaction: The role of nucleation, precursors, and Ostwald ripening. *Geochimica et Cosmochimica Acta,* 54**,** 2657-2677.

STEEL, K. M., ALIZADEHHESARI, K., BALUCAN, R. D. & BAŠIĆ, B. 2013. Conversion of CO_2 into mineral carbonates using a regenerable buffer to control solution pH. *Fuel,* 111**,** 40-47.

STUMM, W., FURRER, G. & KUNZ, B. 1983. The role of surface coordination in precipitation and dissolution of mineral phases. *Croat. Chem. Acta,* 56**,** 593-611.

STUMM, W. & WOLLAST, R. 1990. Coordination chemistry of weathering: Kinetics of the surface ‐ controlled dissolution of oxide minerals. *Reviews of Geophysics,* 28**,** 53-69.

SUMMERS, C. A., DAHLIN, D. C., RUSH, G. E., O'CONNOR, W. K. & GERDEMANN, S. J. 2005. Grinding methods to enhance the reactivity of olivine. *Minerals & Metallurgical Processing,* 22.

SWOBODA-COLBERG, N. G. & DREVER, J. I. 1993. Mineral dissolution rates in plot-scale field and laboratory experiments. *Chemical Geology,* 105**,** 51-69.

SZEKELY, J. & EVANS, J. 1970. A structural model for gas—solid reactions with a moving boundary. *Chemical Engineering Science,* 25**,** 1091-1107.

TEIR, S., ELONEVA, S., FOGELHOLM, C.-J. & ZEVENHOVEN, R. 2009. Fixation of carbon dioxide by producing hydromagnesite from serpentinite. *Applied Energy,* 86**,** 214-218.

TEIR, S., REVITZER, H., ELONEVA, S., FOGELHOLM, C.-J. & ZEVENHOVEN, R. 2007. Dissolution of natural serpentinite in mineral and organic acids. *International Journal of Mineral Processing,* 83**,** 36-46.

VAN ESSENDELFT, D. T. & SCHOBERT, H. H. 2009a. Kinetics of the acid digestion of serpentine with concurrent grinding. 1. Initial investigations. *Industrial & Engineering Chemistry Research,* 48**,** 2556-2565.

VAN ESSENDELFT, D. T. & SCHOBERT, H. H. 2009b. Kinetics of the acid digestion of serpentine with concurrent grinding. 2. Detailed investigation and model development. *Industrial & Engineering Chemistry Research,* 48**,** 9892-9901.

VAN ESSENDELFT, D. T. & SCHOBERT, H. H. 2010. Kinetics of the Acid Digestion of Serpentine with Concurrent Grinding. 3. Model Validation and Prediction. *Industrial & Engineering Chemistry Research,* 49**,** 1588-1590.

VEBLEN, D. R. & WYLIE, A. G. 1993. Mineralogy of amphiboles and 1: 1 layer silicates. Mineralogical Society of America, Washington, DC (United States).

VELBEL, M. A. 1993. Formation of protective surface layers during silicate-mineral weathering under well-leached, oxidizing conditions. *American Mineralogist,* 78**,** 405-405.

WANG, X. & MAROTO-VALER, M. 2011. Integration of CO_2 capture and storage based on pH-swing mineral carbonation using recyclable ammonium salts. *Energy Procedia,* 4**,** 4930-4936.

WEISSBART, E. J. & RIMSTIDT, J. D. 2000. Wollastonite: Incongruent dissolution and leached layer formation. *Geochimica et Cosmochimica Acta,* 64**,** 4007-4016.

WERES, O., YEE, A. & TSAO, L. 1981. Kinetics of silica polymerization. *Journal of Colloid and Interface Science,* 84**,** 379-402.

WERNER, M., HARIHARAN, S. & MAZZOTTI, M. 2014a. Flue gas CO_2 mineralization using thermally activated serpentine: from single- to double-step carbonation. *Physical Chemistry Chemical Physics,* 16**,** 24978-24993.

WERNER, M., HARIHARAN, S., ZINGARETTI, D., BACIOCCHI, R. & MAZZOTTI, M. 2014b. Dissolution of dehydroxylated lizardite at flue gas conditions: I. Experimental study. *Chemical Engineering Journal,* 241**,** 301-313.

WERNER, M., HARIHARAN, S. B., BORTOLAN, A. V., ZINGARETTI, D., BACIOCCHI, R. & MAZZOTTI, M. 2013. Carbonation of Activated Serpentine for Direct Flue Gas Mineralization. *Energy Procedia,* 37**,** 5929-5937.

WEYL, P. K. 1958. The solution kinetics of calcite. *The Journal of Geology***,** 163-176.

WHITE, A. F. & BRANTLEY, S. L. 1995. Chemical weathering rates of silicate minerals: an overview. *Chemical Weathering Rates of Silicate Minerals,* 31, 1-22.

WICKS, F. & O'HANLEY, D. S. 1988. Serpentine minerals; structures and petrology. *Reviews in Mineralogy and Geochemistry,* 19, 91-167.

WILSON, S. A., RAUDSEPP, M. & DIPPLE, G. M. 2006. Verifying and quantifying carbon fixation in minerals from serpentine-rich mine tailings using the Rietveld method with X-ray powder diffraction data. *American Mineralogist,* 91, 1331-1341.

WOGELIUS, R. A. & WALTHER, J. V. 1991. Olivine dissolution at 25°C: Effects of pH, CO_2, and organic acids. *Geochimica et Cosmochimica Acta,* 55, 943-954.

WOGELIUS, R. A. & WALTHER, J. V. 1992. Olivine dissolution kinetics at near-surface conditions. *Chemical Geology,* 97, 101-112.

WOLF, G. H., CHIZMESHYA, A. V., DIEFENBACHER, J. & MCKELVY, M. J. 2004. In situ observation of CO_2 sequestration reactions using a novel microreaction system. *Environmental Science & Technology,* 38, 932-936.

Appendices

Appendix A. Methodology of XRF Analysis

40mm glass beads were prepared using 1.0000 grams of powdered sample which has been pre-dried, weighed out via wax paper and poured into a glass vial.

The ingredients were mixed carefully in a glass vial and transferred to a Pt/Au crucible. The crucible was placed in a high-temperature muffle furnace and allowed to melt and mixed for 15 minutes. The molten flux and sample then was poured into 40mm Pt/Au casting dishes and left to cool before labelling. L.O.I. (loss on ignition) was done on sub-samples at the same fusion temperature (1323 K) as the beads. This loss indicates the presence of organics, volatiles and adsorbed moisture.

Prepared glass beads were measured on the PW2400 WDXRF Spectrometer. The WROXI calibration program was selected, which has been calibrated using certified reference materials and using optimal instrumental operating conditions (e.g., choice of crystal, counting times, line overlaps, background measurement and so on). All elements analysed are expressed as wt. % oxides.

This information is provided by Mark Wainwright Analytical Centre of the University of NSW.

Appendix B. OLI-MSE Validations

B-1. Solubility of CO_2 in Carbonic Acid System

Several previous studies have investigated the properties of CO_2-H_2O system, which have led them to the development of models that can predict the thermodynamic properties of the CO_2-H_2O system (Redlich and Kwong, 1949, Peng and Robinson, 1976, Duan et al., 1992, Duan and Sun, 2003). Among those models, the one proposed by Duan and co-works can predict the solubility of CO_2 in the CO_2-H_2O system up to a high range of temperature and pressure (273-533 K, 0-2000 bar) with an inconsistency of less than 7% as verified by the experimental validation. Henceforth, the equilibrium solubility of CO_2 in the carbonic acid system calculated using OLI-MSE is compared with the well-known Duan & Sun model, as shown in Figure B-1.

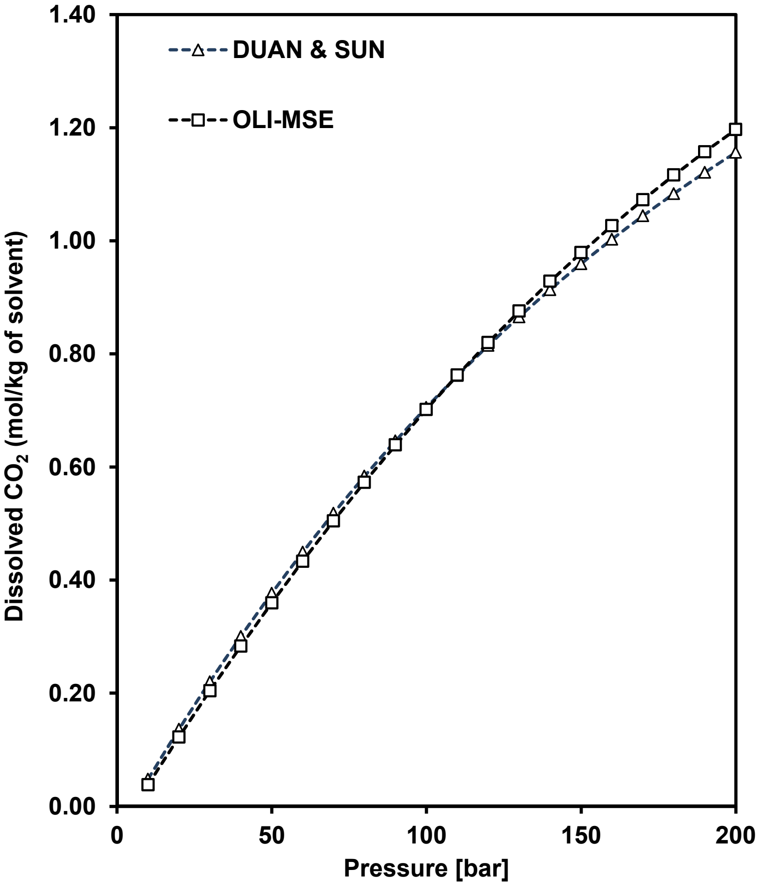

Figure B-1. CO_2 solubility in water at a constant temperature of 423 K and m_{CO2} = 3.7 mol kg^{-1} plotted versus the pressure (calculated with OLI-MSE and compared with the DUAN & SUN model).

It appears that the solubility data obtained from OLI-MSE simulations are in a close agreement within the data reported by Duan and Sun (2003).

B-2. Solubility Product of Magnesite

Accurate knowledge of magnesite thermodynamic properties is important for identifying phase stabilities in the MgO-CO_2-H_2O system. Several previous studies have been investigated the magnesite solubility product at room temperature, as shown in Table B-1. It appears that OLI-MSE is fairly accurate at room temperature. However many authors, such as Bénézeth et al. (2011), discussed that due to the difficulties reflect in measuring the exact phase of carbonate species under high pressure and temperature conditions, many thermodynamic data of magnesite solubilities in databases are associated with the level of uncertainties. In the present study, the calculated solubilities of magnesite by using OLI-MSE are compared with the proposed model by Bénézeth et al. (2011), as shown in Figure B-2.

Table B-1. Summary of literature values for solubility product of magnesite obtained from experimental investigations and OLI-MSE calculations.

T (K)	P_{CO2} (atm)	$\log_{10} K_{spo\text{-}mgs}$	Reference
298	-	-8.03	(Allison et al., 1991) (MINTEQ)
298	-	-8.04	(Johnson et al., 1992) (SUPCRT92)
298	3×10^{-4}	-7.52	(Pokrovsky et al., 1999)
298	1	-8.57	OLI-MSE calculated in the present study

Despite relatively accurate OLI-MSE value for the solubility product of magnesite at atmospheric conditions, the calculated solubility products of magnesite at elevated temperature and pressure conditions are observed to be different from those obtained using Bénézeth et al. model. The OLI-MSE values are roughly lower within the order of magnitude. This magnitude of difference in values is typical of the differences were seen between amorphous and crystalline solids, and it is significant. Nonetheless, there is a consensus in the trend of data. The exact reason of this error is unknown; however, one may postulate that the OLI-MSE uses to extrapolate magnesite solubility data similar to the procedure (using Van't Hoff equation) used by Christ and Hostetler (1970).

In the present study to identify the states of saturation, measured magnesium concentration profiles are compared with the equilibrium solubility of magnesite calculated by OLI-MSE. The magnesite is selected since it has the lowest solubility product compared with other possible carbonate phases in the MgO-CO_2-H_2O system.

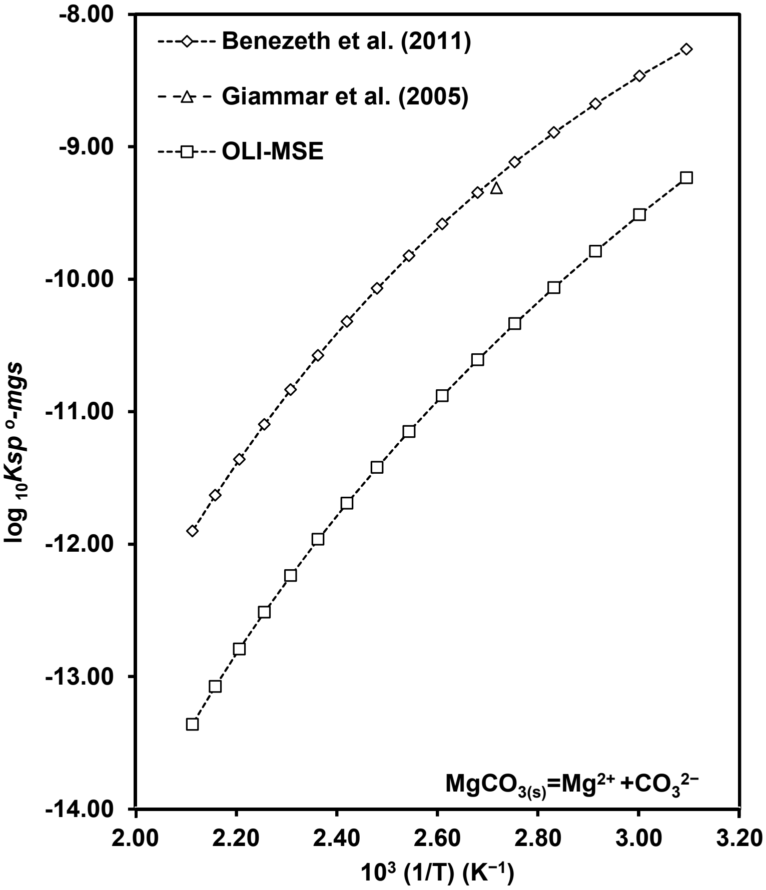

Figure B-2. Logarithm of the solubility product of magnesite obtained from calculations with OLI-MSE, Giammar et al. (2005) experimental data and Bénézeth et al. (2011) empirical model plotted versus reciprocal temperature. OLI-MSE calculations were carried out under the saturated MgO-CO_2-H_2O system at P_{CO2} = 30 bar, in a presence of 0.1 molal NaCl and NaCl free solution.

B-3. Solubility Product of Crystalline and Amorphous Silica

The recognition that the solid-phase amorphous silica is more reactive than its crystalline counterparts is important as it strongly influences the movement of silica between mineral and aqueous phases (Icenhower and Dove, 2000). Knowledge of the fundamental controls on the dissolution mechanism of silica polymorphs is related to the physical and chemical phenomena that govern the reactivity of Si-O bonded phases. Casey and Bunker (1990) stated that the extent of cross-link of SiO_4 tetrahedra in mineral structure influences the leaching characteristics of silicate minerals. Therefore, the total reactivity of crystalline and amorphous materials can be reflected by corrosion resistance of the SiO_4 tetrahedra network. Figure B-2 and Figure B-3 show the OLI predictions for solubility of crystalline and amorphous silica.

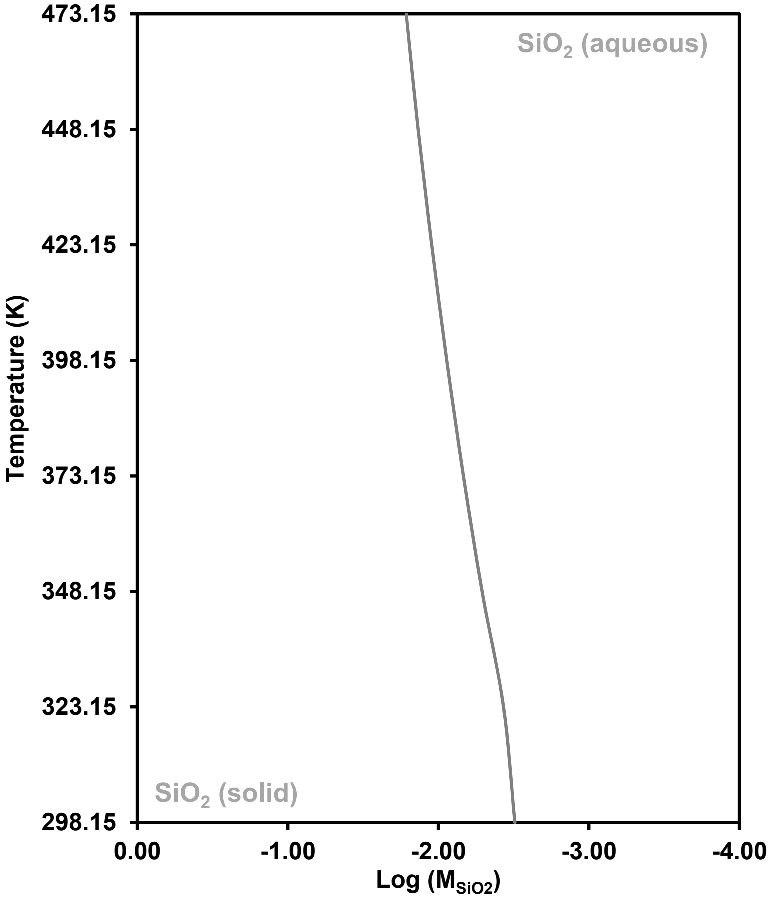

Figure B-3. Solubility of amorphous silica calculated by using OLI-MSE under relevant experimental conditions (saturated CO_2-H_2O, P_{CO2} = 100 bar).

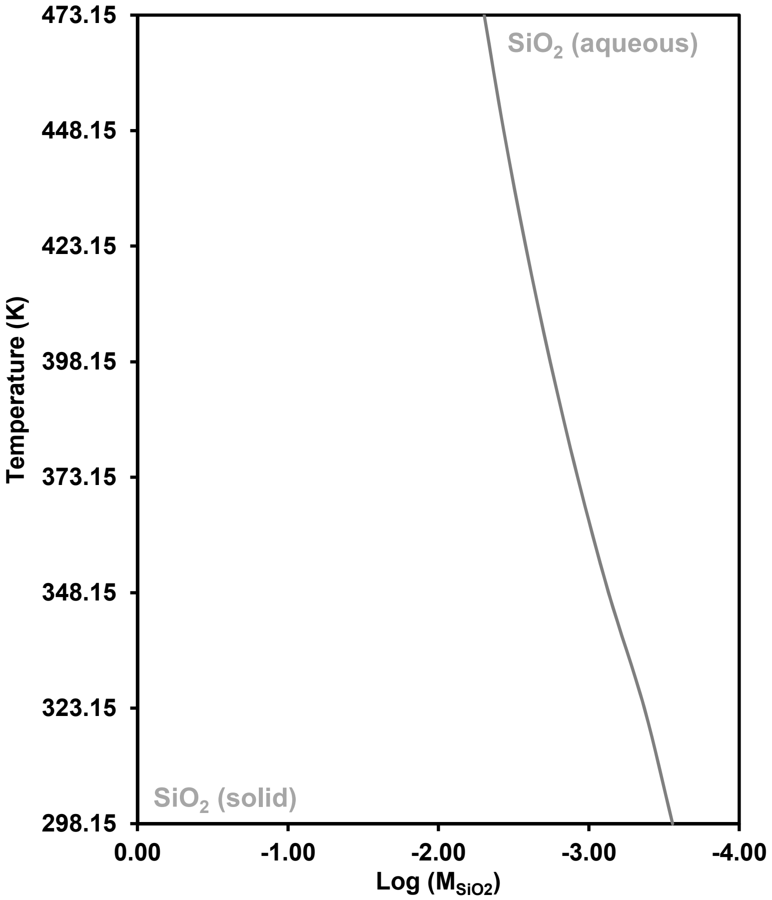

Figure B-4. Solubility of crystalline silica (trigonal) calculated by using OLI-MSE-Geochemical under relevant experimental conditions (saturated CO_2-H_2O, P_{CO2} = 100 bar)

From the surveyed literature, it is understood that in the silica minerals and materials contain highly complex silica phases in their composition, the chemical durability of the Si-O bond impacts the overall dissolution behaviour. In addition, it has been shown that the amorphous forms of silica dissolve more quickly compared with its crystalline form. On the basis of OLI calculations, the amorphous silica exhibits higher solubility product than the crystalline phase. In the present study, almost always the examined research material has almost non-crystalline structure (thermally activated SWOL) – thus measured silica concentration profiles are compared with the corresponding solubility products of amorphous silica, calculated by OLI-MSE.

References

ALLISON, J. D., BROWN, D. S. & KEVIN, J. 1991. *MINTEQA2/PRODEFA2, a geochemical assessment model for environmental systems: Version 3.0 user's manual*, Environmental Research Laboratory, Office of Research and Development, US Environmental Protection Agency Athens, GA.

BÉNÉZETH, P., SALDI, G. D., DANDURAND, J.-L. & SCHOTT, J. 2011. Experimental determination of the solubility product of magnesite at 50 to 200°C. *Chemical Geology,* 286**,** 21-31.

CASEY, W. H. & BUNKER, B. 1990. Leaching of mineral and glass surfaces during dissolution. *Reviews in Mineralogy and Geochemistry,* 23**,** 397-426.

CHRIST, C. L. & HOSTETLER, P. B. 1970. Studies in the system MgO-SiO_2-CO_2-H_2O (II); the activity-product constant of magnesite. *American Journal of Science,* 268**,** 439-453.

DUAN, Z., MØLLER, N. & WEARE, J. H. 1992. An equation of state for the CH_4-CO_2-H_2O system: II. Mixtures from 50 to 1000°C and 0 to 1000 bar. *Geochimica et Cosmochimica Acta,* 56**,** 2619-2631.

DUAN, Z. & SUN, R. 2003. An improved model calculating CO_2 solubility in pure water and aqueous NaCl solutions from 273 to 533 K and from 0 to 2000 bar. *Chemical Geology,* 193**,** 257-271.

GIAMMAR, D. E., BRUANT, R. G. & PETERS, C. A. 2005. Forsterite dissolution and magnesite precipitation at conditions relevant for deep saline aquifer storage and sequestration of carbon dioxide. *Chemical Geology,* 217**,** 257-276.

ICENHOWER, J. P. & DOVE, P. M. 2000. The dissolution kinetics of amorphous silica into sodium chloride solutions: effects of temperature and ionic strength. *Geochimica et Cosmochimica Acta,* 64**,** 4193-4203.

JOHNSON, J. W., OELKERS, E. H. & HELGESON, H. C. 1992. SUPCRT92: A software package for calculating the standard molal thermodynamic properties of minerals, gases, aqueous species, and reactions from 1 to 5000 bar and 0 to 1000 C. *Computers & Geosciences,* 18, 899-947.

PENG, D.-Y. & ROBINSON, D. B. 1976. A New Two-Constant Equation of State. *Industrial & Engineering Chemistry Fundamentals,* 15, 59-64.

POKROVSKY, O. S., SCHOTT, J. & THOMAS, F. 1999. Processes at the magnesium-bearing carbonates/solution interface. I. A surface speciation model for magnesite. *Geochimica et cosmochimica acta,* 63, 863-880.

REDLICH, O. & KWONG, J. N. S. 1949. On the Thermodynamics of Solutions. V. An Equation of State. Fugacities of Gaseous Solutions. *Chemical Reviews,* 44, 233-244.

Appendix C. Reactor Flow Pattern / Experimental Conditions

C-1. Reactor Flow Pattern

Following steps are considered to specify the total volumetric flow rate in the reactor at molality of $m_{CO2} = 3.7$ mol kg^{-1} under the CO_2-H_2O system, a reaction temperature of 423 K and CO_2 partial pressure of 100 bar. Figure C-1 shows the schematic diagram of the experimental set-up.

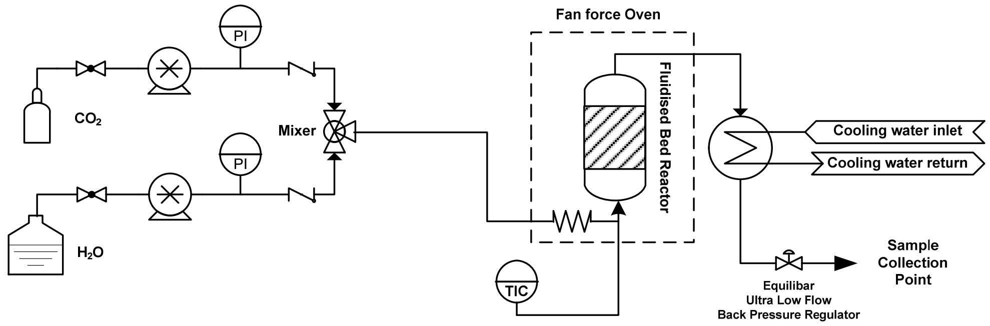

Figure C-1. Schematic view of the experimental set-up.

Following steps used to calculate the total volumetric flow rate for standard conditions:

$$\dot{m} = \dot{V} \times \rho \tag{C.1}$$

$$\dot{m}_{total} = \dot{m}_{CO2} + \dot{m}_{H2O} \tag{C.2}$$

where,

$\dot{m}$	mass flow rate, g min^{-1}
$\dot{V}$	volumetric flow rate, mL min^{-1}
ρ	density, g mL^{-1}
$\dot{m}_{CO2}$	mass flow rate of CO_2, g min^{-1}
$\dot{m}_{H2O}$	mass flow rate of H_2O, g min^{-1}

Table C-1. Summary of total mass flow rates at the inlet or pump conditions.

	Value	Source
T (K)	298	-
P (bar)	100	-
$\dot{V}_{\mathrm{CO2}}$ (mL min^{-1})	0.2	-
ρ_{CO2} (g mL^{-1})	0.82	NIST
$\dot{m}_{CO2}$ (g min^{-1})	0.16	Equation (C.1)
$\dot{V}_{\mathrm{H2O}}$ (mL min^{-1})	1.00	-
ρ_{H2O} (g mL^{-1})	1.00	NIST
$\dot{m}_{H2O}$ (g min^{-1})	1.00	Equation (C.1)
$\dot{m}_{total}$ (g min^{-1})	1.17	Equation (C.2)

$$\dot{m}_m = \dot{V}_m \times \rho_m \tag{C.3}$$

$$\rho_m = \frac{m}{V} \tag{C.4}$$

$$\dot{m}_{total} = \dot{m}_m = \dot{m}_{CO2} + \dot{m}_{H2O} \tag{C.5}$$

where,

$\dot{m}_m$	mass flow rate of the mixture, g min^{-1}
$\dot{V}_m$	volumetric flow rate of the mixture, mL min^{-1}
ρ_m	the density of the mixture, g mL^{-1}
m	total mass (mass of H_2O & mass of CO_2), g
V	total volume, mL

Table C-2. Summary of density and volumetric flow rate of mixture flow at the reaction conditions, $T = 423$ K and $P_{\mathrm{CO2}} = 100$ bar.

	Value	Source
T (K)	423	-
P (bar)	100	-
m (g)	1162.84	OLI-MSE
V (mL)	2111.44	OLI-MSE
ρ_m (g mL^{-1})	0.55	Equation (C.4)
$\dot{m}_{total}$ (g min^{-1})	1.17	Table (C-1)
$\dot{V}_m$ (mL min^{-1})	2.12	Equation (C.3)

$$\dot{V}_m = u \times A \tag{C.6}$$

where,

u	velocity, cm min^{-1}
A_r	the cross-sectional area of the reactor, cm^2

Table C-3. Summary of the superficial velocity of the reactive fluid across the reactor, and cross section surface of the reactor.

	Value	Source
u (cm s^{-1})	0.088	Equation (C.6)
A_r (cm^2)	0.40	Swagelok

The fluidised bed reactor used in the present study involved solid, gas and liquid phases. The reactive fluid is comprised of the mixture of gas and liquid phases. Although the exact regime of this mixture is unknown, it should likely have a bubbly flow pattern. With regards to the reactor hydrodynamics, it is desirable to accomplish homogeneous suspension conditions, where the solid and the reactive fluid are dynamically mixed. Following steps used to estimate the flow pattern across the reactor.

The density of thermally activated SWOL material is determined as ~3 g cm^{-3} through a pycnometer technique. The minimum fluidisation velocity (u_{mf}) is calculated by using a correlation (C.7), recommended by Chitester et al. (1984). This correlation is applicable for fluidisation at high pressure.

$$u_{mf} = \frac{\mu}{d_p\rho_f}\left(\left(28.7^2 + 0.0494\left(\frac{d_p^3\rho_f\left(\rho_s - \rho_f\right)g}{\mu^2}\right)\right)^{0.5} - 28.7\right) \qquad \text{(C.7)}$$

where,

u_{mf}	minimum fluidisation velocity, cm s^{-1}
μ_f	viscosity, g $(\text{cm.s})^{-1}$
ρ_f	the density of the reactive fluid, g cm^3
ρ_s	the density of solid, g cm^3
d_p	intermediate particle size, µm
g	gravitational constant, cm s^{-2}

These parameters at the so-called standard reaction conditions are shown in Table C-4.

Table C-4. Summary of the minimum fluidisation velocity corresponded to the standard conditions.

	Value	Source
T (K)	423	-
P (bar)	100	-
μ_f (g (cm s) $^{-1}$)*	0.001826	OLI-MSE
ρ_f(g cm^{-3})*	0.90	OLI-MSE
ρ_s(g cm^{-3})	3.00	Measured
d_p(cm)	0.007	Measured
g(cm s^{-1})	980	-
u_{mf}(cm s^{-1})	0.047	Equation (C.7)

**properties of aqueous phase were used as the correlation (C.7) is valid for one phase*

Comparing the superficial velocity of the reactive fluid at the standard conditions with the minimum fluidisation velocity (u_{mf}), indicates that the solids are likely fluidised. In order to predict the fluidisation mode, the general flow diagram developed by Grace (1986) for solid-liquid system was adopted. This charts introduces two dimensionless variables, a) particle size parameter d^*, and b) fluid superficial velocity u^*. These parameters are defined with equations (C.8) and (C.9),

$$d^* = d_p \left(\frac{\rho_f(\rho_s - \rho_f)g}{\mu^2}\right)^{1/3} \qquad \text{(C.8)}$$

$$u^* = u \left(\frac{{\rho_f}^2}{\mu(\rho_s - \rho_f)g}\right)^{1/3} \qquad \text{(C.9)}$$

Table C-5. Summary of values of dimensionless parameters of $u^*$and d^*.

	Value	Source
u^*	0.053	Equation (C.9)
d^*	5.75	Equation (C.9)

Interpolation of the obtained values for these dimensionless parameters indicated that the reactor operates within a conventional fluidisation regime.

It is worth noting that in accordance with the Geldart particles classification, the research material is in agreement with the recognisable features of group B, which usually fluidised well (Geldart, 1973).

C-2. Experimental Conditions

By maintaining the volumetric flow rate constant at 2.12 mL min^{-1} (the so-called standard volumetric flow rate in this study) for all of the experimental conditions; thus, the residence time of the reactive fluid passing through the reactor will be constant. By rearranging equation (C.1), equations (C.10 to C.12) are used to calculate the parameters shown in Table C-6.

$$\dot{m}_m = \dot{m}_{H2O}\left(1+\frac{\dot{m}_{CO2}}{\dot{m}_{H2O}}\right) \tag{C.10}$$

$$\dot{m}_{H2O} = \dot{m}_m/\left(1+\frac{\dot{m}_{CO2}}{\dot{m}_{H2O}}\right) \tag{C.11}$$

$$\dot{m}_{CO2} = \dot{m}_m - \dot{m}_{H2O} \tag{C.12}$$

Table C-6. Summary of the CO_2 and H_2O streams mass flow rates, with reference to the standard volumetric flow rate, under the standard conditions.

Reactor Conditions	Value	Source
T (K)	423	-
P (bar)	100	-
$\dot{V}_m$ (mL min^{-1})	2.12	Equation (C.3)
m (mol kg^{-1})	3.70	-
$\dot{m}_{CO2}/\dot{m}_{H2O}$ (kg$_{CO2}$/kg$_{H2O}$)	0.16	-
ρ_m (g mL^{-1})	0.55	Equation (C.4)
$\dot{m}_m$ (g min^{-1})	1.17	Table (C-1)
$\dot{m}_{CO2}$ (g min^{-1})	0.16	Equation (C.12)
$\dot{m}_{H2O}$ (g min^{-1})	1.00	Equation (C.11)

High-pressure Experimental Apparatus

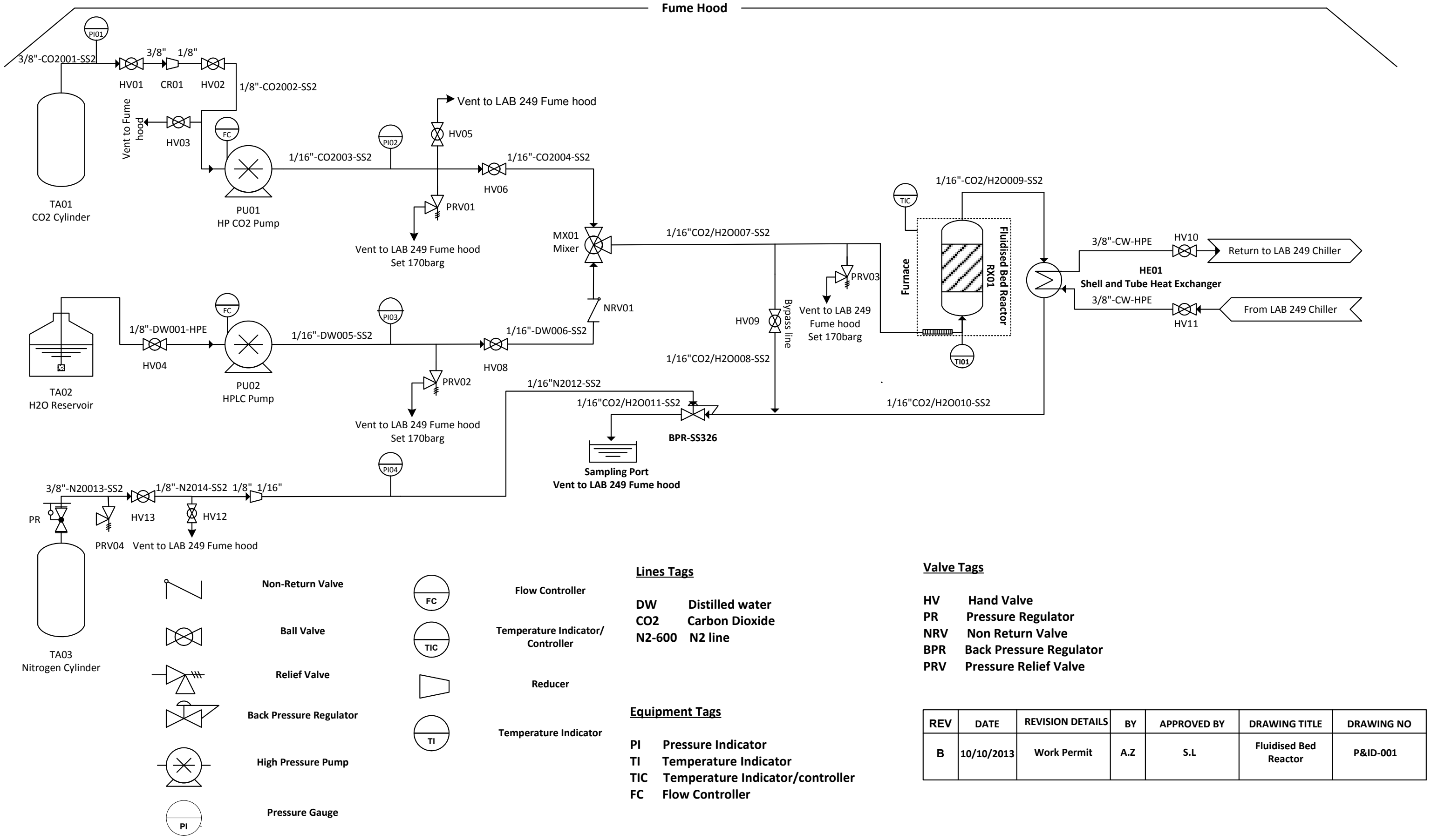

Figure C-2. Process flow diagram of the experimental set-up used for the high-pressure experiments.

Table C-8. Summary of the total mass flow rates, flow densities, and the corresponding volumetric flow rates for experiments carried out at a constant reaction temperature, a constant CO_2 molality, and variable pressures, as indicated in the table.

Constant Temperature Conditions and Variable CO_2 Partial Pressures (molality and total volumetric flow rate constant, (a))

Reactor Conditions

T (K)	423	423	423	423	423	423	423	423	423	423
P (bar)	160	150	140	130	120	110	100	90	80	70
$\dot{V}_m$ (cm^3 min^{-1})	2.12	2.12	2.12	2.12	2.12	2.12	2.12	2.12	2.12	2.12
m_{CO2} (mol kg^{-1})	3.70	3.70	3.70	3.70	3.70	3.70	3.70	3.70	3.70	3.70
m_{CO2}/m_{H2O} (kg_{CO2}/kg_{H2O})	0.16	0.16	0.16	0.16	0.16	0.16	0.16	0.16	0.16	0.16
ρ (g mL^{-1})	0.70	0.68	0.66	0.64	0.61	0.58	0.55	0.52	0.48	0.43
$\dot{m}$ (g min^{-1})	1.49	1.45	1.41	1.35	1.30	1.23	1.17	1.09	1.01	0.92
$\dot{m}_{CO2}$ (g min^{-1})	0.21	0.20	0.20	0.19	0.18	0.17	0.16	0.15	0.14	0.13
$\dot{m}_{H2O}$ (g min^{-1})	1.28	1.24	1.21	1.16	1.12	1.06	1.00	0.94	0.87	0.79
pH of the starting solution*	3.30	3.31	3.33	3.35	3.36	3.38	3.40	3.43	3.46	3.49
Equilibrium solubility of the CO_2 (*aq*) (mol kg^{-1})*	1.02	0.98	0.93	0.87	0.82	0.76	0.70	0.64	0.57	0.51

Pump Conditions

T (K)	298	298	298	298	298	298	298	298	298	298
P (bar)	160	150	140	130	120	110	100	90	80	70
ρ_{CO2} (g mL^{-1})	0.89	0.88	0.87	0.86	0.85	0.83	0.82	0.80	0.78	0.74
ρ_{H2O} (g mL^{-1})	1.01	1.00	1.00	1.00	1.00	1.00	1.00	1.00	1.00	1.00
$\dot{V}_{CO2}$ (mL min^{-1})	0.24	0.23	0.23	0.22	0.22	0.21	0.20	0.19	0.18	0.17
$\dot{V}_{H2O}$ (mL min^{-1})	1.274	1.238	1.203	1.157	1.116	1.056	1.000	0.940	0.866	0.787
Molality (mol kg^{-1})	3.70	3.70	3.70	3.70	3.70	3.70	3.70	3.70	3.70	3.70

**Calculated with OLI-MSE (mol kg^{-1} of solvent)*

Table C-9. Summary of the total mass flow rates, flow densities, and the corresponding volumetric flow rates for experiments carried out at a constant reaction temperature and variable pressures and CO_2 molaities, as indicated in the table.

Constant Temperature Conditions and Variable CO_2 Partial Pressures (water flow rate is constant, molality is variable, (b))

Reactor Conditions

T (K)	423	423	423	423	423	423	423	423	423	423
P (bar)	160	150	140	130	120	110	100	90	80	70
$\dot{V}_m$ (cm^3 min^{-1})	2.12	2.12	2.12	2.12	2.12	2.12	2.12	2.12	2.12	2.12
m_{CO2} (mol kg^{-1})	6.22	5.85	5.40	5.00	4.55	4.10	3.70	3.30	2.90	2.50
m_{CO2}/m_{H2O} (kg_{CO2}/kg_{H2O})	0.27	0.26	0.24	0.22	0.20	0.18	0.16	0.15	0.13	0.11
ρ (g mL^{-1})	0.60	0.59	0.58	0.57	0.57	0.56	0.55	0.54	0.53	0.53
$\dot{m}$ (g min^{-1})	1.28	1.25	1.24	1.22	1.20	1.19	1.17	1.15	1.13	1.11
$\dot{m}_{CO2}$ (g min^{-1})	0.27	0.26	0.24	0.22	0.20	0.18	0.16	0.15	0.13	0.11
$\dot{m}_{H2O}$ (g min^{-1})	1.00	1.00	1.00	1.00	1.00	1.00	1.00	1.00	1.00	1.00
pH of the starting solution*	3.30	3.31	3.33	3.35	3.36	3.38	3.40	3.43	3.46	3.49
Equilibrium solubility of the CO_2 (*aq*) (mol kg^{-1})*	1.02	0.98	0.93	0.87	0.82	0.76	0.70	0.64	0.57	0.51

Pump Conditions

T (K)	298	298	298	298	298	298	298	298	298	298
P (bar)	160	150	140	130	120	110	100	90	80	70
ρ_{CO2} (g mL^{-1})	0.89	0.88	0.87	0.86	0.85	0.83	0.82	0.80	0.78	0.74
ρ_{H2O} (g mL^{-1})	1.00	1.00	1.00	1.00	1.00	1.00	1.00	1.00	1.00	1.00
$\dot{V}_{CO2}$ (mL min^{-1})	0.31	0.29	0.27	0.26	0.24	0.22	0.20	0.18	0.16	0.15
$\dot{V}_{H2O}$ (mL min^{-1})	1.00	1.00	1.00	1.00	1.00	1.00	1.00	1.00	1.00	1.00
Molality (mol kg^{-1})	6.22	5.85	5.40	5.00	4.55	4.10	3.70	3.30	2.90	2.50

**Calculated with OLI-MSE (mol kg^{-1} of solvent)*

Table C-10. Summary of the total mass flow rates, flow densities, and the corresponding volumetric flow rates for experiments carried out at a constant pressure, a constant CO_2 molality and variable reaction temperatures, as indicated in the table.

Constant CO_2 Partial Pressure Conditions and Variable Reaction Temperatures

Reactor Conditions

T (K)	303	333	363	393	423	438	453	468
P (bar)	100	100	100	100	100	100	100	100
$\dot{V}_m$ (cm^3 min^{-1})	2.12	2.12	2.12	2.12	2.12	2.12	2.12	2.12
m_{CO2} (mol kg^{-1})	3.70	3.70	3.70	3.70	3.70	3.70	3.70	3.70
m_{CO2}/m_{H2O} (kg_{CO2}/kg_{H2O})	0.16	0.16	0.16	0.16	0.16	0.16	0.16	0.16
ρ (g mL^{-1})	0.97	0.78	0.67	0.61	0.55	0.52	0.50	0.47
$\dot{m}$ (g min^{-1})	2.06	1.65	1.42	1.28	1.17	1.11	1.06	1.00
$\dot{m}_{CO2}$ (g min^{-1})	0.29	0.23	0.20	0.18	0.16	0.16	0.15	0.14
$\dot{m}_{H2O}$ (g min^{-1})	1.77	1.42	1.22	1.10	1.00	0.96	0.91	0.86
pH of the starting solution*	3.03	3.07	3.17	3.28	3.40	3.47	3.54	3.62
Equilibrium solubility of the CO_2 (*aq*) (mol kg^{-1})*	1.34	1.04	0.83	0.73	0.70	0.69	0.69	0.69

Pump Conditions

T (K)	298	298	298	298	298	298	298	298
P (bar)	100	100	100	100	100	100	100	100
ρ_{CO2} (g mL^{-1})	0.82	0.82	0.82	0.82	0.82	0.82	0.82	0.82
ρ_{H2O} (g mL^{-1})	1.00	1.00	1.00	1.00	1.00	1.00	1.00	1.00
$\dot{V}_{CO2}$ (mL min^{-1})	0.35	0.28	0.24	0.22	0.20	0.19	0.18	0.17
$\dot{V}_{H2O}$ (mL min^{-1})	1.768	1.417	1.218	1.101	1.00	0.954	0.905	0.854
Molality (mol kg^{-1})	3.70	3.70	3.70	3.70	3.70	3.70	3.70	3.70

**Calculated with OLI-MSE (mol kg^{-1} of solvent)*

Low-pressure Experimental Apparatus

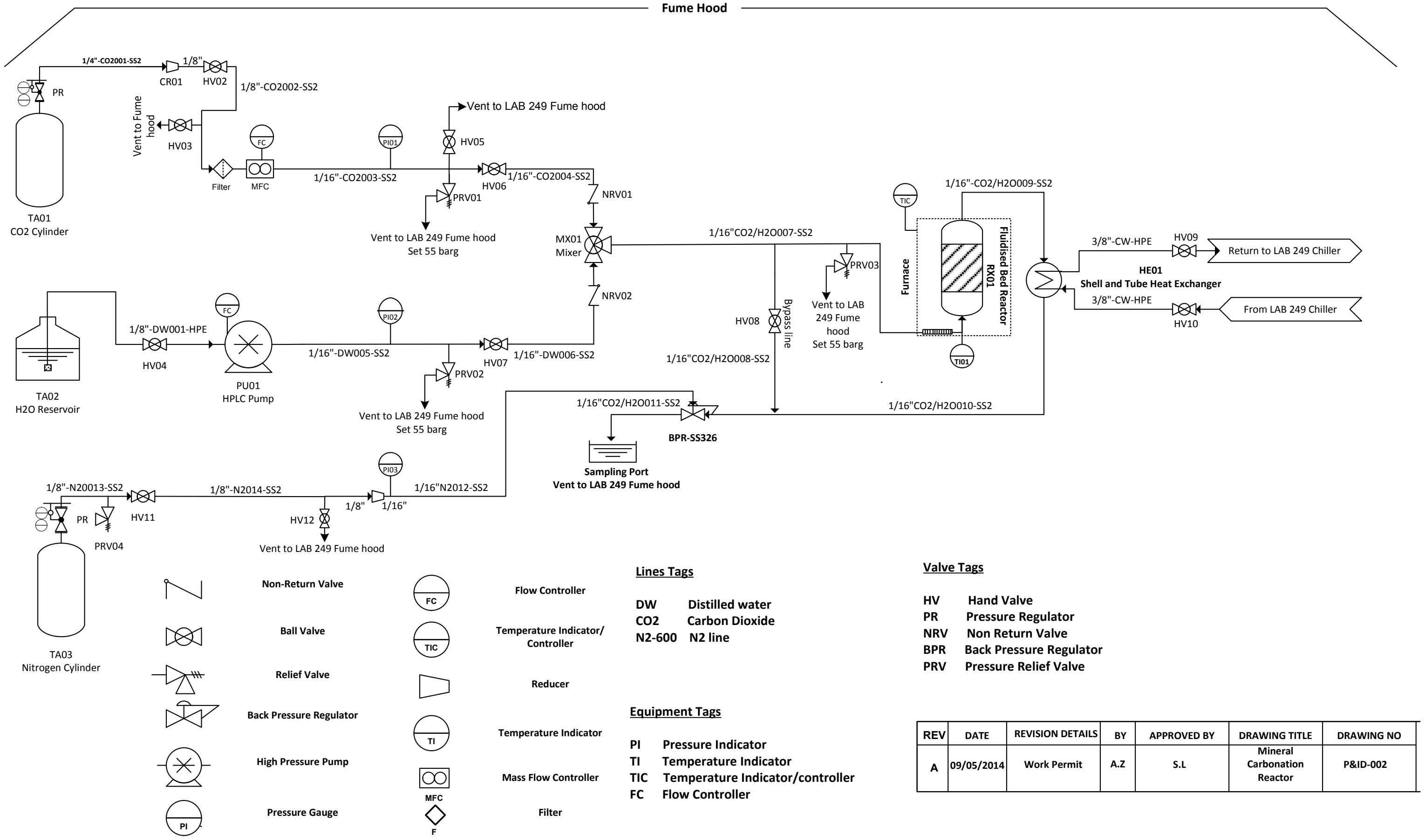

Lines Tags

DW	Distilled water
CO2	Carbon Dioxide
N2-600	N2 line

Equipment Tags

PI	Pressure Indicator
TI	Temperature Indicator
TIC	Temperature Indicator/controller
FC	Flow Controller

Valve Tags

HV	Hand Valve
PR	Pressure Regulator
NRV	Non Return Valve
BPR	Back Pressure Regulator
PRV	Pressure Relief Valve

REV	DATE	REVISION DETAILS	BY	APPROVED BY	DRAWING TITLE	DRAWING NO
A	09/05/2014	Work Permit	A.Z	S.L	Mineral Carbonation Reactor	P&ID-002

Figure C-3. Process flow diagram of the experimental set-up used for the low-pressure experiments.

Table C-11. Summary of the total mass flow rates, flow densities, and the corresponding volumetric flow rates for experimental conditions corresponded to a constant reaction temperature and low-pressure conditions, as indicated in the table.

Constant Temperature Conditions and CO_2 Partial Pressure 10 and 20 bar (variable molality)		
Reactor Conditions		
T (K)	423	423
P (bar)	20	10
$\dot{V}_m$ ($cm^3\ min^{-1}$)	2.12	2.12
m_{CO2} ($mol\ kg^{-1}$)	0.58	0.20
m_{CO2}/m_{H2O} (kg_{CO2}/kg_{H2O})	0.03	0.01
ρ ($g\ mL^{-1}$)	0.48	0.48
$\dot{m}$ ($g\ min^{-1}$)	1.03	1.01
$\dot{m}_{CO2}$ ($g\ min^{-1}$)	0.03	0.01
$\dot{m}_{H2O}$ ($g\ min^{-1}$)	1.00	1.00
pH of the starting solution*	3.80	4.03
Equilibrium solubility of the CO_2 (*aq*) ($mol\ kg^{-1}$)*	0.12	0.04
H_2O Pump Conditions		
T (K)	25	25
P (bar)	20	10
ρ_{H2O} ($g\ mL^{-1}$)	1.00	1.00
$\dot{V}_{H2O}$ ($mL\ min^{-1}$)	1.00	1.00
Mass Flow Controller (MFC) Conditions		
T (K)	298	298
P (bar)	1.00	1.00
ρ_{CO2} ($g\ mL^{-1}$)	0.0017	0.0017
$\dot{V}_{MFC\text{-}CO2}$ ($mL\ min^{-1}$)	13.95	4.81

**Calculated with OLI-MSE (mol kg^{-1} of solvent)*

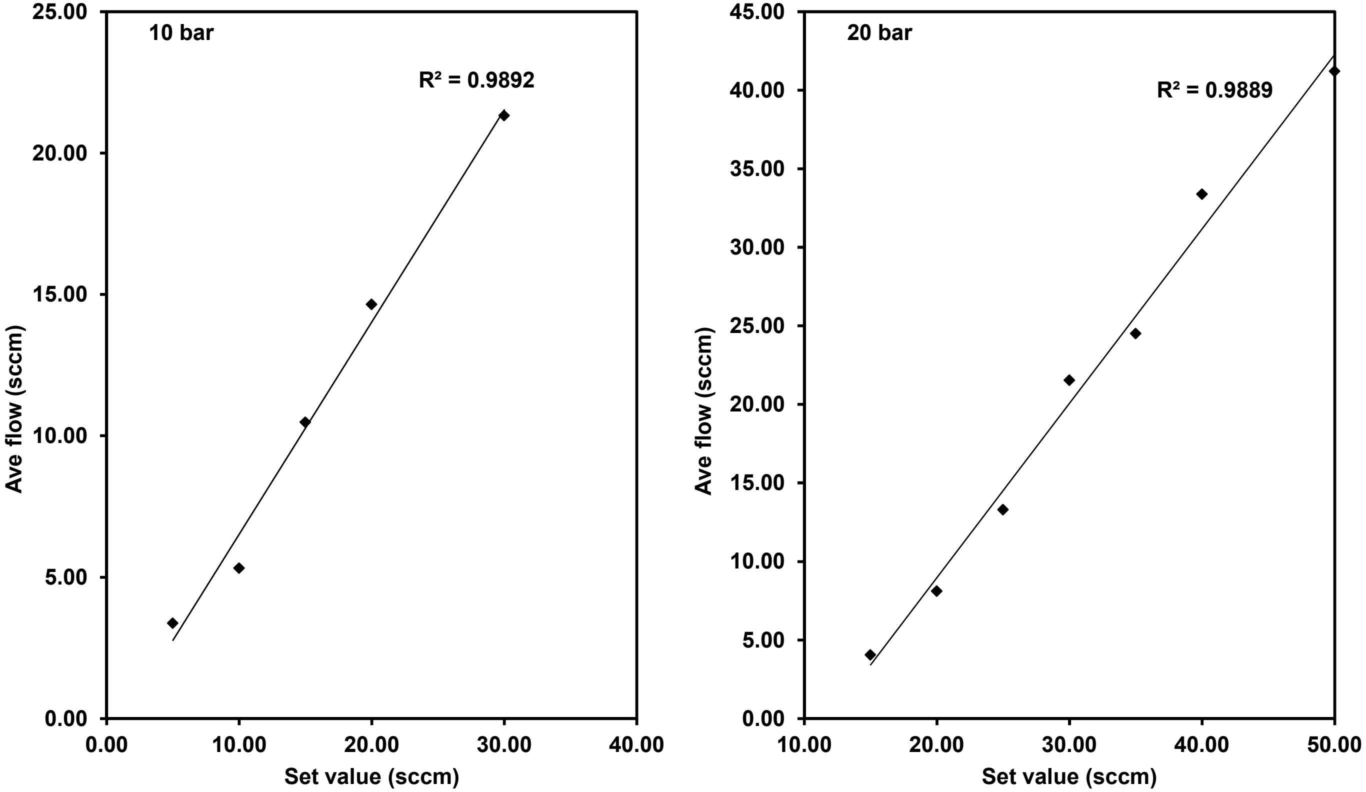

Figure C-4. The calibration curves of carbon dioxide mass flow controller (MFC), used for experiments conducted at CO_2 partial pressures of 10 bar and 20 bar, solid lines indicate the linear regression fitting.

References

CHITESTER, D. C., KORNOSKY, R. M., FAN, L.-S. & DANKO, J. P. 1984. Characteristics of fluidization at high pressure. *Chemical Engineering Science,* 39**,** 253-261.

GELDART, D. 1973. Types of gas fluidization. *Powder technology,* 7**,** 285-292.

GRACE, J. R. 1986. Contacting modes and behaviour classification of gas—solid and other two-phase suspensions. *The Canadian Journal of Chemical Engineering,* 64**,** 353-363.

Appendix D. Data Sets Related to Section 4.3

Table D-1 and Table D-2 show the variation of the reported data sets in Figure4-16 and Figure 4-26, at the selective degrees of conversion. The point is the apparent cluster behaviour of the data indicates more-or-less they are the same and, in fact, proceeding with a very similar trend – it is also clear through the values of the standard deviations.

Table D-1. Magnesium and silica concentrations at the indicated degrees of conversion and the corresponding Mg/Si ratios, for the experimental results presented in Figure 4-16, Figure 4-18, and Figure 4-20, respectively.

T = 423 K, and constant m_{CO2} = 3.7 mol kg^{-1} (variable water flow rate as illustrated in Table C-8)								
Pressure (bar)	C_{Mg} (mol kg^{-1} of solvent)			C_{si} (mol kg^{-1} of solvent)		Mg/Si (-)		
	X_{Mg}=0.10	X_{Mg}=0.30	X_{Mg}=0.50	X_{Si}=0.10	X_{Si}=0.30	X_{Mg}=0.10	X_{Mg}=0.30	X_{Mg}=0.50
70	0.024	0.014	0.006	0.006	0.004	3.166	2.468	1.411
80	0.024	0.013	0.005	0.005	0.005	3.729	2.537	1.171
90	0.021	0.015	0.007	0.006	0.005	3.594	2.639	1.368
100	0.027	0.016	0.011	0.007	0.006	3.661	2.692	1.747
110	0.024	0.015	0.011	0.009	0.007	2.867	1.826	1.349
120	0.028	0.019	0.010	0.007	0.006	4.034	2.722	1.659
130	0.029	0.018	0.010	0.009	0.007	3.586	2.094	1.364
140	0.023	0.016	0.013	0.009	0.008	2.617	2.988	1.582
150	0.036	0.018	0.010	0.009	0.008	4.225	2.049	1.357
160	0.031	0.016	0.009	0.006	0.008	4.513	2.666	1.782
Standard Deviation	±0.004	±0.002	±0.002	±0.002	±0.001	±0.589	±0.363	±0.201

Table D-2. Magnesium and silica concentrations at the indicated degrees of conversion and the corresponding Mg/Si ratios, for the experimental results presented in Figure 4-26, Figure 4-28, and Figure 4-30, respectively.

T = 423 K, and variable m_{CO2} (constant water flow rate as illustrated in Table C-9)								
Pressure (bar)	C_{Mg} (mol kg^{-1} of solvent)			C_{si} (mol kg^{-1} of solvent)		Mg/Si (-)		
	X_{Mg}=0.10	X_{Mg}=0.30	X_{Mg}=0.50	X_{Si}=0.10	X_{Si}=0.30	X_{Mg}=0.10	X_{Mg}=0.30	X_{Mg}=0.50
70	0.023	0.018	0.011	0.008	0.008	3.870	2.227	1.415
80	0.024	0.013	0.008	0.008	0.005	3.211	1.756	1.413
90	0.024	0.017	0.008	0.006	0.005	3.804	2.665	1.342
100	0.027	0.019	0.011	0.007	0.006	3.661	2.505	1.747
110	0.031	0.018	0.009	0.007	0.006	4.016	2.729	1.492
120	0.034	0.020	0.010	0.007	0.005	4.957	2.860	1.588
130	0.028	0.017	0.009	0.007	0.005	4.031	2.710	1.450
140	0.033	0.018	0.008	0.006	0.005	3.640	3.052	1.620
150	0.033	0.016	0.006	0.009	0.007	3.640	1.855	0.829
160	0.031	0.017	0.007	0.006	0.006	5.069	2.913	1.058
Standard Deviation	±0.004	±0.002	±0.002	±0.001	±0.001	±0.588	±0.443	±0.271

Appendix E. Aqueous Leachate / Solid Residual Analysis

Transmission Electron Microscopy (TEM) analysis was performed on the aqueous leachate acquired from the standard dissolution reaction. A JEOL 14400 transmission electron microscope was used at accelerating voltage of 120 kV for this analysis. It is demonstrated that after approximately 96 hours from the termination point of the dissolution reaction, the detached silica particles in the aqueous effluent start to grow in which they were detected by TEM analysis as illustrated in Figure E-1. This observation signified that during the dissolution reactions the nano silica particles were separated from the mineral structure and were released into the aqueous phase. This attribute has been consistently reported in previous studies (e.g., Shao et al., 2011, Cai et al., 2009). Shao et al. (2011) investigated the chemical and physical interactions of the phlogopite-CO_2-H_2O system – through the HR-TEM analysis; they concluded that the aggregated particles in the aqueous phase are likely to be amorphous silica.

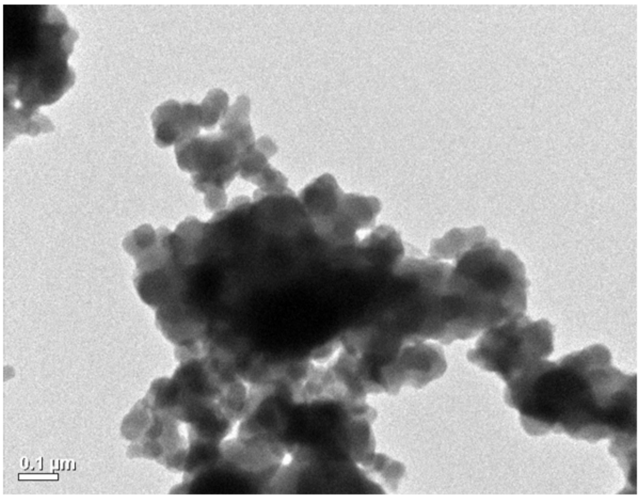

Figure E-1. TEM image is for amorphous silica particles agglomerated in the aqueous leachate obtained from a dissolution reaction of thermally activated SWOL under the saturated CO_2-H_2O system (P_{CO2} = 100 bar, T = 423 K).

In this study, the observed suspended particles in the aqueous phase were separated using a PTFE membrane (containing pore size of 0.1 µm). The accumulated material on the membrane was air-dried and stored for further examinations. The X-ray diffraction (XRD) analysis (using a Shimadzu XRD-6000 with CuK_α X-ray source) was employed to characterise the structure of the acquired synthesised powder. This analysis reveals that powder has a non-crystalline structure as it shown in Figure E-2. This observation is matched with what was reported through previous studies for the XRD examination of amorphous silica (e.g., GUAN and QIU-MIN, 2010, Musić et al., 2011). These authors observed similar XRD spectra with a diffusive peak apparent within a range of 20-30 of the 2θ degrees. They concluded that this XRD pattern is attributed to a typical structure of hydrated amorphous silica. In the present study, further compositional analysis for the accumulated powder is provided in Table E-1, which confirms that these agglomerated particles are mainly comprised of silica along with the minor amount of MgO.

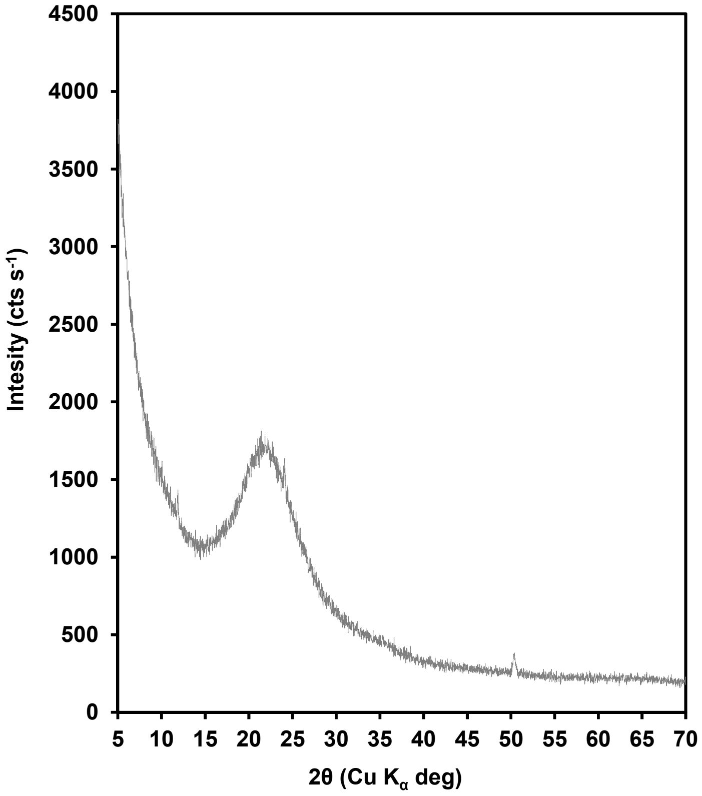

Figure E-2. *Ex situ* powdered XRD for collected powder (filtered material).

Additional studies were conducted to examine the structural transformation of the residual solids acquired from the reactions at standard operating conditions (T = 423 K and P_{CO2} = 100 bar). The qualitative XRD analysis was performed by using a Shimadzu XRD-6000 instrument with CuK$_\alpha$ X-ray source. Scans were taken for 2θ, within a range of 5 to 70 degree with a step size of 0.02 degree per 2θ at a rate of 0.24 deg min^{-1}. The XRD patterns of the residual solids indicate a non-detectable transformation of dominate mineralogical phase related to feedstock over the reactions period (no sign of secondary phases such as thick non-amorphous silica layers or magnesite formation was noted), as illustrated in Figure E-3. Moreover, the evolution of the chemical composition of the residual solids (acquired from the dissolution reactions conducted at standard operating conditions) was evaluated by SEM-EDS analysis as shown in Table E-1. The SEM-EDS method was reported as a useful approach for distinguishing serpentine phases and identifying the chemical composition of minerals (O'Hanley and Dyar, 1998). In the present study, quantitative SEM-EDS analyses were performed to characterise the bulk chemical composition of the feedstocks material and residual solids. All samples were mounted in the epoxy moulds. Moulds were polished within three stages and coated with a 20-25 nm thickness of the carbon. The un-normalised quantitative EDS data were collected based on the calibrated beam current using the standard material (copper). These data are illustrated in Table E-1, which are obtained based on the average of more than 500 spots analysed for each specimen. This analysis shows that the solids are relatively depleted with respect to the initial magnesium content as the reaction time increases, whereas the relative amount of silica remained more-or-less unchanged. This phenomenon may be justified by the dissolution-reprecipitation process that leads to deposit the silica on the reactive surfaces. However, it is noted that the thickness of the developed silica layers should not be sufficient to be detected by the presented XRD patterns or they are highly amorphous.

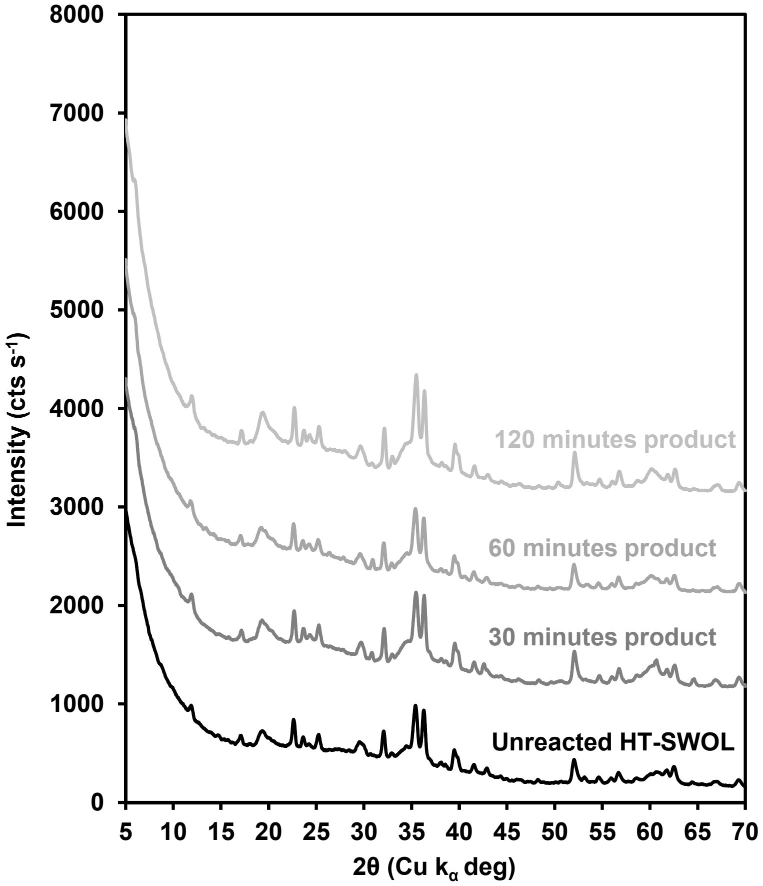

Figure E-3. *Ex situ* powdered XRD for the unreacted thermally activated SWOL (as a parent material) and post-leached products as a function of the reactor residence time.

Table E-1. Summary of the quantitative SEM-EDS analyses for the major components of the indicated materials. The presented total is based on the unnormalised calculation, and the detected Fe spectrum presumably is related to Fe_2O_3 content.

Material	Major components (mass wt.%)					
	MgO	SiO_2	Fe_2O_3	Al_2O_3	NiO	Total
SWOL	36.47	40.01	10.54	1.55	0.05	88.62
HT-SWOL*	42.52	49.00	5.44	1.23	0.14	98.33
30 min Product**	32.02	45.51	10.54	1.72	0.03	89.81
60 min Product**	30.52	47.67	10.12	2.00	0.04	90.35
120 min Product**	22.40	50.06	9.36	2.94	0.31	85.07
Filtered Powder	8.83	80.45	0.03	0.38	0.00	89.69

*45-63 *μm SWOL activated at 900 K for 2 hours*

** *$T = 423$ K and $P_{CO2} = 100$ bar, mass loading factor 0.25 min*

References

CAI, X., HONG, R., WANG, L., WANG, X., LI, H., ZHENG, Y. & WEI, D. 2009. Synthesis of silica powders by pressured carbonation. *Chemical Engineering Journal,* 151, 380-386.

GUAN, J. & QIU-MIN, Z. 2010. Preparation of amorphous silica from oil shale residue and surface modification by silane coupling agent. *Oil Shale,* 27, 37-46.

MUSIĆ, S., FILIPOVIĆ-VINCEKOVIĆ, N. & SEKOVANIĆ, L. 2011. Precipitation of amorphous SiO_2 particles and their properties. *Brazilian journal of chemical engineering,* 28, 89-94.

O'HANLEY, D. S. & DYAR, M. D. 1998. The composition of chrysotile and its relationship with lizardite. *Canadian mineralogist,* 36, 727-740.

SHAO, H., RAY, J. R. & JUN, Y.-S. 2011. Effects of salinity and the extent of water on supercritical CO_2-induced phlogopite dissolution and secondary mineral formation. *Environmental science & technology,* 45, 1737-1743.

Appendix F. Temperature Dependence of the Rate Law

In elementary reactions one of the important parameters influences the rate expression is a function of reaction temperature as shown schematically by equation (F.1).

$$\begin{aligned} r_i &= f(temperature) \cdot f(composition) \\ &= k \cdot f(composition) \end{aligned} \tag{F.1}$$

The temperature-dependence term (k) can be presented in accordance with the Arrhenius expression, as shown by equation (F.2).

$$k = Ae^{-E_a/RT} \tag{F.2}$$

where A is the pre-exponential factor, E_a is the apparent activation energy (kcal mol^{-1}), T is the temperature (K), and R is the gas constant (kcal mol^{-1}). Apparent activation energy (E_a) can be predicted based on the acquired experimental data at two different temperatures. By substituting equation (F.2) into equation (F.1), the apparent activation energy can be estimated in accordance with equation (F.3),

$$ln(r_1/r_2) = E_a/R(1/T_2 - 1/T_1) \tag{F.3}$$

In several previous studies, the apparent activation energy was termed as a pH-dependent activation energy since the equilibrium adsorption and desorption of the protons on the reactive surfaces vary during the reaction depending on the experimental conditions (Chen and Brantley, 1997, Chen and Brantley, 2000). The influence of the pH has led to a considerable variation in published values of the apparent activation energy for forsterite dissolution, as shown in Table F-1. In the present approach of estimating the apparent activation energy, the effect of pH variation is not taken into account. In addition, in order to facilitate the comparison, the calculations are performed with a constant degree of conversion. The apparent activation energy of the elementary reactions participating in dissolution process is evaluated based on the experimental rate values determined for five different reaction temperatures.

Table F-1. Summary of activation energies reported in the literature for forsterite dissolution.

Material	E_α (kcal mol^{-1})	pH	References
Forsterite	14-16	1	(Sanemasa et al., 1972)
Forsterite	19 ± 2.5	1.8-6	(Wogelius and Walther, 1992)
Forsterite	10.2 ± 0.2	1.8-3.8	(Rosso and Rimstidt, 2000)
Forsterite	30 ± 4	2-5	(Chen and Brantley, 2000)
Forsterite	12.65 ± 1.65	2-8	(Hänchen et al., 2006)

Previous studies were underlined that the rate of the dissolution reaction is importantly influenced by the rate of transport of solute away from the reaction interfaces (Weyl, 1958). Therefore, a series of dissolution experiments with a constant volumetric flow rate of the aqueous phase under the saturated CO_2-H_2O system at CO_2 partial pressure of 100 bar and the constant mass loadings (250 mg of the activated SWOL, and corresponding mass loading factor of 0.25 min) conditions was performed. Figure F-1 shows the results obtained for the identical flow and reactor conditions for the concentration of aqueous magnesium in the effluent and corresponding evolution of the degrees of conversion, X_{Mg}.

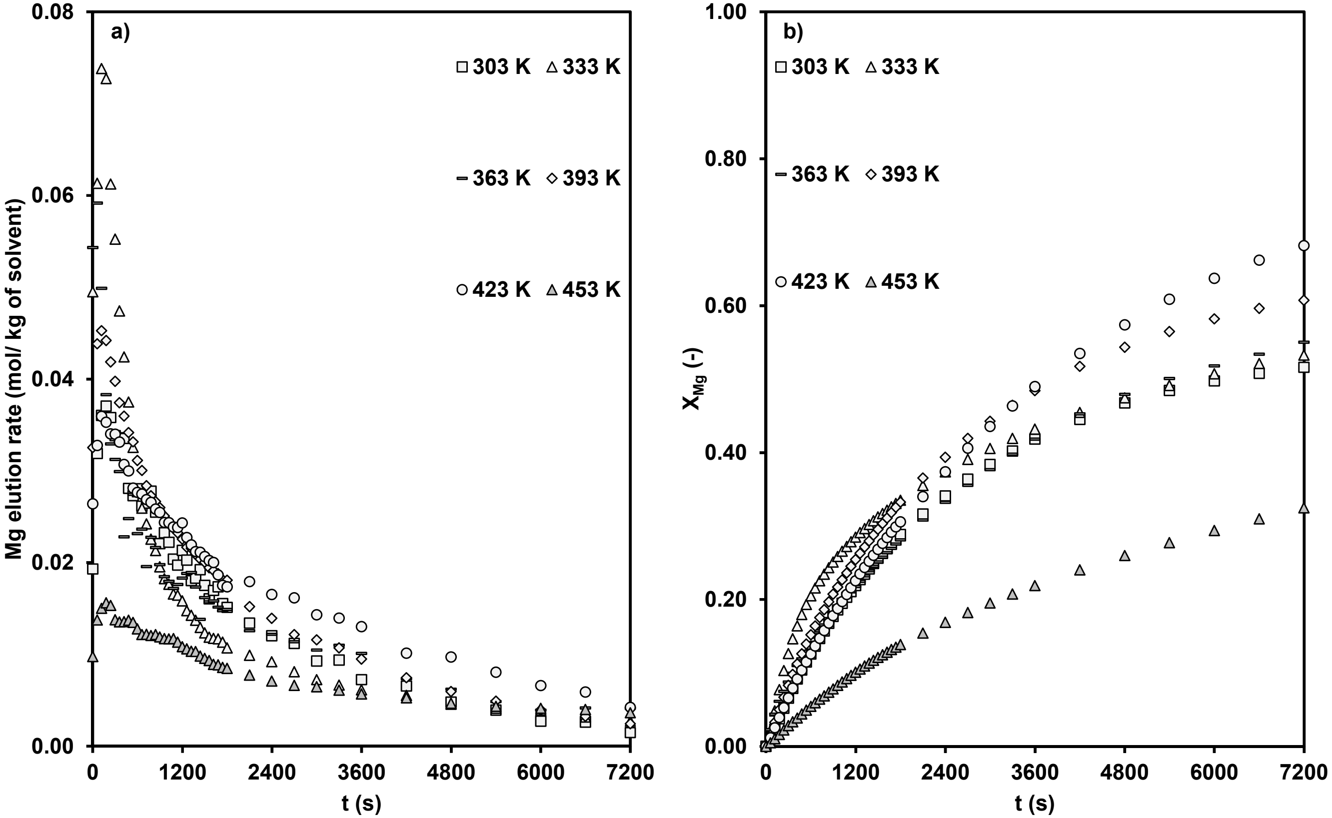

Figure F-1. Dissolution profiles of magnesium for thermally activated SWOL (PSD = 45-63 μm) under the saturated CO_2-H_2O system as a function of the indicated reaction temperatures (in the figure), at P_{CO2} = 100 bar, and 120 minutes reaction time, (a) magnesium concentration, (b) degrees of completion of magnesium extraction.

In order to evaluate the apparent activation energy, the experimental dissolution rates of experiments with different reaction temperatures are interpreted based on the integration of the linear kinetics in accordance with the equation (F.4). This kinetic expression is derived similarly to the experimental studies of water-rock kinetics using the flow-through reactor (Chou and Wollast, 1984, Lasaga, 1998).

$$r = \left(dC_{Mg}/dt\right)V/(A_s M_0) \tag{F.4}$$

where C_{Mg} (mol L^{-1}) is the concentration, t is time (s), V is the volume of the solution (L), A_s (cm^2 g^{-1}) is the specific surface area of the starting material[1] (11.96 m^2 g^{-1}), and M_0 is the mass of material depositing into the reactor (g). A summary of calculations is shown in Table F-2.

Table F-2. Summary of the operating conditions and the experimental conversion rates for experiments carried out under the saturated CO_2-H_2O system at P_{CO2} = 100 bar, 120 minutes reaction period and constant aqueous flow rate.

Temperature (K)	Dissolution Rate (r_{Mg}) (mol cm^{-2} S^{-1})	log (r_{Mg})	Mass Loading Factor (min^{-1})	Extend of Conversion X_{Mg} (%)
303	1.52×10^{-12}	-27.21	0.25	50
333	2.20×10^{-12}	-26.84	0.25	50
363	2.71×10^{-12}	-26.63	0.25	50
393	4.16×10^{-12}	-26.21	0.25	50
423	5.64×10^{-12}	-25.90	0.25	50

According to Arrhenius expression, the slope of the linear regression line must be equal to $-E_a/R$; hence, the apparent activation energy is estimated as ~2.7 kcal mol^{-1}, as shown in Figure F-2.

---

[1] In this study, final surface area of the residual solids is not determined; therefore, in order to evaluate the apparent activation energy, the initial surface area of the used material is employed.

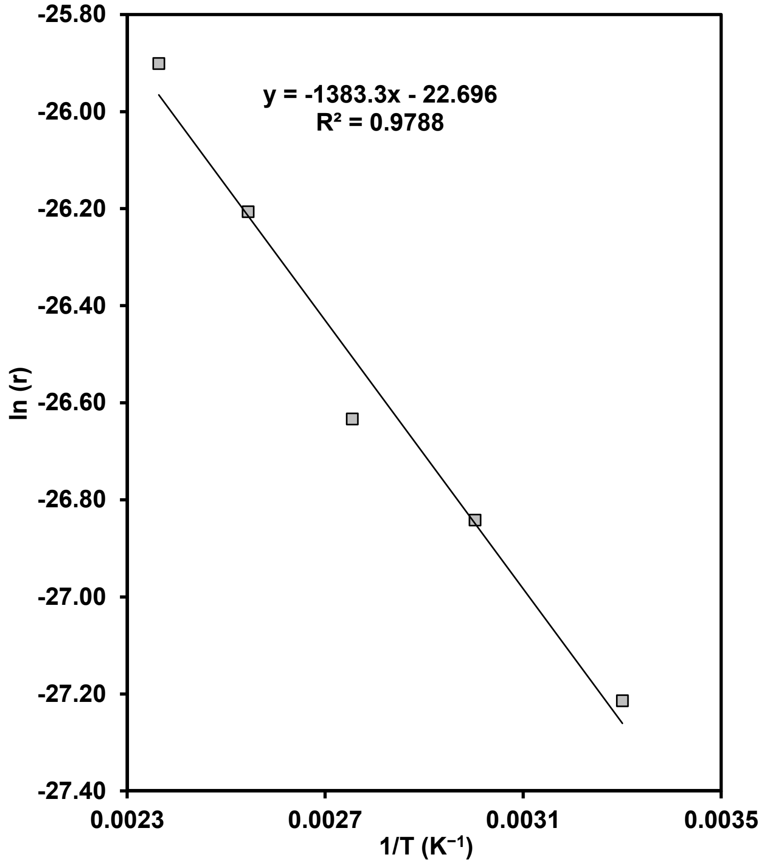

Figure F-2. Arrhenius plot ln(r) versus (1/T), squares represent the experimental data, and the solid line indicates the linear regression fitting.

It is worth noting that the activation energy of an overall reaction is a composite of several activation energies corresponds to a series of elementary reactions comprising the reaction mechanism. Therefore, the calculated activation energy for an overall reaction cannot be represented by any molecular energy barrier (Lasaga, 1998). Additionally, Lasaga et al. (1998) stressed that proportion to the progress of the reaction the pH along with many other variables (e.g., reaction interfaces) changes; thus, the calculated activation energy represents for many terms and must be called an apparent activation energy. According to Lasaga (1981) and Casey and Sposito (1992), low activation energies up to 5 kcal mol^{-1} have been interpreted as an indication for the diffusion-controlled reactions. The relatively low apparent activation energy associated with the presently measured rates, suggesting that the mechanism of the dissolution reactions ultimately controlled by the diffusion process.

References

CASEY, W. H. & SPOSITO, G. 1992. On the temperature dependence of mineral dissolution rates. *Geochimica et Cosmochimica Acta,* 56**,** 3825-3830.

CHEN, Y. & BRANTLEY, S. L. 1997. Temperature-and pH-dependence of albite dissolution rate at acid pH. *Chemical Geology,* 135**,** 275-290.

CHEN, Y. & BRANTLEY, S. L. 2000. Dissolution of forsteritic olivine at 65^{o}C and 2< pH< 5. *Chemical Geology,* 165**,** 267-281.

CHOU, L. & WOLLAST, R. 1984. Study of the weathering of albite at room temperature and pressure with a fluidized bed reactor. *Geochimica et Cosmochimica Acta,* 48**,** 2205-2217.

HÄNCHEN, M., PRIGIOBBE, V., STORTI, G., SEWARD, T. & MAZZOTTI, M. 2006. Dissolution kinetics of fosteritic olivine at 90–150°C including effects of the presence of CO_2. *Geochimica et Cosmochimica Acta,* 70**,** 4403-4416.

LASAGA, A. C. 1998. *Kinetic theory in the earth sciences*, Princeton University Press.

LASAGA, A. C. 1981. Rate laws of chemical reactions. *Rev. Mineral.;(United States),* 8.

ROSSO, J. J. & RIMSTIDT, J. D. 2000. A high resolution study of forsterite dissolution rates. *Geochimica et Cosmochimica Acta,* 64**,** 797-811.

SANEMASA, I., YOSHIDA, M. & OZAWA, T. 1972. The dissolution of olivine in aqueous solutions of inorganic acids. *Bulletin of the chemical society of Japan,* 45**,** 1741-1746.

WEYL, P. K. 1958. The solution kinetics of calcite. *The Journal of Geology***,** 163-176.

WOGELIUS, R. A. & WALTHER, J. V. 1992. Olivine dissolution kinetics at near-surface conditions. *Chemical Geology,* 97**,** 101-112.

Appendix G. Fluid-Particle Reaction Models

Considering the simplest case of solid-fluid reaction,

$$aB_{(fluid\ reactant)} + A_{(s)} \rightarrow \text{products}$$

where A is the solid reacting in fluid B, and it converts to products. Different reaction models were examined in the current study.

G-1. Volumetric Reaction Model

A volumetric reaction model is the one in which the rate of chemical reaction is uniform through the diameter of a reacting particle. It is often assumed that the reaction rate per unit volume is proportional to the concentration of the fluid reactant, and nonetheless is independent of the solid reactant concentration. Under the assumption of this model, the solid contains enough porosity to pass the fluid reactant and the fluid product freely (Ishida and Wen, 1971). The disappearance rate of A (per unit volume), can be shown by equation (G.1),

$$-\frac{dC_A}{dt} = k_v C_A^n C_B \tag{G.1}$$

where C_B is the concentration of fluid reactant, C_A is the concentration of reacting solid and k_v is the rate constant (moles per unit time per unit volume). Assuming the reaction is first order with respect to reactant B, and is independent of the solid concentration ($n = 0$); thus, the molar rate of disappearance of solid A can be written as,

$$-\frac{dN_A}{dt} = kN_B V_A \tag{G.2}$$

where V_A is the volume of a reacting solid particle, and k is the rate constant accounting reaction mechanism,

$$-\frac{dN_A}{dt} = kN_B V_A|_0 (1 - X_A) \tag{G.3}$$

thus, the equation (G.3) can be rearranged to equation (G.4) with respect to the fractional conversion,

$$\frac{dX_A}{dt} = (1 - X_A)\frac{k_v N_B}{N_A|_0} \tag{G.4}$$

therefore, the shape of the rate function $f(X)$ can be written in terms of the dimension less rate as,

$$\therefore \frac{dX_A}{dt} = (1 - X_A) \times C_{Constant} \tag{G.5}$$

G-2. Shrinking Core Models

Typically in shrinking core models, reacting particles may undergo the changing in size and shape during the reaction and even a product layer may be formed around them. The reaction often first initiates at the outer skin of the particles and then moves inwards from the particle surface to the interface between reacted and unreacted solid. Under the conditions that the rates of diffusion through fluid-film and porous reaction layer (interface) are very fast, the overall rate of reaction is only controlled by chemical reactivity of the solid reactant (Levenspiel, 1999). The rate becomes proportional to the available surface of the unreacted core. Figure G-1 shows a schematic diagram of shrinking particle with unreacted shrinking core when the chemical reaction is controlling resistance.

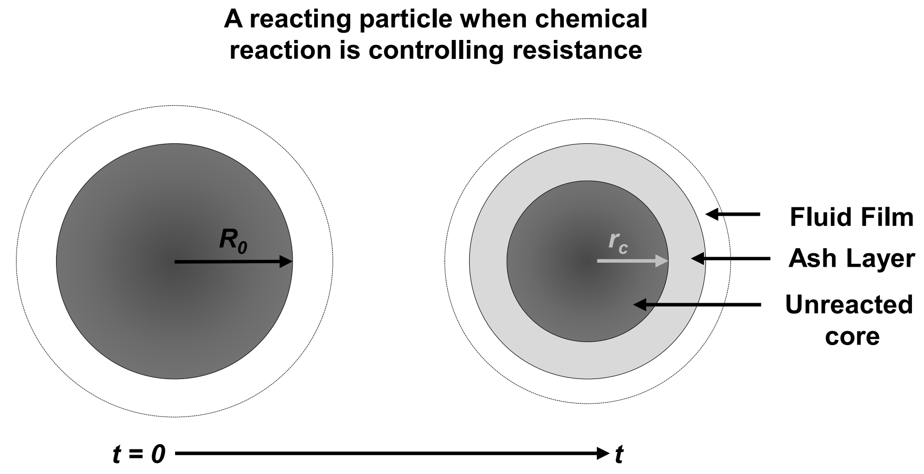

Figure G-1. Representation of a reacting particle when chemical reaction is controlling resistance.

The fractional conversion of solid particles can be written in terms of,

$$1 - X_A = \left(\frac{volume\ of\ unreacted\ core}{total\ volume\ of\ particle}\right) = \frac{\frac{4}{3}\pi r_c^3}{\frac{4}{3}\pi {R_0}^3} = \left(\frac{r_c}{R_0}\right)^3 \qquad (G.6)$$

At the time when a particle with initial diameter of R_0, has shrunk to size r_c, the rate of disappearance reaction of solid A can be rewritten according to equation (G.7),

$$-\frac{1}{S_r}\frac{dN_A}{dt} = ak_B C_B \qquad (G.7)$$

where S_r is the surface of particle (at reaction surface), and k_B is the rate constant based on the dissolution mechanism; therefore, equation (G.7) becomes,

$$-\frac{1}{r_c^2}\frac{dN_A}{dt} = 4\pi ak_B C_B \qquad (G.8)$$

by substituting r_c with $R_0(1 - X_A)^{1/3}$ in equation (G.8),

$$-\frac{dN_A}{dt} = (1 - X_A)^{2/3} \times 4\pi {R_0}^2 a k_B C_B \tag{G.9}$$

then equation (G.9) can be expressed in terms of fractional conversion by equation (G.10),

$$\frac{dX_A}{dt} = (1 - X_A)^{2/3} \times \frac{4\pi {R_0}^2 a k_B C_B}{N_A|_0} \tag{G.10}$$

whereby equation (G.10) can be simplified as,

$$\therefore \frac{dX_A}{dt} = (1 - X_A)^{2/3} \times C_{constant} \tag{G.11}$$

Considering a case in which diffusion through the ash layer is controlling the rate of reaction; hence, the access to the unreacted core may be inhibited as the reaction proceeds. Figure G-2 shows a schematic diagram of shrinking particle with unreacted shrinking core when product layer diffusion is controlling resistance.

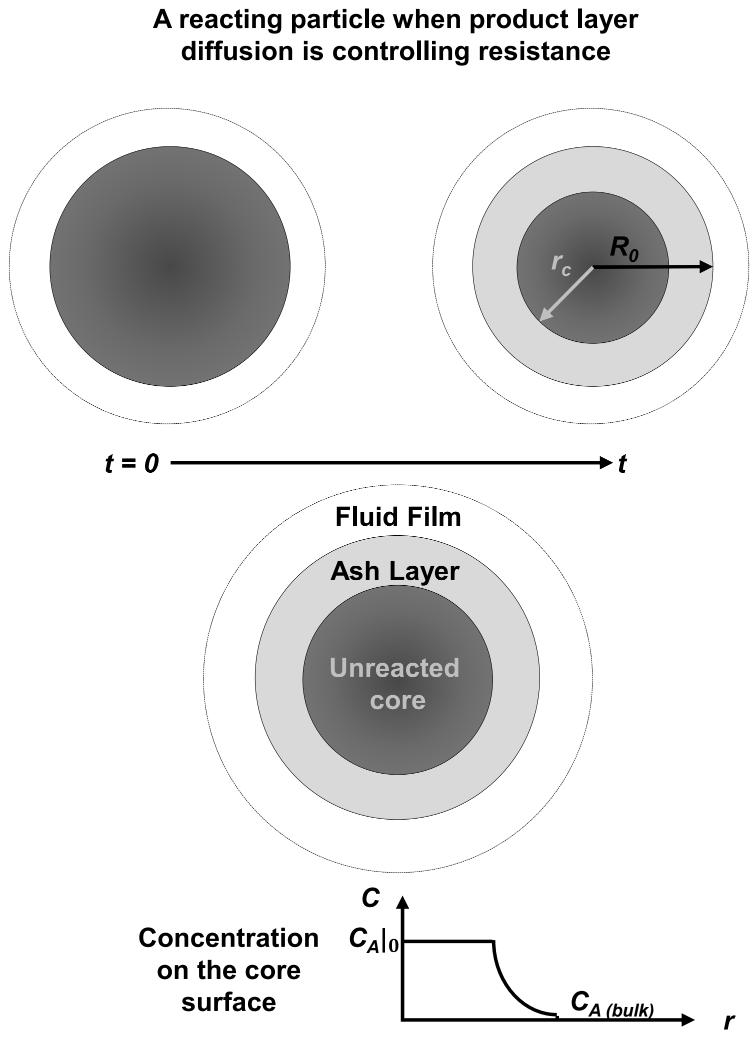

Figure G-2. Representation of a reacting particle when product layer diffusion is controlling resistance.

In the partially reacted particle as shown in Figure G-2, the boundary of the unreacted core move towards the centre of the particle. Assuming the steady-state conditions, the rate of disappearance of *A* at any instant can be written by its rate of diffusion to the reaction surface,

$$-\frac{dN_A}{dt} = 4\pi {R_0}^2 J_{Ar} = 4\pi {r_c}^2 J_{Ar} = constant \tag{G.12}$$

where J_{Ar} is a molar flux of reaction products in the radial direction. Whereby the molar flux can be expressed by Fick's law,

$$J_{Ar} = \mathcal{D}_{eA} \frac{dC_A}{dr} \tag{G.13}$$

where $\mathcal{D}_{eA}$ is the effective diffusion coefficient, and account for the diffusion characteristic of the ash layer. Substitution of the above equations gives,

$$-\frac{dN_A}{dt} = 4\pi {r_c}^2 \mathcal{D}_{eA} \frac{dC_A}{dr} = constant \tag{G.14}$$

integrating across the ash layer from $r_c$to R_0

$$-\frac{dN_A}{dt} \int_{r_c}^{R_0} \frac{dr}{{r_c}^2} = 4\pi \mathcal{D}_{eA} \int_{C_A|_0}^{C_A} dC_A \tag{G.15}$$

assuming negligible mass transfer at the particle surface, the boundary conditions become, $C_A = 0$ at $r = R_0$, and $C_A|_0 = C_{eq}$ at $r = r_c$,

$$-\frac{dN_A}{dt} \left(\frac{1}{R_0} - \frac{1}{r_c} \right) = -4\pi \mathcal{D}_{eA} C_{eq} \tag{G.16}$$

equation (G.16) can be expressed according to equation (G.17),

$$\frac{dN_A}{dt} \left(\frac{R_0}{r_c} - 1 \right) = -4\pi R_0 \mathcal{D}_{eA} C_{eq} \tag{G.17}$$

by substituting ${}^{R_0}/_{r_c}$ in equation (G.17) with $(1 - X_A)^{-1/3}$,

$$\frac{dN_A}{dt} \left((1 - X_A)^{-1/3} - 1 \right) = -4\pi R_0 \mathcal{D}_{eA} C_{eq} \tag{G.18}$$

then equation (G.18) can be written in terms of fractional conversion as shown in equation (G.19),

$$\frac{dX_A}{dt} = \frac{1}{((1 - X_A)^{-1/3} - 1)} \times \frac{4\pi R_0 \mathcal{D}_{eA} C_{eq}}{N_A|_0} \tag{G.19}$$

whereby equation (G.19) can be simplified to equation (G.20),

$$\therefore \frac{dX_A}{dt} = \frac{1}{((1 - X_A)^{-1/3} - 1)} \times C_{constant} \tag{G.20}$$

Therefore, $C_{constant}$ correlations for the models that are presented in Table 5-1, are shown in Table G-1 based on the above derivations.

Table G-1. $C_{constant}$ for the models which are presented in Table 5-1.

Model	$C_{constant}$
Volumetric reaction Model	$\frac{k_v N_B}{N_A\|_0}$
Chemical reaction control	$\frac{4\pi {R_0}^2 a k_B C_B}{N_A\|_0}$
Product layer diffusion control	$\frac{4\pi R_0 \mathcal{D}_{eA} C_{eq}}{N_A\|_0}$

References

ISHIDA, M. & WEN, C. 1971. Comparison of zone-reaction model and unreacted-core shrinking model in solid—gas reactions—I isothermal analysis. *Chemical Engineering Science,* 26**,** 1031-1041.

LEVENSPIEL, O. 1999. Chemical reaction engineering. *Industrial & engineering chemistry research,* 38**,** 4140-4143.

Appendix H. Porosimetry Measurement

H-1. BET Theory and Adsorption & Desorption Isotherms

The Brunauer-Emmett-Teller (BET) method was used for porosimetry measurements in the present study, in which the equation (H.1) is used for determining surface area of solid materials,

$$\frac{1}{W\big((P_0/P)-1\big)}=\frac{1}{W_mC}+\frac{C-1}{W_mC}\left(\frac{P}{P_0}\right) \tag{H.1}$$

where W is the weight of gas adsorbed per weight of sample at a relative pressure of P/P_0, and W_m is the weight of gas adsorbed as a completion of monolayer coverage on the adsorbent surface. The C term is a dimensionless BET constant. Typically, the plot of $1/W\big((P_0/P)-1\big)$ against P/P_0 is linear, and subsequently the value of W_m is required for evaluation of the surface area. The W_m is determined from the slope and intercept of the BET plot. Total surface area S_t was evaluated using the equation (H.2),

$$S_t=\frac{W_mNA_{cs}}{M} \tag{H.2}$$

where M is the molecular weight of the adsorbate molecules, and N is the Avagadro's number (6.023×10^{23} molecules/mole). Nitrogen (N_2) as an adsorbate have the values of M is 28.0123, and A_{cs} is 16.2 $Å^2$ at 77 K. Thereby, the specific surface area of the samples is calculated using equation (H.3),

$$S=S_t/weight_{sample} \tag{H.3}$$

The total pore volume is also calculated from the amount of vapour adsorbed at a relative pressure close to unity (assuming that the pores are then filled with liquid adsorbate) using the equation (H.4),

$$V_{liq} = \frac{P_a V_{ads} V_m}{RT} \tag{H.4}$$

where V_{ads} is the volume of the gas adsorbed (cm^3 g^{-1}), V_m is the molar volume of one mole of liquid nitrogen (34.7 cm^3 mol^{-1}), R is the gas constant (cm^3 kPa K^{-1} mol^{-1}), T and P_a are ambient temperature (K) and pressure (Pa), respectively. The surface areas of the unreacted and reacted (under the standard reaction conditions) research materials were evaluated as 11.96 m^2 g^{-1} and 128.35 m^2 g^{-1}, respectively. Figure H-1 shows the shape of nitrogen isotherms[1] (adsorption and desorption) attained for unreacted material, suggesting that the material is likely disordered and the distribution of pore size and shape is not well defined (Sing, 1985).

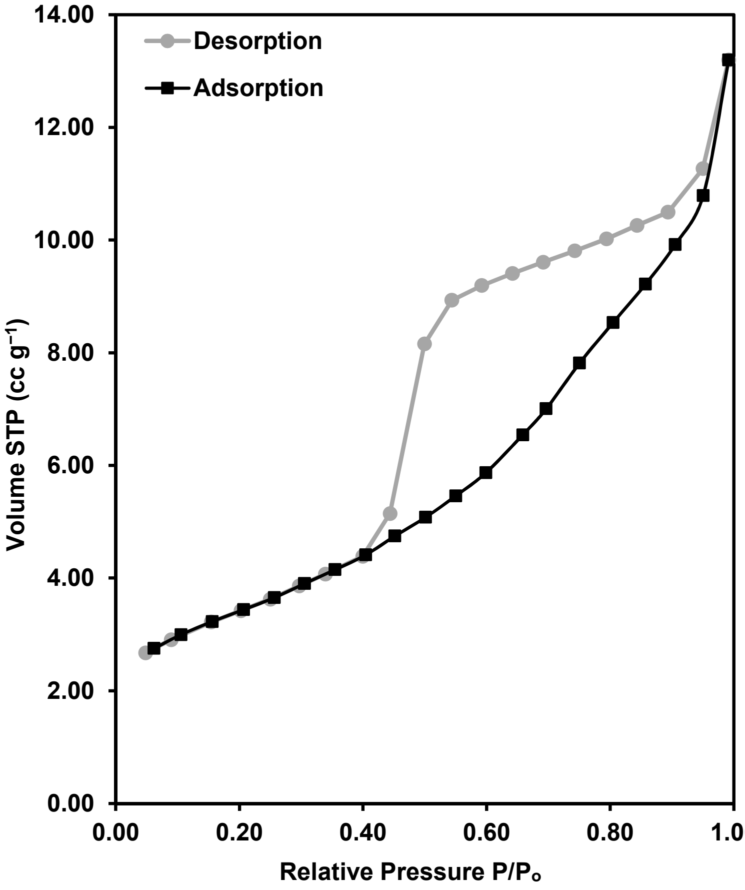

Figure H-1. Nitrogen adsorption/desorption at ~77 K for the unreacted SWOL (thermally activated at T = 900 K for two hours).

---

[1] Adsorption hysteresis loops.

Figure H-2 shows the shape of nitrogen isotherms (adsorption and desorption) attained for the solid residual of the standard dissolution reaction (partially saturated), suggesting that the material is associated with narrow slit pores.

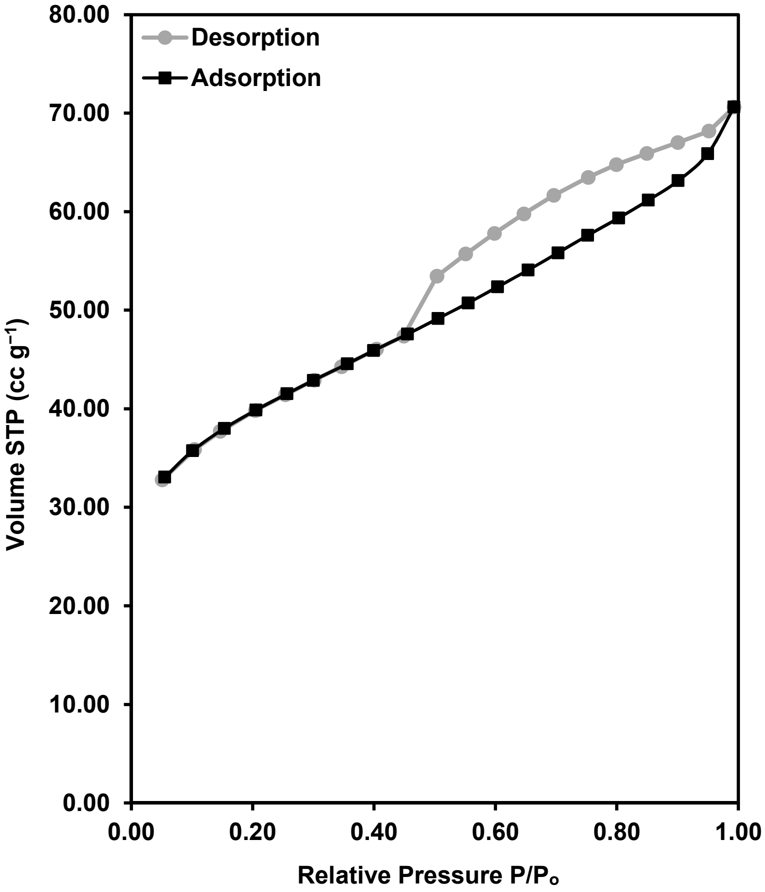

Figure H-2. Nitrogen adsorption/desorption at ~77 K for the reacted SWOL (thermally activated at T = 900 K for two hours) under the standard reaction conditions (partially saturated).

H-2. Pore Size Distribution

The HK analytical method used to show the effective pore distributions from nitrogen adsorption isotherms. The HK approach is based on a fundamental statistical analysis of a fluid confined to a slit-pore (HORVÁTH and KAWAZOE, 1983). Figure H-3 shows the pore size distribution curves for the cases presented in Table 5-2.

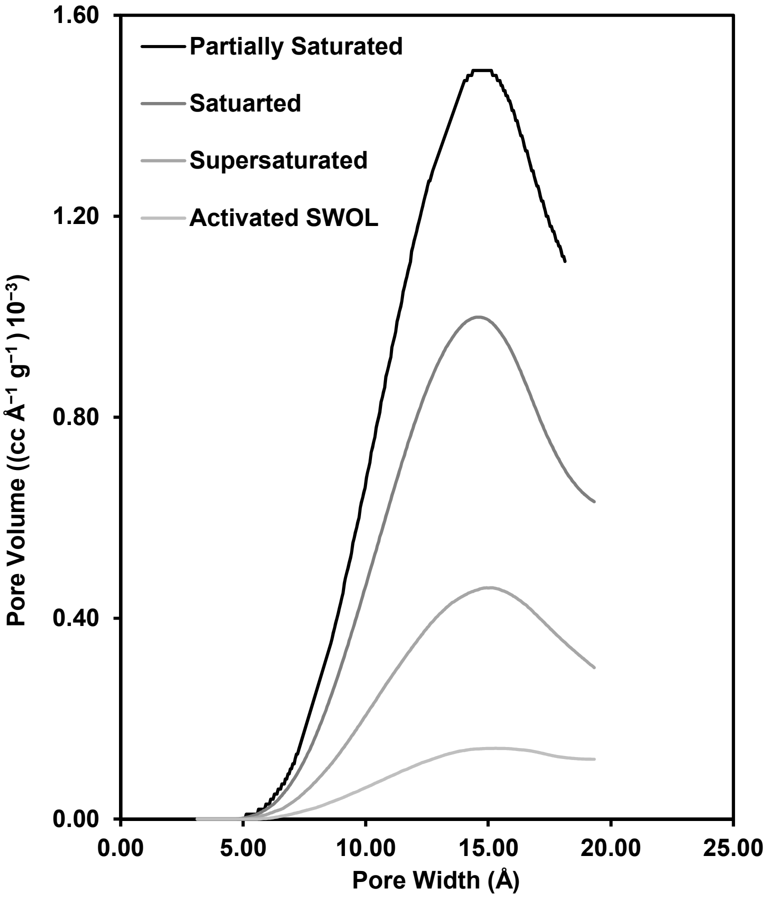

Figure H-3. Horvath and Kawazoe pore size distribution curves for the cases as indicated in the figure**.**

The relative increase in the volume of porous substrate seems to be associated with the increase in the extent of extraction of magnesium and silica.

References

HORVÁTH, G. & KAWAZOE, K. 1983. Method for the calculation of effective pore size distribution in molecular sieve carbon. *Journal of Chemical Engineering of Japan,* 16**,** 470-475.

SING, K. S. 1985. Reporting physisorption data for gas/solid systems with special reference to the determination of surface area and porosity (Recommendations 1984). *Pure and applied chemistry,* 57**,** 603-619.